DISSERTATION

Polyimides - Non-Classical Synthesis and Comprehensive Correlation of Material Properties with Chemical Structure

ausgeführt zum Zwecke der Erlangung des akademischen Grades eines
Doktors der Naturwissenschaften

unter der Leitung von
Prof. Dipl.-Chem. Dipl.-Ing. Dr.rer.nat. Miriam M. Unterlass, MSc
Fachbereich Chemie der Universität Konstanz

eingereicht an der
Technischen Universität Wien
Fakultät für Technische Chemie

von

Dipl.-Ing. Elias Konstantin Bumbaris, BSc
01168254

Wien, am 25.06.2023

Parts of this work were funded by the Austrian Research Promotion Agency *FFG*.
(Project number 874907)

Kurzfassung

Polyimide sind eine weitverbreitete Klasse von Hochleistungspolymeren, welche aufgrund ihrer hervorragenden chemischen, mechanischen, vor allem aber ihrer thermischen Stabilität, in einer Vielzahl an anspruchsvollen Industrieanwendungen eingesetzt werden. Vor allem Letzteres, sowie ihre Fähigkeit, als leicht aufzutragendes Dielektrikum zu fungieren, machen Polyimide für mikroelektronische Anwendungen unverzichtbar. Sie weisen jedoch drei große Nachteile auf: (i) Polyimide werden auf äußerst schädlichen Wegen synthetisiert und verarbeitet. (ii) Sie können mikroelektronische Bauteile nicht vollständig vor Korrosionsschäden schützen, was höchstwahrscheinlich eng mit ihrer intrinsisch gegebenen Tendenz zur Wasseradsorption zusammenhängt. (iii) Ihre thermische Belastbarkeit hängt in hohem Maße von verschiedenen strukturellen Merkmalen ab, die häufig variiert werden, um ihre Verarbeitbarkeit zu verbessern. Die vorliegende Arbeit soll einen Beitrag zur Überwindung dieser drei Problemstellungen leisten und ist daher in drei Teile gegliedert. Im ersten Teil wurden klassische und alternative, grüne Synthesewege für Polyimide genutzt und verglichen, wobei für die alternativen Methoden Monomersalze als Polyimidvorläufer hergestellt und hauptsächlich durch hydrothermale Synthese zu Polyimiden polymerisiert wurden. Letztere Methoden sind nicht nur deutlich weniger schädlich als klassische Synthesewege, sondern führen auch zu einer deutlich höheren Kristallinität der Endprodukte. Im zweiten Teil wurden die Struktur-Eigenschafts-Beziehungen im Hinblick auf das Feuchtigkeitssorptionsverhalten von Polyimiden beleuchtet. Hierfür wurden verschiedene, strukturell unterschiedliche Polyimide synthetisiert und durch Spin-Coating und Drop-Casting in dünnen Filmen auf unterschiedlichen Trägermaterialien aufgetragen, wobei ein klassischer Syntheseweg über lösliche und somit verarbeitbare Vorläuferpolymere angewandt wurde. Zu den strukturellen Variationen gehören Polymere mit oft identischer Zusammensetzung, aber unterschiedlichen Substitutionsmustern innerhalb der Monomerbausteine, sowie unterschiedliche endständige und überbrückende funktionelle Gruppen. Diese Polymere wurden im Hinblick auf die Aufnahme- und Diffusionsfähigkeit von Wasserdampf in den Polyimidfilmen mit Hilfe der dynamischen Dampfsorption intensiv untersucht. Im dritten Teil wurde der Einfluss ebensolcher Strukturvariationen auf die thermische Stabilität dieser Polymere untersucht. Zu diesem Zweck wurden sowohl klassisch als auch hydrothermal synthetisierte Polyimide hinsichtlich ihrer thermischen Zersetzungssignaturen mittels thermogravimetrischer Analyse verglichen, wobei verschiedene Methoden zum Erhalt dieser Daten herangezogen und diskutiert wurden.

Abstract

Polyimides (PIs) are a well-established class of high-performance polymers. PIs are being widely used in a broad range of industrial applications, based on their outstanding chemical, radiative and mechanical stability, but most importantly their thermal resilience. Especially the latter, as well as their capacity to act as an easily applicable dielectric make PIs indispensable in microelectronic components. However, PIs present three major disadvantages: (i) PIs are synthesized and processed by harsh and harmful routes. (ii) They cannot fully protect microelectronic components from corrosion phenomena, which is hypothesized to be closely connected to PIs' inherent affinity to adsorb water. (iii) Their thermal resilience is highly dependent on various structural features which oftentimes are modified to enhance their processability.

This thesis aims at contributing to overcome these three major issues, and is thus subdivided into three parts. In a first part, classical routes and alternative green synthetic pathways toward PIs were utilized and compared. Specifically for the latter, alternative monomer-salt precursors were prepared and converted to PIs primarily by hydrothermal synthesis. Aside being significantly less harmful than classical syntheses, these methods mostly lead to highly increased crystallinity.

In a second part, this thesis aims at shedding light on the structure-property relationships in PIs with respect to moisture sorption behavior. To reach this goal, various structurally different PIs were synthesized and processed into thin films on different supports by spin-coating and drop-casting, employing a classical synthesis pathway via soluble and processable precursor polymers. The structural variations in the synthesized PIs include polymers of oftentimes identical composition yet varying connectivities within the monomeric units' building blocks, as well as different terminal and bridging functional groups. The PI samples were studied intensively with respect to the uptake and diffusivity of water vapor in the PI films utilizing the analytical technique of dynamic vapor sorption.

In a third part, the influence of such structural variations on these polymers' thermal stability were investigated. For that, both classically and hydrothermally synthesized PIs were studied and compared intensively with respect to their thermal signatures of decomposition using thermogravimetric analysis, while utilizing and discussing several methods to obtain this data.

Acknowledgments

Mein größter Dank gilt Miriam M. Unterlass dafür, dass sie mich so unzögerlich in ihr Team aufnahm, mich stets unterstützte, jederzeit großes Vertrauen entgegenbrachte, aber auch dafür, dass sie mir anfangs überzeugende Incentives und Kapazitäten zum Fertigstellen meiner vorherigen Abschlussarbeit einräumte. Diese vier Jahre in ihrem Team waren unglaublich lehrreich und inspirierend. Darüberhinaus danke ich Alexander Bismarck und Herbert Hutter sehr dafür, dass sie mit ihrer wertvollen Zeit und Expertise für die Begutachtung dieser Arbeit zur Verfügung stehen. Großer Dank gilt natürlich auch dem gesamten Team des UnterlassLab -in allen Konstellationen über all die Jahre meiner Mitgliedschaft- für die stets tolle und konstruktive Zusammenarbeit und die freundschaftliche und loyale Atmosphäre. Die zahlreichen Abende in der RaucherInnenlounge, aber auch die vielen Laborspätschichten mit D. Alonso Cerron Infantes, Lukas Leimhofer und viel Retrotanzmusik bleiben unvergessen. Mein besonderer Dank gilt hierbei M. Josef Taubländer, dafür, dass er mich sofort unter seine Fittiche nahm, mich oft genug auf den Boden zurückholte und in so vielen Belangen unterstütze. Ihm, Marianne Lahnsteiner, M. Musthafa Iqbal und Patrick W. Fritz danke ich auch für die wunderbare Freundschaft und die tolle gemeinsame Zeit sowohl innerhalb als auch außerhalb der Arbeit. Des Weiteren danke ich Silvia Larisegger sehr für ihre durchwegs tatkräftige Unterstützung und ihr passioniertes Engagement. Großer Dank gilt auch Alexander Bismarck, welcher mir so bereitwillig zahlreiche Messtage an seiner DVS zur Verfügung stellte.

Natürlich danke ich auch meiner Familie, allen voran meiner Schwester, meiner Mutter und meinem Vater dafür, dass sie immer an mich glaubten und mir von klein auf einen hohen Stellenwert der Bildung vermittelten. Meiner Liebsten Anna danke ich für ihre liebende und bedingungslose Unterstützung, ihr stetiges Motivieren, ihre tatkräftige Beseitigung meiner Zweifel und ihren steten Glauben an mich. Zuletzt danke ich unserer kleinen, gemeinsamen Familie Mochi, Matcha und Shōga für die vielen unterstützenden Momente der Zuneigung und des Gurrens.

Table of Contents

List of Abbreviations

General Abbreviations

ATR-FTIR	Attenuated total reflectance Fourier transform infrared
DTG	Derivative thermogravimetry
DVS	Dynamic vapor sorption
HT	Hydrothermal
HT-PI	Hydrothermally synthesized polyimide
IR	Infrared
MW	Microwave
NMR	Nuclear magnetic resonance
PAA	Poly(amic acid)
PEI	Polyetherimide
PI	Polyimide
PPPI	Poly(*p*-phenylene pyromellitimide)
PTFE	Polytetrafluoroethylene
PXRD	Powder X-ray diffraction
RH	Relative humidity
RT	Room temperature
SCXRD	single crystal X-ray diffraction
SEM	Scanning electron microscopy
SSP	Solid-state polymerization
TGA	Thermogravimetric analysis

Symbols

c	Concentration	[g mol^{-1}]
CY	Char yield	[%]
D	Diffusion coefficient	[cm^{2}s^{-1}]
D_{avg}	Averaged diffusion coefficient	[cm^{2}s^{-1}]
M_∞	Absolute water uptake at equilibrium	[g]
$M(t)$	Absolute water uptake at a time t	[g]
L	Film thickness	[µm]
t	Time	[s]
T	Temperature	[°C]
T_d	Decomposition temperature	[°C]
$T_{d,371}$	Decomposition temperature at 5 % weight loss after reaching 371 °C	[°C]
$T_{d,400}$	Decomposition temperature at 5 % weight loss after reaching 400 °C	[°C]
$T_{d,max}$	Decomposition temperature at maximum decomposition rate	[°C]
$T_{d,onset}$	Decomposition temperature at tangent-derived onset	[°C]

Monomers and Compounds

Abbreviation	Compound Name	CAS Registry Number
6FDA	4,4′-(hexafluoroisopropylidene)diphthalic anhydride	1107-00-2
aBPDA	2,2′,3,3′-Biphenyltetracarboxylic dianhydride	36978-41-3
aODA	3,4′-Oxydianiline	2657-87-6
aODPA	3,4′-Oxydiphthalic anhydride	50662-95-8
APBP	4,4′-Bis(4-aminophenoxy)biphenyl	13080-85-8
8FAPBP	4,4′-Bis(4-aminophenoxy)octafluorobiphenyl	68090-63-1
BAPF	9,9-Bis(4-aminophenyl)fluorene	15499-84-0
BAPP	2,2-Bis[4-(4-aminophenoxy)phenyl]propane	13080-86-9
6FBAPP	2,2-Bis[4-(4-aminophenoxy)phenyl]hexafluoropropane	69563-88-8
BPADA	4,4′-(4,4′-Isopropylidenediphenoxy)bis(phthalic anhydride)	38103-06-9
BPAF	9,9-Bis(3,4-dicarboxyphenyl)fluorene dianhydride	135876-30-1
BTDA	3,3′,4,4′-Benzophenonetetracarboxylic dianhydride	2421-28-5
BuTCA	*meso*-Butane-1,2,3,4-tetracarboxylic acid	4534-68-3
Bz	Benzidine	92-87-5
DABP	4,4′-Diaminobenzophenone	611-98-3
DADF	3,6-Diaminodibenzofuran	10017-73-9
DAF	2,7-Diaminofluorene	525-64-4
DATP	4,4′′-Diamino-*p*-terphenyl	3365-85-3
DMAc	*N*,*N*-Dimethylacetamide	127-19-5
DMF	*N*,*N*-Dimethylformamide	68-12-2
DMSO-d6	Hexadeuterodimethyl sulfoxide	2206-27-1
DSDA	3,3′,4,4′-Diphenylsulfonetetracarboxylic dianhydride	2540-99-0
EDA	Ethylenediamine (used as monohydrate)	6780-13-8
mBAPB	1,3-Bis(4-aminophenoxy)benzene	2479-46-1
mBISA	4,4′-(1,3-Phenylenediisopropylidene)bisaniline	2687-27-6
MDA	4,4′-Diaminodiphenylmethane	101-77-9
mDMBz	2,2′-Dimethylbenzidine	84-67-3
MeBAPF	9,9-Bis(4-amino-3-methylphenyl)fluorene	107934-60-1
mPDA	*m*-Phenylenediamine	108-45-2
1FmPDA	4-Fluoro-1,3-phenylenediamine	6264-67-1
4FmPDA	2,4,5,6-Tetrafluoro-1,3-phenylenediamine	1198-63-6
mTFBz	2,2′-Bis(trifluoromethyl)benzidine	341-58-2
NMP	*N*-Methyl-2-pyrrolidinone	872-50-4
oDFBz	3,3′-Difluorobenzidine	448-97-5
oDHBz	3,3′-Dihydroxybenzidine	2373-98-0
oDIAN	3,3′-Dimethoxybenzidine	119-90-4
oDMBz	3,3′-Dimethylbenzidine	119-93-7
oTFBz	3,3′-Bis(trifluoromethyl)benzidine	346-88-3
pBAPB	1,4-Bis(4-aminophenoxy)benzene	3491-12-1
pBISA	4,4′-(1,4-Phenylenediisopropylidene)bisaniline	2716-10-1
PMA	Pyromellitic acid	89-05-4
PMDA	Pyromellitic dianhydride	89-32-7
pPDA	*p*-Phenylenediamine	106-50-3
sBPDA	3,3′,4,4′-Biphenyltetracarboxylic dianhydride	2420-87-3
sODA	4,4′-Oxydianiline	101-80-4
sODPA	4,4′-Oxydiphthalic anhydride	1823-59-2
THF	Tetrahydrofuran	109-99-9

List of Figures

List of Tables

1. Introduction

1.1 Polyimides

There are several definitions of which organic polymeric material should be considered a high performance polymer, the most important of which is probably the definition related to unusual resistance to high temperatures compared to conventional polymers.[1] Among all high-performance polymers, polyimides (PIs) have been the ones industrially most relevant and prevalent for several decades due to their extraordinarily high thermal stability as well as many other characteristics beneficial for numerous demanding applications, despite their usually limited processability arising from inherent insolubility, infusibility and high glass-transition temperatures.[2,3] Mostly found as part of a five-membered ring, the imide group inherent and eponymous to PIs is defined by an sp^3-hybridized nitrogen atom bound to two carbonyl moieties.[2] In a most straightforward approach, it is formed in a condensation reaction of an amine with two adjacent carboxylic-acid moieties (or one cyclic dianhydride) accompanied by the release of water. Other approaches include the amine reacting with adjacent carboxylic esters or carboxylic-acid halides under the release of an alcohol or hydrogen halide (e.g. HCl), respectively. Although somewhat rare, PIs containing six-membered imide rings are possible as well and can form if two carbonyl substituents participating in an imide bond are not within a vicinal substitution pattern but isolated by an additional carbon atom. Industrially most relevant are those PIs that have a predominantly aromatic character, meaning that the monomeric segments connected by imide groups mostly comprise phenyl moieties, since the resulting high degree of aromaticity is highly beneficial for their overall stability.[2] Nevertheless, if a PI solely consists of (single, C_{ar}-C_{ar}-bridged, or fused) benzene rings connected by imide groups it represents a rigid-rod polymer (cf. fig 1.1) bearing limited to nonexistent molecular and macroscopic flexibility which restricts its industrial applicability.

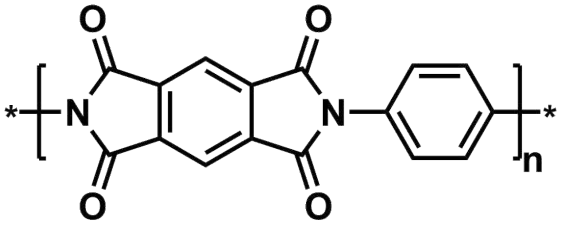

Figure 1.1: Molecular structure of a PI repeating unit. Here, the structurally most simple aromatic PI system PMDA-pPDA is depicted. This PI is derived from the polycondensation of the co-monomers pyromellitic dianhydride (PMDA) and *p*-phenylenediamine (pPDA).

Therefore, most commercially relevant PI products are synthesized from monomers bearing moieties bridging the imide-linked benzene rings such as aliphatic isopropyl moieties, ether bridges, ketone carbonyls or amide linkages resulting in PI materials with improved flexibility.[4] Incorporating these bridging moieties allows for nomenclature-related specifications such as poly(ether imide)s (PEIs), poly(amide imide)s or poly(ketone imide)s. However, since their polymer backbone is comprised of regularly appearing imide moieties which can be considered quite dominant in terms of influence on polymer properties, these subgroups usually are subsumed under the term polyimide within scientific literature and within this thesis. Besides improved flexibility, the incorporation of these additional bridging moieties is accompanied by shifts in other fundamental molecular aspects such as free volume, intra-, and interchain interactions, which is highly likely to have great impact on several other material properties. While maintaining a focus on microelectronic applications, the impact of varying these connectivities on both thermal stability as well as moisture sorption behavior were investigated within this thesis.

1.2 Properties of Polyimides

Today, PIs are widely used as insulating material against cosmic radiation in the aerospace industry,[5–7] for various applications in filtration and membrane technology,[8–10] and as alignment layers for liquid crystal displays,[11–13] among many others, due to their outstanding properties. Moreover, both their electrical properties and their high-temperature resilience have led to a widespread use of PIs in the electronics industry as dielectrics in electronic packaging, flexible substrates and wire insulation.[14–17] Among their electrical properties, their generally low values of relative permittivity (i.e. dielectric constants) are of high importance, since in electronics packaging, materials bearing low permittivity minimize effects of crosstalk and maximize the propagation speed of

signals in electronic devices.[18] The magnitude of polymer permittivity is dependent on "the ability of the polarizable units in a polymer to orient fast enough to keep up with the oscillations of an alternating electric field"[18] by reorientation of these groups in space in response to this field.[19] Although the cyclic imide moiety itself consists of highly polar functionalities, the dipoles of the carbonyl moieties oppose each other in a mirrored arrangement. Moreover, the imide rings directionally oppose each other along the polymer backbone. This geometric constellation of polar groups somewhat neutralizes their polarizability and "simulates the bulk effect of a non-polar polymer making polyimides good dielectric materials".[2] It has to be noted that PIs exhibiting high dielectric constants enjoyed increased scientific interest in recent years, specifically as high-temperature resistant capacitors for energy storage applications.[20–22] Such materials are mostly realized by choosing monomers comprising bulky side groups increasing the motion range of the polar moieties and therefore facilitating their orientation along an induced electric field.[22,23] However, a PI's behavior in electric fields is somewhat co-governed by its eponymous polar groups (among others) allowing for non-negligible interactions with water molecules from ambient humidity. This humidity often times turns out to be the cause for failure of electronic devices incorporating PIs.[24,25] Another aspect which is of significance in many applications which include PI coatings are their coefficients of thermal expansion, since such a coating should ideally exhibit values for thermal expansion comparable to those of the substrate. This topic goes in tandem with the adhesion of these PIs to such substrates, which can naturally be strong depending on the choice of substrate and PI system, or be enhanced by adhesion promoters.[26] However, aspects on both thermal expansion and adhesion are not within the focus of this thesis and have extensively been dealt with in the scientific literature of the past decades.[27–33] Furthermore, the bulk mechanical properties of PIs are amongst the highest of commercially available polymers.[34] This is mainly due to their interchain interactions, aromatic character and molecular rigidity generally causing high values for mechanical strength and elastic moduli over a broad temperature range.[35,36] But not only their mechanical properties are governed by these attributes. They are responsible for the extraordinarily high thermal stability as well, which can be considered the most important feature of PIs. This class of high-performance polymers in most cases comprises mainly strong covalent bonds, such as intercarbon double bonds, carbon-nitrogen bonds and carbonyl bonds, which also allow for extensive resonance stabilization, all of which significantly contribute to their thermal resilience.[1,37] Moreover, the rigid aromatic building blocks and the cyclic imide moieties are able to avert molecular vibrations which can lead to

bond rupture.[1] A high degree of aromaticity also allows for interchain π-π stacking, which generally generates high packing densities in PIs and substantially contributes to their overall stability.[2,38]

Studies focusing on thermal stability and moisture uptake, which are two of the most vital PI properties regarding microelectronic applications, are presented within this thesis, elucidating relationships between molecular structure and resulting properties of numerous PIs. Few publications compare these properties cover the range of different PI systems as extensive as it was done here.

1.3 Synthetic Pathways to Obtaining Polyimides

1.3.1 Classical Synthesis of Polyimides

Bogert and Renshaw first reported syntheses of polyimides by heating the dimethyl ester of 4-aminophthalic acid and specifically by heating 4-aminophthalic anhydride to temperatures above 200 °C in solid state yielding a "polymolecular imide".[39] Defining the anhydride moiety as a single functional group for reasons of simplicity (although the anhydride moiety itself might actually be considered a condensation product of two carboxylic acid moieties which represent two functional groups themselves), in this case of a first PI synthesis a bifunctional monomer having both functional groups necessary for a condensation reaction were found on the same monomer (AB polycondensation). However, synthesizing PIs by AA/BB polycondensation using the two monomer types diamines and dianhydrides,[40] each bearing two similar functional groups which could react with the ones found on the other monomer type, has gained highest industrial prominence. Utilizing this two-monomer approach, most significant pioneer work for commercializing PIs was done by DuPont in the mid-twentieth century, a company which was granted the first patent for PI preparation in 1955[41], followed by several other patents in the field of PI materials and their synthesis. DuPont's Kapton films represent the first commercially produced PI products,[42] and the probably most successful, prominent and abundantly used ones ever since. Moreover, their two-step method for obtaining PIs[43,44] went down in history as the classical synthesis of PI.

The synthetic approach of adding stoichiometrically correct amounts of both monomer types dianhydride and diamine to a suitable, high-boiling solvent and heating the mixture to temperatures close to or above 200 °C is often times included when describing a classical route to PIs in relevant literature.[45–47] However, this single-step method merely

yields powder-like PI products with limited crystallinity and seems to be of scientific interest only. It has been used for analyzing lattice parameters of the semicrystalline products,[48] or for synthesizing oligomers as prepolymers for further reactions to polymers.[49–52] A far more prevalent method for obtaining PIs is utilizing a synthetic approach in two steps, which -if successful- can yield highly continuous materials and is therefore used to generate fibers, foams and especially films and coatings even on an industrial scale. It represents the most established and widespread method of producing PIs on an industrial scale and could therefore be considered the true classical method of PI synthesis.[53]

This route's first step is initiated by combining the two different monomer types dianhydride and diamine in a suitable, anhydrous solvent in which they could form a soluble precursor polymer. It utilizes the tendency of dianhydrides and diamines to undergo nucleophilic substitution reactions due to the amine functionalities being prone to nucleophilic attacks on one of the carbonyl carbons within the anhydride functionalities.[54] Such an attack leads to cleavage of the anhydride group by the formation of an amide bond between both monomers with an adjacent carboxylic acid functionality arising from the anhydride moiety as well. Depending on reactivity of each monomer type, this reaction may already take place below room temperature, and will propagate by occurring on both amine groups of the diamine and both anhydride groups of the dianhydride leading to a polymeric material, which is commonly called poly(amic acid) (PAA). In contrast to the final product this precursor polymer is soluble and can be processed by means of e.g. spin coating, film casting or various forms of fiber spinning. Solvents for synthesizing these PAAs are either high-boiling phenolic or polar-aprotic ones while those most commonly used are amide solvents such as *N*,*N*-dimethylformamide (DMF), *N*,*N*-dimethylacetamide, and (DMAc) *N*-methyl-2-pyrrolidinone (NMP),[54–56] since these "solvent molecules can closely associate with the hydroxyl protons, effectively isolating them from interacting with other anhydrides and amic acids".[2] After the PAA has been brought into shape, it can be converted by either chemical means via dehydration agents such as acetic dianhydride combined with a triamine (both in amounts equimolar to both monomers), or -more preferably- by simply heating to elevated temperatures.[2,57] The temperature range for the latter may already start below 150 °C, however, exposing the precursor polymer temperatures above 200 °C could be recommended for full release of solvent and water (as reaction by-product) from the system.[2,58,59]

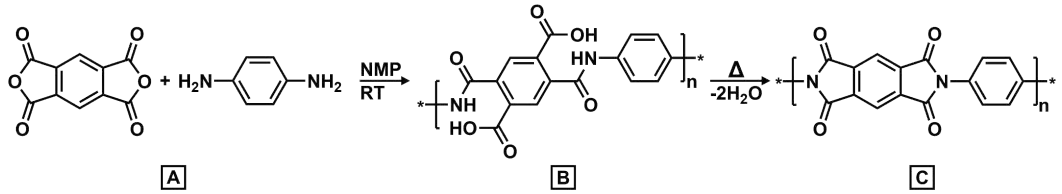

Figure 1.2: Classical two-step synthesis of PIs illustrated using the example of the PMDA-pPDA system. (**A**) Combining the two comonomers pyromellitic dianhydride (PMDA) and *p*-phenylenediamine (pPDA) in a suitable solvent such as anhydrous *N*-methyl-2-pyrrolidone (NMP) at room temperature (RT) yields (**B**) a poly(amic acid) (PAA), which is soluble and can be processed into different shapes and forms. Curing this precursor polymer using high temperatures yields (**C**) a PMDA-pPDA PI via a polycondensation reaction accompanied by elimination of two equivalents of water.

As the reaction from monomers to PIs are polycondensation reactions following a step-growth mechanism, small stoichiometric imbalances caused by impurities or during weighing will most probably result in a significant decrease in average polymer chain length as described in Carother's law.[60,61] Therefore, when aiming for high molecular weight of PIs not only highly balanced equimolarity has to be ensured, also maximum possible purity of the monomers is necessary, which is mostly achieved by means of sublimation. Moreover, water within the system -might it be from an non-anhydrous or hygroscopic solvents or monomers- may cause hydrolysis of the PAA and precipitation of a monomer salt by practically rendering the solvent a protic one. Within this thesis, if a PI was synthesized classically, this two-step method was employed while spin-coating or drop-casting PAAs on a suitable substrate and subsequent thermal curing to obtain PI films.

1.3.2 The Hydrothermal Route

As the name implies, the term hydrothermal synthesis denotes a synthetic procedure which takes place in high-temperature water above 100 °C.[62,63] To reach temperatures above its boiling point, the reaction medium water has to be enclosed in sealed vessels under build-up autogenous pressure in isochoric conditions. Such vessels could be sealed glass tubes, steel-bomb autoclaves or microwave-reactor vials specifically designed for this purpose. The thermal regions in which high-temperature water occurs can be subdivided into three regimes: The hydrothermal regime ranging from approximately 100 °C to 250 °C, the near-critical regime ranging from approximately 250 °C to 350 °C, and the supercritical regime starting above the critical temperature of 374 °C.[64] The hydrothermal regime can be considered the most relevant for organic synthesis, specifically in in the range from 150 °C to 250 °C, a regime in which liquid and gaseous phases coexist

in a dynamic system.[64–67] While heating up, water severely changes its properties under these conditions of high temperatures and high pressures, mainly due to the breakdown of it's hydrogen bonding behavior by reducing the number of hydrogen bonds per molecule and the lifetime of hydrogen bonds.[68–70] On one hand, the ionic product of water shifts to much higher levels compared to room temperature of approximately 2.7 orders of magnitude at 200 °C, up to a maximum of approximately 2.8 orders of magnitude at 250 °C.[71] This means that the concentration of both hydroxyl and hydronium ions increases -equally, due to water's amphoteric character- by more than one order of magnitude.[71,72] As a consequence, the reaction medium itself may act as an increasingly strong acidic, basic or even acido-basic bicatalyst with increasing temperature.[64,73] Secondly, both the density and viscosity of water decrease significantly,[74–76] which is highly beneficial for reactions controlled by diffusion such as non-stirred autoclave reactions. Moreover, the static dielectric constant of water (as a measure of solvent polarity) decreases as well.[77] This means that water becomes a less polar solvent upon heating, resembling the moderate polarity of several organic solvents at room temperature.[64,70] As a consequence, heating water to hydrothermal conditions enables solubilization of otherwise hardly or non-soluble substances or materials.[59,78,79]

Describing the conditions at which water heated to temperatures above it's boiling point acts within the earth's crust, the term *hydrothermal* purely originates from the field of geology.[80] There are several definitions of what hydrothermal synthesis exactly is,[81–85] while most authors agree on it being synthetic procedures in an aqueous medium at temperatures above 100 °C and pressures above one atmosphere.[80] However, it mimics geological processes i.e. the formation of minerals upon cooling of superheated aqueous solutions of inorganic compounds (in e.g. veins),[64] and was adopted by humankind almost two hundred years ago. In the midst of the nineteenth century, pioneering experiments in hydrothermal synthesis of several minerals such as apophyllite, diaspore, and various carbonates were conducted by Bunsen, Wöhler, Haidinger and Sénarmont,[86,87] while Schafhäutl with his synthetic procedures for obtaining quartz crystals was the first to publish on this subject.[88] In the course of the following century, the number of inorganic compounds accessible via hydrothermal synthesis increased tremendously, while the production of some grew to an industrial scale.[89,90]

However, it is only in the last few decades that the hydrothermal approach has been adopted for the synthesis of organic compounds, more specifically for condensation reactions of cyclic connecting moieties. In the 1990s, a group of authors including Dao and Hodgkin published their works (and patents) on the utilization of hydrothermal synthe-

sis for obtaining imide compounds of low molecular weight from aromatic dianhydrides and diamines, which were intended for use as monomers for further polymerization reactions.[63,91,92] Soon after and using similar starting materials, the same circle of authors published several works on the hydrothermal synthesis of polymeric imide materials i.e. PIs,[93–96] which was soon followed by acceleration of these procedures by utilizing microwave irradiation-assisted hydrothermal polymerization.[97,98] However, unlike their inorganic counterparts in geological or industrial processes, these hydrothermally synthesized PIs were mostly amorphous in nature. In 2014, Unterlass and co-workers reported on their successful strategies to hydrothermally synthesize PIs of unprecedentedly high crystallinity:[99] In a first step, a diammonium-dicarboxylate monomer-salt precursor from pyromellitic acid (or the corresponding dianhydride) and *p*-phenylenediamine bearing an ideal equimolar stoichiometry was synthesized via an acid-base reaction in water and isolated (c.f. figure 1.3). Although monomer salts (from non-esterified tetracarboxylic acids) as PI precursors were known to and used by Imai and coworkers for syntheses of PIs in solid state,[100–104] the identification of monomer-salt formation as an intermediate reaction stage in the hydrothermal synthesis of PIs starting from the neat monomeric constituents was accomplished by Unterlass et al.[62]

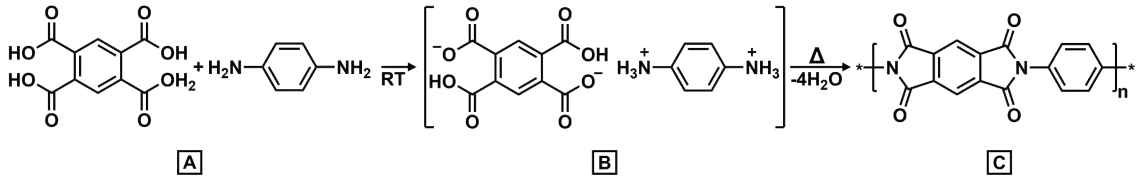

Figure 1.3: Hydrothermal synthesis of PIs illustrated using the example of the PMDA-pPDA system. (**A**) Combining the two comonomers pyromellitic acid (PMA) and *p*-phenylenediamine (pPDA) in a suitable protic solvent such as water at room temperature (RT) precipitates (**B**) a monomer salt. Exposing it to hydrothermal conditions yields a highly crystalline (**C**) PMDA-pPDA PI via a polycondensation reaction accompanied by elimination of four equivalents of water.

Given that the monomers form salts at an one-to-one ratio, isolating these precursors beforehand naturally ensures an ideal stoichiometric ratio of the two co-monomers, which is known to be beneficial for obtaining condensation polymers of high molecular weights (c.f. section 1.3.1). Upon heating the reaction medium containing the dispersed monomer salt to sufficiently high temperatures, the strongly altered physico-chemical properties of water enable the dissolution and simultaneous polymerization of such organic compounds. Intriguingly, as this reaction is a polycondensation with water emerging as a by-product, this reaction does take place despite the fact that water is the reaction medium (in huge excess), and one might therefore expect a shift in the reaction equilibrium toward the starting product side. It is proposed that during this process, a limited

amount of monomer salt dissolves within the medium and polymerizes in solution, after or during which the reaction product can crystallize at existing nucleation sites or out of the solution directly.[47,105,106] Then again, more of the dispersed monomer salt can dissolve, polymerize and crystallize until it is consumed. This process has been shown to yield PIs of unparalleled crystallinity. However, during the process of heating up a fraction of the monomer salt can already polymerize in the lower HT regime, while non-dissolved fractions of the precursor can undergo solid-state polymerization, all of which can lead to lower crystallinity of the product.[105] These effects can be suppressed by adjusting reaction parameters such as precursor concentration or acceleration of the heating process by e.g. microwave-assisted hydrothermal synthesis. Moreover, it has to be noted that the exact mechanistic pathway from monomer salt to PI has not yet been fully elucidated,[62,63,107] which means that -unlike in classical PI synthesis- the existence of intermediate products or transition states is still unknown. Nonetheless, as both in the case of classical pathway via PAA formation and in the case of hydrothermal synthesis starting from tetracarboxylic acids the overall reaction proceeds via cleaved anhydride moieties, the formation of PIs could be considered cyclopolycondensation reactions.[40] Be that as it may, the technique of hydrothermal synthesis proved highly useful for the generation of organocyclic moieties such as imides, pyrrones, and benzimidazoles, and even for hybrid materials of silica and PIs.[67,108–110] Furthermore, no harmful solvents are involved but instead water is the sole reaction medium, which can be fully recovered after cooling to below boiling point. This is in stark contrast to the classical synthesis of PIs, which typically uses hazardous solvents that will inevitably evaporate during the PI curing process, making them difficult to recover. In addition, the classical method must be performed in a constantly inert atmosphere and requires the solvents to be highly pure and anhydrous. In view of the foregoing, hydrothermal synthesis of PIs represents an environmentally benign, highly facile and straightforward method to synthesize PIs of high crystallinity.

2. Aims and Objectives

For several decades now, polyimides have been the polymer type of choice as packaging dielectrics in the vast majority of microelectronic applications. Although commercially available PI products can be applied onto microelectronic components in finely structured patterns and generally protect these components from interference and electrical damage by exhibiting low relative permittivity and high electrical disruptive strength, respectively, they seem to insufficiently protect them from corrosive damage. This is suspected to be due to their intrinsically polar nature causing a fairly significant affinity to water, which can be absorbed from humid environments and thereby allows for a somewhat facilitated ion mobility throughout the material resulting in corrosive phenomena taking place over the course of a component's service lifetime.

In order to gain insights on how the chemical structure of a PI has an influence on its moisture affinity, to identify structural features allowing for a reduction of this effect, and to ultimately reduce corrosive effects taking place within such components, it was aimed for identifying structure-property relationships particularly regarding the moisture absorption behavior of classically synthesized PI films utilizing the analytical method of dynamic vapor sorption.

However, the probably most important aspect of PIs leading to their widespread use in many fields is their generally high thermal stability. It was therefore natural to consider exactly exact structural features from a thermal-stability perspective as well, using the straightforward method of thermogravimetric analysis. Moreover, in order to gain a facile synthetic access to even more PI systems bearing various different structural features and to compare them in terms of thermal stability, it was aimed for obtaining various PI systems by means of hydrothermal synthesis as well. Since both synthetic methods for generating PIs differ fundamentally, their methodological approaches and the appearance, crystallinity and other properties of the resulting polymeric products were to be compared in detail.

3. Comparison of Synthetic Methods

3.1 Classically Synthesized Polyimides

3.1.1 Starting Materials

For obtaining PAAs and subsequently PIs of high molecular weight, it is generally necessary to employ monomers of highest purity possible, since each hydrolyzed anhydride moiety may not participate in the formation of an amic acid and each oxidized amine moiety may not take part in the formation of an imide ring. For ensuring the necessary purity, each monomer used for manufacturing of PI films was sublimed at least once while a few monomers needed for additional purification steps before sublimation. The dianhydrides used were obtained in synthetic grade from *TCI* and *Sigma-Aldrich* and purified by sublimation before use. Sublimations were done in an *Gebrueder Retberg* "Makro" sublimation apparatus having a capacity of up to 20 grams of purified solid. In all cases, pressures of approximately or less than $2.5 \cdot 10^{-3}$ mbar were applied, while heating the glass apparatus to temperatures of up to 270 °C, depending on the type of monomer. Silicone-based heat-transfer oil nominally capable of being heated up to 250 °C could be used above its specifications by heating it in household cooking pots having a highly even bottom surface, which turned out to be necessary to efficiently sublime sBPDA (among other monomers). PMDA readily sublimed at oil-bath temperatures of approximately 200 °C, while sODPA needed for slightly increased temperatures. A constantly refreshed argon atmosphere was ensured while handling and storing these sublimed dianhydrides in order to avoid hydrolytic reactions enabled by ambient humidity.

Diamines used within this work were mostly obtained from *TCI*, *Sigma-Aldrich* and *fluorochem* in technical grade while a few were obtained from a storage facility of TU Wien and a few were synthesized by the author and internship students. Detailed synthetic routes to the latter can be found in appendix B.2. Among the ones obtained from the storage were 3,6-diaminodibenzofuran (DADF), *o*-dianisidine (oDIAN), *o*-tolidine (oDMBz), *m*-tolidine (mDMBz) and benzidine (Bz). While the first four could be purified by a single sublimation step, benzidine -which was obtained as dihydrochloride- required for basic precipitation from aqueous solution to obtain the diamine, followed by two subsequent sublimation steps, as a fraction of its impurities sublimed in a temperature range close to the desired substance itself. These impurities could be observed as yellowish fraction

precipitating on the outer layer of the sublimed diamine during sublimation, indicating a slightly elevated temperature necessary for subliming these. A second sublimation step after manually removing the contaminated outer layers yielded white crystals of benzidine. The relatively large, stiff and highly aromatic diamine 4,4′′-diamino-*p*-terphenyl required for the most laborious purification procedure consisting of recrystallization from THF followed by two subsequent sublimation steps.

3.1.2 Synthesis of Poly(Amic Acid) Precursors

PAA solutions as precursors for continuous PI films were manufactured in evaporator flasks of 50 ml volume, each one customized with a valve and equipped with an oval rare-earth magnetic stir bar to facilitate stirring in case of more viscous precursor solutions. Before charging a flask it was thoroughly cleaned with water and detergent, then rinsed with deionized water and acetone, dried with a heat gun and closed with a glass stopper to avoid contamination by dust. Each glass stopper was equipped with a thin PTFE ring to enable tight but easily reversible sealing after it had been charged with the components necessary to synthesize the planned PAA. When calculating the stoichiometric charge of each PAA, it was aimed for a 10 - 20 g of total precursor maintaining a mass fraction of solids ranging between 5 % and 12 % within the precursor solution. Generally it was aimed for obtaining rather viscous PAA solutions by choosing rather high concentrations, since spin-coating and drop-casting seemed to have a higher rate of success in terms of continuous material application if the solutions were more viscous. Moreover, lower concentrations are known to decrease the stability of PAAs.[2,111,112] However, it was simultaneously aimed for keeping a solution's viscosity low enough to allow for magnetic stirring.

After cleaning and drying a flask it was first charged with the diamine component on a recently calibrated analytical microbalance while maintaining highest precision in the weighing process. In case any deviations occurred, the charge of the dianhydride had to be recalculated in order to keep the stoichiometric ratio exactly as planned. After adding the diamine, anhydrous NMP was added after which the flask was purged with argon and the mixture was magnetically stirred until the diamine was completely dissolved. An amount of dianhydride was weighed, slightly exceeding equimolarity by less than one milligram, since a slight excess of dianhydride is suspected to lead to an increase in its thermo-oxidative stability.[113] For this, coated weighing paper was used in order to minimize losses due to substance remaining on the rough surface of standard weighing

paper. The dianhydride was added to the diamine solution while ensuring with utmost care that no substance was left on the paper and that it did not touch the flask's joint, as its rough surface could retain it on contact. During dianhydride addition a constant stream of argon was maintained in order to avoid ambient humidity getting into contact to the solution, as this might facilitate hydrolysis of the forming PAA and therefore lower its molecular weight.[114–116] It should be noted that this sequence of monomer addition was chosen since it is known that dissolving the (mostly less soluble) dianhydride in a solution of diamine leads to PAAs having the highest possible molecular mass.[2,117,118] In case of nearly all precursor solutions, a sudden and intense coloring of the solution could be observed shortly after addition of the dianhydride. The argon stream was then stopped and the flask was sealed with a glass stopper equipped with a PTFE ring as mentioned before. Within the following hours of stirring, each PAA solution's viscosity increased severely, depending on the choice of monomers. Monomer combinations including fully aromatic, stiff monomers such as PMDA-Bz, PMDA-DATP and PMDA-pPDA in particular led to PAA solutions exhibiting the highest apparent viscosities, whereas an increasing fraction of flexible linkages within the employed monomers led to a decrease in viscosity. Notably, PAA solutions including fluorinated diamines such as mTFBz or 4FmPDA exhibited lower viscosities compared to their non-fluorinated pendants, due to inhibited intermolecular interactions or decreased chain length of the precursor polymer arising from lower diamine reactivity, respectively. In most cases, the stirring speed soon had to be reduced to the lowest setting possible in order to keep up the stirring process without compromising it by letting the rotational speed of the magnetic field induced by the stirrer get ahead of the maximum possible rotational speed of the stir bar limited by the solution's viscosity. If one solution turned out to get too viscous to be stirred magnetically, it was either diluted with more dry NMP until stirring was possible or in the case of one PMDA-pPDA precursor, mechanical stirring was applied. The PAA solutions were stirred for approximately 20 h to 24 h before transferring the flasks to a freezer in order to store them at approximately -20 °C (including the stir bar) until further use. Storage at lower temperatures is recommended, since PAAs are known to be quite unstable in solution, which might reflect in a solution's viscosity decreasing over time.[112]

3.1.3 Specimen Manufacturing

Spin-coating the PAA solutions was done on square-shaped (100) Si wafers with native oxide layer, having a side length of 30 mm, which were carefully wiped with microfiber tissues before applying the precursor solutions. The solutions were taken out of the freezer approximately half an hour prior to spin-coating in order to allow them to warm up slightly. The flask containing the PAA to be processed was opened while simultaneously starting to lead a mild stream of argon through its valve in order to keep ambient humidity out of the container. PAA was applied with a flat spatula spreading the solution evenly across the surface of the wafer and making sure that the surface area of this wafer's polished side was completely and generously covered by this solution. Immediately afterwards the specimen was placed in the center of the spinning stage of a spin coating device (*Specialty Coating Systems* G3P-12 Spincoat) and a preset program was started. It consisted of an initial acceleration step to a certain rotational speed of 60 s duration followed by another 60 s of maintaining this speed, a sudden acceleration to a significantly higher speed, which was held for 2 s and a final deceleration step to 0 rpm within 10 s. Depending on the viscosity of each PAA solution to be processed, the speeds for these steps were chosen rather arbitrarily, while higher speeds were chosen for precursor solutions of higher viscosity. They ranged from 600 rpm to 800 rpm for the first stages, and 1000 rpm to 1600 rpm for the second stage. The latter was intended to reduce the effect of precursor solution accumulating on the outer borders of the substrate, which was caused by the solution's surface tension preventing it from getting spun off the substrate. It has to be noted that this procedure of applying the PAA and spin-coating the wafers represented the first and only phase of significant duration in which the precursors were in contact with ambient air. The now coated substrate specimens were carefully taken off the stage with the help of a razor blade and PTFE tweezers and put on a sheet of flat glass, which was placed on top of a leveled hot plate. The heating setting was adjusted to reach a temperature of 70 °C on the surface of the glass sheet. While any specimen was on top of the heated glass, it was made sure that it was exposed to a mild stream of nitrogen, realized by a reversed funnel connected to a supply line of technical grade nitrogen held a few centimeters above the surface. There, all specimens were held for at least one hour, in order to slowly evaporate most of the solvent contained in the spin-coated PAA solution, a process which may be called soft bake or pre-bake.

For manufacturing specimens to be analyzed with regards to their moisture uptake, simi-

lar but smaller square-shaped silicon wafers with 10 mm side length were used. Here, the precursor solutions were applied via drop-casting of specific amounts onto the wafers' polished surfaces instead of spin-coating indiscriminate amounts. A detailed description of this process can be found in section 4.2.2.

3.1.4 Curing

After this process was done, all samples were brought to a tube furnace while being placed in a box filled with argon atmosphere in order to minimize potential hygroscopic effects of the PAAs during the several-minute transfer. Along its full length, the tube of the furnace was equipped with two steel rods which enabled leveling of the samples along one axis in order to avoid them being tilted during the following curing process. Within the furnace, the specimens were distributed among the surface area of two sheets of flat glass which were placed at locations surrounded by the furnace's heating coils. This setup allowed simultaneous curing of up to eight square-shaped specimens of 30 mm length or a high number of 10-mm specimens. During the process of sample loading, a constant stream of technical-grade nitrogen was maintained. While keeping up this nitrogen stream the tube was sealed with a lid having a small outlet for gaseous exhaust and a customized heating program was started. It consisted of heating from 90 °C to 400 °C at a rate of 2 K min^{-1} with isothermal plateaus at 150 °C, 210 °C, and 300 °C (30 min duration each) and one final temperature step at 400 °C which was held for 60 min. This curing program was followed by slowly letting the furnace cool down to ambient temperature over the course of several hours. The nitrogen supply was turned off after the last temperature plateau was reached, assuming no significant amounts of moisture evaporating from the samples or being present in the furnace atmosphere. After the program was complete, the furnace including the cured samples was left to cool down to room temperature slowly overnight in a static nitrogen atmosphere.

For preparing samples for DVS measurements, the soft-bake step was realized in the tube furnace as well, since heating from below, as it would be the case on a heating plate, often led to severe inhomogeneities in these rather thick samples. Accordingly, an additional isothermal step at 90 °C for one hour was implemented before heating to the otherwise first isothermal step at 120 °C within the previously specified heating program. During this additional step (and during heating from room temperature to the target temperature) the nitrogen purge was kept more intense than during the following steps, as an increased amount of evaporating solvent was expected. The resulting

PI films showed moderate to high adhesion to the substrate surface they were cured on. With the help of an unused razor blade, which was briefly immersed in deionized water beforehand, many films could be detached by moving the sharp side of the blade between film and substrate on one edge of the specimen and cautiously moving it across the entire area. However, specifically PI systems containing ether linkages within their molecular backbone exhibited high adhesion to the silicon substrate and represented the most difficult to detach manually. These samples had to be immersed in deionized water during detachment, while detaching on two adjacent corners first, then slowly moving the blade from the side formed by the two detached corners to the other while applying slightly more force in direction of the specimen surface than for the other samples. The spin-coated PI films were used for X-ray diffraction measurements presented within this thesis, as well as laser-ablation and ion-diffusion experiments, which were conducted by colleagues and were not part of this thesis.

3.2 Hydrothermally Synthesized Polyimides

For synthesizing PIs hydrothermally, reactions were done both in steel autoclaves and stirred microwave-reaction vessels. In most cases, diamines purified by sublimation were employed in HT-PI synthesis as well, in order to enable high purity of the PI products. However, if a diamine was not purified beforehand and the reaction media not kept somewhat inert, the HT-PI products merely turned out to be more brownish in color, without any detectable differences in terms of thermal stability, X-ray diffraction or infrared absorption. For both the syntheses of monomer salt and hydrothermal reactions to PIs, the available dianhydrides were hydrolyzed to their corresponding tetracarboxylic acids by microwave reactions in hydrothermal conditions with deionized water. For that, amounts of more than one gram of dianhydride were given into a microwave vial containing 18 ml of deionized water and heated to 210 °C for several minutes while stirring vigorously. The reaction progress was followed by optical means via the built-in camera of the microwave reactor, while complete dissolution of a dianhydride was assumed to translate to complete hydrolysis to tetracarboxylic acid. While heating at a rate of approximately 60 K min^{-1}, complete dissolution of the dianhydride was observed at approx. 120 °C for BTDA, approx. 130 °C for sODPA, approx. 135 °C for 6FDA, approx. 145 °C for aODPA, approx. 150 °C for DSDA, and approx. 195 °C for BPAF. Merely the hydrolyzed counterpart of PMDA, pyromellitic acid (PMA), was used as received from a commercial source.

For numerous PI systems, monomer salts have been synthesized as precursors for HT-PIs. The solvent for this synthesis in most cases was technical grade acetone containing approximately 10 vol.% deionized water. This mixture of acetone and water was found to be a suitable polar and protic solvent for monomer-salt synthesis, since most monomers were readily soluble in acetone (except for Bz and DATP, which only exhibited low solubility), but their respective monomer salts in many cases precipitated more or less readily. For synthesizing and precipitating a monomer salt from solution, approximately equimolar amounts of both monomers were fully dissolved in two separate beakers each containing the prepared solvent. Then both solutions were carefully combined in one of these beakers, the other one rinsed with minor amounts of the same solvent (and adding it to the mixture), and the mixture was briefly stirred with a glass rod, while trying not to provoke "premature" crystallization by scratching the surface of the beaker. In most cases a monomer salt precipitated after several seconds to few minutes. After suction-filtering a monomer salt over a glass filter (por. 3), it was washed with the same solvent used for synthesizing it several times, in order to wash potentially remaining monomer residues from the precipitate. This included one final washing step with acetone only in order to facilitate subsequent drying. After letting the product dry in the filter via suction for at least 30 min, the monomer salt was collected, after which the container was flushed with argon in order to prevent oxidative decomposition during storage, which was observed before in some rare cases. For some systems, namely sODPA-mPDA, sODPA-oDMBz, sODPA-oDIAN, and sODPA-mTFBz, which could not be crystallized from acetone and the monomers were not readily soluble in water, monomer-salt precipitation could be achieved from a methanol solution containing approximately 5 vol.% deionized water. However, in a few cases no precipitation of monomer salt could be achieved at all, which was the case for sBPDA-4FmPDA, sBPDA-1FmPDA, sBPDA-DATP, PMDA-oTFBz, aBDPA-pPDA, and all four ODPA-ODA systems. These HT-PI systems were obtained by charging equimolar amounts (no excess of one component as in PAA synthesis) of the diamine and the tetracarboxylic acid (total monomer mass of approximately 0.3 g) in 10 - 18 ml of argon-bubbled, deionized water, briefly homogenizing the dispersion by immersing the vial in an ultrasonic bath and subsequent hydrothermal reaction. It has to be noted that monomer-salt preparation of low-solubility monomers in deionized water treated in an ultrasonic bath for several hours seemed promising. This has been done for the systems sBPDA-Bz, PMA-mTFBz, and 6FDA-pPDA, while ATR-FTIR spectroscopy for monitoring the reaction progress indicated close-to full conversion of the monomers after one hour. Note that although the

reaction started at room temperature, the water within the ultrasonic bath warmed up to approximately 40 °C, which most probably had an influence on the solubility of the monomers in water.

For converting a monomer salt or monomer mixture to a PI hydrothermally in an autoclave, in virtually all cases the starting components (total monomer mass of approximately 0.3 g) were given into borosilicate-glass vials having a capacity of 20 ml, after which 10 - 18 ml of argon-bubbled, deionized water were added and the dispersion homogenized by briefly immersing it in an ultrasonic bath. In most cases, two drops of Hünig's base (*N*,*N*-diisopropylethylamine) were added to approximately 250 ml of the deionized water before treating it with argon and using it as reaction medium for hydrothermal synthesis. The charged vials were each placed inside a steel-bomb autoclave (equipped with a PTFE inlay), covered with argon and closed tightly. Then each autoclave was placed in a forced-convection oven operating at 200 °C and kept in it for at least 60 h in order to ensure largely complete conversion of monomers to PI. Afterwards, the autoclaves were taken out of the oven and cooled by immersing them halfway in a bath of cold tap water. After cooling down to room temperature for several hours, the autoclaves were opened and the reaction products were filtered over a Büchner funnel and washed with deionized water and acetone several times in order to ensure no unreacted monomers being present in the precipitates. After the last washing step, the products were left in the filter for drying by suction for more than one hour.

Microwave reactions were done additionally using an *Anton Paar* Monowave 400 and G30 glass vials. Here, HT-PI synthesis was done by heating monomer salts dispersed in 15 - 18 ml of argon-bubbled, deionized water while magnetically stirring the argon-covered suspension. The heating rates in these microwave reactions were much higher than in autoclave reactions, as reaction-medium temperatures of 200 °C could be reached in less than two minutes as compared to presumably more than one hour in autoclave reactions. Moreover, most HT-PI reactions were considered complete after a reaction time of four hours while stirring vigorously. Regarding washing and drying, the products of microwave reactions were subjected to the same procedure as autoclave PIs. For syntheses of both monomer salts and PI films, reaction progress was monitored utilizing attenuated total reflectance Fourier transform infrared (ATR-FTIR) spectroscopy, as this method allows for quick and reliable distinction between the different stages of PI synthesis from neat monomers to final product. Figure 3.1 depicts such ATR-FTIR spectra of the neat monomers pyromellitic acid (PMA) and benzidine (Bz), and of a PAA film, a PI film, a monomer salt and a HT-PI of the PMDA-Bz system. Amongst the most obvious

changes in IR absorption upon reaction from monomer to precursor and final product are the distinct N-H stretching modes of the diamine above 3000 cm^{-1}, which in most cases completely vanished upon reaction. Instead, the monomer-salt spectrum exhibits broad aromatic ammonium-related stretching modes below 3000 cm^{-1}. In case for Bz these amine modes were found at $\tilde{\nu}$(N-H) ≈ 3558, 3384, 3207, 3033 cm^{-1} and converted to broad ammonium modes at $\tilde{\nu}_a$(Ar-NH_3^+) ≈ 2855 cm^{-1} and $\tilde{\nu}_s$(Ar-NH_3^+) ≈ 2580 cm^{-1}. Moreover, the prominent carbonyl mode of PMA at $\tilde{\nu}$(C=O) ≈ 1694 cm^{-1} split up upon salt reaction to give deprotonated carbonyl modes at lower wavenumbers. In case of PAA formation two modes could be found which might be attributed to carbonyl stretching within the amide moiety and the free carboxylic acid, which in this case were found at $\tilde{\nu}$(C=O) ≈ 1720 cm^{-1} and $\tilde{\nu}$((N)C=O) ≈ 1655 cm^{-1}, respectively. However, it has to be kept in mind that residual solvent might corrupt proper absorption-band assignment when analyzing PAAs, as in most cases high-boiling amide solvents are being employed in their synthesis, which can not easily be fully removed and might show absorption modes in similar regions as the PAAs would. Upon conversion to PI, the infrared spectra in most cases flattened in the absorption regions above 2000 cm^{-1}, except for aliphatic C-H stretching modes below 3000 cm^{-1} in the cases of PI systems containing aliphatic side groups or bridging moieties. The most prominent absorption modes to be found for aromatic PIs are the asymmetric and symmetric imide-carbonyl stretching modes, $\tilde{\nu}_as$(C=O) and $\tilde{\nu}_s$(C=O), respectively, and aromatic C-N stretching bands $\tilde{\nu}$(C_{Ar}-N). In case for PMDA-Bz films the carbonyl stretching modes were found at $\tilde{\nu}_as$(C=O) ≈ 1777 cm^{-1} and $\tilde{\nu}_s$(C=O) ≈ 1712 cm^{-1}, and the C-N stretching band at $\tilde{\nu}$(C_{Ar}-N) ≈ 1355 cm^{-1}. For HT-PIs of PMDA-Bz the C-N stretching band was shifted to $\tilde{\nu}$(C_{Ar}-N) ≈ 1393 cm^{-1} and the asymmetric carbonyl-stretching mode to $\tilde{\nu}_as$(C=O) ≈ 1784 cm^{-1}. Interestingly, the peak for the symmetric carbonyl-stretching mode was split, including one maximum located at the same value as for the PI films and another one at $\tilde{\nu}_s$(C=O) ≈ 1720 cm^{-1}. One possible reason for the mode shifts observed when comparing HT-PIs and PI films of the same systems could be found in the fact that most of these systems turned out to be drastically more crystalline when synthesized hydrothermally, which could influence the mobility of such stretching motions when being confined in a lattice structure. However, the peak splitting of the symmetric stretching mode could not be explained. It should be noted that of most aromatic dianhydrides (except for PMDA) the carbonyl stretching modes appeared virtually identical to those of the imide in terms of shape, but could be found at values approximately 60 cm^{-1} higher.

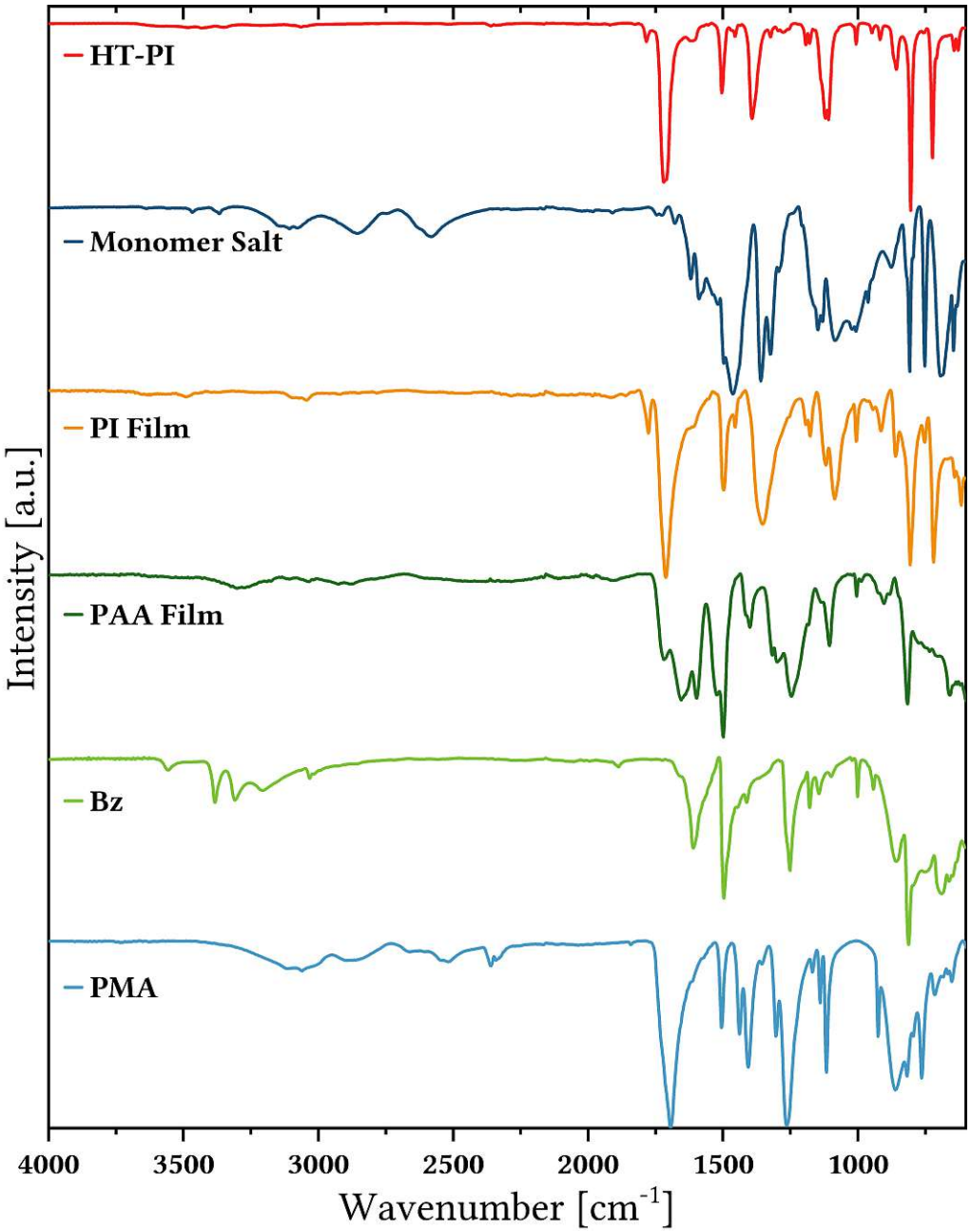

Figure 3.1: ATR-FTIR spectra of the neat monomers, PAA film, PI film, monomer salt and HT-PI of the PMDA-Bz system.

3.2.1 Properties of Polyimide Products

Morphological Appearance

The two main methods of PI synthesis this thesis focused on led to two fundamentally different forms of high-performance polymers even though their monomeric constituents were the same, as it can be seen in figure 3.2. Samples of classically synthesized PI films represented continuous materials consisting of more or less entangled polymer chains (if structurally possible), which were colored in a range of bright yellow to

dark orange and consistently transparent. Hydrothermally synthesized PIs, however, were of a powder-like nature in virtually all cases, being crystalline particles of several-micrometer dimensions, while the color range was broader including dark brown and nuances of red and violet.

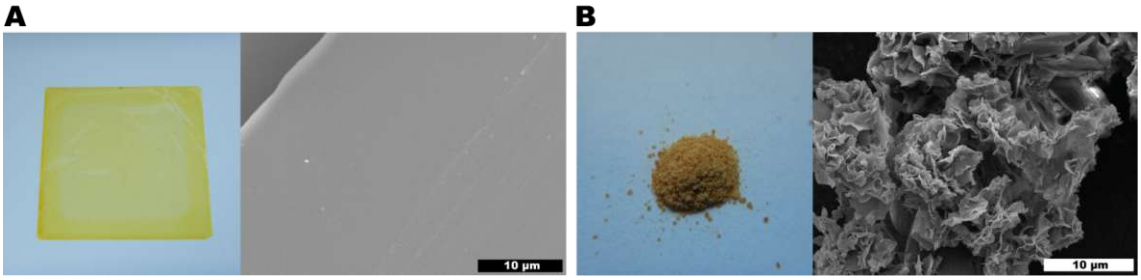

Figure 3.2: Photos and scanning electron micrographs of (**A**) a PI film of PMDA-APBP and (**B**) a HT-PI of PMDA-oDIAN synthesized in a microwave reactor.

As they usually are rather small particles, HT-PIs can take various forms ranging from platelets to microflowers. A certain degree of morphological control could be exerted by adjusting the parameters of HT synthesis such as synthesizing in autoclaves or in a stirred microwave reactor, while microflowers could predominantly be observed using the latter method. Moreover, it is known that a HT-PI's morphological outcome could even be tuned by incorporating water-soluble additives into the reaction medium for HT synthesis.[119]

Apparent Crystallinity

Classically synthesized PIs -foremost PI films, since they represent the most widely used form of PIs- are mostly found to be amorphous polymeric products. Hydrothermally synthesized PIs, however, are known to exhibit extraordinarily high degrees of crystallinity.[47,62,66,105,120–122] Within the framework of this thesis, a large amount of both hydrothermally synthesized PIs and PI films were manufactured and their powder X-ray diffraction (PXRD) patterns collected. This extensive collection of PXRD patterns of PIs and their precursors can be found in appendix C. Figure 3.3 compares the PXRD patterns of a PMDA-pPDA film and its PAA precursor (left), which both exhibited mostly one amorphous halo, and of a hydrothermally synthesized PMDA-pPDA PI and its monomer salt precursor (right), which both were of high crystallinity exhibiting very little to no amorphous halos.

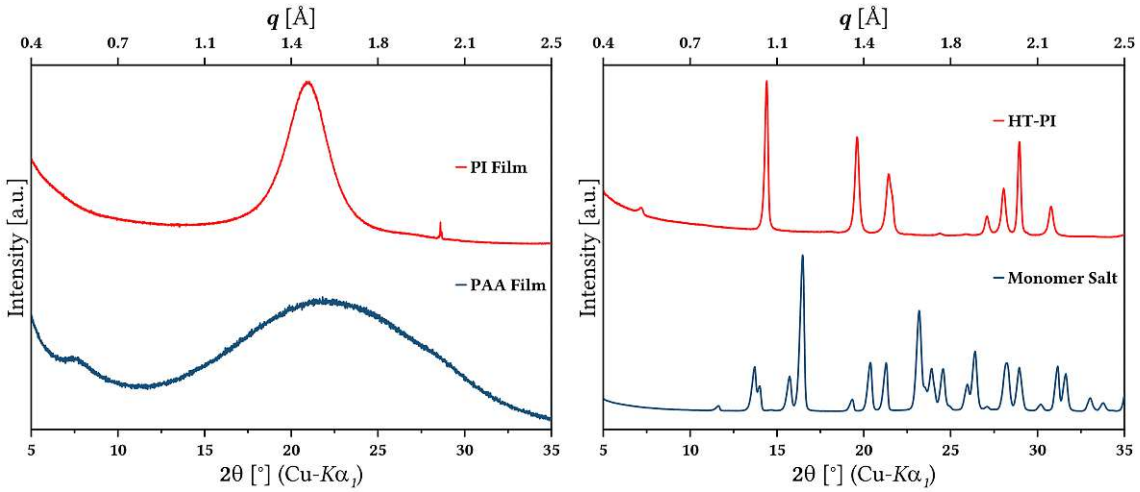

Figure 3.3: PXRD patterns of a PMDA-pPDA PI film and its PAA precursor (left) and hydrothermally synthesized PMDA-pPDA PI and its monomer salt precursor (right).

As this PI system can be considered the most stiff and linear one of all aromatic PIs, it represents a very telling example for high crystallinity achieved by hydrothermal PI synthesis. Another one could be found in PMDA-Bz, which represents a fully linear and highly stiff PI system as well, containing one rotational degree of freedom within the biphenyl linkage. While the diffractograms of PAA and PI films of this system (cf. figure 3.4) were almost identical to those of PMDA-pPDA, subtle differences could be found in those of the HT-PI: Apart from the different peak positions, which were simply due to this system's differences in crystal structure, comparing PMDA-Bz to PMDA-pPDA revealed a slightly worse resolution of peaks, which probably arised from its slightly increased flexibility.

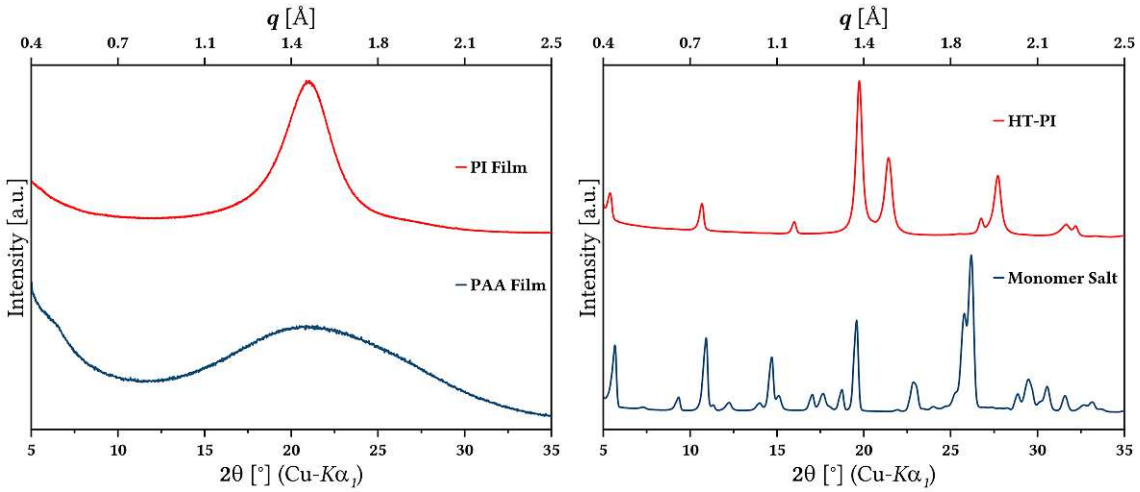

Figure 3.4: PXRD patterns of a PMDA-Bz film and its PAA precursor (left) and hydrothermally synthesized PMDA-Bz PI and its monomer salt precursor (right).

For PMDA-DATP (cf figure C.4), which contained one additional flexible biphenyl linkage, the outcome was quite similar to PMDA-Bz, as their diffractograms' peak resolution appeared to be quite similar. HT-PIs based on sBPDA as dianhydride (see figures C.5, C.6, C.7, C.9 and C.10), however, seemed to yield significantly less crystalline materials, most probably due to this dianhydride's slightly kinked structure, while an increasing fraction of flexible linkages (from sBPDA-pPDA, to sBPDA-Bz, to sBPDA-DATP) clearly resulted in even more amorphous products. Moreover, it could be observed that the pendant side groups on benzidine derivatives decrease crystallinity on PMDA-based PIs (figures C.11 to C.18) compared to PMDA-Bz to different but significant extents, which could be due to these groups' inherent bulkiness probably impairing the approximation of the polymer chains necessary for ordering. Similar observations could be made for sODPA-based PIs containing benzidine derivatives (figures C.36 to C.40). However, sODPA-based PIs appeared to be slightly less crystalline than PMDA-based ones, which was probably due to the ether bridge contained in sODPA allowing for rotational flexibility (figures C.34 and C.35), while the introduction of a second ether bridge per repeating unit intensified this effect (cf. figure C.41). Similarly, while single ether bridges per repeating unit in PMDA-sODA and PMDA-aODA (cf. figures C.19 and C.20) led to quite crystalline PIs, the introduction of a second one (cf. figures C.21, C.22, C.25 and C.26) seemed to lead to less crystalline polymers. Hydrothermally synthesizing the other fully stiff systems PMDA-DAF (figure C.30) and PMDA-DADF (figure C.31) yielded quite crystalline materials, while again, flexible linkages such as methylene moieties (cf. figure C.29), isopropyl moieties (cf. figures C.23, C.24 and C.27), hexafluoroisopropyl moieties C.28 led to significantly less crystalline PIs. Extreme kinks in structure seemingly prevented efficient molecular packing leading to almost fully amorphous HT-PIs in cases in which diamines BAPF (C.32) or MeBAPF (C.33), or dianhydrides aODPA -except for the aODPA-pPDA system- (C.41), aBPDA (C.43) or BPAF (C.45) were employed in synthesizing PIs hydrothermally. In these cases, it seemed as if softening phenomena could have occurred to some degree during synthesis, as parts of these products appeared as slightly fused powder to give brittle, roundish shapes.

3.3 PIs from Ortho-Substituted Benzidine Derivatives

Generally, HT-PIs obtained from autoclave and microwave reactions merely exhibited differences in their morphology, whereas differences in terms of crystallinity i.e. in their PXRD patterns were hardly conceivable. However, some -for certain PI systems

significant- differences were found indeed, as they exhibited an extraordinarily high amount of intense reflections within their diffractograms when being synthesized via microwave reactions. This was the case for the systems PMDA-oDIAN, PMDA-oDMBz, PMDA-oTMBz and PMDA-oDFBz, which all showed a significantly higher amount of reflections when synthesized hydrothermally in stirred microwave reactions as compared to autoclave synthesis (cf. figures 3.5A to 3.5D). Interestingly, each of these PMDA-based PI systems consisted of benzidine derivatives as diamine fractions, which had substituents in ortho position to the amine moieties. When encountering this phenomenon for the first times while synthesizing PMDA-oDIAN, it was assumed that it only occurred if conditions of synthesis were of highest purity. Despite initial doubts, it also occurred if non-degassed water was used, if the diamine, from which the monomer salt was synthesized, was partially degraded (recognizable by intense coloring of monomer and salt) and even when using neat monomers instead of monomer salt, which would generally result in a stoichiometric imbalance.

In case of PMDA-oDIAN, synthesis of this highly crystalline product was repeated numerous times under varying conditions, of which the heating rate applied while reaching the desired reaction temperature of 200 °C turned out to be the key factor in obtaining these products. A series of experiments was conducted heating the same amounts of a monomer salt for PMDA-oDIAN in the same volume of water to 200 °C at different heating rates in the microwave reactor, while maintaining the same stirring speed and an isothermal reaction time of four hours after reaching 200 °C throughout this series. Figure 3.6 shows PXRD patterns of these experiments, in which this monomer salt was heated in time spans from 40 seconds over several minutes to one hour. Here, it could clearly be seen that the occurrence of these additional reflections depended on the heating rate during hydrothermal synthesis: When the reaction mixture was heated to the desired temperature within one hour, which more or less corresponded to a heating rate found in autoclave reactions, the product exhibited a PXRD pattern analogous to the ones obtained from those autoclave reactions. When heating it within 30 minutes, the reflections attributed to the second phase started being visible. With increasing heating rates these reflections became more intense, while heating up the reaction mixture in less time than 4.5 minutes did not seem to increase the intensity of these peaks but rather led to a slight decrease. It has to be noted that the heating rate within a single experiment was not fully linear, since the initially quick heating process got slower over the last few degrees before reaching set reaction temperature, which most probably was

due to a safety measure of the microwave reactor intended for not overstepping the set temperature.

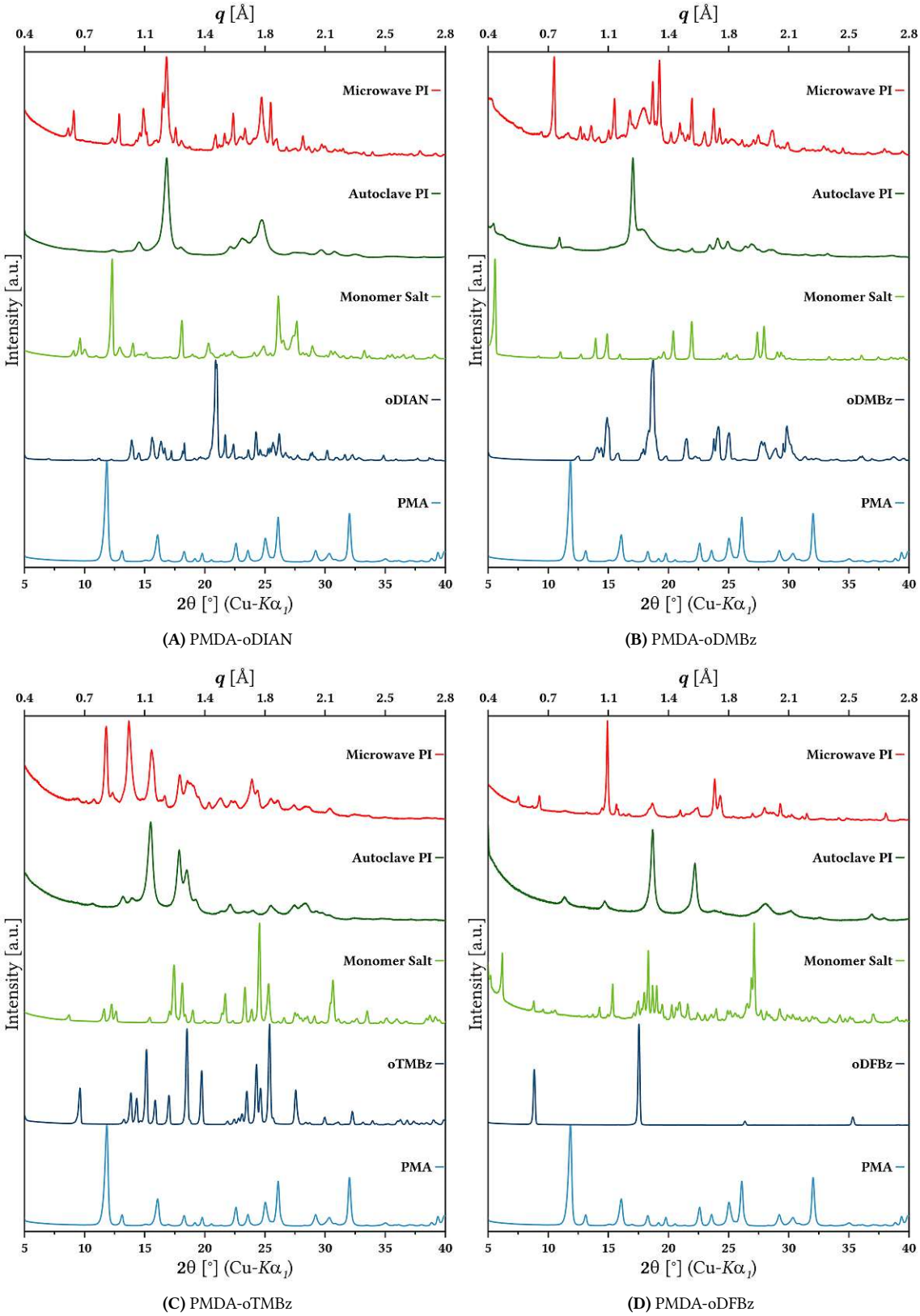

Figure 3.5: PXRD patterns of microwave- and autoclave-synthesized HT-PIs of (A) PMDA-oDIAN, (B) PMDA-oDMBz, (C) PMDA-oTMBz and (D) PMDA-oDFBz, each compared to their respective monomer salts and neat monomers.

Baumgartner and Unterlass found that high heating rates in hydrothermal synthesis reduced polymerization in the subhydrothermal regime, which would otherwise lead to less crystalline products, and that sufficiently high rates might lead to products including significant fractions of dimeric and oligomeric species which would result in additional reflections visible in these products' PXRD diffractograms.[121] The observations made within this thesis could be in analogy to these postulates. Increases in heating rate led to increased fractions of a second phase occurring along with the expected HT-PI product, which indeed could be dimeric or oligomeric species as this phase corresponded neither to the neat monomers, nor the bulk monomer salt or the bulk PI product. In the course of trying to find out what this extra number of reflections represented, these presumably highly crystalline PIs were again subjected to hydrothermal conditions in steel bomb autoclaves for up to ten days using reaction parameters analogous to the other autoclave reactions without the use of additional catalyst. In any case, autoclave treatment of twelve hours did not change the diffractograms at all. For PMDA-oDIAN (cf. figure 3.7A), this treatment resulted in these unassignable peaks vanishing, leading to a PXRD pattern almost identical in terms of peak positions to the autoclave product of PMDA-oDIAN. However, each remaining reflection was implied in the pattern of the autoclave PI, but in this case the reflections were significantly more sharp and therefore the peak resolution improved significantly. Therefore, hydrothermally post-treating this microwave product led to a PI more crystalline than when synthesized in the autoclave directly. This led to the assumption that these reflections might have arised from an oligomeric species forming a second crystalline phase. However, since these observations were only made in cases in which ortho-substituted diamines were reacted, it could be possible that these oligomers did not fully cyclodehydrate to form imide rings. These quite bulky substituents located in ortho position to the amine moieties could have exerted some degree of sterical hindrance, which might have hampered imide formation after one carboxylic acid reacted with an amine moiety to form an amide bond. The result would be an amic-acid intermediate, which could have formed alongside other HT-PI species, representing a second crystalline phase within these products of hydrothermal synthesis. However, if these intermediate amic-acid species were subjected to sufficiently long lasting hydrothermal conditions, the effect of sterical hindrance could have been overcome to fully react these to oligo- or polyimides. Consequently, if this assumption bore any truth it could shed some light on the underlying reaction mechanisms of hydrothermal PI synthesis.

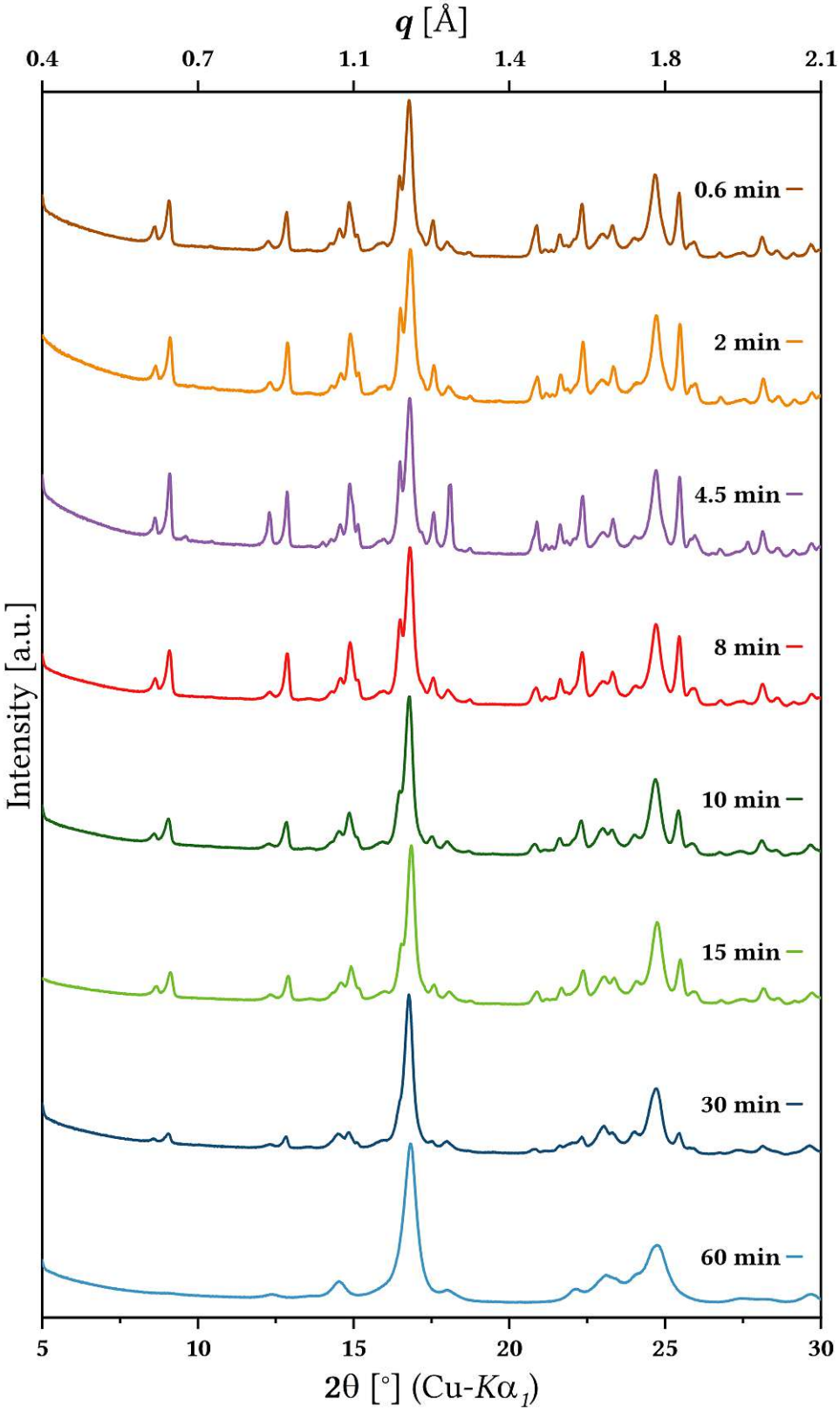

Figure 3.6: PXRD patterns of PMDA-oDIAN synthesized hydrothermally in a microwave reactor using different heating rates. The time indicator represents the minutes it took to heat uniformly from room temperature to 200 °C.

Results of ATR-FTIR analysis could be interpreted similarly, as two peaks at $\tilde{\nu} \approx 3485$ & 3379 cm^{-1} found in the microwave product vanished upon autoclave treatment, which could be assigned to amide-inherent N-H stretching vibrations. Another peak at $\tilde{\nu} \approx 1688\ cm^{-1}$, which could be interpreted as an amide-carbonyl stretching mode, seemed to decrease in intensity. However, as it heavily overlapped with the imide-carbonyl mode its assignment could not be done with a sufficient degree of certainty. Another two peaks at $\tilde{\nu} \approx 1292$ & 1242 cm^{-1} vanished as well, which could not be assigned to any vibrational mode.

In case of PMDA-oDMBz, this treatment merely led to a lower relative intensity of these extra peaks (cf. figure 3.7B). Additionally, IR spectra of both sample types seemed virtually congruent. This could mean that if these intermediate species formed in case of this monomer combination, the sterical hindrance could not be overcome that easily and would probably need even longer exposition to hydrothermal conditions or maybe even temperatures above 200 °C. Intriguingly, the PMDA-oTMBz system behaved quite differently (cf. figure 3.7C). Here, the microwave PI again showed a higher number of reflections while including those of the autoclave PI. However, when subjecting this microwave PI to long-lasting hydrothermal conditions, the product did not just show less intense reflections of the presumably second phase or a refined pattern of the autoclave PI. It rather showed a pattern which partially appeared to be a somewhat refined diffractogram of the microwave PI while still including all autoclave-PI reflections and most reflections of the microwave product, while some peaks of the microwave product seemed to have vanished and some new reflections seemed to have appeared (which were not congruent with the neat diamine's pattern as well). Moreover, since the diamine oTMBz contained two methyl substituents adjacent to each amine functionality, which could both sterically hinder not only a cyclization reaction but also an amide-condensation reaction, this system's behavior could to some extent contradict aforementioned assumptions of an emerging second phase consisting of oligomeric amic-acid intermediates. This might indicate these second phases possibly being related to salt-like intermediate species without any condensation reactions at all. However, the results of ATR-FTIR analysis seemed contradictory but inconclusive. Here, the autoclave-treated product exhibited two distinct peaks at $\tilde{\nu} \approx 3400$ & 3324 cm^{-1}, which appeared similar to the amine-stretching modes of the correspondent diamine but shifted by 30 -40 cm^{-1} to lower wavenumbers, and which could be assigned to amide-stretching modes. Moreover, the imide-carbonyl mode found at $\tilde{\nu} \approx 1719\ cm^{-1}$ seemed to have split up to give another, overlapping peak at $\tilde{\nu} \approx 1728\ cm^{-1}$, whereas the latter could not be assigned, as other

possible species such as amide, carboxylic acid and deprotonated carboxylic acid give values for carbonyl-stretching modes at significantly lower wavenumbers than imide-related (or anhydride-related) ones. In addition to that, at lower wavenumbers more differences between both products could be found without them allowing for structural elucidation of the microwave PI or its autoclave-treated counterpart.
Taking a look at the PXRD patterns of the PMDA-oDFBz products (cf. figure 3.7D) it again seemed as if the reflections of the autoclave product were included in the pattern of the microwave PI. A treatment of the latter in hydrothermal conditions, however, yielded a virtually different material. As this material's PXRD pattern showed high congruence with the pattern obtained from analyzing the pure diamine, it could be assumed that a reverse reaction from PI to diamine and tetracarboxylic acid took place, while the latter might not be seen in the diffractogram as it could have stayed in solution and might have been contained in the filtrate of the reaction mixture after filtering. However, IR data of the autoclave-treated material clearly evinced the presence of imide-carbonyl modes, although weak in intensity, which contradicted the assumption of full PI hydrolysis. Be that as it may, the reason for the hydrothermal treatment of the microwave PI leading to its seemingly full hydrolysis could not be fully explained but might be connected to the rather low amount of product employed for this reaction.

Assuming that these additional fractions might be soluble, small amounts of products were given into small vials closed with septums and stirred in deuterated dimethyl sulfoxide at room temperature for several days. The resulting suspensions were extracted from the vials, filtered through syringe filters and the filtrates subjected to fourier transform nuclear magnetic resonance (NMR) analysis. For PMDA-oDIAN no soluble fraction could be observed at all, as no significant signals could be recorded except for those of water and solvent. Both PMDA-oDMBz and PMDA-oTMBz contained soluble fractions for which the aromatic signals of the diamine fractions were found to be more dominant than the singlet of the PMDA fraction. However, more precise quantification of the stoichiometric proportions was not possible, as the ratios between the areas each integrated peak tuplets had were strongly dependent on the relaxation delay during NMR measurements and differed greatly between each measurement. The outcome of analyzing PMDA-oDFBz via NMR was quite similar while here amine modes were visible, which indicated incomplete polymerization maybe caused by reduced reactivity of the amine moieties resulting from the electron-withdrawing effects of the fluorine substituents lowering their nucleophilicity.

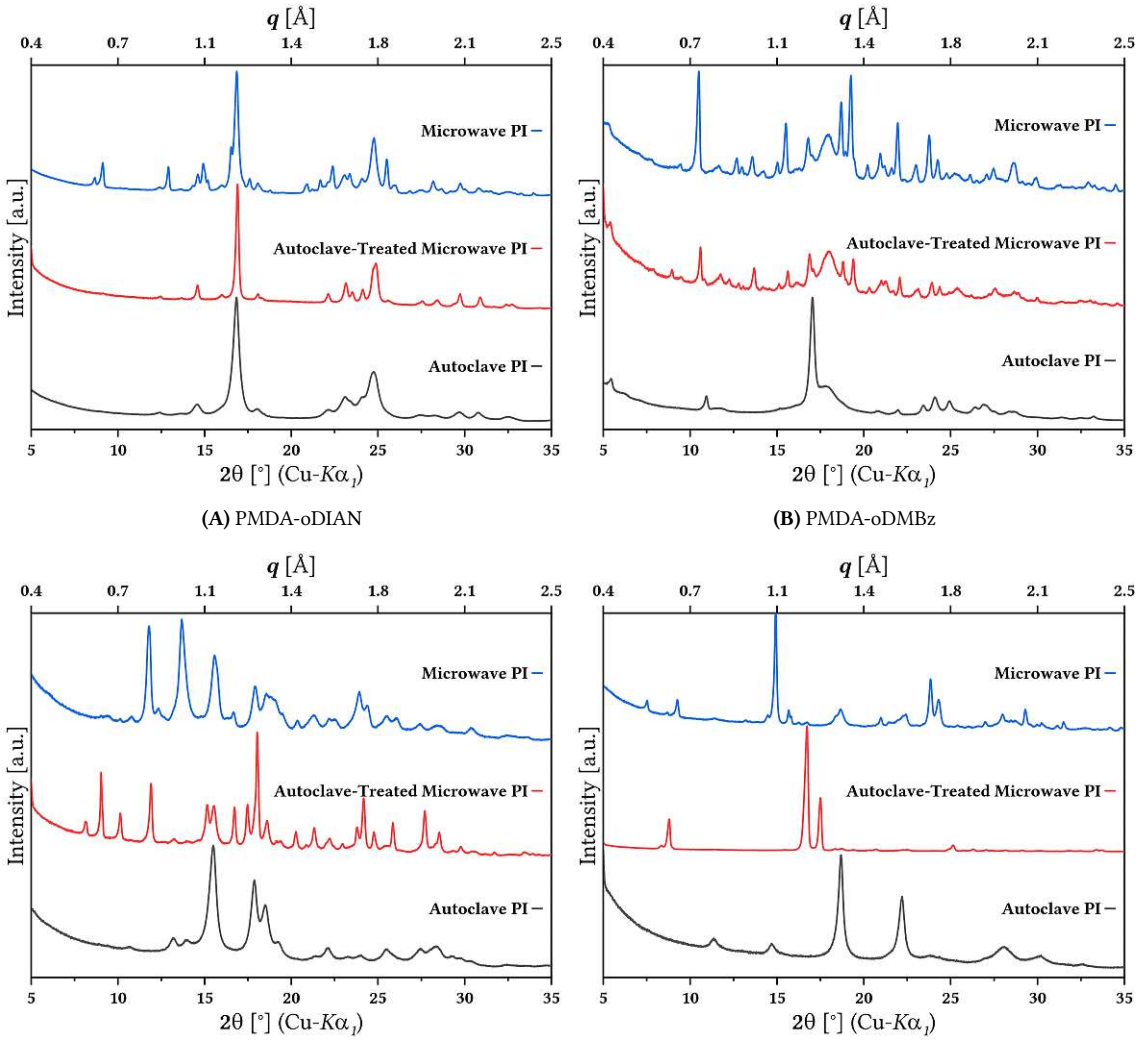

Figure 3.7: PXRD patterns of microwave-synthesized HT-PIs subjected to hydrothermal conditions in autoclaves for several days.

To sum up, when synthesizing certain PI systems bearing substituents in the diamines' ortho position to the amine functionalities while employing high heating rates, the obtained products' diffractograms exhibited more reflections than their analogues synthesized by heating up more slowly. These reflections seemed to be due to additional phases forming, which in some cases decrease upon further hydrothermal treatment. However, although there were indications that these phases were related to low molecular weight compounds consisting of the monomers employed which formed due to sterical hindrance of the amine functionalities, their chemical nature could not be clarified within this work and further investigations would be necessary to do so.

3.4 Non-Classical Synthesis of Polyimide Foams

3.4.1 Context

Not only films or fibers are being used for numerous industrial and scientific applications, but also porous, low-density forms of PI materials such as PI foams or aerogels have been subject to extensive research in recent years.[123–131] Such materials were of particular interest for highly demanding applications in cosmo- and astronautics where low weight and good thermal insulation are factors of vital importance.[126,129,130] Moreover, their comparatively low rates of heat release and of smoke and CO production in fire conditions is considered highly beneficial for such applications.[124] Due to their extraordinarily low dielectric permittivity, PI foams and aerogels also offer promising potential as substrates for lightweight transmission systems in aerospace applications.[127]
Several methods exist for the manufacturing of porous, low-density PI materials: One approach is to synthesize alkyl esters of polyamic(acid)s in solution, dry these and heat the resulting solid products in an oven or mold. Here, the alkyl alcohols and water arising from the imidization upon heating act as so-called blowing agents causing porosity in the resulting material by evaporation from melted intermediate product.[123,132] However, this method is very likely to require incorporation of additional blowing agents to achieve sufficient foaming.[123,132] Another approach is based on the use of diisocyanates instead of diamines for PI synthesis. Subjecting a solution of diisocyanates and dianhydrides in a high-boiling solvent such as dimethyl sulfoxide to slightly elevated temperatures, both monomer types react to form PIs under release of CO_2 as side product, which allows for the formation of a PI foam.[133] Here, the blowing agent is somewhat contained in the monomers themselves and arises upon combining these, while the use of catalysts can lower the temperature range in which this reaction takes place down to room temperature. However, any solvent used for enabling the reaction would have to removed eventually, while side reactions of impurities and water with isocyanate moieties are likely. In order to obtain polyimide aerogels one rather elaborate approach is to form gels by cross-linking anhydride-capped polyamic(acid) oligomers with triamines via chemical imidization in solution of a high-boiling solvent and subsequent solvent removal by supercritical fluid extraction.[126] Therefore, this method does not require any intrinsic or external blowing agent causing a significant fraction of voids within the material.
Caused by a series of serendipitous events within the framework of this thesis, a mono-

mer salt as PI precursor was found, which precipitated after combining aqueous solutions of *meso*-butane-1,2,3,4-tetracarboxylic acid (BuTCA) and ethylenediamine, which allowed for another, highly facile (an arguably fourth) method of manufacturing polyimide foams (representing a modified version of the first method discussed before). Intriguingly, this novel monomer salt transitioned through a somewhat liquid state when subjecting it to temperatures of approximately 200 °C in order to transform it into a fully aliphatic PI. Although softening phenomena upon polymerization have been observed for monomer salts for polyamide synthesis,[134–136] this behavior has not been reported for monomer salts for PIs, which usually undergo polymerization in solid state and retain the salt particles' shapes.[137] As the temperature range in which this liquid state occurred coincided with polymerization of the monomer salt, this liquid state allowed for the formation of a continuous PI foam, driven by water vapor emerging from this reaction. Upon cyclodehydration of a conventional monomer salt obtained from an acid-base reaction of an tetracarboxylic acid and a diamine, theoretically four moles of water could arise from one mole of monomer salt upon full polymerization. However, since this novel monomer salt crystallized as a dihydrate (cf. section 3.4.3) one mole of it contained two moles of crystal water, which would -in addition to the water emerging from polymerization- leave the material as vapor upon polymerization as well. Since in case of this material evaporating water served as sole blowing agent, the existence of this crystal water would mean a mass increase in blowing agent of 50 % compared to the neat monomers reacting with each other. With respect to the total mass of the monomer salt hydrate, it contained a total mass fraction of 32 % blowing agent inherent to the substance itself, which would be released upon sufficient heating. This most likely contributed to this PI precursor's extraordinary capability of being transformed into a PI foam. This section presents this novel monomer salt as a precursor for polyimide foams, which upon heating underwent a liquid state and ultimately resulted in a rigid, insoluble PI foam.

3.4.2 Synthesis

For synthesizing this monomer salt, approximately 80 g of *meso*-butane-1,2,3,4-tetracarboxylic acid (BuTCA) were given into a beaker filled with 800 ml of deionized water. The mixture was stirred until the tetracarboxylic acid was completely dissolved. An equimolar amount of ethylenediamine (EDA) monohydrate was added dropwise while stirring after which the solution was left to crystallize overnight. The precipitate was separated

by filtration and washed with cold deionized water several times. The product crystallized quantitatively as white polycrystalline powder. To obtain single crystals suitable for single-crystal X-ray diffraction, the product was slowly crystallized from an aqueous solution slightly the saturation concentration in water, which was roughly determined to be less than 1 wt%, and slow evaporation of solvent. NMR analysis confirmed the monomer salt's composition of H_2EDA^{2+} : $BuTCA^{2-}$ = 1 : 1.

^{1}H NMR (250.13 MHz, D_2O:) δ 2.43 - 2.68 (m, 4H), 2.88 - 2.89 (m, 2H), 3.37 (s, 4H)

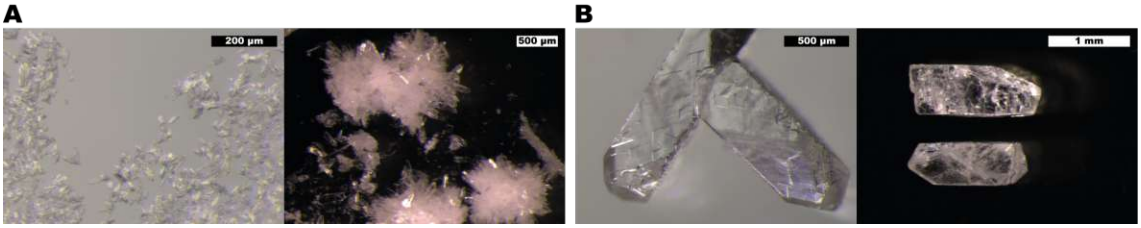

Figure 3.8: Optical microscopy images of (**A**) polycrystalline $[H_2EDA^{2+}\ BuTCA^{2-}]\cdot 2H_2O$ and (**B**) large single crystals of the same.

3.4.3 Characterization

Single crystal X-ray diffractometry of the obtained single crystals revealed the absolute structure of the monomer salt, which in fact crystallized as a dihydrate with the general formula $[H_2EDA^{2+}\ BuTCA^{2-}]\cdot 2H_2O$ (cf. figure 3.9).

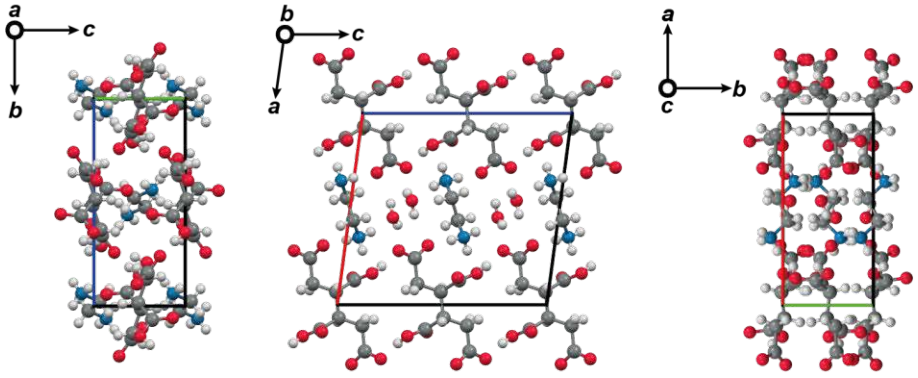

Figure 3.9: Crystal structure of the monomer salt hydrate $[H_2EDA^{2+}\ BuTCA^{2-}]\cdot 2H_2O$. These aspects are viewed along a-axis (left), b-axis (center) and c-axis (right). It crystallizes in the monoclinic space group $P2_1/c$ (no. 14) with lattice parameters a = 11.352(4) Å, b = 5.3571(17) Å, c = 12.299(4) Å and β = 97.511(8)°.

Comparing the powder X-ray diffractogram simulated from the crystal structure via CDCC Mercury software (versions 3.10.2 to 4.3.1) to the patterns obtained from analyzing several batches of the polycrystalline monomer salt, the congruence seemed virtually perfect (cf. figure 3.10). Moreover, after more than one year of storage in semi-closed

containers at room temperature, the diffractograms of all monomer-salt samples as well as their overall appearance remained unchanged, which indicated a generally high shelf life.

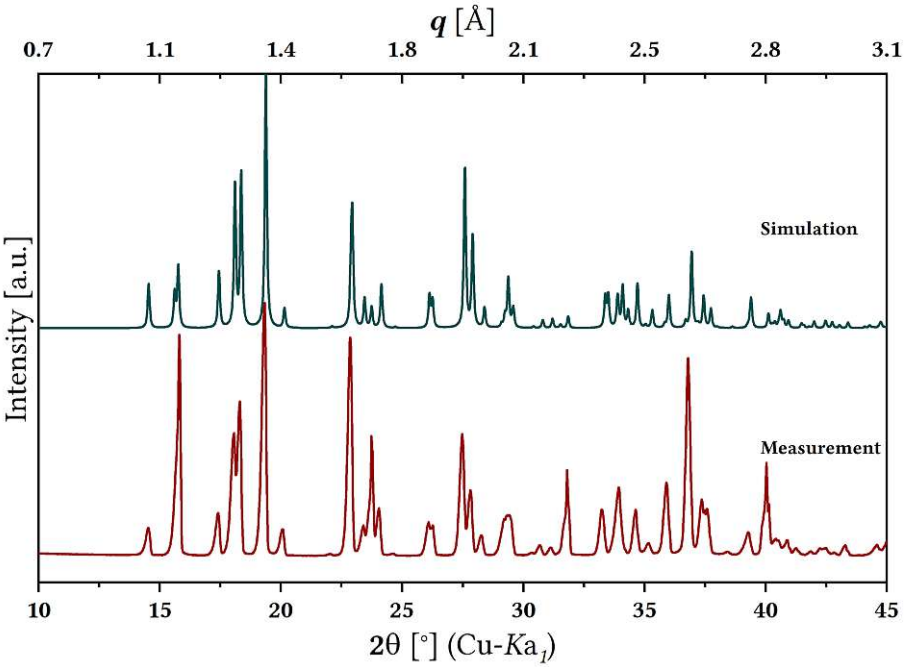

Figure 3.10: Powder X-ray diffractograms of polycrystalline $[H_2EDA^{2+}\ BuTCA^{2-}]\cdot 2H_2O$. The measured diffractogram matches the simulated one obtained from calculating the reflections from the salt's crystal structure. Differences in intensity of single reflections were due to preferential crystal orientation during sample preparation.

Thermogravimetric measurements were conducted following a method of measurement specified in section 5.2.1 and methods of result retrieval specified in section 5.2.2 of chapter 5, which is fully dedicated to thermogravimetric analyses of numerous PIs. Measuring at a rate of 10 K min^{-1}, four samples obtained from two batches of monomer salt were analyzed in each dry N_2 and dry air. Initial sample masses ranged from 13.3 g to 26.8 g, whereas for analyzing dehydrated monomer salt in N_2 one 11.40 g sample of salt dried at 80 °C in vacuo was used. Upon heating $[H_2EDA^{2+}\ BuTCA^{2-}]\cdot 2H_2O$, starting from above 50 °C until approximately 170 °C a mass-loss event could be observed, which perfectly fitted the calculated mass loss of 10.91 % upon theoretical release of crystal water. This mass-loss event did not occur when analyzing the sample of dehydrated monomer salt, which did not exhibit any mass loss in this region, confirming the assumption of crystal water being released from the neat monomer-salt samples. All samples showed a second mass-loss event setting on at approximately 200 °C, which was identified as the expected cyclodehydrative polymerization process. The third mass-loss event observed in each of these measurements represented the resulting polymer's decomposition process, de-

scribed by following indicators of thermal stability: Averaged over all measurements, the polymer exhibited $T_{d,400}$ of 465 °C in nitrogen atmosphere and 464 °C in air, $T_{d,onset}$ of 467 °C in nitrogen atmosphere and 459 °C in air, and $T_{d,max}$ of 492 °C in nitrogen atmosphere and 479 °C in air. $T_{d,400}$ and $T_{d,onset}$ describe two indicators for the beginning of the polymer-decomposition process, while $T_{d,max}$ depicts the temperature of maximum decomposition rate of the polymer. Compared to fully aromatic PIs, which range around 600 °C for $T_{d,400}$, these values seemed quite low. However, since it was shown in section 5.3.4 and later sections that already marginally allocated aliphatic moieties within the PI structure lead to tremendous losses in thermal stability and given the fact that a polymer obtained from $[H_2EDA^{2+}\ BuTCA^{2-}]\cdot 2H_2O$ must be fully aliphatic, this polymer could indeed be considered quite stable. Compared to other fully aliphatic PIs found in literature, this polymer's thermal stability seemed to be superior,[138,139] or highly comparable.[140] However, numbers obtained from thermogravimetric measurements are strongly dependent on several method-intrinsic factors, which renders any direct comparison of decomposition temperatures throughout different literary sources somewhat obsolete. For more detailed explanations and further contextualization of the decomposition temperatures obtained for this PI, the reader is referred to chapter 5.

Attenuated total reflectance Fourier transform infrared (ATR-FTIR) analysis of the monomer salt $[H_2EDA^{2+}\ BuTCA^{2-}]\cdot 2H_2O$ indicated full conversion of the starting products to monomer salt: Distinct aliphatic N-H stretching modes of the diamine at $\tilde{\nu}$(N-H) ≈ 3296 - 3263 cm^{-1} and ≈ 3393 - 3383 cm^{-1} vanished. Moreover, a N-H bending mode at $\tilde{\nu}$(N-H) ≈ 1597 cm^{-1} vanished, whereas aliphatic C-H stretching modes at $\tilde{\nu}$(C-H) ≈ 2930 - 2861 cm^{-1} were found to be less pronounced. Instead, broad aliphatic -NH_3^+ stretching modes above $\tilde{\nu}$(N-H) ≈ 3000 cm^{-1} were visible. Highly distinct carbonyl stretching modes at $\tilde{\nu}$(C=O) ≈ 1695 cm^{-1} of the tetracarboxylic acid shifted to $\tilde{\nu}$(C=O) ≈ 1684 cm^{-1} upon reaction to monomer salt. Moreover, a very distinct mode at 3404 cm^{-1} indicated the presence of crystal water. This peak completely vanished upon drying the monomer salt at 80 °C in vacuo. Simultaneously, the carbonyl stretching mode shifted to $\tilde{\nu}$(C=O) ≈ 1678 cm^{-1} upon drying while another one at $\tilde{\nu}$(C=O) ≈ 1657 cm^{-1} arised. This could have indicated the existence of two carbonyl modes, one belonging to the deprotonated carboxylate anion and the other one to the protonated carboxylic acid moiety, while another mode at 3084 cm^{-1} vanished, but instead one at 3152 cm^{-1} emerged. Both observations could have correlated with a carboxylate-carboxylic acid dimer (-CO_2^-…HO_2C-), which would mean that, in a salt-dihydrate state, both moieties shared a proton and were therefore spectroscopically equivalent.

ATR-FTIR analysis of the polymerization product revealed the absence of modes characteristic for the starting compounds and the monomer-salt precursor. Instead, intense modes indicative for full conversion to PI were found: Highly distinct imide-carbonyl stretching vibrations at $\tilde{\nu}_{as}$(C=O) ≈ 1774 cm^{-1} and $\tilde{\nu}_{s}$(C=O) ≈ 1688 cm^{-1} were present, as well as two stretching modes centered around the nitrogen atom within the imide moieties $\tilde{\nu}$(-H$_2$C-N) ≈ 1396 cm^{-1} and $\tilde{\nu}$(-OC-N) ≈ 1357 cm^{-1}.

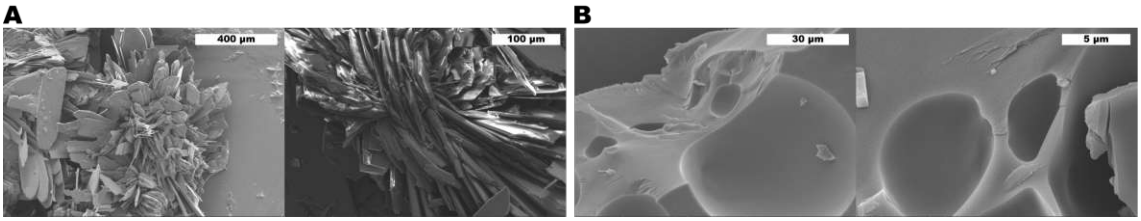

Figure 3.11: Scanning electron micrographs of (**A**) polycrystalline [H$_2$EDA^{2+} BuTCA^{2-}]·2H$_2$O and (**B**) its solid-state polymerized PI. The polymer exhibited clear signs of softening phenomena during polymerization.

3.4.4 Manufacturing of Polyimide Foams

Converting this monomer salt into a PI generally could be done by simply heating it up to temperatures close to 200 °C. However, in order to obtain a PI product exhibiting a considerable fraction of pores, it seemed crucial to heat it up rather quickly in order to avoid premature evaporation of the crystal water and ensure the salt transitioning through a liquid phase during the process of heating. It was observed throughout numerous improvised trials that if the monomer salt was heated too slowly, both the occurrence of a liquid phase and the effect of foaming did not seem to be dominant. This was most probably due to the water molecules contained in the crystals evaporating too quickly, which could indicate the liquid phase originating rather from a dissolution of the salt in water released from the crystal structure (possibly from oligomerization reactions as well) at sufficiently high temperatures than from a pure melting process, or a combination of both. On the other hand, if the emerging water could not leave the reaction vessel at a sufficient rate, the liquefied salt would not react sufficiently to convert to PI (or a possible precursor state) and any bubble formed would eventually collapse since the salt would stay liquid unless cooled. It was found that the probably most efficient way of obtaining PI foams from [H$_2$EDA^{2+} BuTCA^{2-}]·2H$_2$O was exposing it to monomode microwave irradiation in a semi-closed vessel. This was achieved utilizing an Anton Paar Monowave 400 microwave reactor equipped with a G30 wide-neck vial, which was capped with a lid containing a PTFE septum which was modified by cutting a

2-mm wide notch in order to allow the release of emerging water vapor during the reaction. The inner surface of the glass vial was manually coated with a thin layer of mineral heat-transmission oil to facilitate demolding of the foam product. Approximately 1.5 g of the monomer salt were given into the vial and heated to 200 °C within 2 min and the temperature was held for 5 min. After one minute of heating while still at temperatures below the final polymerization temperature, the monomer salt started melting at the top of it's pile (which could be found in the central region of the vial) while the first signs of melting could be observed occurring on the pile's side facing the microwave source (cf. figure 3.12). The melting process quickly spread along the cross-sectional area and downwards simultaneously forming a continuous liquid phase in a period of less than 13 seconds from the occurrence of first signs of melting, while this entire process was accompanied by a vigorous formation of bubbles within the liquefied monomer salt. In the course of the following minutes of constant heating, stiffening of the foamed liquid phase was observed alongside significant browning. Since full conversion of monomer salt to PI could not be assumed due to the product's relatively bright color, the foam was demolded and cured in a convection oven at 200 °C for several hours. The obtained product was a stiff, intensely brown-colored PI foam. This experiment was repeated several times with slight procedural variations such as different heating rates and mass of monomer salt but with highly similar outcomes. However, the size and local distribution of voids within the obtained PI-foam products did not seem homogeneous.

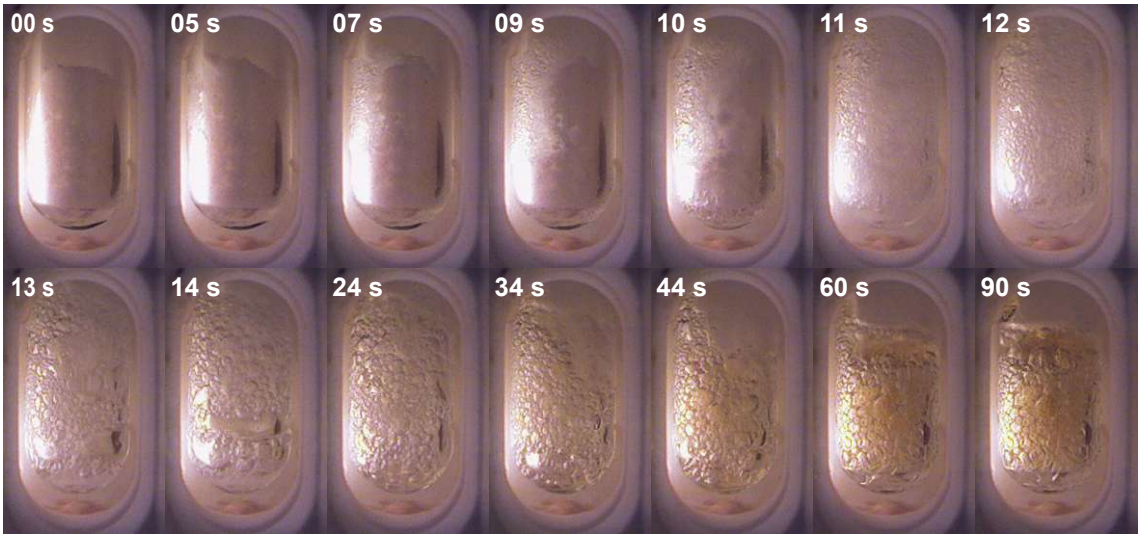

Figure 3.12: Image sequence of $[H_2EDA^{2+}\ BuTCA^{2-}]\cdot 2H_2O$ polymerized in a microwave reactor. The time signature in this series started immediately when the first signs of melting were visible after approximately one minute of heating. Within 13 s, all monomer salt inside the vial was in a liquid state, whereas after approx. 60 s stiffening of the foamed material could be observed.

3.4.5 Structural Possibilities

Considering the rotational flexibility of these fully aliphatic monomers along their C-C single bonds, most likely facilitated by high temperatures and the liquid state occurring in the process of polymerizing this monomer salt, numerous combinations of reactive sites to form amide and imide links could be considered possible. This would result in several isomeric structures after imide ring closure upon cyclodehydration, among which two five-membered rings connected by one C-C single bond (cf. figure 3.13 **A**), two fused six-membered rings (cf. figure 3.13 **B**), and a structure consisting of a five-membered ring fused with a seven-membered ring (cf. figure 3.13 **C**) could be considered being the ones most likely to occur.[141,142] Although these structures may have exhibited differences in thermodynamic stability, kinetic products could be expected from a polymerization reaction fast enough to cause a significant foaming effect using this PI precursor. On the other hand, especially amide linkages but also imide rings can be hydrolyzed in the presence of water if acidic or basic conditions, respectively, can be found in the moieties' close proximity,[143,144] which could potentially cause reverse reactions and favor thermodynamic products during polymerization. Regardless of the likelihood of this scenario occurring, it should additionally be mentioned that there might also be the possibility of intramolecular bisimides forming from a single monomer salt molecule if one $BuTCA^{2-}$ ion fully reacted with a single H_2EDA^{2+} molecule upon sufficient heating. Moreover, sporadic formation of amide crosslinks across longer polymer chains could seem possible, which would contribute to the fact that PIs obtained from this monomer salt were virtually insoluble in any common organic solvent. Merely swelling in hot, concentrated sulfuric acid could be observed. However, since all these scenarios seemed probable and simulative approaches to elucidating preferred structural compositions utilizing ATR-FTIR spectroscopy did not yield any results within the framework of this thesis, it was assumed that all possible combinations during condensation could occur.

3.4.6 Outlook

A monomer salt as precursor for fully aliphatic PIs was synthesized and characterized using inexpensive monomers and a highly facile route of synthesis exhibiting quantitative yields. In combination with its excellent storability, its inherently high content of blowing agent , and the fact that it readily melted and formed a foamed structure upon

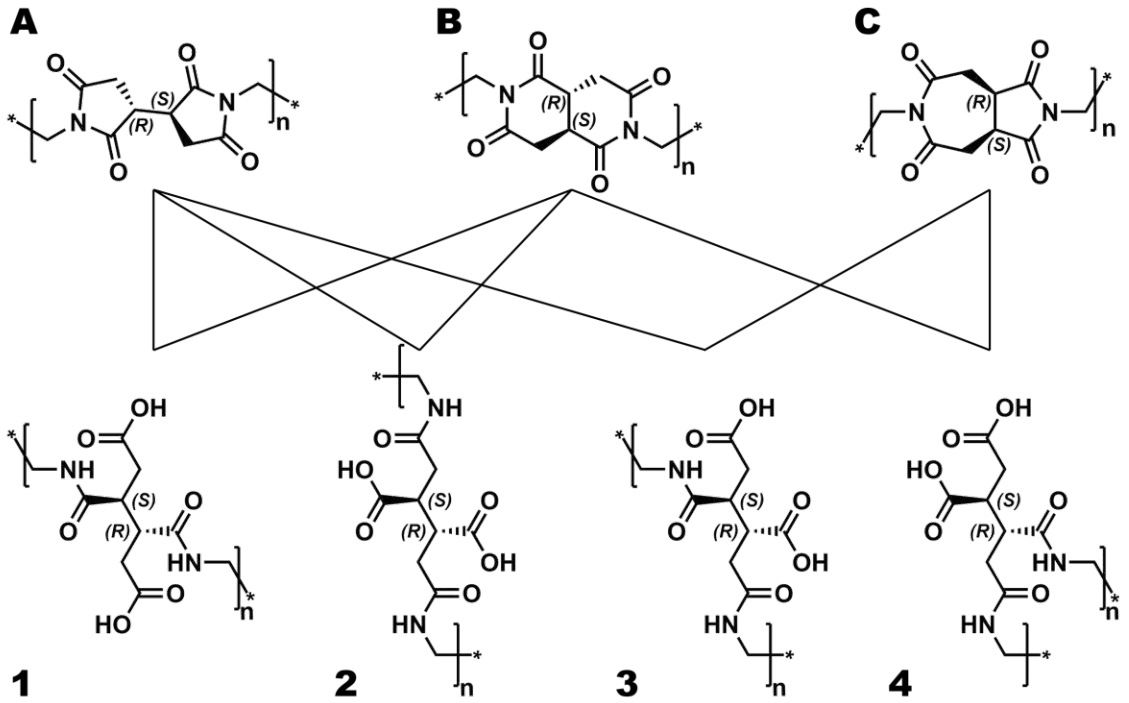

Figure 3.13: Three possible structures (**A**-**C**) polymers obtained from heating the monomer salt $[H_2EDA^{2+}$ $BuTCA^{2-}]\cdot 2H_2O$ could exhibit. Although mechanistic pathways of the reaction from monomer salt to PI are not fully understood,[62,63,107] intermediates (**1**-**4**) including amide linkages and pendant carboxylic-acid (or carboxylate) moieties seemed probable. Intermediates **1**,**2** and **3** could form PI structure **A**, two five-membered rings connected by one C-C single bond. Intermediates **1**,**2** and **4** could form PI structure **B**, two fused six-membered rings. Intermediates **3** and **4** could form PI structure **C**, a five-membered ring fused with a seven-membered ring.

quick heating by means such as irradiation by microwaves, it represented (an ideal candidate as) precursor for easily obtainable high-performance polymer foams and offered great potential representing an environmentally benign route to PI foams.

However, several processing-related aspects would have to be studied more extensively in order to reliably produce well-performing PI foams from it, such as optimization of the foaming process in terms of adjusting the water-vapor exhaust during heating, or ensuring a higher degree of homogeneity of the pores in terms of size and local distribution. Naturally, methodical aspects of upscaling the foam production from this precursor would pose another challenge which would require tackling.

Moreover, some degree of clarification if the monomer salt's liquidification upon heating is a melting process of the salt itself or rather a solution of the salt in water originating from the crystals themselves combined with water arising from oligomerization reactions could be beneficial for optimizing foaming procedures from an engineering perspective. This, but also a structural elucidation of the polymeric products obtained from polymerizing $[H_2EDA^{2+}$ $BuTCA^{2-}]\cdot 2H_2O$ would even be of scientific interest.

4. Vapor-Sorption Analyses

4.1 Introduction

Several reasons exist for why in the past decades PIs have been the polymer class of choice for dielectric applications in the electronics and microelectronics industry. In this field, the most relevant characteristics of PIs are their generally low dielectric constants and their extraordinarily high thermal stability. However, PIs cannot prevent corrosion phenomena from occurring during a (micro)electronic device's service lifetime, often times resulting in considerable device reliability issues. In this context, corrosion is closely related to the presence of water in the affected site's close proximity, as water can solvate ionic impurities in PIs and enable their participation in conductive processes,[145–147] which could ultimately lead to electrolytic corrosion.[148,149]

Several scientists' observations on how PIs are able to absorb water were somewhat contradictory: In their pioneer research on the (di)electric behavior and water permeation properties of the PMDA-sODA system, Sacher and Susko indicated that polar moieties within PIs, namely carbonyl groups and ether linkages, play a crucial role in this PI's sorption properties.[146,148] In 1989, Melcher et al. confirmed bond-like interactions of water molecules with the carbonyl mioeties, while excluding significant amounts of water to be sorbed at internal clusters or the PI chain ends.[150] Both groups estimated the amount of water absorbable to be approx. 0.67 - 1.03 mol water per mol of repeating unit of the PMDA-sODA system. A possible PI-water interaction mechanism is presented in figure 4.1.

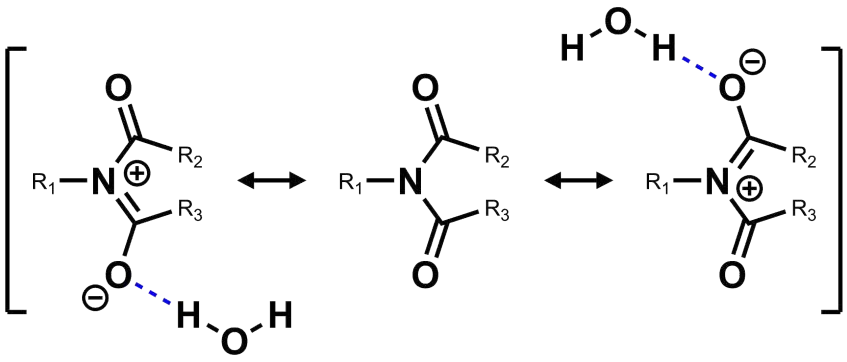

Figure 4.1: Intrinsic polarity of PI materials due to the eponymous imide moiety itself. Negative partial charges can exist statistically on each of the oxygen atoms involved in the imide bond. These sites are very likely to be subject to interactions with water molecules, most probably in terms of hydrogen bond formations.

On the other hand, Denton et al. proposed in 1985 that the uptake of moisture in PIs is mainly driven by water molecules occupying free volume in the polymeric material, which could be lowered by densification of the PI film by e.g. increasing cure temperature. Upon densifying a PI film, the polymer's free volume is lowered, resulting in a decreased velocity of moisture diffusion.[14,151] Moreover, in 1998 Buchhold et al. postulated that in PIs water molecules are absorbed exclusively in microvoids[152,153] ranging from 0.5 nm to 0.8 nm in diameter[154] and that the sorption behavior is "not directly related to the presence of polar groups",[153] thereby negating any effects polar moieties such as carbonyl groups could have on the water sorption of PIs. However, in cooperation with Buchhold, Dlubek et al. found in 1999 that below 30 %RH, the water sorption process in PIs might be dominated by single water molecules occupying larger pores, whereas at higher relative humidities (RHs) multiple occupancy of these pores and interstitial free volume might occur, while synergistic effects from water molecules hydrogen bonding to carbonyl groups might exist.[155] Nonetheless, several authors agreed in that it most likely is a subtle combination of both steric and electronic effects[156] being responsible for water sorption in PIs: Already in 1991, Moylan et al. stated that among different PIs, differences in water-sorption behavior could be due to discrepancies in chemical affinity for water molecules or in internal volume available for water permeation, or both.[157] More recently, Seo et al. also included both aspects of water affinity to polar groups,[158,159] as well as (free) volume in the polyimide arising from polymer-chain orientation and intermolecular packing order leading to differences in water sorption.[158,160,161] Furthermore, it has to be noted that crystalline regions in a PI serve as impenetrable obstacles, which reduce the overall volume available for water (and solvent) sorption.[28,162,163]

Although the permeation of water into a PI initiates by adsorption of a monolayer on the PI surface,[146] the overall uptake behavior was shown to be a bulk absorption phenomenon,[164] while the sorption of water in PI films is a fully reversible diffusion process.[152] Since they are mostly used below their generally high glass transition temperatures, PIs can be classified as glassy polymers, which includes the water diffusion to deviate from ideal Fickian behavior.[165–167] However, the kinetics of water diffusion into PIs fairly obey Fick's second law of diffusion and can therefore be modeled by it.[152,155,157,166,168]

In 1855, Adolf Fick formulated his second law of diffusion (one-dimensional case) to be

$$\frac{\partial c}{\partial t} = D\frac{\partial^2 c}{\partial y^2} \tag{4.1}$$

where c denotes the concentration of the penetrant at time t and at a distance y from the substrate's surface (gradient of concentration only along the y-axis), while the constant D is the so-called diffusion coefficient.[169–171] John Crank presented a solution to this equation for a plane sheet model in 1975, while assuming one-dimensional diffusion and thereby neglecting effects of penetration into the edges of the plane sheet:

$$M(t) = M_\infty(1 - \sum_{n=0}^{\infty} \frac{8}{(2n+1)^2\pi^2} e^{\frac{-D(2n+1)^2\pi^2 t}{4L^2}}) \tag{4.2}$$

$M(t)$ denotes the absolute water uptake at a time t, M_∞ denotes the absolute water uptake at equilibrium, while L denotes the thickness of the plane sheet (film) and D again denotes the diffusion coefficient, which is a measure for the diffusion velocity of a penetrant into solid matter.[170] This equation and its simplified approximations provide a convenient way of obtaining D from mass uptake experiments,[172] and has successfully been used for describing diffusion of water into PI films by numerous authors,[158–162,166,168] and will therefore be utilized within this chapter.

As the term polyimide merely describes a class of polymers, PIs' molecular structures can differ greatly depending on which monomers have been employed for their synthesis. Since its structural composition has a great impact on the resulting PI's moisture sorption behavior,[152,157] it is of vital importance for its intended application to predict both how much water can be taken up by the PI and how quickly the diffusion through the material takes place. Although the fields of interest in PIs' structure property relationships are widespread and some applications, such as gas-separation membranes, aim for high uptake and diffusivity,[167] this thesis' chapter was mainly motivated by systematically lowering PIs' moisture uptake and diffusivity. For that, several PIs from (in most cases) commercially available monomers were synthesized and the employed monomers' influence on both the moisture uptake (relative to sample mass) and this absorption process' velocity (diffusivity) of the resulting PIs were analyzed and compared systematically.

4.2 Experimental Approach

4.2.1 Method of Measurement

Classically, and as defined by standards set by ISO[173] and ASTM[174], moisture uptake of polymers is determined via gravimetric analysis of samples exposed to either full im-

mersion in water[173,174] or to storage conditions at 50 %RH[173], while changes in sample mass are detected on analytical balances capable of reading to 0.1 mg. This requires for quite large specimen sizes having a dry weight of 2 g to 10 g to compensate for inherent inaccuracies of analytical balances.[175] Moreover, as it is a static type of measurement in which the specimen is weighed after certain durations of exposure, these methods intrinsically pose a very limited temporal resolution and therefore do not allow for analyzing the kinetics of the sorption processes.

Therefore, the obvious method of choice for analyzing the sorption behavior of PIs within this work was dynamic vapor sorption (DVS). It allows for freely customizable programs of relative humidity exposure, sample masses in milligram range, as well as continuously recorded parameters. All DVS measurements were conducted on a DVS Intrinsic (*Surface Measurement Systems Ltd.*, London, UK), which was located in the laboratories of the *Polymer and Composite Engineering Group* at the University of Vienna.

To describe its operating principle in a simple manner, the DVS instrument continuously floods a sample chamber with gaseous nitrogen, which has been humidified by effervescence within a separated water reservoir, while a humidity sensor controls the relative humidity in the sample chamber. Within the course of a measurement, the sample, which has been placed on top of a sample pan, which again is attached to a sensitive digital microbalance, gets exposed to different, controlled levels of relative humidity while the microbalance detects changes in sample mass. From such a measurement several parameters, such as sample mass, target humidity, (actual) relative humidity, etc., are obtained along a time axis, in a temporal resolution and at a temperature chosen by the operator. Preliminary measurements showed that changes in specimen dimensions of the same PI system lead to significant differences in water uptake in the measurement (cf. Figure A.1). Here two specimens of the PI system PMDA-Bz were cut out from the rather even, central region of 900-mm^2 sized spin-coated PI films, both having different thickness and surface area. Based on this insight, it was considered crucial for a general comparability of a sample series to have similar and defined dimensions. Therefore, all following samples were prepared on square-shaped silicon wafers having a surface area of 100 mm^2 on their polished side. Each obtained specimen had one flat side which was attached to the substrate's surface and another one being slightly uneven due to more material depositing in the outer regions upon curing, known as the coffee-ring effect. By fully covering the polished side of the wafer with sample material, all samples had the same size in two dimensions (10 mm), whereas the average thickness of each film depended on the amount of material applied and the material itself, and ranged from 24

to 49 µm. It was assumed that possible effects arising from deviant total surface areas within the entirety of the samples could be minimized by this approach.

For analyzing the samples in terms of water vapor uptake two fundamentally different programs of humidity exposure had been utilized within this thesis. The chronologically first one included more and consecutively increasing steps in humidity, less duration per step and a relatively low scanning frequency of 1 min^{-1} as compared to the second program. Two to three specimens per PI system were analyzed following this method. It consisted of an initial drying step at targeted 0 %RH for 420 min, followed by steps of 180 min at 20 %RH, 180 min at 40 %RH, 300 min at 50 %RH, 180 min at 60 %RH, 400 min at 80 %RH, 500 min at 85 %RH, one desorption step for 180 min at 50 %RH and one final step at 0 %RH for 200 min. A different approach was chosen when the second program was used to analyze various PI materials more thoroughly. For this, since several measurements conducted using the first method showed a linear behavior between RH and water vapor uptake, only four levels of RH were chosen: An initial drying step at 0 %RH, then absorption steps at 20, 50 and 85 %RH, each absorption step followed by a desorption step at 0 %RH. This allowed for a more thorough investigation of the chosen PIs' sorption behavior, as for each level of RH both absorption and desorption isotherms until mass equilibrium were recorded. The duration of each step increased with increasing humidity levels, since an increase in time necessary for sample weight equilibration was observed when increasing RH during measurements. Moreover, since the PIs showed huge differences in absorption velocity, each program had to be adapted individually in terms of step duration, which led to total measurement lengths ranging from 46 to 120 h per program. The details of each humidity program employed are specified in each subsection of the results section. A scanning frequency of 30 min^{-1} ensured a finer resolution, which was considered appropriate for approximating experimental absorption curves by equation 4.2. The DVS instrument did not exactly reach the target RHs as assigned by the selected program. In all drying phases within all programs the actual RH oscillates slightly below 1 %RH but never at 0 %RH, which might be either due to residual humidity from the technical grade nitrogen supply or just a limitation inherent to the device. At higher target RHs, values for actual RH slightly deviated from the targeted RH: aiming for 20 %RH led to an actual 18.3 – 18.8 %RH, targeted 50 %RH to actual 50.8 – 51.0 %RH, and targeted 85 %RH to actual 85.4 – 85.9 %RH. After a neighboring laboratory had suffered a fire, the DVS device's humidity sensor was recalibrated by an authorized service technician sent out by the manufacturer. After that, the deviations of actual RH to targeted RH changed: aiming for 20 %RH led to an actual 17.8 – 18.2 %RH, targeted

50 %RH to actual 48.1 – 48.8 %RH, and targeted 85 %RH to actual 82.0 – 83.2 %RH. In all cases, approx. 10 s after the program set a change in target RH, a significant change in actual RH could be detected, whereas several minutes were necessary for the device to equilibrate at a stable actual RH. All measurements were conducted at a stable temperature of 25.0 °C within the sample chamber.

4.2.2 Manufacturing of Specimens

For obtaining PI samples for DVS measurements PAAs (cf. chapter 3) were drop casted onto (100) Si wafers and cyclocondensated at temperatures up to 400 °C. The precisely cut, square-shaped wafers had a side length of 10 mm and a polished side covered by a few-nanometer thin native oxide layer. The amount of substance applied on the wafers depended on the planned comparison. For comparing fraction of imide moieties within PIs, the weight of cured PI was kept constant at approx. 3.6 mg. For all other specimens, the amount of cured PI ranged from 9.6 - 10.0 µmol (with the exception of samples of approx. 6.6 µmol in preliminary measurements of PMDA-APBP and PMDA-8FAPBP). The amount of substance refers to the quantity of repeating units of the respective PI assuming infinite chain lengths. For applying the PAAs, the substrates' polished surface was wetted by PAA using a clean spatula which has been immersed in the polymer solution before. Complete wetting until the very edges of the substrate was ensured with utter care since flaws in wetting lead to a withdrawal of the polymer from affected sites during curing. Then, more PAA solution was added dropwise until the desired weight of applied precursor solution was reached, whereas the dry mass of each PAA solution after curing was either calculated assuming infinite polymer chain length or in some cases by weighing samples on a microbalance before and after curing. Several specimens were prepared for each polymer system. This whole process was done on a *Sartorius* analytical balance, which was capable of reading to 0.1 mg. This balance's relatively low sensitivity might be the main reason for slight deviations from the desired weight of the final product when then weighed with the microbalance within the DVS device during measurements. Immediately after application each sample was given into a tube furnace and pre-baked at 90 °C in a slight stream of nitrogen ensuring inertness within the sealed tube and removal of solvent from the casted precursor polymer solutions. Approximately one hour after the last sample was given into the tube furnace, all content of the furnace was subjected to a specific curing program while maintaining a slight nitrogen flow. It consisted of heating from 90 °C to 400 °C at a rate of 2 K min^{-1} with

isothermal plateaus at 150 °C, 210 °C, 300 °C (30 min duration each) and one final temperature step at 400 °C which was held for 60 min. This curing program was followed by slowly letting the furnace cool down to ambient temperature over several hours in static nitrogen atmosphere. Free-standing PI films for DVS measurements were obtained by carefully detaching each cured polymer film from the substrate with an unused razor blade. This manual procedure occasionally led to damages at the corners of single PI films, which therefore were not subject to any DVS measurement. PI systems containing ether linkages (polyetherimides - PEIs) showed a comparably high affinity to the substrate, which made it necessary to immerse those specimens in deionized water during manual detachment. The specimens immersed in water were subsequently dried in a drying cabinet at 60 °C for several hours and then transferred to glass vials flushed with argon, whereas all other samples were stored in LDPE bags at ambient conditions prior to measurement.

4.2.3 Determination of Sample Thickness

After application of the PAAs onto the wafers, the applied material covered all surface in a drop-like fashion, confined by the edges of the substrate. Upon drying and curing, each specimen showed a ring-like deposition of the PI material with slightly thicker outer regions. For calculating diffusion coefficients, the average sample thickness had to be determined. Measuring the thickness of a sample by means of profilometry directly requires non-covered regions of the substrate as points of zero height on opposing sides. Since this would require cutting off parts of the sample, a different approach was chosen. After characterization in the DVS device, it was attempted to evenly re-attach each sample to square-shaped silicon wafers of 30 mm side length. These attempts were successful only in 6 out of 29 cases, since most samples exhibited a slight curvature after detaching them from the original substrate while having only limited flexibility. However, every specimen's thickness could be determined with the help of a *Mitutoyo* digital micrometer series 293 0-1"(*Mitutoyo Corporation*, Kawasaki, Japan), although the values obtained hereby seemingly overestimated sample thickness, due to the measuring faces' rather high surface area of approx. 32 mm^2 and the resulting low lateral resolution. Assuming the thickness determined via profilometry being more representative of the actual one, an average ratio between profilometer-derived (average of four measurements across the film with an offset of approx. 45°) and micrometer-derived (average of four areas in each corner and two central areas) was calculated for the samples which could be analyzed

via profilometry. For each sample, the ratio of 0.70 was then multiplied with the values for thickness derived by the micrometer method to get the final thickness which was taken for the calculation of the diffusion coefficients.

4.2.4 Retrieval of Results

For determining the absolute moisture uptake of each PI, the increasing sample mass at each humidity step was set in relation to its dry weight, given in per cent. The last value of sample mass of the initial drying step (approx. 1 %RH) was set to be the dry weight, while the last value of sample mass at the end of each absorption step depicted the absolute mass uptake at this level of humidity. However, for several measurements, slight shifts in the baseline for sample mass could be observed, which affected processing of the data derived by the second, refined type of measurement method. One, rather rare type of such inconsistencies manifested in sudden shifts to slightly higher or lower values of sample mass at some point within the data series, which most probably occurred due to percussions the device was exposed to, in spite of the numerous measures taken for shock absorption. The other two -rather subtle- types of shifts in the baseline could be observed over the whole course of few single measurements, when the sample mass at the end of a drying stage had values either lower or higher than at the end of the previous drying stage. As those phenomena were consistent within one sample (values always increasing but never decreasing within one measurement or vice versa), this behavior could also originate from material-inherent properties. However, when determining the absolute moisture uptake, these shifts were easily corrected by not referring to the initial dry weight of the sample but to the dry weight obtained from the previous drying stage.

For deriving the diffusion coefficients of the materials, each sorption step's complete series of data points was separately subjected to curve-fitting to equation 4.2. The originally continuous time signature was set to zero at the beginning of each step via subtracting the first value of measurement time (in s) from all following data points of this sorption step. Since equation 4.2 takes into account the mass change of ab- or desorbed water, these values were derived via subtracting the sample mass at the beginning of each sorption step from all following data points within this step. If percussive shifts in the data curve -as mentioned previously - occurred rather late within one sorption step, fitting of the experimental curve was done until the shift occurred and all following data points were not included. If such a percussive shift occurred within the first half of the

sorption steps duration, the measurement was repeated. The other, constant shifts in dry weight did not affect the calculations of the diffusion coefficients, as each ab- and desorption step was handled separately.

Equation 4.2 describes the development of ab- or desorption of water as a function of time, with constant parameters of film thickness, initial (=0 mg) and final values for mass of absorbed water and diffusion coefficient ($cm^2 \cdot s^{-1}$). With thickness being a known parameter, the simulated curve was fitted by adjusting the diffusion coefficient for the material at each sorption step, converging toward the final mass value of the experimental curve (which is negative for desorption curves). The obtained measurement data for each sorption step was separately processed in a Python[176,177] (version 3.8.5) environment, utilizing the Python libraries NumPy[178] (version 1.19.2), mpmath[179] (version 1.1.0) and SciPy[180] (version 1.5.2). For each sorption step, a simulated curve was fitted to experimentally obtained data using the *SciPy.optimize.curve_fit* function applying a *Levenberg-Marquardt* algorithm within a damped non-linear least squares method. After an initial guess, the diffusion coefficient was refined by repeating the curve fit calculation at least two times while inserting the obtained value of the previous calculation as first guess of the new one. The results obtained consist of six different diffusion coefficients per sample, one for each absorption step (from 0 %RH to 20, 50 and 85 %RH) and one for each desorption step (from 20, 50 and 85 %RH to 0 %RH). Ranging between $2.72 \cdot 10^{-10}$ $cm^2 s^{-1}$ to $3.04 \cdot 10^{-7}$ $cm^2 s^{-1}$, the values for the diffusion coefficients retrieved from these calculations agree very well with the ones found in literature[14,151,158,159,162,168,181], while each material showed similar values for all associated diffusion coefficients. For each PI system, an average diffusion coefficient D_{avg} was calculated, taking into account all sorption stages of the respective measurement. For reasons of simplification, this averaged coefficient was used to compare the diffusion behavior of the analyzed PI systems within the results section, while a higher D_{avg} denotes a higher velocity of water diffusion into a PI material.

4.3 Results

The first three subsections of this section first discuss the results of the measurement method employed initially as described in 4.2.1, analyzing two or more specimens per PI system and consisting of shorter exposition times in absorption mode only. Nevertheless, they show a linear relation between RH and mass increase due to absorbed water and already point to tendencies in the moisture uptake behavior of the PIs analyzed. This

was followed by the analysis of both moisture uptake as well as diffusion coefficients obtained from the second, refined measurement method employing four different stages of ab-/desorption and longer exposition times. One to two specimens per PI system were analyzed using this method. The samples analyzed for all following subsections were subject to the refined method of measurement only, as it contains more processable information and rendering the first method somewhat obsolete. For interpreting the graphs showing the absolute moisture uptake of PIs within this chapter, it has to be noted that 0 %RH could not be reached using this device but instead RH was oscillating below 1 %RH. Nevertheless, as the sample mass at the fictious value of 0 %RH could not be determined, the sample mass at <1 %RH was set to 0 wt% moisture uptake.

4.3.1 Fraction of Imide Moieties within PI Material

The idea behind this measurement series was to analyze PI systems comprised of fully aromatic segments connected by imide moieties and compare them in terms of the effect mass fraction the imide moiety makes up within each PI's structure. There is only a limited number of monomers commercially available, which do not contain heteroatoms or aliphatic regions outside their amine or anhydride functionalities. The diamines 1,4-phenylenediamine (pPDA), benzidine (Bz) and 4,4′′-diamino-*p*-terphenyl (DATP) contain one, two or three benzene rings, respectively, in a linear fashion and are therefore suitable for such a comparison. For the dianhydride counterpart only pyromellitic dianhydride (PMDA) and 3,3′,4,4′-biphenyltetracarboxylic dianhydride (sBPDA) were available, containing one and two benzene rings, respectively. It should be noted that employing sBPDA, although being symmetric, does not lead to fully linear polymer chains when polymerized due a kink resulting from the bonding of the two benzene rings, which is in meta-position to one anhydride functionality on each side. Total linearity on the dianhydride side (except for PMDA) would only have been possible employing naphthalene-2,3,6,7-tetracarboxylic dianhydride and anthracene-2,3,6,7-tetracarboxylic dianhydride, containing two and three benzene rings, respectively. These two monomers were not available commercially at any point during this work, whereas synthesizing them directly did not seem feasible, as sufficiently detailed reports about their synthetic routes were not to be found in literature and studies toward this direction would have exceeded the framework of this thesis.

Several PI samples of six different combinations of the three diamines and two dianhydrides mentioned before were prepared (cf. chapter 3). The PI system PMDA-pPDA has

an approx. 48 % mass fraction of imide moieties (counting both carbonyl groups and one nitrogen per imide group), assuming infinite chain length within the fully cured product. PMDA-Bz and sBPDA-pPDA both contain approx. 38 %, whereas PMDA-DATP and sBPDA-Bz both contain approx. 32 %. The system sBPDA-DATP contains the lowest fraction of imide moieties of approx. 27 %. It was assumed that with lowering the fraction of imide moieties within the same amount of PI material the moisture uptake would decrease, since this functionality intrinsically is significantly more polar compared to the aromatic parts of the PIs and therefore would offer a higher relative and absolute number of sites on which single water molecules could interact with. In order to investigate the effect, the number of imide moieties has on moisture uptake, the sample mass has to be equal across the series of PI systems. Keeping the sample mass constant results in differences in molar amount of sample material and therefore in differences in number of imide moieties, according to the size of each PI's repeating unit. It was set to approx. 3.6 mg. Effects of the PI chains' terminal amine or anhydride/acid functionalities were considered as being negligible in the moisture uptake behavior of the PIs synthesized.

Initially, three specimens per PI system within this sample series were analyzed following the first measurement method described in 4.2.1, except for the PI system PMDA-DATP, for which only 2 specimens were analyzed. As it can be seen in Figure 4.2, for each specimen a clearly linear behavior could be observed: With increasing RH the increase in sample mass increased as well. These linear dependencies of RH and moisture uptake have been reported before.[14,151,153,164] A slight scattering of values for moisture uptake could be observed as well, which became more apparent in both PI systems having the highest total moisture uptake and especially at higher values of RH. These discrepancies are most likely due to differences in specimen weight resulting from the low sensitivity of the balance used for sample preparation, and to the rather short duration of each absorption stage within this measurement method. PMDA-pPDA exhibited the highest overall uptake of more than 4 wt% at 85 %RH. With about 2 wt%, the PMDA-Bz system's moisture uptake was roughly half the one of the previous system, although it only had a 20 % lower imide mass fraction. A significantly lower uptake could be seen in the systems PMDA-DATP and sBPDA-pPDA, which were slightly overlapping, followed by sBPDA-Bz and sBPDA-DATP showing the lowest moisture uptakes. It seemed as if a lower fraction of imide moieties indeed decreased the moisture uptake, although the resolution within the samples of lower uptake left room for improvement.

Therefore, a second measurement series was undertaken employing a program consisting of less absorption stages but with highly prolonged exposition durations adding up

to 116 h per sample in order to ensure getting closer to each PI system's sorption equilibrium (cf. section 4.2.1). The program comprised an initial drying step for 840 min at 0 %RH, absorption steps at 20, 50 and 85 %RH for 1200 min each, while each absorption step was followed by a desorption step for 840 min at 0 %RH. For this measurement series, two specimens per PI system were analyzed simultaneously. Here again, while all systems showed a linear absorption behavior, PMDA-pPDA (48 % imide mass fraction) exhibited the highest uptake of 4.2 wt% at targeted 85 %RH, followed distantly by PMDA-Bz (38 % imide mass fraction) with 2.1 wt% (cf. 4.3). PMDA-DATP (32 % imide mass fraction) showing an uptake of 1.4 wt%, was rather closely followed by sBPDA-pPDA (38 % imide mass fraction) with 1.3 wt%, and by sBPDA-Bz (32 % imide mass fraction) with 1.2 wt%. Having an uptake of 0.8 wt% at targeted 85 %RH the PI system sBPDA-DATP (27 % imide mass fraction) again had the lowest moisture uptake of all systems within this measurement series. These results clearly demonstrated that lowering the amount of imide moieties in the PI material lowers the amount of water being absorbed by it. However, the moisture uptake did not directly scale with the fraction of imide moieties within the PI. Differences in uptake are larger from PMDA-pPDA to PMDA-Bz and from the latter to the following systems, whereas it was expected that sBPDA-pPDA would show moisture uptake values rather in the region of PMDA-Bz than below PMDA-DATP. Instead, a general tendency toward lower uptake could be observed when incorporating sBPDA as dianhydride.

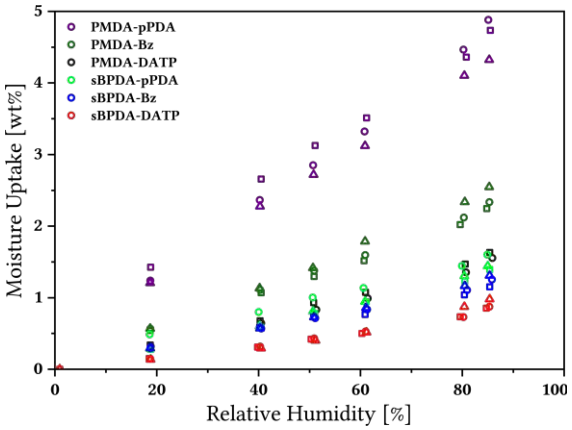

Figure 4.2: Initial DVS measurements of the sample series comparing moisture uptake of PIs with different imide fractions. Samples having lower imide fractions exhibit lower moisture uptake.

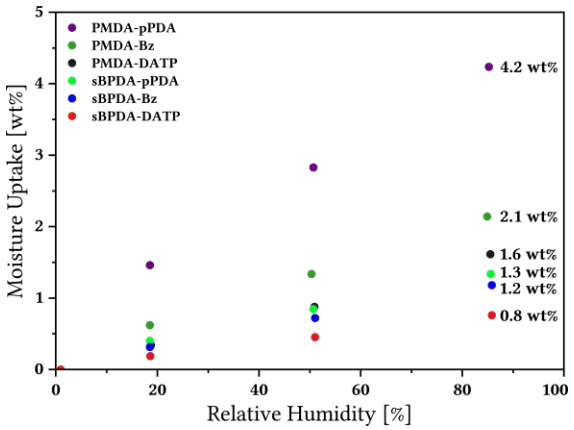

Figure 4.3: DVS measurements of the sample series comparing moisture uptake of PIs with different imide fractions following the refined method. Samples having lower imide fractions exhibit lower moisture uptake.

PIs based on PMDA could only form straight polymer chains, whereas rotational degrees of freedom are only existent along the axis of biphenyl linkages within the diamines Bz

and DATP. Moreover, as PMDA-pPDA, PMDA-Bz, as well as PMDA-DATP do not possess any empirically detected T_g,[182–184] alignment of the polymer chains during the chosen curing conditions most probably did not take place,[157] while any entanglement of polymer chains is hardly possible due to their rigid nature. Since the polymer chains did not undergo any directional alignment when drop-casting the precursor material onto the substrate as compared to spin-coating or tape-casting,[185] the PMDA-PIs must consist of an agglomerate of randomly aligned, stiff polymer chains. In case of PMDA-pPDA this macroscopically manifested in a very brittle material, which could manually be bent to only a very small extent before bursting asunder. Although the samples of PMDA-Bz and PMDA-DATP turned out to be surprisingly flexible, it was not assumed that these PIs' polymer chains could in fact entangle, as they are known to be rigid-rod polymers.[186] Their flexibility must therefore be solely due to the rotations possible along the diamines' biphenyl linkages. All this would mean that the packing densities of these three PI systems must be quite similar. Therefore, the only factor left being the cause of differences in moisture uptake observed for these PIs was in fact the difference between each material's fraction of imide moieties, while a lower fraction leads to lower uptake and vice versa.

The reason for sBPDA-PIs showing a generally lower uptake could be found in the somewhat higher flexibility arising from the slightly kinked biphenyl linkage within this dianhydride, as sBPDA-PIs have been shown to be quite linear but have two favored rotational conformations along the biphenyl linkage of sBPDA.[29] Although fully straight chains might pack more densely,[187,188] tighter packing could be possible due to a higher mobility of chains during the curing process at 400 °C, a temperature which is above the T_g of sBPDA-pPDA.[185,189,190] Moreover, since the polymer chains could not align during manufacturing, the slightly more bent structure of the sBPDA-PI chains will lead to a higher degree of polymer-chain entanglement, whereas PIs based on PMDA could only form straight polymer chains, which most probably will not have any preferred orientation. This entanglement could in this case eventually lead to a decrease in free volume within the PI bulk, as compared to randomly distributed, fully straight polymer chains, which could result in lower moisture uptakes for sBPDA-PIs compared to PMDA-PIs, since lowering the free volume of a PI decreases the amount of sites water molecules could occupy.[151] In addition to that, the effect of decreased moisture uptake after reduction of the material's imide-moiety fraction could also be observed within the series of sBPDA-PIs, meaning that these two effects could stack, rendering sBPDA-DATP the PI system with the lowest moisture uptake of this series. It has to be noted at this point

that PIs possessing molecular structures being more kinked than the sBPDA-PIs within this series exhibited significantly increased moisture uptakes and diffusion coefficients, as it will be demonstrated within the course of this chapter.

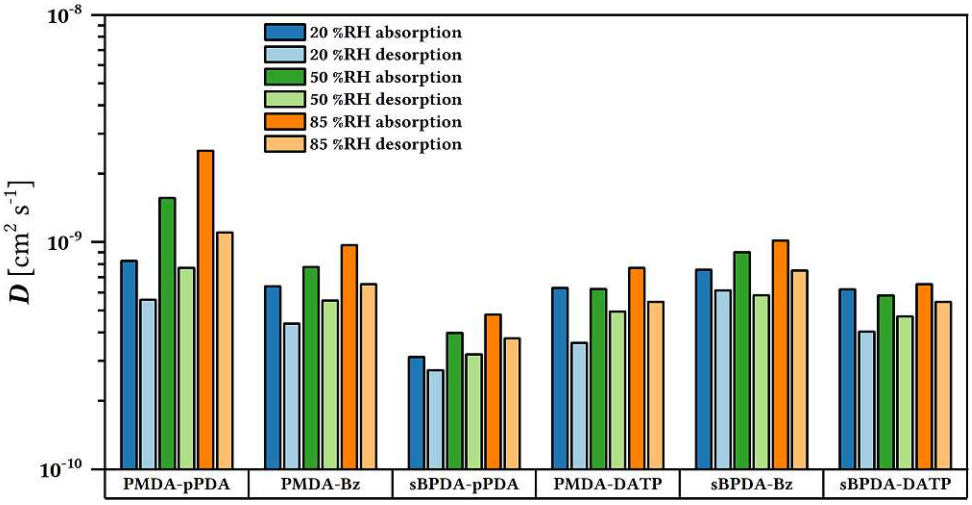

Figure 4.4: Diffusion coefficients of the imide-fraction series obtained from fitting measurement data of the refined method. The trends in diffusion coefficients did not follow the trends in fraction of imide moieties.

When observing the results of the diffusion-coefficient calculations in figure 4.4, the trends in diffusion coefficients turned out to be not as clear as it was for the moisture uptake. The system PMDA-pPDA had the highest average diffusion coefficient (D_{avg}) of $1.22 \cdot 10^{-9}$ $cm^2 s^{-1}$ (taking into account all sorption stages), which means that gaseous water penetrated the PI material the quickest among all PIs within this series. In order of decreasing D_{avg}, the second system was sBPDA-Bz (D_{avg}= $7.69 \cdot 10^{-10}$ $cm^2 s^{-1}$), closely followed by PMDA-Bz (D_{avg}= $6.71 \cdot 10^{-10}$ $cm^2 s^{-1}$), PMDA-DATP (D_{avg}= $5.70 \cdot 10^{-10}$ $cm^2 s^{-1}$), and sBPDA-DATP (D_{avg}= $5.45 \cdot 10^{-10}$ $cm^2 s^{-1}$). With D_{avg}= $3.59 \cdot 10^{-10}$ $cm^2 s^{-1}$, sBPDA-pPDA exhibited not only the lowest diffusion coefficients within this series but even of all systems characterized within this thesis. Contradicts assumption that more tight packing automatically is responsible for lower absolute moisture uptake (or that the more biphenyl linkages, the better the packing is). Interestingly, all throughout this sample series, each sample's absorption stages tend to give a significantly higher D than for the desorption stages. According to Denton et al., this asymmetry in the diffusion coefficients is due to their concentration dependence, "which is typical in high polymers".[151] However, throughout this study this behavior could only be observed in PIs containing no heteroatoms outside the imide moieties and no side groups attached to the aromatic backbone, while this effect also vanishes with increasing the degree of aromatic fluorine substitution.

4.3.2 Perfluorinated Segments within PI Backbone

The measurement series presented within this subsection aimed for shedding light on how substitution of hydrogen atoms with fluorine atoms attached to aromatic segments within the PI backbone structure affects the PIs' moisture sorption behavior. Generally, fluorinated PIs are known to be more hydrophobic.[191,192] This hydrophobicity is generally attributed to the fact that the C-F bond exhibits a severely low polarizability, due to these atoms' high difference in electronegativity,[192,193] which significantly reduces the probability of van-der-Waals interactions with water molecules.[194]

While perfluorinated, aromatic dianhydrides are commercially not available at all, perfluorinated diamines or diamines containing a high number of aromatic fluorine-substitution sites are, although their availability is somewhat limited.[195] Octafluorobenzidine would have been a great fit for a comparison between non- and perfluorinated monomers in PIs, but it is known that this diamine's reactivity is so low, one can not prepare continuous PI films from it.[196] This non-reactivity is due to a strong positive inductive effect caused by a high number of adjacent fluorine atoms, severely lowering the amines' nucleophilicity and therefore inhibiting acylation reactions necessary for PAA and PI formation.[195,197,198] Instead, it was found that the diamine 4,4′-bis(4-aminophenoxy)octafluorobiphenyl (8FAPBP) (synthesis described in appendix B.2) was a perfect candidate for this study, as (i) it has got a fully fluorinated biphenyl center which (ii) does not compromise the reactivity of its amine functionalities due to their distance to the fluorination sites, (iii) its synthesis is quite facile and (iv) it's non-fluorinated counterpart 4,4′-bis(4-aminophenoxy)biphenyl (APBP) is commercially available. In the PI system PMDA-8FAPBP approx. 44 % of all possible sites in the repeating unit's structure (8 out of 18) are fluorinated. In 1991, Mercer and Goodman already aimed on comparing the sorption behavior of two PIs containing APBP and 8FAPBP, respectively, polymerized with PMDA, but did not obtain continuous films of each PI due to embrittlement of the material upon curing.[24]

Initially, two specimens of each PMDA-APBP and PMDA-8FAPBP, each specimen having a molar amount of PI-repeating units of 6.6 µmol, were analyzed following the first measurement method described in 4.2.1. In order to keep comparability between these and the samples of PMDA-Bz, BPDA-pPDA and all PI systems following in later sections of this study, specimens with 10 µmol of PI were prepared and analyzed following the refined measurement method. This method consisted of an initial drying step at 0 %RH for 330 min, followed by an absorption step at 20 %RH for 180 min, which again was fol-

lowed by a desorption step at 0 %RH for 330 min, a second absorption step at 50 %RH for 510 min and a final absorption step at 85 %RH for 630 min, each followed by desorption steps at 0 %RH for 390 min.

As it can be seen in both figure 4.5 and figure 4.6 the relationship between RH and moisture uptake again is quite linear for all samples, while both methods gave quite similar results despite their differences in sample amount and therefore in thickness and surface to volume ratio. At targeted 85 %RH, PMDA-APBP exhibited a moisture uptake of 2.4 wt%, while PMDA-8FAPBP had a significantly lower uptake of 1.2 wt% (cf. figure 4.6). The fact that the fluorinated PI-system took up only half as much water as the non-fluorinated did confirms the expected increase in hydrophobicity when incorporating diamines with aromatic fluorine substitution sites. It has to be noted that the mass uptake in per cent naturally refers to a higher sample mass in case of PMDA-8FAPBP, since the molecular mass of this PI's repeating unit was higher.

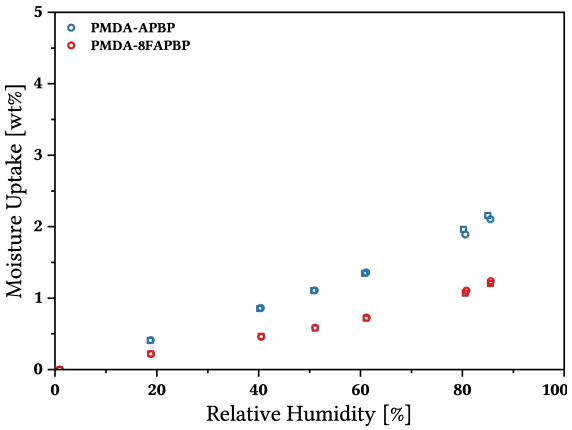

Figure 4.5: Initial DVS measurements of the sample series comparing moisture uptake of isomeric PIs being non-fluorinated and having perfluorinated segments, respectively. Flourinated samples exhibit lower moisture uptake.

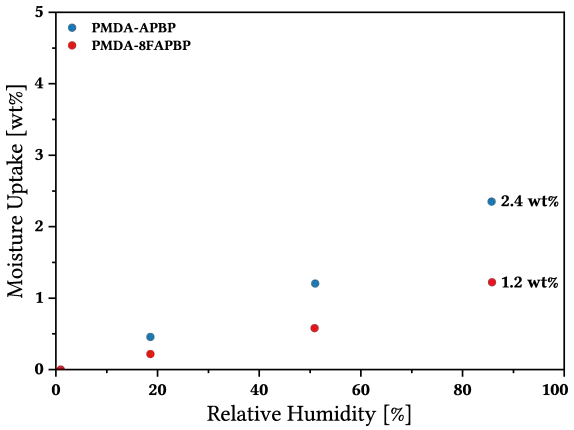

Figure 4.6: DVS measurements of the sample series comparing moisture uptake of isomeric PIs being non-fluorinated and having perfluorinated segments, respectively, following the refined method. The flourinated sample exhibits a lower moisture uptake.

The results of the diffusion-coefficient calculations (cf. figure 4.7) show a quite opposite trend: The fluorinated PI-system PMDA-8FAPBP has a significantly higher D_{avg} ($2.56 \cdot 10^{-8}$ $cm^2 s^{-1}$) than the non-fluorinated system PMDA-APBP (D_{avg}= $1.32 \cdot 10^{-8}$ $cm^2 s^{-1}$). This means that the fluorinated PI takes up less water but at the same time this water can penetrate the material at a higher rate. The reason for the differences in D_{avg} is most probably to be found in the differences between each PI's chain-packing ability. On one hand there are indications derived by theoretical models that the "fluorination of aromatic carbon in the main chain does not cause obvious effects on chain packing",[188] and when observing the crystal structure of the 8FAPBP-precursor molecule, the dihedral

angle within the perfluorinated biphenyl center is rather small in equilibrium compared to non-fluorinated biphenyl derivatives,[199] which could lead to the assumption that interchain π-π stacking might be facilitated in case of the fluorinated diamine. On the other hand, there are convincing hypotheses which contradict the aforementioned assumptions and are capable of explaining the higher values for D_{avg} in case of the fluorinated PI: Since fluorine's ionization potential is among the highest of all atoms, the electron dipole and therefore the van der Waals attractive forces between the perfluorinated moieties should be rather small.[193] Moreover, since fluorine atoms have larger van der Waals radii than hydrogen atoms, interchain π-π stacking could be slightly inhibited.[192,193] Most of all, as fluorine strongly withdraws delocalized electrons from aromatic rings,[200] these electrons' participation in interchain π-π stacking is inhibited and therefore interactions between PI backbones are decreased.[201] This leads to an increased mobility of the polymer chains, which is already known to increase diffusion coefficients of gases in several fluorinated polymers,[201,202] and which was assumed to be the reason for the observed increase in D_{avg} within this study. Interestingly, both PIs exhibited diffusion coefficients, which were up to two orders of magnitude higher than the ones found in 4.3.1. This is clearly due to the bridging oxygen atom within the PI backbone, as the resulting structural bending generates a big deal of intermolecular free volume,[188] and therefore severely facilitates permeation of water throughout the material. The same effect was observed in most cases of bridging oxygen along the PI backbone during this study, as it can be seen in the following sections.

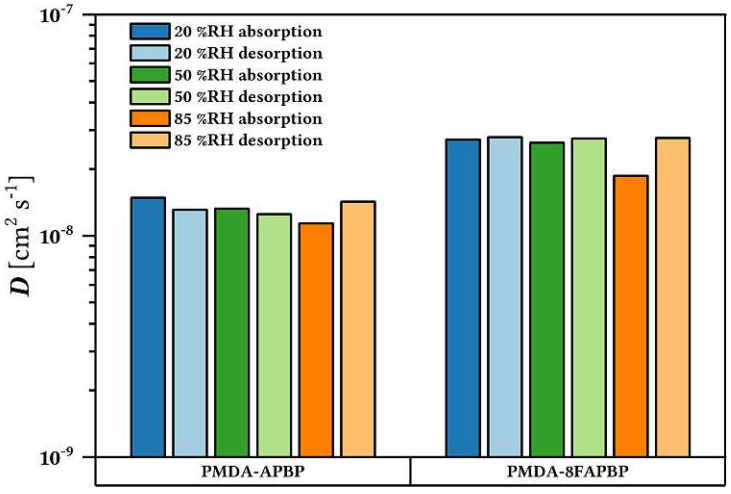

Figure 4.7: Diffusion coefficients of the non- and perfluorinated samples obtained from curve-fitting to measurement data of the refined method. The fluorinated sample exhibits increased diffusion coefficients.

4.3.3 Fluorination and Connectivity: Phenylenediamine

Since it was shown in the previous section that perfluorinated segments have a significant impact on the moisture sorption behavior of PIs, this measurement series originally aimed for a stepwise increase in number of fluorinated sites in 1,3-phenylenediamine (mPDA) throughout a series of PIs in order to investigate if partial fluorination of PI-backbone segments allows for gradually tuning PIs' moisture sorption behavior. However, all attempts to synthesize di- and trifluoro derivatives of mPDA compounds from their dinitro precursors were not successful. Instead, only 4-fluoro-mPDA (1FmPDA) and 2,4,5,6-tetrafluoro-mPDA (4FmPDA) were employed as fluorinated diamines for PI synthesis in this study, since these two diamines were available commercially. The two fluorinated PIs were compared to PIs containing mPDA as non-fluorinated diamine component, while this also allowed for comparing these to PIs containing pPDA, as a change from para- to meta-connectivity in the structural backbone might lead to significant differences in terms of moisture sorption behavior. Fluorinated derivatives of pPDA were not taken into consideration for this study, since 4FpPDA was expected to be not reactive enough for manufacturing continuous PI films,[197] and due to the low availability of other fluoro-pPDA derivatives. It was observed previously that the conversion of PAAs containing only PMDA and mPDA as monomers into PIs did not yield continuous PI films, due to severe embrittlement of the materials upon curing. Therefore, sBPDA was chosen as dianhydride throughout this measurement series. This dianhydride contains a biphenyl linkage, which provides a certain degree of rotational flexibility along the biphenyl axis and therefore allowed for manufacturing of continuous PI films containing mPDA and its derivatives. For a preliminary measurement series, two specimens per PI system have been analyzed, whereas results of three measurements of BPDA-pPDA from subsection 4.3.1 were included in this comparison. For the refined method including less steps and longer exposition times, again, one specimen per PI system was analyzed. Both series show similar trends of sorption behavior for the PIs analyzed. Comparing sBPDA-pPDA and sBPDA-mPDA displays the severe impact varying the arene substitution pattern within a PI's backbone structure has on the sorption behavior: While sBPDA-pPDA exhibits a moisture uptake of 1.3 wt% and D_{avg} of $3.59 \cdot 10^{-10}$ $cm^2 s^{-1}$), sBPDA-mPDA exhibits a more than doubled moisture uptake of 3.8 wt% and D_{avg} of $5.67 \cdot 10^{-9}$ $cm^2 s^{-1}$, which differs more than one order of magnitude. This strong increase in uptake and D_{avg} in the sBPDA-mPDA system was most likely due to the inherently more bent structure arising from the meta position in which each

dianhydride is attached to the diamine within each repeating unit of this polymer. This bent structure most probably led to a significantly increased free volume within the material, offering sites for increased accumulation and facilitated penetration of water molecules into the material.[153,161] Including sBPDA-4FmPDA into this comparison shows that the perfluorinated segment (which is the diamine) partially compensates for the increased moisture uptake, which in this case is 2.8 wt% and lies between the two previously mentioned systems. But, similarly to the comparison in section 4.3.2, segmental perfluorination of the PI backbone again seems to increase the diffusion coefficients (D_{avg}= 1.94·10^{-8} cm^{2}s^{-1}) significantly. It has to be mentioned that the fraction of fluorinated sites within the aromatic backbone in sBPDA-4FmPDA is 40 %, which is less than in PMDA-8FAPBP (44 %). In the system sBPDA-1FmPDA, only one of four possible sites within the diamine is fluorinated. Here, the trend is slightly different, since the diffusion coefficients (D_{avg}= 8.21·10^{-9} cm^{2}s^{-1}) are -as expected- slightly increased as compared to sBPDA-mPDA, whereas the moisture uptake (4.0 wt%) is slightly increased as well. This could mean that such a low degree of fluorination (10 %) already increased the free volume of the polymer significantly, but did not sufficiently increase the PI's hydrophobicity to compensate for that, leading to an simultaneous increase in water uptake.

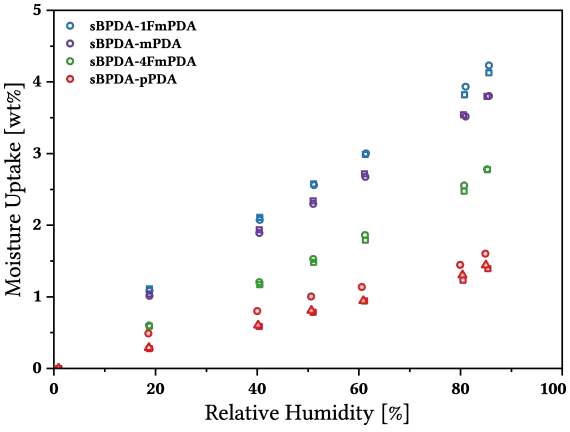

Figure 4.8: Initial DVS measurements of the sample series comparing moisture uptake of PDA-derivative PIs with different arene substitution patterns and with partial fluorination. Kinks from meta connectivities increase moisture uptake, whereas fluorination partially decreases moisture uptake.

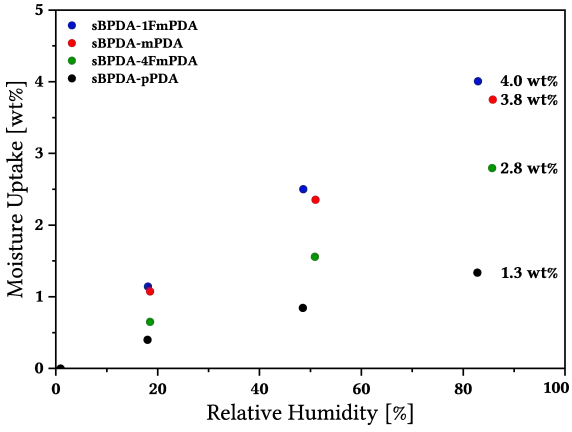

Figure 4.9: DVS measurements of the sample series comparing moisture uptake of PDA-derivative PIs with different arene substitution patterns and with partial fluorination following the refined method. Kinks from meta connectivities increase moisture uptake, whereas fluorination partially decreases moisture uptake.

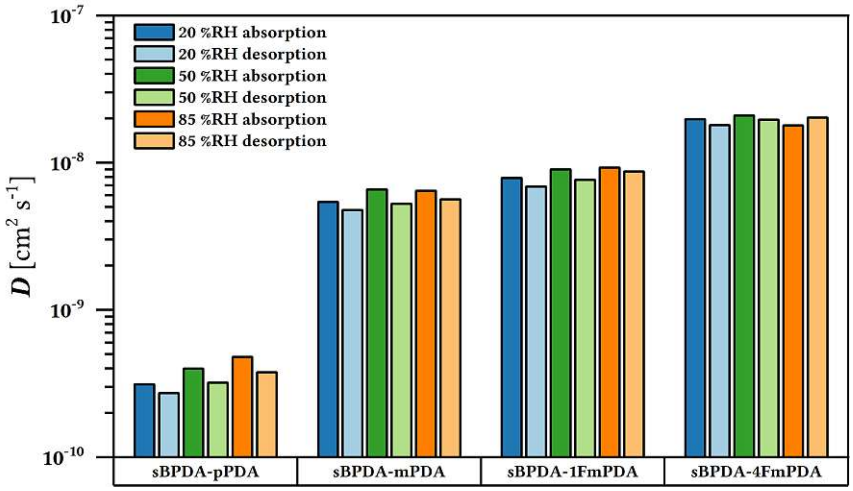

Figure 4.10: Diffusion coefficients of non- and perfluorinated PI samples obtained from curve-fitting to measurement data of the refined method. Kinks from meta connectivities increase diffusion coefficients, whereas fluorination increases them even more.

Samples of sBPDA-mPDA, sBPDA-1FmPDA, and sBPDA-4FmPDA, when measured with the refined method, were subject to an initial drying step for 330 min at 0 %RH, followed by an absorption step at 20 %RH for 180 min, which was followed by a desorption step at 0 %RH again for 330 min, a second absorption step at 50 %RH for 510 min and a final absorption step at 85 %RH for 630 min, each followed by desorption steps at 0 %RH for 390 min. Sample sBPDA-pPDA was subject to a prolonged measurement of 116 h, simultaneously analyzing two specimens, as specified in section 4.3.1.

4.3.4 Backbone Connectivity: PMDA-m/pPDA

Comparing the PI systems PMDA-pPDA and PMDA-mPDA would pose an intriguing study, since their imide mass fraction is identical, but their morphological outcomes could hardly be more different: whereas PMDA-pPDA could only form straight polymer chains, PMDA-mPDA could only form a somewhat helical structure. Several attempts on manufacturing a continuous film of pure PMDA-mPDA did not lead to a satisfying outcome, due to extreme embrittlement of material upon curing. Nonetheless, a film sample of a statistical co-PIs containing 30 % mPDA and 70 % pPDA could be manufactured. For reasons of comparability, dosage of PAA during manufacturing was aimed to have a dry weight of cured PI similar to the samples of PMDA-pPDA. The relatively large fraction of randomly distributed meta substitutions led to a PI consisting of rather stiff but bent polymer chains, which would -due to their non-linearity- most probably not be able to align with high symmetry and therefore give rise to a significant fraction of free volume within the material. As expected, the increased free volume in the co-PI

system PMDA-[0.3·mPDA+0.7·pPDA] was reflected in both an increased water uptake of 5.9 wt% and an increased D_{avg} of $7.24 \cdot 10^{-9}$ $cm^2 s^{-1}$, and confirmed the observations from section 4.3.3.

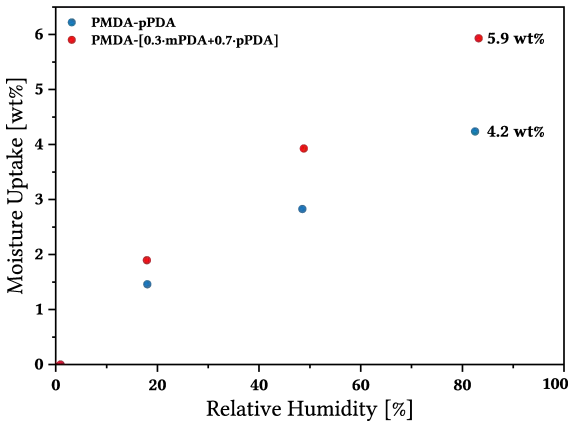

Figure 4.11: DVS measurements of the sample series comparing moisture uptake of PMDA-m/pPDA PIs following the refined method. Kinks from meta connectivities increase moisture uptake significantly.

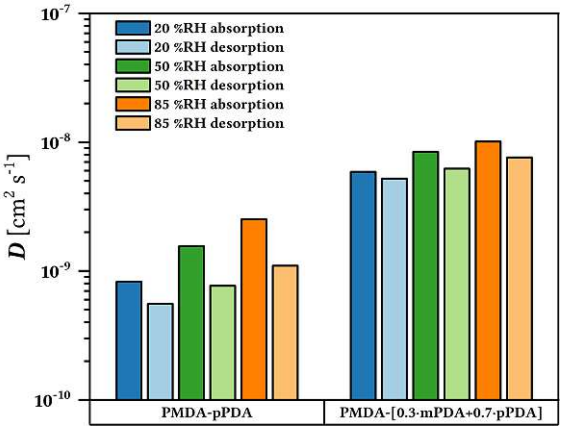

Figure 4.12: Diffusion coefficients of PMDA-m/pPDA PIs obtained from curve-fitting to measurement data of the refined method. Kinks from meta connectivities increase diffusion coefficients significantly.

The PI sample of PMDA-[0.3·mPDA+0.7·pPDA], when measured with the refined method, was subject to an initial drying step for 330 min at 0 %RH, followed by an absorption step at 20 %RH for 180 min, which was followed by a desorption step at 0 %RH again for 330 min, a second absorption step at 50 %RH for 510 min and a final absorption step at 85 %RH for 630 min, each followed by desorption steps at 0 %RH for 390 min (similarly to section 4.3.3). Sample sBPDA-pPDA was subject to a prolonged measurement of 116 h, simultaneously analyzing two specimens, as specified in section 4.3.1.

4.3.5 Backbone Connectivity: Oxydianiline

The study of the effect of meta connectivities within the PI backbone was extended to the two isomeric PI systems PMDA-sODA and PMDA-aODA containing the diamine 4,4′-oxydianiline and 3,4′-oxydianiline, respectively. The first one is generally known under the trademark name Kapton and represents the industrially and academically most popular PI, whereas the latter is comprised of the same dianhydride but with an asymmetrical isomer of the diamine, resulting in a meta connection between this PI's repeating units. Since both PIs contain an ether linkage in their backbone, they can be referred to as polyetherimides (PEIs). PMDA-sODA exhibited a water uptake of 3.2 wt% and D_{avg} of $5.68 \cdot 10^{-9}$ $cm^2 s^{-1}$, whereas PMDA-aODA exhibited an uptake of 3.0 wt% and D_{avg} of $2.69 \cdot 10^{-7}$ $cm^2 s^{-1}$. Both systems showed a significant increase in both uptake and

D_{avg} when comparing them to the previously discussed systems PMDA-Bz and sBPDA-pPDA, which probably arised from the effect the ether bridge might have had on the sorption behavior. It was not clear if this increase in water uptake could be attributed to the increased polarity arising from the ether oxygen present in the backbone, since information on its role in interaction with water is contradictory: While there are indications that water molecules "are more associated" with such ether linkages,[146] recent infrared-spectroscopic studies combined with molecular-dynamics simulations "demonstrated that their interaction with water was negligible, if present".[203]

Nonetheless, one possible reason seemed to be the increased rotational flexibility of the PI chains enabled by the ether linkage resulting in a higher fraction of free volume within these PEIs, into which water (and solvent) molecules could penetrate more freely.[163]

Comparing the diffusion coefficients of both samples, it was noteworthy that PMDA-aODA exhibited a D_{avg} almost two orders of magnitude higher than that of PMDA-sODA, and which in fact represented the highest D_{avg} of all PI systems discussed within this thesis. Since the water uptake did not differ much at all, and PMDA-aODA even showed a slightly lower uptake than PMDA-sODA, this tremendous difference in D_{avg} might not be exclusively attributed to the differences in free volume of the PIs. While some researchers explain their findings on the lower gas diffusivity in 3,4'-oxydianiline PIs compared to 4,4'-oxydianiline PIs by a presumably lower chain mobility in solid state due to steric hindrance of rotations in case of the meta derivative,[204,205] it has to be noted that PIs containing said meta derivative generally exhibit a drastically lower T_g compared to PIs containing the para derivative.[190,204] This difference could imply a generally increased chain mobility[206,207] for PMDA-aODA compared to PMDA-sODA and therefore could offer an explanation for the increased water diffusivity. Another possible explanation could be that segments within a single PMDA-aODA chain can assume a somewhat helical conformation, which might offer local channels for facilitated diffusion of water molecules and thereby enhance macroscopic permeability of water (cf. Figure 4.13).

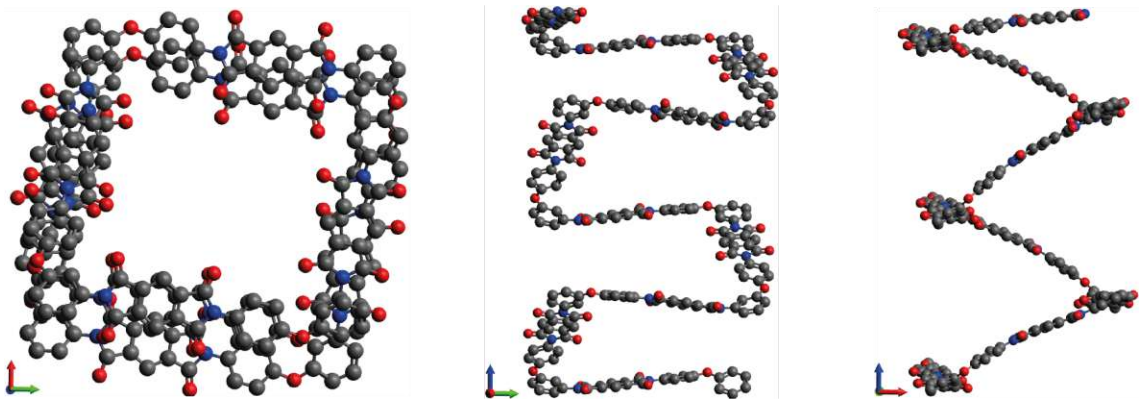

Figure 4.13: Possible conformation of a ten-repeating-unit segment of the PMDA-aODA system. Automated force-field optimization within the Avogadro[208] visualization software (version 1.2.0) clearly shows that a rather tight helical structure can exist within a single polymer chain of PMDA-aODA.

Moylan et al. compared these two PI systems with respect to their water sorption behavior already in 1991, but obtained results highly contrary to the findings of this study: PMDA-sODA was found to show a lower water uptake and a higher diffusivity than PMDA-aODA, although the discrepancies between these and this thesis' results might be due to the fact that samples in their study were spin coated and only approx. 2 µm in thickness, which resulted in "substantially more in-plane orientation than that of thicker films" and made the results hardly comparable.[157] In 1999, Seo et al. found no significant differences in the water sorption behavior of both PI systems (spin-coated films of 10 - 14 µm thickness) at all.[209]

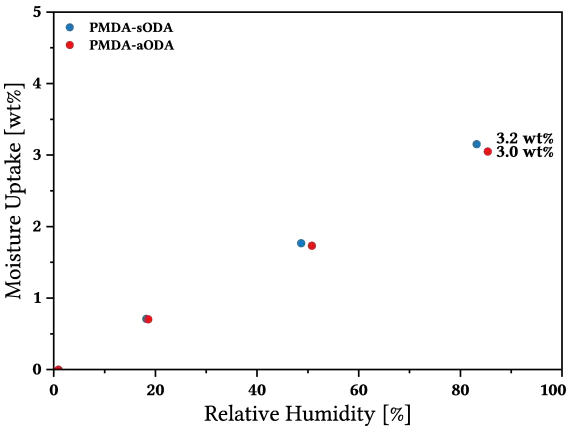

Figure 4.14: DVS measurements of the sample series comparing moisture uptake of PMDA-s/aODA PIs following the refined method. Differences in molecular structure of the PIs do not reflect in moisture uptake significantly.

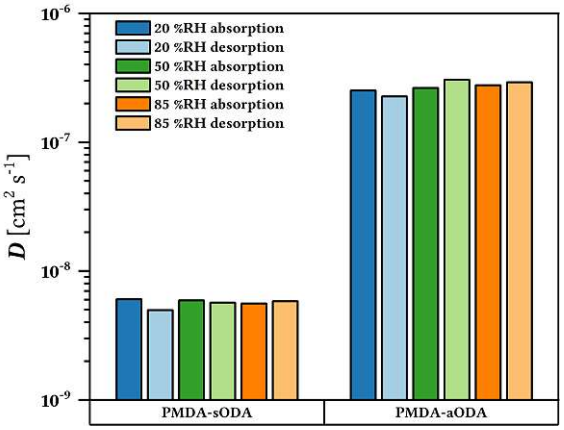

Figure 4.15: Diffusion coefficients of PMDA-s/aODA PIs obtained from curve-fitting to measurement data of the refined method. Kinks from meta connectivities increase diffusion coefficients significantly.

Samples of PMDA-sODA and PMDA-aODA were subject to an initial drying step for 330 min at 0 %RH, followed by an absorption step at 20 %RH for 180 min, which was

followed by a desorption step at 0 %RH again for 330 min, a second absorption step at 50 %RH for 510 min and a final absorption step at 85 %RH for 630 min, each followed by desorption steps at 0 %RH for 390 min.

4.3.6 Backbone Connectivity: Bis(4-aminophenoxy)benzene

To further investigate the effect of meta-substitution patterns in the PI backbone, two additional PI systems containing 1,4-Bis(4-aminophenoxy)benzene (pBAPB) and 1,3-Bis(4-aminophenoxy)benzene (mBAPB), respectively, were synthesized and analyzed. Both diamines consist of three benzene rings connected by two ether linkages, while in mBAPB the two ether moieties are in meta position to each other on the central benzene ring. PMDA-pBAPB exhibited a moisture uptake of 2.5 wt% and D_{avg} of $8.04 \cdot 10^{-9}$ $cm^2 s^{-1}$, while PMDA-mBAPB had a significantly decreased uptake of 1.2 wt% and an only slightly lower D_{avg} of $6.33 \cdot 10^{-9}$ $cm^2 s^{-1}$. It has been postulated by Madzarevic et al. in 2018 that PMDA-pBAPB had a structure similar to PMDA-sODA, and should therefore have a similar fraction of free volume, whereas a prominent kink in the backbone as found in mBAPB led to inhibited chain packing and therefore to increased free volume.[210] However, this sorption study found that the values for moisture uptake of PMDA-pBAPB were slightly lower than that of PMDA-sODA, whereas PMDA-mBAPB had an uptake of less than half of its isomeric system, which was not congruent with the assumption of a higher fraction of free volume. Moreover, D_{avg} of PMDA-mBAPB was the one very close to that of PMDA-sODA, while PMDA-pBAPB exhibited slighly higher D_{avg}. The observed trends could only be explained by a somewhat higher degree of entanglement due to its more kinked structure and thereby tighter packing of PMDA-mBAPB. An increased mobility of the polymer chains within its structure, which can be suspected from its lower T_g compared to PMDA-pBAPB,[190,211] would in turn facilitate the diffusion of moisture to some extent, making the differences in D_{avg} less pronounced than they were in the moisture uptake.

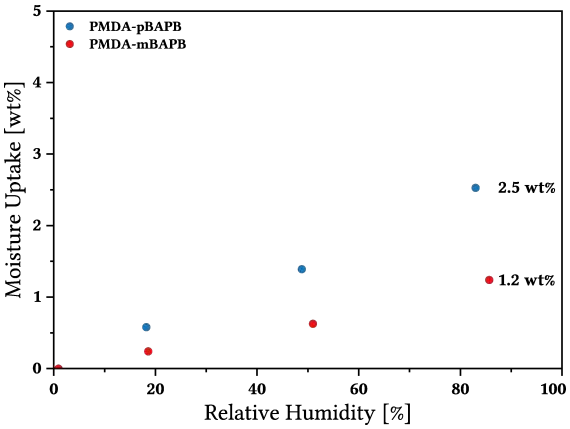

Figure 4.16: DVS measurements of the sample series comparing moisture uptake of PMDA-p/mBAPB PIs following the refined method. The meta derivative exhibits significantly decreased moisture uptake.

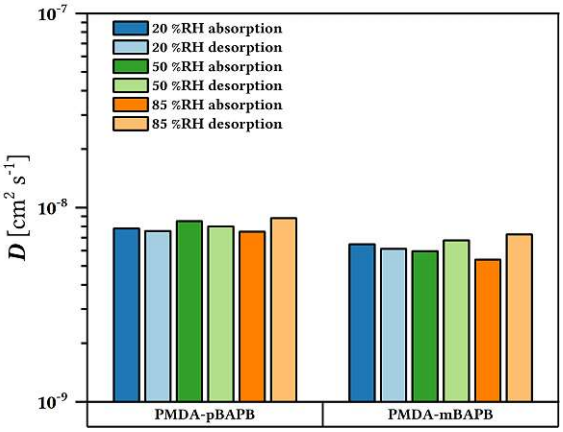

Figure 4.17: Diffusion coefficients of PMDA-p/mBAPB PIs obtained from curve-fitting to measurement data of the refined method. Differences in molecular structure of the PIs do not reflect in diffusion coefficients significantly.

Samples of PMDA-pBAPB and PMDA-mBAPB were subject to an initial drying step for 330 min at 0 %RH, followed by an absorption step at 20 %RH for 180 min, which was followed by a desorption step at 0 %RH again for 330 min, a second absorption step at 50 %RH for 510 min and a final absorption step at 85 %RH for 630 min, each followed by desorption steps at 0 %RH for 390 min.

4.3.7 Bulkiness of Connecting Moiety

Since the commercially available diamine bisaniline P (4,4′-(1,4-phenylenediisopropylidene)bisaniline, pBISA) seemed to be structurally similar to pBAPB, comparing the previously analyzed PI system PMDA-pBAPB to PMDA-pBISA seemed promising. A comparison between mBAPB and bisaniline M (4,4′-(1,3-phenylenediisopropylidene)-bisaniline, mBISA) could not be made, since the PI system PMDA-mBISA did not yield continuous PI films due to embrittlement upon curing the precursor. PMDA-pBISA exhibited a D_{avg} of $3.43 \cdot 10^{-8}$ $cm^2 s^{-1}$, being approx. half an order of magnitude higher than that of PMDA-pBAPB (cf. figure 4.19). This increase was most probably due to a somewhat more disrupted PI-chain packing resulting from both the increased bulkiness of the isopropyl connectivities within the diamine segment and sharper angles between the benzene rings connected by the isopropyl moieties leading to a slightly more kinked polymer backbone, which is also expected to create more free volume by inhibiting efficient chain packing.[210] This assumed increase in interchain distance also reflects the values for d-spacing obtained by WAXD measurements of 4.9 Å for PMDA-pBISA as compared to 4.6 Å for PMDA-pBAPB. While this increased free volume of PMDA-pBISA

could explain the facilitated diffusion of water into the material, it did not explain the slightly decreased uptake of water (2.2 wt%) of this system (cf. figure 4.18), as it was expected to increase as well. A possible explanation for this behavior could be found in the lower polarity of the isopropyl moieties compensating for the higher free volume by offering less sites of interaction with water molecules than the ether moieties would do in case of PMDA-pBAPB.

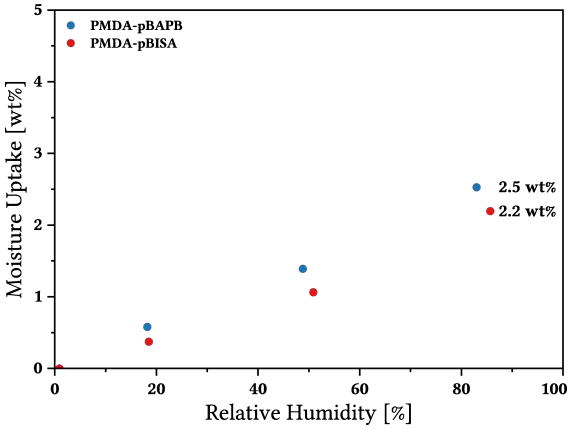

Figure 4.18: DVS measurements of the sample series comparing moisture uptake of structurally similar PIs with different degrees of connecting-moiety bulkiness following the refined method. The bulkier, but less polar PI PMDA-pBISA exhibited slightly decreased moisture uptake.

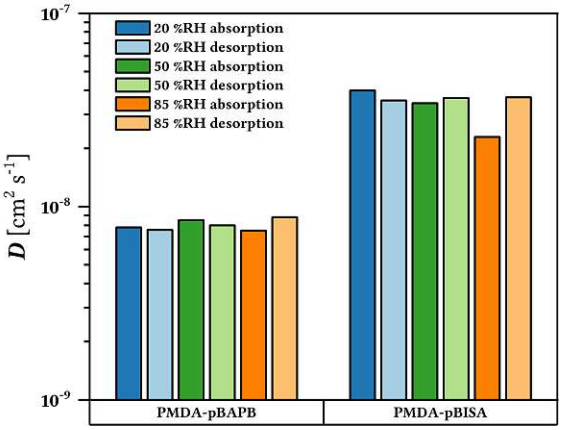

Figure 4.19: Diffusion coefficients of structurally similar PIs obtained from curve-fitting to measurement data of the refined method. The bulkier PI PMDA-pBISA exhibited significantly increased diffusion coefficients.

Samples of PMDA-pBAPB and PMDA-pBISA were subject to an initial drying step for 330 min at 0 %RH, followed by an absorption step at 20 %RH for 180 min, which was followed by a desorption step at 0 %RH again for 330 min, a second absorption step at 50 %RH for 510 min and a final absorption step at 85 %RH for 630 min, each followed by desorption steps at 0 %RH for 390 min.

4.3.8 Effects of Side Groups: PMDA PIs

Intrigued by the effect the bulkiness of a linking moiety in the PI backbone had on the sorption behavior, investigating effects of bulky pendant side groups in an otherwise fully straight PI chain seemed promising. Therefore, a series of PIs consisting of PMDA as dianhydride combined with benzidine and three of its commercially available derivatives, namely 2,2′-dimethylbenzidine (*m*-tolidine, mDMBz), 2,2′-bis(trifluoromethyl)benzidine (mTFBz), and 3,3′-dimethoxybenzidine (*o*-dianisidine, oDIAN), were synthesized and subject to DVS measurements. All these PIs consisted of a fully straight polymer backbone, while the three benzidine derivatives contributed pendant

side groups of varying chemical composition and bulkiness, which allowed for separating possible side-group effects from other structural features such as backbone kinks. Although oDIAN had its aromatic substituents in a position adjacent to the amino groups, it was used despite a slight lack in comparability to mDMBz and mTFBz, since its meta derivative was not available. As it can be seen in figure 4.20, PMDA-Bz exhibited a moisture uptake of 2.1 wt% (already presented in 4.3.1), while the introduction of methyl moieties in case of PMDA-mDMBz led to a highly increased uptake of 3.4 wt%, most probably due to a significantly increased free volume of the PI resulting from the bulkiness of the methyl moieties leading to looser molecular packing.[188] This also reflected in the significant increase of D_{avg} from $6.71 \cdot 10^{-10}$ $cm^2 s^{-1}$ for PMDA-Bz to $3.59 \cdot 10^{-9}$ $cm^2 s^{-1}$ for PMDA-mDMBz (cf. Figure 4.21), meaning that the pendant methyl groups led to both an increased uptake and diffusion velocity. Although fluorine atoms are not much larger than hydrogen atoms, trifluoromethyl moieties are significantly more voluminous than methyl moieties,[193] causing the PI system PMDA-mTFBz to exhibit a D_{avg} of $2.62 \cdot 10^{-8}$ $cm^2 s^{-1}$, which was approx. one order of magnitude higher than that of PMDA-mDMBz and the highest within this series. Here, the trifluoromethyl groups again increased the free volume of the PI and inhibited efficient chain packing even more than methyl groups did.[192] Interestingly, this effect did not reflect in the moisture uptake of PMDA-mTFBz at all. With 1.9 wt%, it even showed a lower uptake than PMDA-Bz, rendering it the PI system with the lowest uptake within this series. This could only mean that the fluorine atoms decreased the overall polarity of the PI, making it less prone to interact with water molecules, while at the same time the bulkiness of the trifluoromethyl groups severely facilitated their diffusion throughout the material. PMDA-oDIAN exhibited the highest moisture uptake of 3.6 wt%, while on the other hand D_{avg} ($5.60 \cdot 10^{-9}$ $cm^2 s^{-1}$) was only slightly higher than that of PMDA-mDMBz. It has been found by Terui et al. that the pendant methyl groups of the mDMBz monomer cause the molecular packing in PIs to be more loose than in analogous PIs containing dianisidine monomers, despite the methoxy substituents being more voluminous than methyl substituents.[188] This would explain the low difference in D_{avg} of PMDA-oDIAN as compared to PMDA-mDMBz, as the free volume within this PI might even be slightly smaller than in PMDA-mDMBz due to tighter chain packing, counteracting the effect of increased volume of the methoxy substituents. Only considering this effect, the moisture uptake of PMDA-oDIAN could be expected to be very similar to that of PMDA-mDMBz as well. Nonetheless, it exhibited a highly increased moisture uptake of 4.6 wt%, which most probably resulted from the increased polarity contributed by the methoxy groups, offer-

ing additional sites of interaction with water molecules, negating the assumed effect of tighter chain packing. These trends in chain packing also reflected in d-spacing to some extent: while it increased from 4.2 Å for PMDA-Bz to 5.0 Å for PMDA-mDMBz to 5.2 Å for PMDA-mTFBz, d-spacing for PMDA-oDIAN exhibited a value of 5.2 Å, which was higher than expected and thereby contradicted aforementioned assumptions regarding the tighter chain packing of PMDA-oDIAN.

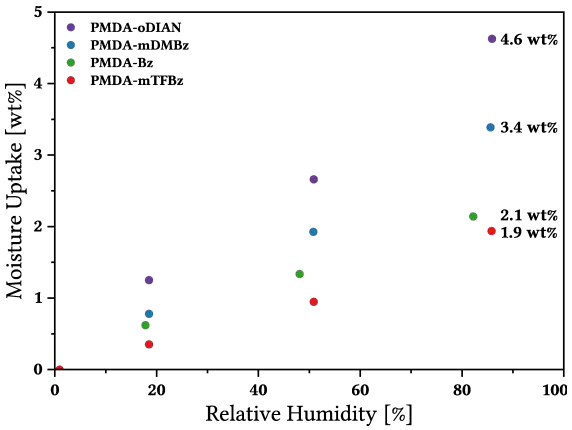

Figure 4.20: DVS measurements of the sample series comparing moisture uptake of PIs comprised of various benzidine derivatives polymerized with PMDA following the refined method. The bulkier and polar the side groups got, the more increased this PI's moisture uptake, whereas fluorinated moieties strongly reduced this effect.

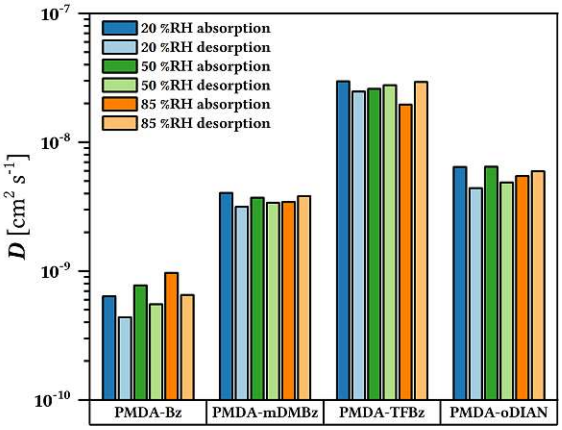

Figure 4.21: Diffusion coefficients of PIs comprised of benzidine-derivatives polymerized with PMDA obtained from curve-fitting to measurement data of the refined method. The increasing bulkiness and influence on chain packing significantly increased diffusion coefficients.

All samples within this series were subject to an initial drying step for 330 min at 0 %RH, followed by an absorption step at 20 %RH for 180 min, which was followed by a desorption step at 0 %RH again for 330 min, a second absorption step at 50 %RH for 510 min and a final absorption step at 85 %RH for 630 min, each followed by desorption steps at 0 %RH for 390 min.

4.3.9 Effects of Side Groups: ODPA PIs

For another series of PIs, an approach analogous to 4.3.8 was chosen for comparing the effects of pendant side groups, employing the same diamines as in the previous study, all polymerized with a different dianhydride, namely 4,4'-oxydiphthalic anhydride (sODPA). This dianhydride contained an ether linkage between both aromatic anhydride moieties, thereby introducing a more flexible backbone into this comparison of PIs. The overall trends for moisture uptake and D_{avg} are quite similar to the previous comparison employing PMDA as dianhydride. As it can be seen in figure

4.22, sODPA-oDIAN exhibits the highest uptake of 3.6 wt% due to increased free volume and increased number of polar sites for interaction with water molecules, closely followed by sODPA-mDMBz with 3.4 wt%, while sODPA-mTFBz (1.4 wt%) and sODPA-Bz (1.2 wt%) followed more distantly. While sODPA-mDMBz exhibits the same value as PMDA-mDMBz did (within an assumed measurement error), sODPA-mTFBz showed an uptake slightly higher than sODPA-Bz, meaning that the decreased polarity due to the pendant trifluoromethyl groups is not sufficiently able to fully compensate for the arising increase in free volume, probably due to this moiety's lower fraction within the repeating unit's increased molecular weight (as compared to PMDA-mTFBz). Interestingly, almost all of these systems exhibited moisture uptakes being smaller than that of their analogs in 4.3.8. This observation is in sharp contrast to the overall increased values for D_{avg} in this sample series: Here, sODPA-Bz exhibited the by far lowest diffusion coefficients (D_{avg}= $9.97 \cdot 10^{-10}$ $cm^2 s^{-1}$) within this series, while sODPA-mDMBz -analogous to PMDA-mDMBz- showed a highly increased D_{avg} of $1.09 \cdot 10^{-8}$ $cm^2 s^{-1}$, again due to the bulkiness of the pendant methyl groups affecting the free volume within this PI, thereby greatly increasing both moisture uptake and diffusion velocity. In analogy to the PI containing mTFBz in the previous study, sODPA-mTFBz proved to have the highest D_{avg} of $3.20 \cdot 10^{-8}$ $cm^2 s^{-1}$ within this series, while this value is only marginally higher than that of PMDA-mTFBz. Here again, the trifluoromethyl groups increased the free volume of the PI and inhibited efficient chain packing even more than methyl groups did.[192] Apart from this series' highest moisture uptake, sODPA-oDIAN exhibited a D_{avg} of $7.45 \cdot 10^{-9}$ $cm^2 s^{-1}$) being slightly lower than that of sODPA-mDMBz, confirming the statements of Terui et al. regarding the tighter chain packing and resulting lower free volume of a oDIAN-PI compared to an analogous mDMBz-PI (cf. section 4.3.8). Again, the trends in D_{avg} also reflected in the values obtained for d-spacing, which increased from 4.5 Å for sODPA-Bz to 5.1 Å for sODPA-mDMBz to 5.7 Å for sODPA-mTFBz, while the oDIAN PI (sODPA-oDIAN) again exhibited a value higher than expected by accounting for 5.3 Å.

Comparing the results of this section's PIs with the ones obtained from analyzing their analogous PIs based on PMDA in section 4.3.8, it could be noticed that the PIs of the sODPA series generally showed higher values for D_{avg} while exhibiting lower moisture uptakes, despite being more polar due to the ether moieties they contained. Explanations for this behavior could be found in analogy to the previous sections: As PIs based on PMDA and benzidine derivatives were fully straight PI chains, they might not entangle as well as their more flexible sODPA analogues, leading to increased free volume in case of the PMDA series and therefore higher moisture uptake (cf. section 4.3.1). Si-

multaneously, the polymer chains of the sODPA PIs were more flexible and therefore exhibited a somewhat increased chain mobility, which facilitated the diffusion of moisture throughout the material (cf. section 4.3.5).

Interestingly, the measurement data of sODPA-oDIAN exhibited the by far biggest deviation from the simulated curves (cf. Appendix A.25) among all measurements. As it can be seen in Figure A.65, the sample mass increased/decreased unusually slowly, but still significantly, after a steep increase at the beginning of each sorption step and the following center of curvature. This could indicate that this PI is swelling the most upon exposure to moisture, while relaxation of segmental motions within this PI might be rather slow.[172]

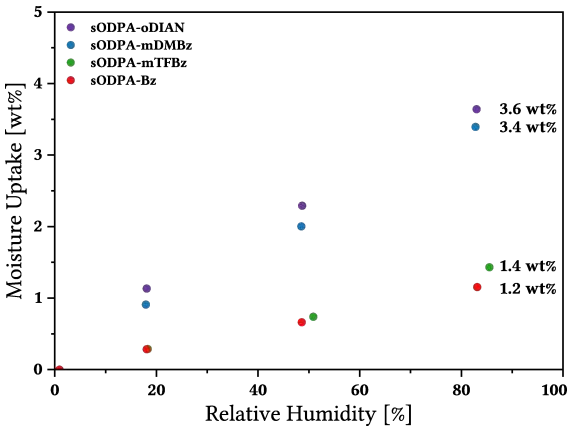

Figure 4.22: DVS measurements of the sample series comparing moisture uptake of PIs comprised of various benzidine derivatives polymerized with sODPA following the refined method. The bulkier and polar the side groups got, the more increased this PI's moisture uptake, whereas fluorinated moieties strongly strongly reduced this effect.

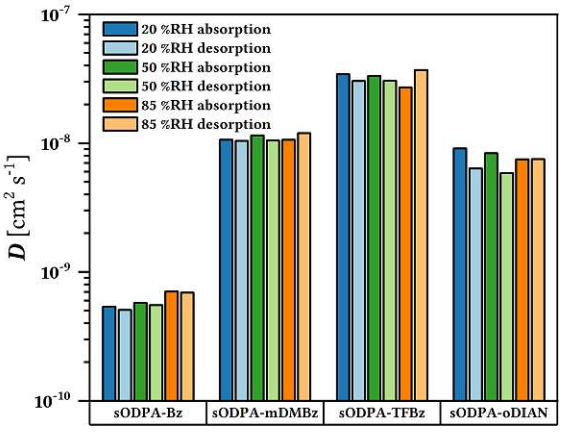

Figure 4.23: Diffusion coefficients of PIs comprised of benzidine-derivatives polymerized with sODPA obtained from curve-fitting to measurement data of the refined method. The increasing bulkiness and influence on chain packing significantly increased diffusion coefficients.

All samples within this series (except for sODPA-Bz) were subject to an initial drying step for 330 min at 0 %RH, followed by an absorption step at 20 %RH for 180 min, which was followed by a desorption step at 0 %RH again for 330 min, a second absorption step at 50 %RH for 510 min and a final absorption step at 85 %RH for 630 min, each followed by desorption steps at 0 %RH for 390 min. The specimen of sODPA-Bz was subject to a prolonged measurement in which each desorption step had a duration of 900 min and each absorption step 1200 min.

4.4 Conclusions

This chapter presented a method of preparation of PI films and thorough analysis and comparison of their moisture-sorption behavior. Since these samples were drop-casted, it was possible to manufacture PI films of defined amount of material, while retaining highly similar specimen dimensions only varying in thickness in the micrometer range, and therefore possessing comparable surface-to-volume ratios. This allowed for comparison of a broad range chemical and structural features PIs can exhibit, while effects of polymer-chain alignment arising from directional manufacturing methods (spin-coating, tape-casting) such as increased crystallinity could be avoided. All samples were analyzed utilizing the method of dynamic vapor sorption in order to determine their moisture uptake, while the obtained experimental sorption curves were reasonably well fitted to using a Fickian diffusion model, which allowed for retrieving diffusion coefficients as a quantitative measure of diffusion velocity. It could be demonstrated in section 4.3.1 that the imide moiety, the nexus between the monomers units defining the PI, itself had a huge impact on the moisture uptake, as it is a polar one and therefore intrinsically offers sites of interaction with water molecules. Simultaneously, it could be seen that slightly more flexible chains seemed to improve chain packing compared to fully straight, stiff PI chains and thereby lowered moisture uptake. Figure 4.24 gives an overview of all PIs included in this comparison, showing both moisture uptake and D_{avg}, while these PIs only consist of benzene rings connected by imide moieties without any heteroatoms outside of the imide groups.

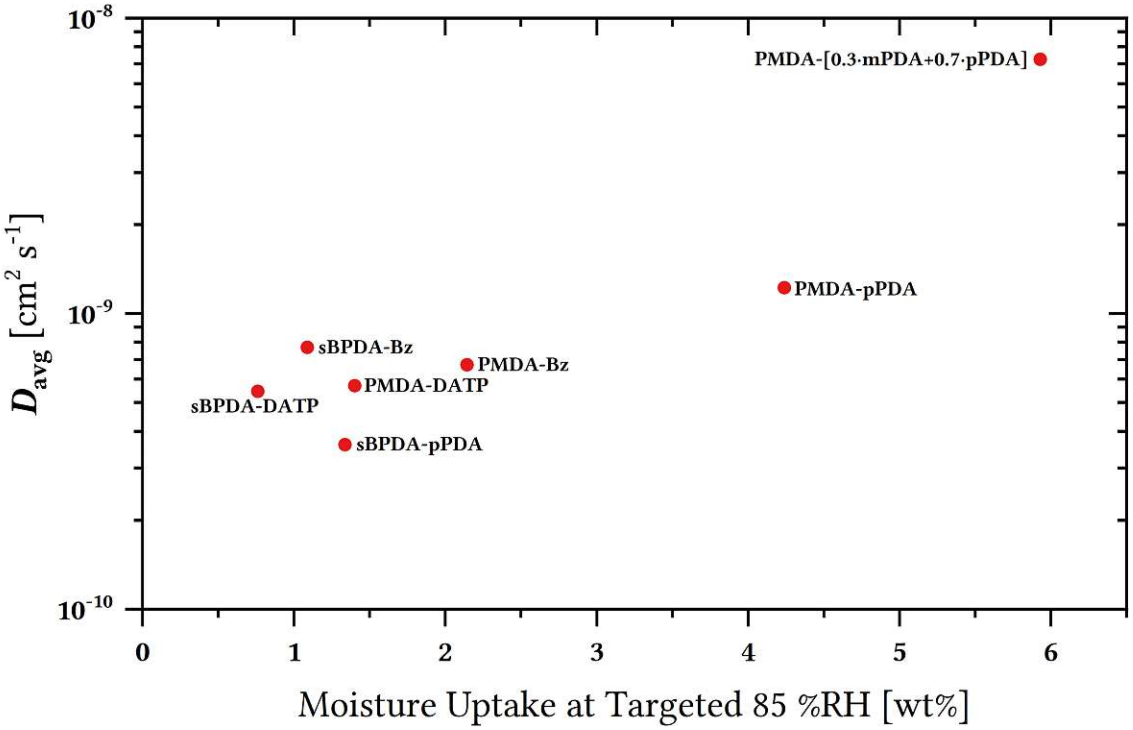

Figure 4.24: Two-dimensional map of all PI systems being comparable by having the same sample mass per specimen, therefore allowing for comparison of differences in fraction of imide moieties.

Fluorination of the aromatic PI backbone led to accelerated diffusion of moisture in all cases by decreasing interchain interaction, but simultaneously lowered the uptake of moisture by lowering the overall polarity of the PI, if the degree of fluorination is high enough (cf. section 4.3.2 & 4.3.3). Moreover, more kinked structures resulting from introducing meta-connected chain segments increased the polymer's free volume and thereby led to both an increased moisture uptake and diffusion velocity (cf. section 4.3.3 & 4.3.4), although meta connectivities do not necessarily lead to more kinked structures (cf. sections 4.3.6 & 4.3.5). In section 4.3.7 it could be seen that increased bulkiness of connecting moieties could also contribute to an increased free volume and thereby to an acceleration of the diffusion process, while these moieties' polarity also played a role in the overall moisture uptake. Finally, a study comprising two sample series showed a severe impact of pendent side groups attached to the PI backbone on both the moisture uptake and diffusion velocity (cf. section 4.3.8 & 4.3.9). The more voluminous the side groups got, the more both attributes increased due to increased interchain distance, whereas these groups' polarities again exhibited a regulating effect on the moisture uptake. Figure 4.25 gives an overview of all PIs of this study, which were comparable by having a molar amount of approx. 10 µmol, showing both moisture uptake and D_{avg}.

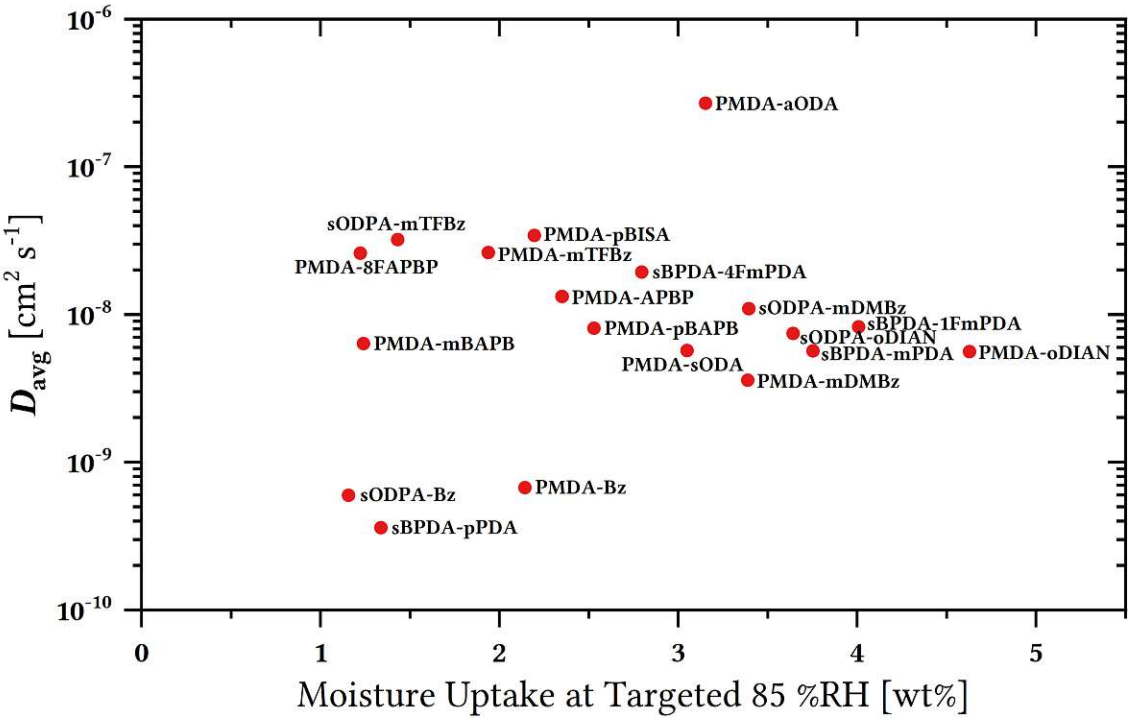

Figure 4.25: Two-dimensional map of all PI systems being comparable by having the same molar amount of polymer per specimen, therefore allowing for comparison of differences in molecular structure with constant fraction of imide moieties.

To conclude, several structural factors influencing the moisture sorption behavior of PIs were found. With knowledge of such factors, PIs could be designed according to the demands an intended application would have on the material's sorption behavior. High overall moisture uptake combined with slow diffusion or vice versa, or any combination of both attributes could be achieved by the right choice of monomers to build a PI from. As in microelectronic applications a combination of low uptake and slow diffusion might be desirable in order to minimize the occurrence of corrosion, the choice of monomer combination might tend to lead to the lower left region within figure 4.25. However, the overview this study offered is far from being complete considering the vast amount of monomers available and suitable for PI synthesis. Moreover, a direct comparison of manufacturing methods in terms of film application might provide useful insights, as directional alignment of PI chains would probably influence this material's sorption behavior significantly.

5. Thermogravimetric Analyses

5.1 Introduction

"Thermal stability is the capacity of the polymer to withstand well-defined thermal conditions before degradation occurs."[1] In applications which require polymeric materials to be particularly performant with regards to this materials property, PIs have been the polymer class of choice for several decades. Especially aromatic polyimides withstand high temperatures in harsh environments due to their mostly high degree of aromaticity, mainly ring-containing molecular structures, and usually high packing densities, typically resulting in decomposition temperatures above 450 °C in air and exceeding 500 °C in nitrogen atmosphere for brief intervals.[2] Among many others, such applications include the use as inter-layer dielectric films in semiconductor devices during which they must withstand a large number of essential high-temperature process operations,[212] or as adhesives in jet engines[33] or as advanced composite matrices in other aerospace-related applications.[213] In their extensive research on the thermal stability of PIs in the 1970s, Sazanov et al. found that the decomposition behavior of PIs can not easily be assessed from analyzing their corresponding model compounds,[214] since defects in the polymer chain result in significant differences between values obtained for actual polymers and those of ideal molecular units.[214,215] These defects could comprise fragments containing anhydride, amine, amide and carboxyl groups, which could remain from preparation or form later,[214] since all these moieties are inherent to the monomers employed for synthesis or to the PAA used as PI precursor, provided that the classical two-step method of PI synthesis was employed. Among the mentioned moieties, amine groups are the most prone to degrade via oxidization, which might result in a noticeable reduction in thermal stability of a PI.[113] In temperature ranges close to 500 °C, amine groups could also react with carbonyl groups in imide moieties causing numerous consecutive degradation processes including high-temperature hydrolysis of the imide rings, facilitated by water molecules emerging from this particular reaction in both inert and oxygen-containing atmosphere.[214] Moreover, pendant carboxyl groups possibly arising from incomplete conversion of PAA to PI or from hydrolytic processes within the PI pose significant weak spots in PI chains, since they can further participate in hydrolysis of their immediate surroundings or even vanish through decarboxylation.[214] Generally, decomposition processes are initiated and propagated by bond ruptures and based on radical reactions,[216,217] while a significant number of recombination reactions could be

facilitated by enclosing of terminal radicals at the chain ends by their molecular environment not allowing radicals to leave the reaction site (the so-called "cage effect").[217] However, in the decomposition of a PI numerous processes are involved, most of them occurring simultaneously, rendering the obtainment of structure-property relationships quite complex,[216,217] and kinetic calculations from thermal analysis obsolete.[218,219]
This thesis' chapter nonetheless aimed for providing basic insights into the relationship of structural features and thermal decomposition behavior and comparing the PIs obtained by classical and hydrothermal synthesis in respect of thermal stability. It was aimed for a high degree of comparability within all results by careful preparation of PIs ensured by stoichiometrically precise use of purified monomers and highly uniform curing conditions for both PI films and HT polymers (in order to minimize the aforementioned defects), as well as providing highly uniform conditions of thermal analysis for all samples.

5.2 Experimental Approach

5.2.1 Method of Measurement

For assessing the thermal stability of each sample within this thesis, thermogravimetric analysis (TGA) was chosen. This technique exposes a sample contained in a furnace to a certain gaseous atmosphere while scanning through a temperature range at a certain rate and logging the sample mass detected by a microbalance. Several other parameters such as temperature and flow rate of purge gas within the furnace are recorded as well, each dependent on a time scale t. The result of such a TGA measurement is classically displayed in a so-called thermogravimetry (TG) curve, a two-dimensional plot, in which the sample mass (mostly in wt% of original sample mass) is plotted as an ordinate against the according temperature the sample was exposed to in that moment as abcissa. While allowing for visual assessment of the analyzed sample's thermal behavior, such a TG curve might give the impression of being a rather simple mathematical function. However, it has to be noted that plotting the domain m against domain T does not represent a function in a mathematical sense, since both domains are each dependent on the domain t but not on each other, and therefore a single element of m is not a direct assignment to an element of T.
All TGA measurements within this chapter were conducted on a Perkin-Elmer TGA 8000 thermogravimetric analyzer using open alumina sample pans. The samples analyzed ei-

ther consisted of cut pieces of PI films or of powder-like HT-PIs evenly distributed across the sample pan's bottom. Most samples had an initial mass between 2 mg to 10 mg (with few exceptions broadening the range from 1.2 mg to 16.3 mg), while the average sample mass was approx. 5.3 mg.

The heating programs ranged from 30 °C to 900 °C for samples analyzed in dry nitrogen purge gas and 30 °C to 800 °C for samples analyzed in dry air from a compressed air supply line, each measurement employing a heating rate of 10 K min^{-1} and scanning rate of 2 s^{-1}. In each case the purge-gas flow rate was 20 ml s^{-1}. Unless stated otherwise, for each sample type at least two (averaged) measurements were conducted in nitrogen atmosphere and at least one measurement in air, which in some cases includes several similar sample types per PI system.

These parameters were chosen considering general recommendations of ASTM E2550-17 for thermal analysis of polymers via TGA:[220] heating rates between 10 K min^{-1} and 20 K min^{-1}, sample mass of approx. 5 mg and measurement temperatures ranging from room temperature to 600 °C. Since most PI samples exhibited decomposition temperatures close to the upper limit of this temperature range, the range was expanded to 900 °C. One has to bear in mind that the occurrence of any thermal event within a TGA measurement always depends on the heating rate applied and comparability among various measurements strictly requires uniformity of heating rates. While recommending heating rates in TGA measurements below 10 K min^{-1}, Hergenrother considered isothermal TGA being a better method to assess the thermal stability of a high-performance polymer. For this method, high-performance polymer samples are kept at e.g. 371 °C (choosing this rather odd number goes back to the US aerospace and aircraft industries' formal demands regarding polymer stability at 700 °F)[221] for several hundred hours while their mass-loss behavior is compared.[1] This extraordinarily time-consuming method was hardly applicable for the comparison of a wider array of PI systems, which this chapter was intended to be, not to mention the repeating of measurements for ensuring the reliability of results. Moreover, cross-linking reactions at high temperatures unduly influence the obtained results using this technique, which should be avoided.[222] Besides, the probably most useful way of assessing a polymer's thermal performance in a application-oriented sense would be measuring the retention of its physical/mechanical properties when exposing it to its intended application conditions.[1] Moreover, it might be criticized that "the TGA technique by itself is inadequate for reflecting the thermal stability of polymers, since degradation reactions such as crosslinking or chain extension could occur with [only] a small accompanying weight loss",[223] and one should rather re-

fer to such data as "procedural decomposition temperatures".[224] Nonetheless, due to its versatility, simplicity and straightforwardness, TGA still represents the most common and widely used method for determining the thermal stability of polymers and other materials.[222,224–228]

5.2.2 Retrieval of Results / Processing of Data

There are several well-established approaches to determining a polymer's T_d utilizing the TGA technique: ISO 11358-1:2020 recommended using extrapolated onset temperatures determined by the intersection of a tangent along the apparent mass baseline before the event and one tangent along the decomposition curve placed at the point of maximum decomposition rate within the decomposition gradient.[229] This gradient is depicted by the so-called derivative thermogravimetry (DTG) curve, in which the point of highest decomposition rate (negative slope) is found at the minimum of this curve. Traditionally, this DTG curve was displayed often times in a context of TGA measurements in order to e.g. distinguish between overlapping and identifying minor mass-loss events,[225] or for compositional analysis of polymer blends.[230]

As discussed in the previous section 5.2.1, the DTG curve can only be a differential quotient of the function m(t) (but not of m(T)), since m is a direct assignment to t but not to T. However, since each element of t can be assigned an discrete element of T, displaying a DTG curve (as "derivative") sharing an abscissa T with the TG curve is somewhat justifiable. Furthermore, since the balance calibration for this TGA device intrinsically used extrapolated onset temperatures of the curie points of several metals and alloys, this method somewhat possessed its own rationale. Among other ones, the method of extrapolated onset temperatures according to ISO 11358-1:2020 was included in the processing of this thesis' TGA data. It was realized by using a custom built LabTalk script within OriginLabs OriginPro 2021 software received from Paul Jusner of *BOKU* in Tulln, Austria. Here, each dataset's series of values for m was smoothed via a local regression method (locally weighted scatterplot smoothing, LOWESS span of 0.05), after which a gradient against T was calculated in order to obtain the DTG curve, then tangents were placed automatically along the TG curve at the corresponding points of the DTG curves' global maximum (representing the initial baseline) and global minimum (representing the maximum decomposition rate), and finally the corresponding value for T at their intersection point was recorded. It should be noted that this only worked as intended in TGA measurements in which the mass-loss event for PI decomposition was the by far

most prominent one. Although the processing software included in the sale of the TGA device allows for manually placing tangents along the TG curve in order to find extrapolated onset temperatures, one should refrain from doing so, as it allows for strongly biased processing.

As another standardized method, ASTM E2550-17 recommended finding a decomposition onset temperature either by selecting a point on the mass-loss curve when a deflection from an established baseline is first observed (at a vertical zoom rate of 1 % on a graphical user interface), or when a deflection within a derivative thermogravimetry curve is first observed.[220] This method required a completely steady baseline for the sample mass prior to a significant mass-loss event, which could hardly be observed in these materials. Moreover, determining such a deflection by eye can not exclude human bias. Additionally, it was shown that this point of initial mass loss is overly sensitive to procedural parameters and does not correlate directly with later decomposition stages.[218] Therefore, this method was discarded.

According to Hergenrother, a high-performance polymer's thermal stability should be assessed by determining the value of temperature at the sample's 5 % weight loss, assuming that a neat polymer's mechanical properties underwent a substantial reduction at this point.[1] This was the central method for assessing the thermal stability this thesis' PI systems. Although it is implied that 5 wt% mass loss refer to a sample's initial weight at the beginning of each measurement, this method was modified for this thesis. In many cases minor, sometimes also quite continuous mass-loss events were observed during a TGA measurement at lower temperatures before the main polymer decomposition event. These were most probably due to loss of absorbed water or residual solvent, incomplete polymerization, pendant end groups in short chain segments decomposing or reacting for further polymerization.[196,221] Moreover, these mass-loss events are known to account for more than 7 % of initial sample mass.[231] Since they obviously did not represent decomposition temperatures of the pure polymeric segments themselves they were considered neglectable. Therefore, each measurement's values at a precise 5.0 % mass loss starting from 400.0 °C and 371.0 °C were recorded, assuming that the aforementioned processes were complete and that the following mass-loss event represented decomposition of the polymeric segments. In some samples the first mass-loss events starting at approx 350°C due to decomposition of non-polymerized segments were so prominent they overlapped with subsequent mass-loss events due to polymer decomposition, rendering any values obtained for T_d invalid. Those measurements were therefore discarded. In summary, the methods employed for assessing the thermal stability of all

PI systems within this thesis included the 5 wt% mass loss starting from either 400.0 °C (as $T_{d,400}$), or in few cases from 371.0 °C if the mass-loss events were too close to the 400.0 °C threshold (as $T_{d,371}$), the tangent-derived onset temperatures ($T_{d,onset}$), but also the temperature of highest decomposition rate ($T_{d,max}$). For reasons of completeness the char yield (CY) for samples measured in nitrogen atmosphere was included as well, representing the mass percentage of carbonized residues at 900 °C, after all polymer-related mass-loss events took place. It has to be noted that at temperatures higher than 900 °C further reactions take place.[216] Comparisons of PI systems within the results section were mainly done using $T_{d,400}$ of measurements conducted in nitrogen atmosphere. It turned out that $T_{d,onset}$ tended to overestimate T_d of samples measured in air, which was due to the more pronounced steepness of the mass-loss curve after the decomposition onset, leading to tangent intersections being found at significantly higher abscissa values compared to the samples measured in nitrogen atmosphere. Accordingly, $T_{d,max}$ for measurements in air were found to be giving greatly increased values compared to nitrogen measurements as well. For this study, datasets of approximately 400 measurements were used and processed, not including the ones discarded due to their invalidity. Structural formulae of all PI systems employed in the studies within this chapter are depicted in appendix A.1 and A.2.

5.3 Results

5.3.1 Methods of Synthesis

This first section within the results of this study focused on the impact of synthesis method on the thermal stability of the resulting material. For that, the most simple and at the same time extremely stiff aromatic PI system was chosen, which was expected to have a rather high thermal stability. Several samples of PMDA-pPDA (PPPI) were synthesized by different methods as indicated by the "type" column of table 5.1. Film, HT and MW samples represent samples synthesized classically into films, hydrothermally polymerized monomer salt in an autoclave (64 h, 200 °C) and in a microwave reactor (8 h, 200 °C, 800 rpm stirring), respectively, all as described in chapter 3. NMP depicted samples of monomer salt polymerized in refluxing *N*-methyl-2-pyrrolidone (NMP) at approx. 200 °C for 20 h, and SSP solid-state polymerized monomer salt in a convection oven overnight (200 °C). All samples were polymerized at 200 °C, except for the film samples, which were exposed to temperatures up to 400 °C. In all cases, $T_{d,400}$ for samples

measured in air was significantly lower than for the ones measured in nitrogen. This behavior was expected, since it is known that the hydrolysis step in decomposition reactions is faster when oxygen is present.[214] Moreover, the diamine components' phenyl rings are most vulnerable to thermo-oxidative degradation.[217] Both film and SSP samples exhibited the lowest crystallinity of all samples within this comparison (cf. figure 5.1), and at the same time highest char yields. It is known that PPPI particles obtained via SSP of their monomer-salt precursor retain the shape of the monomer salt crystallites to some extent.[137] These crystallites are naturally bigger than the ones found in HT-PIs, which would mean that SSP-PPPI was more of a agglomerate of rather amorphous PI product in which a fraction of the PI was not that much exposed to oxygen during measurements in air, slightly approximating the obtained values for $T_{d,400}$ to the values of nitrogen measurements. A continuous film is very likely to isolate a fraction of its polymeric segments from oxygen as well, which could explain why both SSP and film samples exhibited the lowest differences in $T_{d,400}$ between both purge gases. Similarly, this effect of enclosing inner segments could also account for both sample types showing the highest char yields, since less gaseous product could leave the decomposing material until 900 °C were reached during the measurement. This enclosure somewhat might have decreased the decomposition velocity to some extent, which would be consistent with the fact that lower heating rates lead to significantly higher char yields in other polymers.[232] Moreover, it could also explain the highest $T_{d,400}$ of 639 °C for the SSP-PPPI to some extent, although the film sample having a $T_{d,400}$ of 620 °C seemed to contradict this assumption. With a $T_{d,400}$ of 625 °C in nitrogen, HT-PPPI was the second most stable PI in this comparison, although it has to be noted that its $T_{d,onset}$ of 638 °C was found to be very similar to SSP-PPPI. Its high thermal resilience could be explained by this material's extraordinarily high crystallinity posing an additional energetic barrier in the process of decomposition. However, MW-PPPI exhibited T_d being consistently lower ($T_{d,400}$ = 615 °C in nitrogen) when compared to HT-PPPI despite being similarly crystalline. This could be explained by particle sizes being expected to be smaller in case of MW-PIs compared to HT-PIs synthesized in autoclaves, since smaller particle sizes are known to be resulting in lower thermal stability of polymers and other organic materials.[233–236]

Table 5.1: Thermal stability indicators for PMDA-pPDA PIs obtained from various methods of synthesis.

PI system	type	purge	$T_{d,400}$ [°C]	$T_{d,onset}$ [°C]	$T_{d,max}$ [°C]	CY [%]
PMDA-pPDA	film	N_2	**620**	624	663	53
		air	614	629	671	
	NMP	N_2	**600**	631	665	43
		air	566	614	658	
	HT	N_2	**625**	638	667	44
		air	592	624	660	
	MW	N_2	**615**	627	661	44
		air	580	610	659	
	SSP	N_2	**639**	637	663	49
		air	620	633	673	

The PPPI samples obtained from refluxing NMP exhibit the lowest stability within this comparison with a $T_{d,400}$ of 600 °C in nitrogen. This could be due to its comparably low crystallinity combined with both rather small particle sizes and potentially low agglomeration resulting from the vigorous stirring of the reaction solution during synthesis.
The char yields obtained for HT-, MW- and NMP-PPPI were highly uniform, whereas the char yields for film and SSP-PPPI were increased, as discussed above. Since it is known that CO (CO_2 in air) is the first and most prominent gaseous product during PI decomposition[214,237] and that nitrogen atoms rarely leave the decomposing material in the temperature range applied,[216] the char yields presented in this thesis could not be used for verifying the materials' elemental compositions.
For most following comparisons both HT and film samples were analyzed. Some additional comparisons were done just using HT samples, due to the PI synthesis being more facile and parallelizable when done hydrothermally in autoclaves.

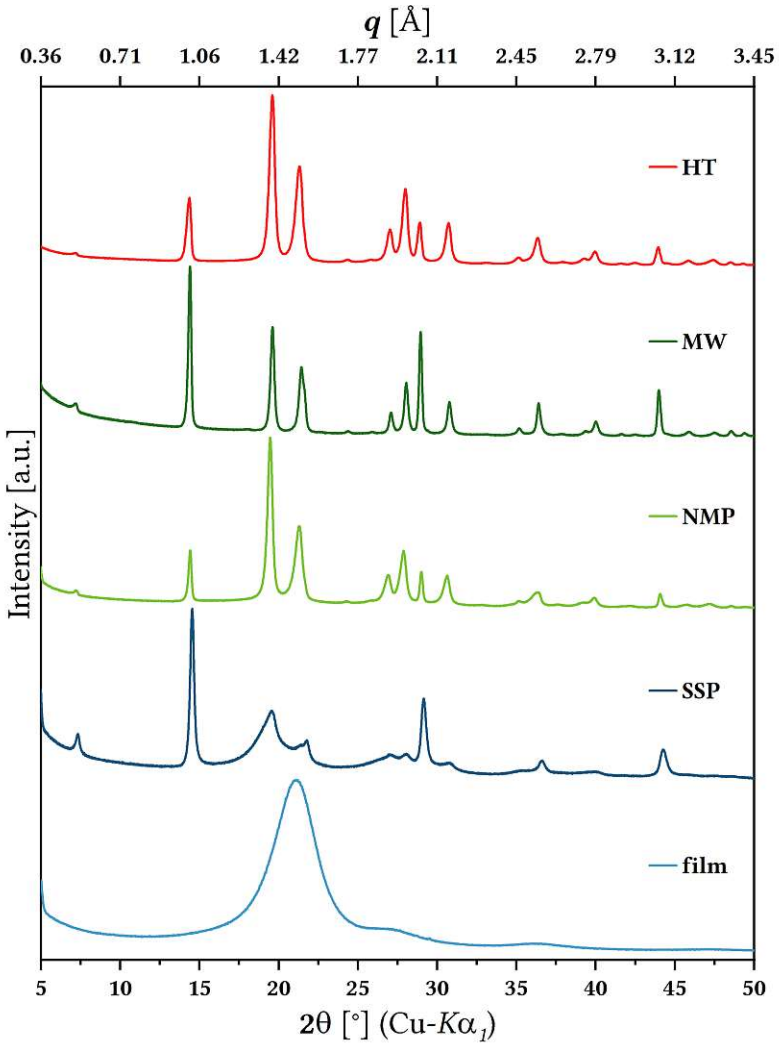

Figure 5.1: PXRD patterns of PMDA-pPDA PIs obtained from various methods of synthesis.

5.3.2 Linear Aromatic Polyimides

In analogy to the first comparison of moisture sorption behavior drawn in the previous chapter 4.3.1, thermal stability was assessed (cf. table 5.2) for the same PI systems, both as film samples and hydrothermally synthesized powders. Here several trends could be observed, which held true for all following comparisons within this chapter: In all cases except for PMDA-pPDA, HT samples generally give lower T_d as compared to film samples. One explanation for this behavior might be found in the intrinsically higher surface area of HT particles as compared to film samples, as for this reason smaller particle sizes are known to be resulting in lower thermal stability of polymers and other organic materials.[233–236] This effect could also explain the increased differences in $T_{d,400}$ between samples measured in nitrogen and the ones measured in air in case of HT samples. Although it was the case for most PI systems, HT samples exhibited a lower $T_{d,400}$

when analyzed in air, which again might be due to the highly increased surface area of HT particles offering more sites for thermo-oxidative degradation initiated by oxygen.[238] Moreover, the gases which evolve from the decomposition reactions have to diffuse through the sample in order to be removed by the purge gas,[239] a process which naturally is highly facilitated if the material consists of powder-like particles. Film-like samples could temporarily enclose emerging gases and thereby retard the occurrence of weight loss, which is the only reaction indicator in a thermogravimetric measurement, and which could contribute to their increased values for $T_{d,400}$ as well. Similarly to the observations made in section 5.3.1, char yields for film samples were generally higher than for HT samples, which again might be because of the minimally retarded heating rates due to this enclosing leading to significantly higher char yields.

While in all results $T_{d,onset}$ in case of nitrogen purge gave values quite close to $T_{d,400}$, when measured in air the values for $T_{d,onset}$ were significantly increased. This overestimation was due to mass-loss events comprising more relative sample mass decomposing in air measurements after the decomposition onset, since all material decomposed without any residues. This resulted in a more pronounced steepness of the mass-loss curve, leading to tangent intersections being found at much higher abscissa values and therefore to highly increased values for both $T_{d,onset}$ and $T_{d,max}$ compared to samples measured in nitrogen atmosphere. Here again, for measurements of HT samples in air $T_{d,onset}$ gave values exceeding the range of $T_{d,400}$, while for all samples measured in air $T_{d,max}$ again were extraordinarily high compared to $T_{d,400}$.

For all film samples measured in nitrogen atmosphere $T_{d,400}$ were highly similar, as films of PMDA-pPDA,sBPDA-pPDA and sBPDA-Bz exhibited a $T_{d,400}$ of 620 °C and PMDA-Bz of 618 °C, whereas both systems containing DATP, namely PMDA-DATP and sBPDA-DATP exhibit slightly elevated $T_{d,400}$ of 629 °C and 625 °C, respectively. The obtained values for $T_{d,onset}$ from 609 °C to 626 °C and for $T_{d,max}$ from 643 °C to 663 °C in nitrogen were quite close to each other as well. Moreover, for measurements of film samples conducted in air, $T_{d,400}$ were ranging from 614 °C to 632 °C, while values for $T_{d,onset}$ were even more homogeneous ranging from 628 °C to 634 °C, but with $T_{d,max}$ being quite scattered ranging from 665 °C to 756 °C (excluding PMDA-Bz, since this measurement has not been done). This general homogeneity of primarily $T_{d,400}$ but also of $T_{d,onset}$ clearly showed that there was no obvious difference in thermal stability of these materials when being continuous film samples. Similar observations regarding T_d for rigid-rod polyimides have been made by Koton in 1975,[222] while associated researchers linked this phenomenon to the presence of an undisturbed and efficient conjugation system within

Table 5.2: Thermal stability indicators for various PIs bearing different fractions of imide groups.

PI system	type	purge	$T_{d,400}$ [°C]	$T_{d,onset}$ [°C]	$T_{d,max}$ [°C]	CY [%]
PMDA-pPDA	film	N_2	**620**	624	663	53
		air	614	629	671	
	HT	N_2	**625**	638	667	44
		air	592	624	660	
PMDA-Bz	film	N_2	**618**	615	654	61
	HT	N_2	**595**	615	650	48
		air	579	611	654	
PMDA-DATP	film	N_2	**629**	626	656	64
		air	629	634	756	
	HT	N_2	**598**	572	661	55
		air	560	598	656	
sBPDA-pPDA	film	N_2	**620**	609	647	62
		air	619	629	729	
	HT	N_2	**615**	608	650	54
		air	599	628	678	
sBPDA-Bz	film	N_2	**620**	612	643	64
		air	628	628	665	
	HT	N_2	**611**	610	648	56
		air	600	627	678	
sBPDA-DATP	film	N_2	**625**	615	647	66
		air	632	636	743	
	HT	N_2	**584**	578	622	49
		air	572	611	652	

these polymers.[217,240] Hence, the existence of biphenyl linkages within the PI backbone could not be considered a disadvantage in terms of thermal stability. Moreover, the slightly elevated values of $T_{d,400}$ in both nitrogen and air for the DATP-containing PIs might indicate a somewhat improved stability toward high temperatures possibly due to their relatively high fraction of uninterrupted aromatic regions facilitating interchain π-π stacking.

However, the differences in $T_{d,400}$ for HT samples in nitrogen were slightly more pronounced. The PI systems which exhibited the highest $T_{d,400}$ as films, PMDA-DATP ($T_{d,400}$ = 598 °C) and sBPDA-DATP ($T_{d,400}$ = 584 °C) were among the lowest performing ones when synthesized as HT PIs. This might be again due to DATP's high fraction of aromatic rings, generally lowering its solubility, an effect which was observed when synthesizing monomer salts from it: When combining corresponding monomer solutions in acetone, precipitation occurred so quickly potential co-precipitation of monomers could not be excluded. This effect was avoided by using tetrahydrofuran instead of acetone

for dissolving monomers and their combination. However, since DATP might also have a very low solubility in high-temperature water at 200 °C, it could mean that the PI particles emerging from respective HT synthesis might have been extraordinarily small, leading to a highly increased surface-to-volume ratio and therefore to a lower thermal resilience, compared to more soluble monomer combinations. This effect of quick precipitation was less pronounced but still recognizable when preparing monomer salts with benzidine, which could offer a similar explanation for the relatively low performance of these HT PIs as well. Interestingly, the hydrothermally synthesized PMDA-pPDA PI turned out to be the only case, in which a HT PI was slightly more thermally stable material than its film counterpart. An explanation could be found in the extraordinarily high crystallinity of this material compared to the others, as the overcoming of energy barriers for breaking crystal lattices might negate an effect of higher surface-to-volume ratio which would otherwise lead to lower T_d.

5.3.3 Meta-connectivites & Fluorination

While in the previous section only rather linear PIs were discussed, this section focused on the influence of meta-linkages in the PI backbone on the thermal resilience of the material, since these linkages' effect on the moisture sorption behavior was tremendous (cf. section 4.3.3) and indications toward lower thermal stability of meta connectivities could be found in literature.[241] Simultaneously, effects of partial fluorination within the diamine fraction of the PI backbone was investigated, finalized by a comparison including perfluorinated central segments in analogy to section 4.3.2.

The first comparison was made between PIs composed of sBPDA polymerized with pPDA, mPDA or fluorinated derivatives of the latter, while attempts to synthesize sBPDA-4FmPDA hydrothermally did not seem to result in sufficiently polymerized samples.

Figure 5.3 shows that when introducing a meta kink into the PI backbone by polymerizing sBPDA with mPDA instead of pPDA, all values of $T_{d,400}$ and $T_{d,onset}$ from both sample types and purge gases decreased significantly. For film samples analyzed in nitrogen, $T_{d,400}$ dropped from 620 °C for sBPDA-pPDA to 597 °C for sBPDA-mPDA, whereas for HT samples in nitrogen the drop was from 615 °C to 602 °C. Both $T_{d,400}$ and $T_{d,onset}$ of HT samples of sBPDA-mPDA were consistently higher than for film samples, which seemed quite uncommon, but nonetheless they were quite close to each other. In analogy to the reasoning in chapter 4.3.3, the intrinsically more kinked structure introduced by mPDA could lead to a greater fraction of free volume within the material and therefore reduce

the molecular interactions, such as interchain π-π stacking, which could result in a lower thermal stability in case of sBPDA-mPDA as compared to sBPDA-pPDA.

Another possible explanation for this behavior could be found in a mechanistic aspect of the decomposition reactions of these materials: As proposed by Zurakowska-Orszagh et al. in 1976 and Laius et al. in 1984, one of the two decomposition reactions being the most likely to occur is the homolytic cleavage of the bond between one carbonyl carbon atom and the amine nitrogen atom within the imide ring (the other one being the homolytic cleavage of the N-C_{Ar} bond adjacent to the imide ring).[217,242] The immediate result of this reaction would be a carbonyl radical and a nitrogen-centered radical, both at the ends of the two resulting chain segments. The former is quite unstable and dissociates under elimination of CO, rendering this reaction irreversible and quite likely leading to a full split of the PI chain.[217] The nitrogen-centered radical on the other hand could more easily be resonance-stabilized by its adjacent aromatic system. If another amine functionality attached to the benzene ring in para (or ortho) position to the radical, this second amine could directly participate in statistically distributing the radical position by offering more possible positions for the radical than an amine functionality in meta position would (cf. figure 5.2). This would stabilize the radical and could therefore retard further propagation of radical reactions, an effect which is prominently utilized in e.g. Wurster's radicals.[243] This positive mesomeric effect of amine functionalities could not be utilized to that extent if these moieties were in meta position, offering another possible explanation for the lower thermal stability of sBPDA-mPDA compared to sBPDA-pPDA.

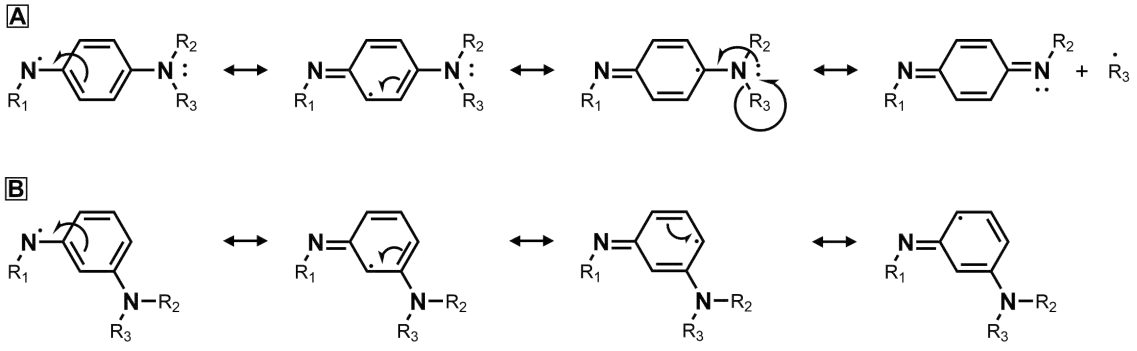

Figure 5.2: Mesomeric stabilization of radicals during PI decomposition. Para substitution in case of pPDA (**A**) resulted in improved stabilization compared to mPDA (**B**). Note that (**A**) includes an implicit resonance structure not depicted here.

Introducing a fluorine-substitution site in case of sBPDA-1FmPDA led to an increase in $T_{d,400}$ to 611 °C for films and a decrease to 582 °C for HT samples in nitrogen. The increase

in case of film samples in nitrogen could indicate a slightly increased thermal stability due to the strong C-F bond found in the PI backbone, although this effect should also be visible in measurements in air, since the fluorine atom should reduce electron density in the phenyl nucleus of the diamine component and therefore render it less prone to thermo-oxidative degradation.[217] Instead, $T_{d,400}$ of films of sBPDA-1FmPDA in air turned out to be at only 598 °C, although $T_{d,onset}$ in air having 627 °C came close to that of sBPDA-pPDA films. $T_{d,400}$ of HT samples of sBPDA-1FmPDA (582 °C in nitrogen) exhibited a higher discrepancy from the value obtained for film samples than expected. This discrepancy came close to those of DATP-based systems discussed in section 5.3.2, which could be indicative of similar solubility issues. Since the decreased solubility of 1FmPDA compared to mPDA in water was already noticeable when preparing the hydrothermal reactions, lower particle sizes and therefore lower thermal stability could be considered a possible explanation for this behavior. For films of sBPDA-4FmPDA both values of $T_{d,400}$ are quite similar, while both were very close to the ones for sBPDA-mPDA, merely $T_{d,onset}$ of sBPDA-4FmPDA (and sBPDA-1FmPDA) came quite close to sBPDA-pPDA. This could on one hand mean that fluorination sites on the PI backbone did not obviously influence the material's thermal stability. On the other hand there could be a possibility of effects of increased thermal resilience due to aromatic fluorination sites being compensated by shorter chain segments due to the fluorine atoms negative inductive effect lowering the reactivity of the diamines. Shorter chain segments could result in a higher fraction of terminal functional groups that could degrade more easily and therefore cause a lower thermal stability of the material.[113] However, the effect of partial fluorination of the PI backbone on thermal stability seemed rather inconclusive at this point.

Table 5.3: Thermal stability indicators for PIs from sBPDA and various PDA derivatives.

PI system	type	purge	$T_{d,400}$ [°C]	$T_{d,onset}$ [°C]	$T_{d,max}$ [°C]	CY [%]
sBPDA-pPDA	film	N_2	**620**	609	647	62
		air	619	629	729	
	HT	N_2	**615**	608	650	54
		air	599	628	678	
sBPDA-mPDA	film	N_2	**597**	588	648	57
		air	597	610	656	
	HT	N_2	**602**	598	644	55
		air	578	622	671	
sBPDA-1FmPDA	film	N_2	**611**	605	665	61
		air	598	627	677	
	HT	N_2	**582**	597	659	55
		air	552	602	648	
sBPDA-4FmPDA	film	N_2	**599**	603	657	54
		air	594	617	650	

The study of the influence of meta connectivities was extended to co-PI films composed of PMDA polymerized with different fractions of each pPDA and mPDA. While results for PMDA-pPDA (0 % mPDA) were already presented in sections 5.3.1 and 5.3.2, the system PMDA-mPDA (100 % mPDA) resulted in a highly brittle material, rendering it rather unsuitable for film applications but still useful for a thermogravimetric study to reveal structure-property relationships. Co-polymers of PMDA were polymerized statistically with a mixture of pPDA and different fractions of mPDA (5 %, 10 %, 30 % and 50 %) in order to reveal tendencies in successively increasing the amount of meta kinks in the PI backbone. It has to be noted that three of four co-PIs, namely PMDA-[0.05·mPDA+ +0.95·pPDA], PMDA-[0.1·mPDA+0.9·pPDA], and PMDA-[0.5·mPDA+0.5·pPDA] were analyzed using only one measurement in nitrogen atmosphere, therefore somewhat limiting the statistical power of this comparison. Table 5.4 showed the results of this comparison. PMDA-pPDA had the highest thermal stability with $T_{d,400}$ of 620 °C, whereas PMDA-mPDA exhibited a significantly decreased $T_{d,400}$ of 595 °C, confirming the observations made when studying sBPDA-based PIs at the beginning of this section. Replacing a 5 % or 10 % fraction of pPDA by mPDA led to a significant decrease of thermal stability down to 607 °C in case of PMDA-[0.05·mPDA+0.95·pPDA] and 606 °C in case of PMDA-

[0.1·mPDA+0.9·pPDA]. The similarity of these values could be explained by the rather insignificant difference of mPDA fraction. Increasing the mPDA fraction to 30 % again led to a decrease of $T_{d,400}$ to 596 °C in case of PMDA-[0.3·mPDA+0.7·pPDA]. A further increase in mPDA fraction to 50 % again led to a decrease in $T_{d,400}$ down to 590 °C. This again could indicate that a increasing fraction of kinks in the PI chain would lead to a decrease in thermal stability. However, since this value was below that of pure PMDA-mPDA, this statement could not be confirmed by any degree of linearity between the fraction of backbone kinks and resulting thermal stability. Merely tendencies toward this behavior could be considered observable.

Table 5.4: Thermal stability indicators for PI systems of PMDA polymerized with combinations of pPDA and mPDA. All PIs were synthesized classically as films and analyzed in nitrogen atmosphere.

PI system	$T_{d,400}$ [°C]	$T_{d,onset}$ [°C]	$T_{d,max}$ [°C]	CY [%]
PMDA-pPDA	620	624	663	53
PMDA-[0.05·mPDA+0.95·pPDA]	607	615	658	53
PMDA-[0.1·mPDA+0.9·pPDA]	606	617	666	54
PMDA-[0.3·mPDA+0.7·pPDA]	596	596	641	55
PMDA-[0.5·mPDA+0.5·pPDA]	590	589	635	53
PMDA-mPDA	595	596	641	54

A similar approach was chosen for studying the influence of meta connectivities on the thermal stability of hydrothermally synthesized (co-)PIs (cf. Figure 5.5). HT samples of PMDA-pPDA exhibited average $T_{d,400}$ of 625 °C in nitrogen, as presented before, while a statistical co-PI containing equal amounts of pPDA and mPDA, namely PMDA-[0.5·mPDA+0.5·pPDA], showed highly decreased $T_{d,400}$ of 589 °C. However, PMDA-mPDA exhibited $T_{d,400}$ of 630 °C, which slightly exceeded the thermal resilience of PMDA-pPDA, rendering it the thermally most stable HT PI within this chapter. Tendencies of values for all thermal stability indicators obtained from measurements in both nitrogen and air were quite similar throughout this comparison. Both PMDA-pPDA and PMDA-mPDA consisted of highly stiff polymer chains, while on a micro-structural level the former would only be able to form rigid rods and the latter could only form helical structures. A distinction between both systems in terms of structural favorability could not be made, since both HT PIs seemed similarly crystalline. Intriguingly, X-ray diffractograms of the co-PI exhibit reflections less intense but fully congruent with PMDA-pPDA but not with PMDA-mPDA. This led to the conclusion that the significantly decreased thermal sta-

bility of the co-PI could have been due to distortion of structural long-range order and resulting lower crystallinity.

Table 5.5: Thermal stability indicators for different hydrothermally synthesized PI systems of PMDA polymerized with combinations of pPDA and mPDA.

PI system	purge	$T_{d,400}$ [°C]	$T_{d,onset}$ [°C]	$T_{d,max}$ [°C]	CY [%]
PMDA-pPDA	N_2	**625**	638	667	44
	air	592	624	660	
PMDA-[0.5·mPDA+0.5·pPDA]	N_2	**589**	608	651	44
	air	579	609	652	
PMDA-mPDA	N_2	**630**	634	669	48
	air	605	626	675	

Since it was shown in section 4.3.2 that the introduction of perfluorinated segments in the PI backbone had a significant impact on the moisture sorption behavior, an analogous comparison was drawn for further assessing the influence of fluorination on the material's thermal stability. Again, for that not only PI films but also hydrothermally synthesized samples of the PI systems PMDA-APBP and PMDA-8FAPBP were analyzed. It could be seen in figure 5.6 that in case of film samples analyzed in nitrogen atmosphere the introduction of the perfluorinated segment significantly increased $T_{d,400}$ from 588 °C for PMDA-APBP to 612 °C for PMDA-8FAPBP. The increase in $T_{d,400}$ for film samples in air and for HT samples in nitrogen was also significant, although less pronounced. Merely $T_{d,400}$ for HT samples of PMDA-8FAPBP measured in air was lower than for PMDA-APBP. Also in this series, the stability indicators for films were generally higher than for HT samples and for samples analyzed in nitrogen higher than for the ones pyrolyzed in air, while values of $T_{d,onset}$ again were quite close to $T_{d,400}$ in the case of measurements of films in both nitrogen and air and for HT samples in nitrogen. Char yields for HT samples again were lower than for films in both cases.

The general increase in thermal stability in case of the fluorinated PI system was expected, but in this comparison the increase in thermal stability was more visible than it was for the samples discussed in section 5.3.3. This indicated that the introduction of fluorine substituents could indeed lead to increased thermal resilience of a material by offering strong C-F bonds and lowering the electron density in the perfluorinated aromatic segments,[221] i.e. the octafluorobiphenyl moiety (cf. section 5.3.3). Moreover, this effect did not seem to be obfuscated by a lower stability due to shorter polymer chains

arising from a lower reactivity of diamines in case of the fluorinated diamine. This could be due to the electron-withdrawing effect of the fluorine substituents being sufficiently separated from the amine moieties by oxyphenylene groups. Comparing these numbers to the thermal stability indicators of the linear-chain reference systems in section 5.3.2, a slight but general decrease in thermal stability could be observed. This most likely was due to the existence of ether bridges in the PI backbones of both PMDA-APBP and PMDA-8FAPBP, which could be found enclosing the (octafluoro)biphenyl center in the diamine segment of the polymer. These bridging moieties seemingly posed a weak spot, which was further investigated in the following section.

Table 5.6: Thermal stability indicators for PIs from PMDA-APBP and PMDA-8FAPBP.

PI system	type	purge	$T_{d,400}$ [°C]	$T_{d,onset}$ [°C]	$T_{d,max}$ [°C]	CY [%]
PMDA-APBP	film	N_2	**588**	579	613	57
		air	585	584	712	
	HT	N_2	**573**	580	617	47
		air	561	593	637	
PMDA-8FAPBP	film	N_2	**612**	604	641	53
		air	602	614	651	
	HT	N_2	**586**	570	529	46
		air	552	577	613	

5.3.4 Bridging Moieties & Connectivity

Since a general decrease in thermal stability arising from bridging moieties between aromatic segments of the PI backbone could be seen in the previous section, this effect was further investigated by assessing the stability of several other PI systems. In table 5.7 the indicators of thermal stability for PMDA-sODA and PMDA-aODA are presented, both comprising PMDA polymerized with a symmetric (4,4′-) and an asymmetric (3,4′-) oxydianiline derivative, respectively. The diamine segments of both PI systems had an ether bridge connecting the two phenylamine moieties, while in PMDA-aODA, the amine moiety was located in meta position to the ether oxygen on one side, which posed another structural feature to be investigated in terms of thermal stability. This comparison was done in analogy to section 4.3.5 of chapter 4, in which the moisture sorption behavior of both systems was assessed. Here as well, both PI systems exhibited a generally lower thermal stability compared to the rather rigid reference systems

in section 5.3.2. In a temperature range close to PMDA-APBP in the previous section, PMDA-sODA and PMDA-aODA had $T_{d,400}$ of 593 °C and 584 °C, respectively, for films analyzed in nitrogen atmosphere, while HT samples in nitrogen had values of 582 °C and 574 °C, respectively. Again, HT samples had lower $T_{d,400}$ than films and values for $T_{d,onset}$ again were quite close to these, except for samples in air, as observed in the comparisons before. Here as well, $T_{d,400}$ of samples in air were lower than in nitrogen, and the char yields of films were higher than for HT samples. The generally lower thermal stability of these systems containing flexible ether bridges was most likely due to their disruption of the system of conjugated electrons,[217,244] which is known to be the main reason for fully aromatic PIs exhibiting a higher thermal resilience.[240] Although oxyphenylene groups in PIs are considered quite stable toward thermal and thermo-oxidative degradation and differences to fully aromatic PIs may have been considered close-to-negligible,[113] the differences observed within this study were significant. Another reason could be found in the decreased rigidity of these flexible PIs, decreasing intermolecular interactions.[113] Comparing both systems among each other, PMDA-aODA exhibited consistently lower thermal stability indicators, although these differences were rather small, as values for $T_{d,400}$ differed by less than 10 °C. Similar results could be found in literature, while the differences in thermal stability between both systems were considered negligible.[190]

Table 5.7: Thermal stability indicators for PMDA-sODA and PMDA-aODA PIs.

PI system	type	purge	$T_{d,400}$ [°C]	$T_{d,onset}$ [°C]	$T_{d,max}$ [°C]	CY [%]
PMDA-sODA	film	N_2	**593**	586	617	56
		air	592	606	709	
	HT	N_2	**582**	591	629	47
		air	565	601	650	
PMDA-aODA	film	N_2	**584**	574	607	57
		air	589	606	717	
	HT	N_2	**574**	571	610	46
		air	567	600	646	

The next comparison extended the study of the influence of both ether bridges as connecting moieties and arene substitution pattern on the thermal stability by including PIs consisting of PMDA polymerized with either pBAPB (1,4-Bis(4-aminophenoxy)benzene) and mBAPB (1,3-Bis(4-aminophenoxy)benzene), in analogy to section 4.3.6.

Table 5.8 shows the thermal stability indicators for both PI systems as films and HT

samples. It could be observed that $T_{d,400}$ of film samples of PMDA-pBAPB in nitrogen is virtually identical to PMDA-sODA being 594 °C, while the values for films in air and both values for HT samples (570 °C in nitrogen) of this system were lower than they were for PMDA-sODA. The values of $T_{d,400}$ PMDA-mBAPB exhibited for measurements in nitrogen atmosphere did not differ significantly from PMDA-pBAPB, as $T_{d,400}$ for films was slightly lower being 589 °C and for HT samples was slightly higher being 576 °C. Moreover, these values were found to range between those of PMDA-sODA and PMDA-aODA. As the latter systems were already considered uniform in terms of thermal stability and PMDA-pBAPB and PMDA-mBAPB exhibited even lower differences, this rendered their thermal stability being virtually identical. Interestingly, $T_{d,400}$ in air was consistently lower than it was the case in PMDA-sODA and PMDA-aODA. Comparing these systems to PMDA-APBP (cf. section 5.3.3), which counted for two ether bridges among four phenyl moieties in the diamine fraction, the PMDA-ODA systems had one ether bridge among two phenyl moieties, while the PMDA-BAPB systems had two ether bridges among three phenyl moieties. Since all these PI systems just mentioned exhibit highly uniform thermal stability indicators, but differ significantly from the fully aromatic PIs assessed earlier, it could be assumed that incorporating ether bridges generally led to lower thermal stability, while increasing the fraction of such weak points within the material did not seem to have any obvious effect. Moreover, meta connectivities within the arene substitution patterns also did not obviously influence the stability of these PIs, indicating that the effect of connectivities in meta position observed in section 5.3.3 could not be found here, since the ether-oxygen moieties may not be prone to participate in mesomeric conjugation behavior. On the other hand, it could be considered that other parameters related to manufacturing of the samples might have led to a scattering of the measurement results large enough to obfuscate potentially existing effects of different arene substitution patterns and ether-bridge fractions.

Table 5.8: Thermal stability indicators for PMDA-pBAPB and PMDA-mBAPB PIs.

PI system	type	purge	$T_{d,400}$ [°C]	$T_{d,onset}$ [°C]	$T_{d,max}$ [°C]	CY [%]
PMDA-pBAPB	film	N_2	**594**	590	621	53
		air	579	617	712	
	HT	N_2	**570**	582	615	43
		air	549	582	641	
PMDA-mBAPB	film	N_2	**589**	580	604	55
		air	581	605	686	
	HT	N_2	**576**	570	600	47
		air	559	586	633	

A similar behavior was observed when the bridging moieties did not consist of oxygen but of isopropyl groups. Here, PMDA was polymerized with either bisaniline P (4,4′-(1,4-phenylenediisopropylidene)bisaniline) or bisaniline M (4,4′-(1,3-phenylenediisopropylidene)bisaniline) to yield PMDA-pBISA and PMDA-mBISA, respectively. As it can be seen in table 5.9, PMDA-pBISA exhibited $T_{d,400}$ of 534 °C for films and 522 °C for HT samples in nitrogen atmosphere, while PMDA-mBISA had $T_{d,400}$ of 531 °C for films and 526 °C for HT samples. Differences in thermal stability between both PI systems were virtually nonexistent, except for $T_{d,400}$ of film samples analyzed in air, for which PMDA-mBISA exhibited a significantly lower value than PMDA-pBISA did. Interestingly, values of $T_{d,400}$ for measurements of films in air compared to measurements conducted in nitrogen were significantly lower than they had been for most systems previously assessed, resembling differences found when comparing HT samples. This could indicate a generally lower resilience to thermo-oxidative conditions caused by the isopropyl groups connecting the phenyl moieties within the diamine fraction, whereas it was not possible to differentiate between both arene substitution patterns containing either para or meta connectivities within both diamines. Furthermore, the isopropyl moieties found in these PI systems seemed to have caused a tremendous decrease in overall thermal stability compared to the fully aromatic reference systems in section 5.3.2. This decrease was significantly more pronounced than it was for ether bridges found in the previously assessed PIs, which was most probably due to the isopropyl moieties' aliphatic nature efficiently interrupting the conjugation system between the neighboring phenyl moieties as well as offering rather unstable bonds between sp^3-hybridized carbon atoms within the moieties themselves. Therefore, these aliphatic groups could be considered a weak

spot within the otherwise aromatic polymer materials, substantially reducing their thermal stability. Another interesting observation could be made when comparing the char yields, as the difference between these values of film and HT samples was approximately 4 % in both PI systems, while these values generally were among the lowest of all systems compared within this chapter. This could not only be due to both systems decomposing relatively early resulting in a higher fraction of decomposed material when 900 °C were reached, since some systems assessed later within this chapter exhibited lower thermal stability while simultaneously resulting in higher char yields than it was the case for the PMDA-BISA systems. A possible explanation could be found in the fact that the most vulnerable parts of these systems were located in the backbone of the PI structure (unlike PIs discussed later in section 5.3.5). As these regions seem to initiate decomposition of the polymer, a higher degree of fragmentation might be expected upon thermal degradation. This could also be the case for the previously discussed PEIs, which would explain their generally lower char yields compared to the fully aromatic PIs, but in the cases of PMDA-BISA systems the isopropyl moieties themselves made up for a larger fraction of total sample mass, resulting in even lower char yields.

Table 5.9: Thermal stability indicators for PMDA-pBISA and PMDA-mBISA PIs.

PI system	type	purge	$T_{d,400}$ [°C]	$T_{d,onset}$ [°C]	$T_{d,max}$ [°C]	CY [%]
PMDA-pBISA	film	N_2	**534**	532	554	40
		air	514	577	695	
	HT	N_2	**522**	523	546	36
		air	491	546	621	
PMDA-mBISA	film	N_2	**531**	528	551	43
		air	490	555	678	
	HT	N_2	**526**	527	550	39
		air	492	536	624	

Two additional comparisons were done assessing hydrothermally synthesized PIs only while mainly focusing on connectivities within the arene substitution patterns. For the first one, the dianhydride sODPA (4,4′-oxydiphthalic anhydride) was polymerized with either pPDA or mPDA, while aODPA (3,4′-oxydiphthalic anhydride) was polymerized with pPDA. The values for $T_{d,400}$ for sODPA-pPDA (577 °C) and sODPA-mPDA (575 °C) in nitrogen were virtually identical, whereas $T_{d,onset}$ and $T_{d,max}$ for sODPA-pPDA were significantly higher than for sODPA-mPDA, nevertheless indicating slightly increased

thermal stability of the former. However, both systems seemed to be quite similar in terms of stability, despite the meta connectivity introduced by mPDA within the sODPA-mPDA system having led to significantly decreased indicators of thermal stability before (cf. section 5.3.3), indicating that the ether bridge within the dianhydride fraction of these PIs probably represented the most dominant weak spot in thermal decomposition. Therefore, these two systems were quite comparable to PMDA-sODA and PMDA-aODA, both in terms of stability as well as marginal influence of arene substitution patterns. The aODPA-pPDA system on the other hand exhibited strongly decreased thermal resilience, for both $T_{d,400}$ (512 °C in nitrogen) and $T_{d,onset}$. As the polymer chain of aODPA-pPDA might exhibit a structure similarly bent as sODPA-mPDA would be, the reason for the lower stability of the former could not be found in the connectivity but rather within the monomer aODPA itself. When synthesizing PIs based on aODPA, the ortho substitution of anhydride moieties could lead to highly pronounced kinks in the polymer chain that decreased molecular interaction and chain packing,[245] which is why it is mostly used when aiming to yield soluble PIs.[246] In contrast to sODPA-mPDA, these kinks were located in closest proximity to the ether moieties of the dianhydride, which resulted in a great deal of steric hindrance for potential rotations around the associated O-C_{Ar} bond.[245,247] This reduction in degrees of freedom would result in this bond's decreased capacity to absorb thermal energy, which would ultimately lead to lower thermal stability by rendering this ether moiety an even more significant weak spot than the ether moiety in case of sODPA-based PIs was.

Table 5.10: Thermal stability indicators for hydrothermally synthesized sODPA-pPDA, aODPA-pPDA, and sODPA-mPDA PIs.

PI system	purge	$T_{d,400}$ [°C]	$T_{d,onset}$ [°C]	$T_{d,max}$ [°C]	CY [%]
sODPA-pPDA	N_2	**577**	576	672	47
	air	567	616	655	
aODPA-pPDA	N_2	**512**	505	608	53
	air	540	566	691	
sODPA-mPDA	N_2	**575**	560	597	51

The second additional comparison included four hydrothermally synthesized PEI systems composed of two different ODPA dianhydrides combined with two different ODA diamines each, namely sODPA-sODA, sODPA-aODA, aODPA-sODA and aODPA-aODA. Here, each PI's repeating unit included two ether bridges, each connecting two phenyl

moieties, which naturally were connected via imide groups. Symmetric monomers in this comparison (sODPA and sODA) would lead to rather linear PIs and asymmetric ones (aODPA and aODA) to rather bent structures, while it should be noted that aODA could in theory also lead to rather linear segments and that these ether bridges inherently connect two adjacent phenyl moieties in an angular fashion. Depending on the choice of monomers, the obtained PIs should have resulted in rather linear (sODPA-sODA), quite kinked (sODPA-aODA), more kinked (aODPA-sODA) and strongly kinked (aODPA-aODA) polymer structures. In relation to the previous comparison, sODPA-pPDA and sODPA-sODA are known to have quite similar decomposition behavior, while the latter tends to decompose at slightly lower temperatures,[248] which could also be observed in this study as sODPA-sODA exhibited $T_{d,400}$ of 570 °C in nitrogen atmosphere, as seen in figure 5.11. When combining this symmetric dianhydride with the asymmetric diamine aODPA to yield sODPA-aODA, $T_{d,400}$ decreased to 547 °C. This decrease in thermal stability was attributed to the higher fraction of kinks in the polymer backbone leading to an decrease in intermolecular interactions. However, this assumption could not be confirmed by the observations made when comparing both ODA diamines polymerized with PMDA at the beginning of this section (cf. figure 5.7). A combination of the asymmetric dianhydride aODPA with symmetric sODA to yield aODPA-sODA exhibited $T_{d,400}$ of 512 °C, which was significantly lower than for sODPA and tremendously lower than for sODPA-sODA. This was probably due to the fact that the kinks arising from the substitution pattern of aODPA could lead to a overall more strongly bent polymer structure, while certain rotational movements within the polymer chain were strongly suppressed as discussed in the previous comparison. Moreover, it has been found by other researchers that there is the possibility of cyclic oligomers forming upon polymerization of this monomer combination,[245] which could also play a role in these observations. When both monomers were asymmetric, as it was the case for aODPA-aODA, the material exhibited an even lower $T_{d,400}$ of 506 °C, probably due to even more kinks being possible in the polymer structure, although it should be noted that the difference to aODPA-sODA could not be considered significant. The results of this comparison seemed to show some kind of relationship between number and "severity" of kinks in the polymer structure and the resulting thermal stability of the material. However, no linearity within this behavior could be identified, as each monomer contributed individually to the overall thermal performance of the resulting material.

Table 5.11: Thermal stability indicators for PI systems from combinations of derivatives of ODPA dianhydrides and ODA diamines. All PIs were synthesized hydrothermally and analyzed in nitrogen atmosphere.

PI system	$T_{d,371}$ [°C]	$T_{d,onset}$ [°C]	$T_{d,max}$ [°C]	CY [%]
sODPA-sODA	570	559	605	56
sODPA-aODA	547	540	573	56
aODPA-sODA	512	510	586	53
aODPA-aODA	506	506	554	54

5.3.5 Side Groups

So far, this chapter studied the thermal decomposition behavior of several PIs which differed exclusively in composition of and connectivity within their polymer backbones. This section aimed for shedding light on what influence various side groups on the thermal resilience of a PI might have, since employing monomers containing such pendant moieties for PI synthesis is a well-established method for tuning these materials' properties such as solubility[2,249–251] or optical transparency.[1,252–256] For the first comparison within this study PMDA was polymerized with several derivatives of the diamine benzidine, resulting in fully linear rigid-rod PIs bearing side groups on the diamine segments. Compared to PMDA-Bz, which was discussed in section 5.3.2, a PI composed of PMDA polymerized with 2,2′-dimethylbenzidine (*m*-tolidine, mDMBz) to yield PMDA-mDMBz exhibited tremendously decreased $T_{d,400}$ of 535 °C for films and 516 °C for HT samples in nitrogen atmosphere, which differed from PMDA-Bz by approximately 80 °C for both sample types. The DTG curves of both sample types of PMDA-mDMBz (only in nitrogen atmosphere) revealed two detectable mass-loss events in a single measurement, while the second one could be located at a temperature region slightly above 600 °C, which was quite congruent with the single mass-loss event observed for PMDA-Bz measurements. This indicated that the first mass-loss event, which determined the thermal stability of this PI, was due to the methylene side groups decomposing first. However, as there was no plateau in the TGA curve between both mass-loss events and the second event started at approximately 20 % mass loss, it was clear that the decomposition process -presumably initiated at or in close proximity to the methylene groups- did not halt before the second event. Instead, it continued and exhibited an increase in velocity ($T_{d,max}$ was 622 °C and 612 °C, for films and HT samples, respectively) during the second mass-loss event, which might be cleavage of the imide rings in parts of the macromolecule in which these

did not already decompose. For measurements of HT samples in air a single continuous mass-loss event could be observed. Interestingly, this $T_{d,400}$ of 549 °C was significantly higher than for same sample type in nitrogen, but nevertheless represented a decrease in stability compared to PMDA-Bz.

Comparing previous PI system to its isomer PMDA-oDMBz, which contained 3,3′-dimethylbenzidine (*o*-tolidine, oDMBz) as diamine, a significant increase in $T_{d,400}$ (570 °C for films in nitrogen and 565 °C for HT samples) could be observed. One reason for the increased thermal stability of PMDA-oDMBz compared to PMDA-mDMBz could possibly be found in the ortho position of the methylene substituents, which could stabilize radicals arising from the homolytic cleavage of the imide ring proposed by Zurakowska-Orszagh et al.[242] and Laius et al.[217] and described in section 5.3.3. As the possible positions of the radical in the benzene ring adjacent to the cleaved imide bond are found at ortho and para positions, the positive inductive effect of the methylene moiety in ortho position could stabilize the radical electron at this location more efficiently than the same substituent would in meta position (as in PMDA-mDMBz). However, since the conjugated system also includes the other benzene ring of the biphenyl moiety (in para position to the cleaved imide moiety), the radical electron could here find mesomeric locations being meta-positioned to the other (non-cleaved) imide moiety, which would not be directly stabilized by the second methylene group within this symmetric monomer unit. Following this concept, both diamine isomers should even be rather equal in terms of radical stabilization, which could be considered partially supported the fact that the values of $T_{d,onset}$ for PMDA-oDMBz differed from those of PMDA-mDMBz to a much smaller extent than $T_{d,400}$. However, since also PMDA-oDMBz was significantly less thermally stable than PMDA-Bz, it could be assumed that the dominant decomposition mechanisms directly included the methylene substituents as weak points rather than stabilizing factors as there are indications of rather slowly proceeding radical demethylations to be found in literature.[242] Another reason for the increased thermal stability of PMDA-oDMBz compared to PMDA-mDMBz could be that both methylene substituents within the diamine fraction of the latter were facing each other, hindering rotation around the biphenyl linkage to some extent,[199] and thereby possibly lowering this rotational movement's capacity of compensating for increasing thermal energy. Moreover, as methylene substituents are known for their positive inductive effect, it could be considered that the amine moieties of oDMBz might have profited more from this increase in electron density as they would have in case of mDMBz, and therefore possessed an increased reactivity toward polymerization with anhydride moieties, which could ulti-

mately have led to an increased molecular mass and thereby increased thermal stability of PMDA-oDMBz polymers. Interestingly, only one mass-loss event was visible within the TGA curves of PMDA-oDMBz, which could mean that decomposition of methylene moieties in this case was more closely related to the other possible decomposition processes of the polymer. It should be noted that all attempts to synthesize films of this PMDA-oDMBz led to a rather inhomogeneous material, which contained a visibly large fraction of opaque regions indicating precipitation of solids during curing. Nevertheless, as their X-ray diffractograms revealed no sign of increased crystallinity and their thermograms showed homogeneous decomposition behavior, these films were treated as samples comparable to others.

When employing 3,3′-dimethoxbenzidine (*o*-dianisidine, oDIAN) as diamine to yield PMDA-oDIAN, $T_{d,400}$ was 502 °C for films and 497 °C for HT samples in nitrogen. This again represented a tremendous decrease in thermal stability compared to PMDA-Bz, which has been reported by other researchers.[257] It is known that in this PI system decomposition was initiated by homolytic cleavage of the H_3C-O bond which would result in methyl radicals and resonance-stabilized oxygen-containing radicals of the PI chain.[242] Consequently, this mechanism should lead to two consecutive mass-loss events of which the second one is related to cleavage of the imide moieties,[242] and which could indeed be observed in this study's DTG curves of PMDA-oDIAN. Similarly to the observations on PMDA-mDMBz, both decomposition steps most probably were directly intertwined, as there were no plateaus in the TGA curves between both mass-loss events to be observed. However, same authors reported this decomposition step to occur at significantly lower temperatures than it was observed here.
In this study, another rather prominent diamine, namely 2,2′-bis(trifluoromethyl)benzidine (mTFBz), was polymerized with PMDA to yield PMDA-mTFBz. It exhibited $T_{d,400}$ of 600 °C for films in nitrogen atmosphere, which was only slightly lower than for films of PMDA-Bz, and 589 °C for HT samples, which in fact was highly similar to those of PMDA-Bz. Comparing this system to its non-fluorinated analog PMDA-mDMBz, it was clear that the substitution of hydrogen atoms of the methylene groups by fluorine atoms very much compensated for the introduction of side groups to these fully linear polymers, since the increase in thermal stability from PMDA-mDMBz to PMDA-mTFBz was tremendous. Although there were minor traces of a preceding mass-loss event in case for HT samples, the thermograms of PMDA-mTFBz seemed to exhibit only one main decomposition step, which -in context of the low differences to PMDA-Bz- would in-

dicate that these side groups most likely did not pose a significant weak spot in terms of thermal stability. It should be considered that a greater inter-chain distance induced by the bulkiness of the trifluoromethyl moieties might also have played a role in the (insignificantly) lower thermal stability compared to PMDA-Bz, which in fact should be considered for all side-group bearing PIs of this study.

Unfortunately, due to its highly tedious low-yield synthetic procedure, merely minor amounts of the ortho derivative 3,3′-bis(trifluoromethyl)benzidine (oTFBz) were available, which excluded manufacturing of films of the PI system PMDA-oTFBz. HT samples of PMDA-oTFBz exhibited $T_{d,400}$ of 575 °C in nitrogen atmosphere, which represented a minor decrease in thermal stability compared to PMDA-mTFBz, whereas values for $T_{d,onset}$ were insignificantly increased. Moreover, measurements in air yielded significantly decreased $T_{d,400}$ but significantly increased $T_{d,onset}$ of PMDA-oTFBz compared to PMDA-mTFBz. Comparing both TFBz-based PIs, it seemed as they were quite similar in terms of thermal resilience. Possible stability-decreasing effects of hindered rotation around the biphenyl axis in case of PMDA-mTFBz or decreased reactivity of amine moieties caused by the negative inductive effects of the adjacent trifluoromethyl groups and therefore lower molecular mass in case of PMDA-oTFBz could have approximated both PIs' thermal behavior.

Another ortho-substituted benzidine derivative that was used within this study was 3,3′-dihydroxybenzidine (oDHBz) which was polymerized with PMDA to yield PMDA-oDHBz. HT samples of this PI system exhibited $T_{d,400}$ of 542 °C in nitrogen, which was located between those of PMDA-oDMBz and PMDA-oDIAN. It is known that aromatic polyimides containing hydroxy moieties in ortho position to the nitrogen substituents are able to form polybenzoxazoles upon heating to a temperature region of 350 - 500 °C.[258] Indeed, the mass-loss curves of this material allowed for distinguishing two separate mass-loss events in the upper part of this region. However, the observed decomposition behavior was similar to the other samples within this study, as the first step included a mass loss of more than 20 % and seamlessly merged with the second event. Moreover, since there are indications that the heating rate applied during all measurements of this study was too high for allowing for a sufficient conversion to polybenzoxazoles,[258] it was assumed that the mass losses observed for these samples were predominantly related to polymer decomposition and that the temperatures obtained as indicators of thermal stability could be considered valid.

Similarly to oTFBz, for 3,3′-difluorobenzidine (oDFBz) only minor amounts were available to synthesize one HT sample of PMDA-oDFBz. Since this sample decomposed at

relatively low temperatures, it was the only PI within this comparison for which $T_{d,371}$ was taken for assessment of thermal stability. This sample analyzed in nitrogen atmosphere exhibited $T_{d,371}$ of 395 °C, which represented the by far lowest thermal stability of all systems within this study. This was not expected, as fluorination of aromatic segments led to rather increased or similar stability before (cf. section 5.3.3). The thermogram exhibited three mass-loss events of which the first one was the most dominant and responsible for the stability indicators, whereas the second step was negligible and the third one was located above 600 °C, which could have been related to cleavage of the remaining imide bonds. Although these mass-loss steps were comparably easy to distinguish, they still were rather continuously connected over the course of the measurement, indicating that the decomposition process indeed started with the first mass loss event, which would lower the possibility of secondary reactions not directly related to thermal degradation. As the infrared spectrum of this sample showed highly prominent imide-vibration modes and did not exhibit amine-related modes, it was assumed to indeed be a fully converted PI, although its decomposition behavior could not be explained.

Table 5.12: Thermal stability indicators for several PIs based on PMDA polymerized with various benzidine derivatives.

PI system	type	purge	$T_{d,400}$ [°C]	$T_{d,onset}$ [°C]	$T_{d,max}$ [°C]	CY [%]
PMDA-Bz	film	N_2	**618**	615	654	61
	HT	N_2	**595**	615	650	48
		air	579	611	654	
PMDA-mDMBz	film	N_2	**535**	541	622	61
	HT	N_2	**516**	532	612	48
		air	549	582	626	
PMDA-oDMBz	film	N_2	**570**	553	592	65
		air	530	574	622	
	HT	N_2	**565**	555	595	56
PMDA-oDIAN	film	N_2	**502**	483	520	59
	HT	N_2	**497**	482	521	52
		air	459	534	621	
PMDA-mTFBz	film	N_2	**600**	602	642	49
	HT	N_2	**589**	596	639	35
		air	554	579	622	
PMDA-oTFBz	HT	N_2	**575**	603	640	50
		air	511	598	646	
PMDA-oDHBz	HT	N_2	**542**	530	572	52
		air	517	564	619	
PMDA-oDFBz*	HT	N_2	**395***	380	403	45

Most of the diamines employed for synthesizing the PIs presented in the previous comparison were also polymerized with the dianhydride sODPA in order to yield polymers of a more bent and flexible nature, which was assumed to reduce possible effects of decreased interchain interaction due to bulky moieties on the PIs' thermal behavior. The thermal stability indicators of the resulting PIs are presented in figure 5.13. This study's reference system was sODPA-Bz, which exhibited $T_{d,400}$ of 603 °C for films and 570 °C for HT samples in nitrogen atmosphere. Compared to PMDA-Bz, it showed a slight but clear decrease in thermal stability, most likely due to the ether bridge located in the dianhydride fraction representing a weak spot within the polymer backbone (cf. section 5.3.4). The decrease was more pronounced for HT samples, both in nitrogen and air, although there were no obvious differences in crystallinity between HT samples of PMDA-Bz and sODPA-Bz.

Similar to the first comparison within this section, the introduction of methylene groups into the polymer structure by employing mDMBz to yield sODPA-mDMBz decreased $T_{d,400}$ to 527 °C for films and to 469 °C for HT samples in nitrogen. Compared to sODPA-Bz, the differences in $T_{d,400}$ for films were quite close to the differences found when comparing PMDA-Bz and PMDA-mDMBz, whereas sODPA-mDMBz and PMDA-mDMBz surprisingly exhibited highly similar $T_{d,400}$ for measurements of both sample types in nitrogen. HT samples of sODPA-oDMBz exhibited $T_{d,400}$ of 534 °C, which was slightly increased compared to sODPA-mDMBz, although the increase was not as high as it was observed for their PMDA-based analogs.

The introduction of methoxy moieties in sODPA-oDIAN led to $T_{d,400}$ of 492 °C for films and 477 °C for HT samples in nitrogen atmosphere. Similarly to the observations made in the previous comparison, these methoxy groups seemed to significantly lower a PI's thermal stability, whereas the thermal-stability indicators for samples of sODPA-oDIAN are slightly lower than for their PMDA-based analogs.

The fluorinated PI system sODPA-mTFBz exhibited $T_{d,400}$ of 586 °C for films and 569 °C for HT samples in nitrogen. In analogy to the previous comparison, these values indicated a partial compensation of reduced thermal stability caused by the introduction of side groups enabled by strong C-F bonds within the side moieties. The discrepancies between sODPA-mTFBz and sODPA-Bz are similar to those between PMDA-mTFBz and PMDA-Bz, whereas the sODPA-based PIs possessed lower thermal stability.

In summary, the tendencies for thermal stability to change with different side groups attached to the aromatic PI backbone of these sODPA-based polymers were very similar to those observed for the analogous PMDA-based polymers presented earlier in this sec-

tion, as such side groups generally pose weak spots in terms of thermal resilience leading to reduced performance in any case. However, due to almost all indicators of thermal stability for these sODPA-based PIs (which contained ether bridges as additional weak spots) being consistently lower than for their PMDA-based analogs, it could be assumed that effects of weak spots might have stacked to result in an overall lower thermal stability.

Table 5.13: Thermal stability indicators for PIs based on sODPA polymerized with various benzidine derivatives.

PI system	type	purge	$T_{d,400}$ [°C]	$T_{d,onset}$ [°C]	$T_{d,max}$ [°C]	CY [%]
sODPA-Bz	film	N_2	**603**	593	631	61
	HT	N_2	**570**	573	625	51
		air	544	610	652	
sODPA-mDMBz	film	N_2	**527**	529	634	64
	HT	N_2	**516**	495	618	53
		air	486	553	614	
sODPA-oDMBz	HT	N_2	**534**	517	555	59
sODPA-oDIAN	film	N_2	**492**	478	502	57
	HT	N_2	**477**	462	497	51
sODPA-mTFBz	film	N_2	**586**	584	632	54
	HT	N_2	**569**	572	618	51
		air	572	588	632	

5.3.6 Various Monomer Combinations

The final section of this chapter presents and discusses thermal stability assessments for various PI systems obtained from several commercially available monomers, whose comparability to the other systems discussed before was somewhat limited, as they did not comply with the structure-property systematics of the previous sections. It aimed for providing a brief glance on a variety of structural feature which could be incorporated into PIs and their effect on the thermal stability of the resulting polymers. All these samples have been synthesized hydrothermally, due to this method's straightforwardness and facile parallelizability. Table 5.14 lists the thermal stability indicators obtained for PI systems based on various diamines polymerized with PMDA.

4,4′-diaminodiphenylmethane (MDA) ia a widely used diamine[221,259,260] which consists

of two phenylamine moieties connected via a methylene moiety. Although it was structurally quite similar to PMDA-sODA, the PI system PMDA-MDA exhibited significantly lower $T_{d,400}$ of 531 °C in nitrogen atmosphere, which in fact was very close to the values for BISA-based systems found in section 5.3.4. This led to the assumption that aliphatic connectivities would generally represent a weak spot in the PI backbone, whereas the differences between the effects of methylene and isopropyl moieties on the thermal stability of the polymer seemed to be negligible. However, in thermo-oxidative conditions this system performed better than the BISA-based systems, as $T_{d,400}$ for measurements in air was quite close to nitrogen-atmosphere measurements.

Likewise, a PI composed of PMDA and BAPP (2,2-Bis[4-(4-aminophenoxy)phenyl]propane) showed a similar $T_{d,400}$ of 527 °C in nitrogen, most likely due to the aliphatic isopropyl linkage between the two central phenyl moieties within this diamine. Since there were two additional ether bridges in a molecule of BAPP located between these central phenyl moieties and two terminal phenylamine moieties, the system PMDA-BAPP was expected to yield lower thermal stability indicators, since it was shown at the end of the previous section that effects of different weak spots could add up to result in lower thermal stability (cf. section 5.3.5). However, it turned out that in this case no stacking of weak-linkage effects could be observed, as PMDA-BAPP exhibited $T_{d,400}$ very close to the other systems containing only aliphatic linkages such as isopropyl (found in PMDA-pBISA and PMDA-mBISA) and methylene moieties (found in PMDA-MDA), meaning that the isopropyl moieties represented the most dominant weak spot for decomposition without any obvious influence of the ether bridges on thermal performance. This result would limit previously stated assumption of different weak spots stacking to result in an overall lower thermal performance (cf. section 5.3.5) to structures, in which these vulnerabilities are not exclusively found in the polymer backbone but distributed among both side groups and backbone linkages.

The structure of the diamine 2,7-diaminofluorene (DAF) was somewhat based on a benzidine framework, in which two aromatic carbon atoms in ortho position to the biphenyl linkage were additionally bridged by a methylene moiety. This second linkage resulted in a slightly bent but fully planar and highly stiff structure of this "tricyclic fused ring diamine",[261] but simultaneously represented a weak spot for thermal degradation. This reflected in a reduced $T_{d,400}$ for PMDA-DAF of 575 °C in nitrogen atmosphere compared to PMDA-Bz. Nevertheless, since these methylene linkages were not the sole connection between the phenyl moieties within the diamine fraction of the PI, PMDA-DAF significantly outperformed the other PI systems bearing aliphatic linkages mentioned before.

The biphenyl linkage might still have played an important role in stabilizing the PI structure during thermal decomposition. Moreover, measurements in air gave values close to those in nitrogen, which could indicate that the bridging methylene moieties found in PMDA-MDA and PMDA-DAF might be more resilient to thermo-oxidative conditions than isopropyl moieties.

The only diamine employed for PI synthesis not being commercially available during the course of this work was 3,6-diaminodibenzofuran (DADF). A decades-old container containing large, partially degraded amounts of this diamine was obtained from a storage facility of *Technische Universität Wien*. This monomer was purified by sublimation twice before use, yielding white crystals of high purity. Structurally, DADF based on a planar framework similar to DAF containing an ether bridge instead of the methylene linkage, although the amine moieties were located in different positions, which limited the comparability of both diamines to some extent. The PI system PMDA-DADF exhibited $T_{d,400}$ of 615 °C in nitrogen with a virtually identical value for measurements in air, therefore outperforming PMDA-DAF significantly and ranking among this chapter's best-performing PI systems. This increase in thermal stability compared to PMDA-DAF was most probably due to the ether linkage being more resilient to both thermal and thermo-oxidative degradation than the methylene bridge, although the amine positions must have led to a highly kinked polymer structure, which in other cases led to lower thermal performance (cf. section 5.3.3). However, as PMDA-DADF must have had a highly stiff and kinked structure, it could be considered most comparable to PMDA-mPDA, which also exhibited extraordinarily high thermal stability. It should be noted that this system represented the best-performing hydrothermally synthesized PI for TGA measurements conducted in air.

The diamine 9,9-Bis(4-aminophenyl)fluorene (BAPF) represented another widely known monomer, which is classically employed when aiming to synthesize PIs soluble in various organic solvents.[262,263] This characteristic is mostly due to this diamine's bulkiness severely decreasing interchain interaction, which was most probably one of the main reasons for the comparably low thermal stability of this study's HT samples of PMDA-BAPF. Another key feature defining this system's thermal behavior most probably was its central sp^3-hybridized carbon atom bridging four phenyl moieties and bearing weak linkages for thermal decomposition, which led to $T_{d,400}$ of 493 °C in nitrogen atmosphere. Interestingly, it exhibited higher $T_{d,400}$ of 546 °C when analyzed in air. Employing 9,9-Bis(4-amino-3-methylphenyl)fluorene (MeBAPF) as a diamine in PMDA-MeBAPF led to a further decrease in $T_{d,400}$ to 434 °C, as this derivative of BAPF contained methylene

side groups adjacent to its amine moieties, which most probably introduced additional weak points for thermal decomposition. Similarly to PMDA-BAPF, this system's $T_{d,400}$ was significantly increased (492 °C) when analyzed in air.

The last diamine to be assessed regarding its influence on thermal stability when polymerized with PMDA was 4,4′-diaminobenzophenone (DABP). Its structure was quite similar to MDA whereas the central carbon atom did not exist as an methylene moiety but within an carbonyl group rendering this molecule a diaminoketone, which could also be utilized when aiming for cross-linking effects upon thermal curing in oxygen-containing atmosphere.[259] The hydrothermally synthesized PI system PMDA-DABP exhibited $T_{d,400}$ of 575 °C in nitrogen and a similar value for measurements in air. Therefore, its thermal performance ranked among other, more flexible PIs containing ether bridges such as the PMDA-ODA, PMDA-BAPB or sODPA-PDA systems, which indicated that the carbonyl linkages were similarly prone to initiate thermal decomposition as ether moieties in the polymer backbone were.

Table 5.14: Thermal stability indicators for hydrothermally synthesized PI systems based on PMDA polymerized with various diamines.

PI system	purge	$T_{d,400}$ [°C]	$T_{d,onset}$ [°C]	$T_{d,max}$ [°C]	CY [%]
PMDA-MDA	N_2	**531**	543	593	46
	air	519	591	633	
PMDA-BAPP	N_2	**527**	522	566	37
	air	487	550	614	
PMDA-DAF	N_2	**575**	585	633	53
	air	568	598	641	
PMDA-DADF	N_2	**615**	619	662	55
	air	616	629	660	
PMDA-BAPF	N_2	**493**	479	589	58
	air	546	576	620	
PMDA-MeBAPF	N_2	**434**	415	521	52
	air	492	532	617	
PMDA-DABP	N_2	**574**	576	632	43
	air	578	609	665	

Furthermore, such a benzophenone-based structure could also be found for the dianhydride counterpart, namely in 3,3′,4,4′-benzophenonetetracarboxylic dianhydride (BTDA), which is arguably the most commonly used[52,54,55] one of all dianhydrides presented in table 5.15, which lists the thermal stability indicators obtained for PI systems based on various dianhydrides polymerized hydrothermally with different diamines. The PI system BTDA-pPDA exhibited $T_{d,400}$ of 606 °C in nitrogen atmosphere and therefore slightly outperformed previous analog system PMDA-DABP. As both systems could be considered structurally quite similar, the differences in thermal stability could only be explained by a possibly more linear polymer-chain structure in case of BTDA-pPDA or by differences in monomer reactivity. As the carbonyl moiety is able to withdraw electron density from it's neighboring phenyl moieties via negative inductive and mesomeric effects, the reactivity of the amine groups within DABP might have been somewhat lowered, whereas in case of BTDA the effect might be the opposite. This might have led to a lower molecular weight (or particle size) in case of PMDA-DABP and a higher molecular weight (or increased particle size) in case of BTDA-pPDA. However, combining both benzophenone-based monomers to yield BTDA-DABP the drop in thermal stability was tremendous. This system exhibited $T_{d,371}$ of 421 °C in nitrogen and had $T_{d,onset}$ as low as 383 °C. As insufficient polymerization could be excluded by the absence of amine-related vibrational modes in this material's IR spectrum, the extraordinarily low thermal resilience of this system could not be explained.

9,9-Bis(3,4-dicarboxyphenyl)fluorene dianhydride (BPAF) could be considered the dianhydride counterpart to the diamine BAPF discussed in the previous comparison (cf. Table 5.14. BPAF-pPDA exhibited $T_{d,400}$ of 580 °C in nitrogen, which was an tremendous increase in thermal stability compared to its analog PMDA-BAPF. Despite this increase seeming to high for such an explanation, it was assumed that the superior thermal resilience of BPAF-pPDA could have been due to its more linear structure compared to PMDA-BAPF. However, combining both diphenylfluorene monomers to yield BPAF-BAPF (which could be considered structurally even more bulky) led to $T_{d,400}$ of 574 °C in nitrogen, which was highly similar to BPAF-pPDA and still immensely higher than $T_{d,400}$ for PMDA-BAPF. Since all three PIs containing one or both diphenylfluorene monomers were equally amorphous and therefore differences in crystallinity as criterion for thermal resilience could be excluded, no explanation for the differences in thermal stability between the BAPF-based and BPAF-based PIs could be found.

As one of the few commercially available fluorinated dianhydrides, 4,4′-(hexafluoroisopropylidene)diphthalic anhydride (6FDA) has extensively been used by numerous re-

searchers, mostly to obtain soluble or optically transparent PIs.[196,197,264] Hydrothermally synthesized samples of 6FDA-pPDA were neither transparent nor soluble but exhibited $T_{d,400}$ of 538 °C in nitrogen. Interestingly, each indicator of thermal stability was the same for measurements with both purge gases. This could mean that this system was -unlike most other PIs discussed within this chapter- not overly susceptible to decomposition in thermo-oxidative conditions, which might give a hint on which PIs to use for applications in oxygen-rich atmosphere. However, due to the anhydride fraction's aliphatic linkage this system's overall thermal stability ranked among those of other systems containing aliphatic moieties, which generally were disadvantaged over fully aromatic and linear PIs or even those which bore ether bridges within their backbones, despite 6FDA's fluorine substituents suggesting otherwise.

Being the main dianhydride constituent in several commercially successful PI products,[2] 4,4′-(4,4′-isopropylidenediphenoxy)diphthalic anhydride (BPADA) could be employed when aiming to obtain melt-processable PIs.[265] It could be considered as the dianhydride equivalent to the diamine BAPP, bearing a central isopropyl linkage and two ether bridges connecting four phenyl moieties. Accordingly, BPADA-pPDA exhibited $T_{d,400}$ of 524 °C in nitrogen atmosphere being highly similar to PMDA-BAPP, which was most probably due to the aliphatic linkage dominating this system's thermal stability. This again showed that -when manufacturing or producing PI products- advantages in terms of e.g. facilitated processing might easily come at the cost of decreased thermal stability.

The last monomer to be discussed within this chapter was 3,3′,4,4′-diphenylsulfone tetracarboxylic dianhydride (DSDA), which could be considered fundamentally different from all other monomers discussed here due to its sulfone moiety acting as linkage between both phthalic anhydride groups. Dianhydrides but also diamines bearing such sulfone moieties generally are employed in PI synthesis when aiming for melt-processable products.[266] As the sulfone moieties are strongly withdrawing electron density, hydrothermal synthesis of PIs with sulfone-containing diamines within this thesis were of rather low success, while opposite was true for the sulfone-containing dianhydride DSDA. The PI system DSDA-pPDA $T_{d,400}$ of 535 °C in nitrogen, while this value was increased for measurements in air. Therefore, it could be assumed that sulfone moieties as linkages in the backbones of PIs would probably lead to a decrease in thermal stability comparable to PIs containing aliphatic linkages.

Table 5.15: Thermal stability indicators for hydrothermally synthesized PI systems based on various dianhydrides polymerized with various diamines.

PI system	purge	$T_{d,400}$ [°C]	$T_{d,onset}$ [°C]	$T_{d,max}$ [°C]	CY [%]
BTDA-pPDA	N_2	**606**	602	634	49
	air	583	613	662	
BTDA-DABP*	N_2	**421***	383	584	47
BPAF-pPDA	N_2	**580**	569	616	63
	air	545	588	624	
BPAF-BAPF	N_2	**574**	551	599	66
6FDA-pPDA	N_2	**538**	532	573	49
	air	537	542	572	
BPADA-pPDA	N_2	**524**	520	544	48
	air	531	592	695	
DSDA-pPDA	N_2	**535**	526	566	45
	air	567	596	641	

5.4 Conclusions

The effects of several structural features on the thermal stability of numerous PI systems have been identified and discussed within this chapter utilizing different approaches of processing data obtained from several hundred uniformly conducted thermogravimetric measurements. Fully aromatic, rather linear PIs which comprise phenyl moieties connected solely by imide groups and biphenyl linkages represented the systems being most resilient to thermal and thermo-oxidative degradation. Side groups attached to aromatic segments led to lower thermal stability in all cases, while the position and nature of these substituents clearly played a role in the extent of this decrease. The introduction of meta linkages via implementation of mPDA within the diamine fraction into such linear PIs led to more bent polymeric structures and lower thermal stability, most likely due to decreased interchain interactions arising from increased free volume and decreased mesomeric stabilization of radical decomposition products. However, meta connectivities did not seem to have any effect on thermal stability when aromatic regions were interconnected by ether bridges or aliphatic linkages. On one hand this might have been due to the impact of altered polymer-chain geometry being obfuscated by effects inherent to such linking moieties, as ether bridges significantly lowered thermal stability while

aliphatic ones led to drastic decreases. On the other hand, another possible reason for that might also be found in that the differences between arene substitution patterns did not result in different degrees of mesomeric radical stabilization, since the conjugated systems were interrupted by these linkages. Fluorination of aromatic segments within the polymer backbone seemed to have a stability-improving impact, at least if these segments were perfluorinated. Fluorination of aliphatic side groups or linking moieties seemed to improve stability compared to their non-fluorinated analogs, although this could not compensate for the reduced stability caused by these side groups or linkages themselves. In most cases, film samples were more stable than their hydrothermally synthesized counterparts, especially in thermo-oxidative conditions. Reasons for that could be found e.g. in the drastically increased surface area of HT samples or retarded mass loss detection due to enclosure of gaseous decomposition products in film samples.

However, clarification is required on how parameters of manufacture for HT particles might influence their thermal performance, but also on how system-intrinsic factors such as solubility of monomers or oligomers might influence a product's particle size, since they could therefore have an impact on thermal stability. Moreover, since crystallinity of hydrothermally synthesized particles might also have played a role in stability, more systematic investigations should be undertaken, in order to relate degrees of crystallinity to thermal stability of such polymers.

What also remained unclear is if stability-lowering effects of seemingly independent molecular features such as different linkages or substituents could stack to yield even lower stability, since in some cases they did stack (cf. section 5.3.5) and in some they did not (cf. section 5.3.6). Another intriguing question to be answered would be if it was possible to generally increase the thermal stability of PIs by incorporating structural elements such as fused benzene rings in polycyclic segments or if their stability was indeed limited by decomposition mechanisms concerning the imide moieties themselves. The reader is referred to research works of Sazanov et. al for procedural methods for increasing thermal stability of PIs such as ensuring full imidization,[215] the use of *ortho*-phophoric acid,[113] or avoiding excess diamine content.[113,215]

Anyhow, for more thorough investigations on which and how structural features of particular monomers are responsible for initiating thermal decomposition, it would probably be necessary to know more about the mechanisms of thermal and thermo-oxidative decomposition of PIs, which seem to be quite complex and remain largely unknown. Although many monomers have been employed for synthesizing PI samples in this work, this chapter's collection of decomposition data is far from being complete given the vast

amount of compounds available for PI synthesis. However, the author hoped to have given a useful overview nevertheless.

6. Closing Remarks

Within this thesis polyimides were obtained taking two fundamentally different synthetic approaches which yield just as differing polymeric products: The so-called classical synthesis of PIs is a two-step route requiring highly purified monomers, which are to be combined in rather harmful, high-boiling solvents to form processable prepolymer solutions before curing them to obtain the desired PI material by exposing them to high temperatures in ideally inert atmospheres and constantly anhydrous conditions. If performed correctly, the product of a classical PI synthesis is a dense, mostly amorphous, and continuous polymer film. In contrast, hydrothermal synthesis of PIs can be performed by simply combining monomers in water and heating the mixture in closed vessels, utilizing the strongly altered physical and chemical properties of liquid water above it's standard boiling point under autogenously formed pressure. In many cases, this approach leads to highly crystalline PI microparticles, in virtually all cases it results in PI microparticles exhibiting significantly higher levels of crystallinity than their classically synthesized counterparts.

Focusing on both the moisture sorption behavior of PI films and the thermal stability of PI films and hydrothermally synthesized microparticles, this work compared several structurally different PI systems obtained by polymerizing numerous commercially available monomers. This allowed extensive insight into the structure-property relationships underlying these polymer systems with respect to these characteristics. Taking up on the concept of the two-dimensional plots presented in section 4.4, which map several PI systems in terms of their moisture diffusivity and moisture uptake, such a plot can be extended to include a thermal-stability indicator, which allows these polymers to be compared and even ranked in terms of three highly relevant properties (cf. figure 6.1).

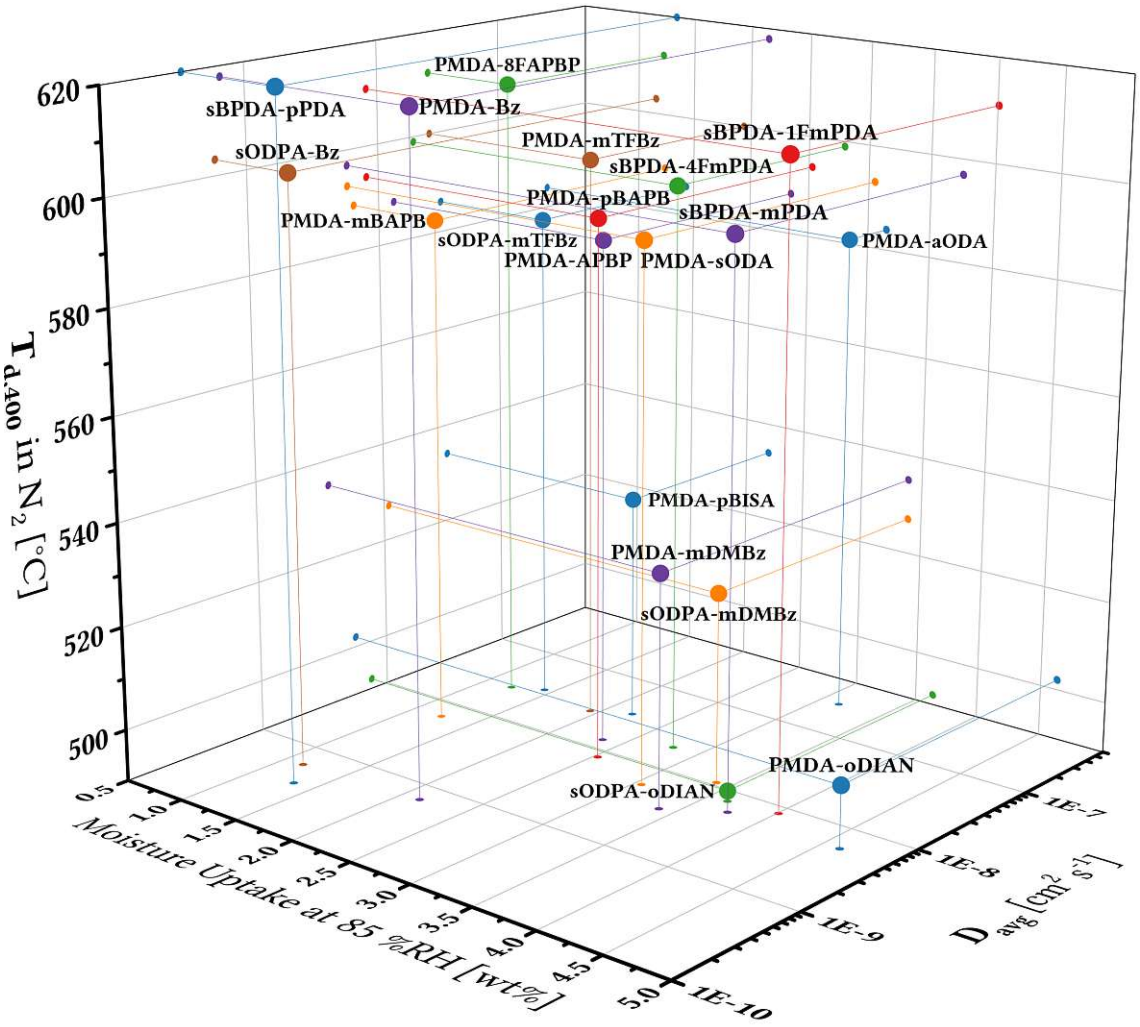

Figure 6.1: Three-dimensional map depicting various comparable PI systems in terms of diffusivity and moisture uptake as done in figure 4.25, extended by a thermal stability indicator.

However, there are many more properties that have to be considered when designing PIs from the plethora of monomers commercially available, depending on which criteria the desired product has to fulfill as there are many other properties a possible PI formulation's suitability depends on. Among these are the thermal expansion characteristics, electrical breakdown strength, sorption behavior towards gases and fluids (which are not water as analyzed here), solubility, softening behavior and mechanical properties, adhesion to certain substrates, to name a few, but also seemingly obvious characteristics such as a PI's color might be highly relevant for some applications. Thus, depending on the characteristics most important for the desired applications, it is conceivable that multidimensional models following the same concept would be suitable for identifying candidate PI systems, if the data situation is sufficiently comprehensive.

References

[1] Hergenrother, P. M. The use, design, synthesis, and properties of high performance/high temperature polymers: An overview. *High Performance Polymers* **2003**, *15*, 3–45.

[2] Bryant, R. G. *Ullmann's Encyclopedia of Industrial Chemistry*, 7th ed.; Wiley-VCH Verlag GmbH: Weinheim, Germany, 2014; pp 1–27.

[3] Irwin, R. S.; Sweeny, W. Polyimide fibers. *Journal of Polymer Science Part C: Polymer Symposia* **1967**, *19*, 41–48.

[4] Wright, W. W.; Hallden-Abberton, M. *Ullmann's Encyclopedia of Industrial Chemistry*, 6th ed.; John Wiley & Sons, Ltd: Weinheim, Germany, 2000.

[5] Yonetoku, D.; Murakami, T.; Gunji, S.; Mihara, T.; Sakashita, T.; Morihara, Y.; Kikuchi, Y.; Takahashi, T.; Fujimoto, H.; Toukairin, N.; Kodama, Y.; Kubo, S. Gamma-Ray Burst Polarimeter (GAP) aboard the Small Solar Power Sail Demonstrator IKAROS. *Publications of the Astronomical Society of Japan* **2011**, *63*, 625–638.

[6] Plis, E. A.; Engelhart, D. P.; Cooper, R.; Johnston, W. R.; Ferguson, D.; Hoffmann, R. Review of Radiation-Induced Effects in Polyimide. *Applied Sciences* **2019**, *9*, 1999.

[7] Pavlenko, V. I.; Cherkashina, N. I.; Yastrebinsky, R. N. Synthesis and radiation shielding properties of polyimide/Bi2O3 composites. *Heliyon* **2019**, *5*, e01703.

[8] Sanaeepur, H.; Ebadi Amooghin, A.; Bandehali, S.; Moghadassi, A.; Matsuura, T.; Van der Bruggen, B. Polyimides in membrane gas separation: Monomer's molecular design and structural engineering. *Progress in Polymer Science* **2019**, *91*, 80–125.

[9] Vanherck, K.; Koeckelberghs, G.; Vankelecom, I. F. Crosslinking polyimides for membrane applications: A review. *Progress in Polymer Science* **2013**, *38*, 874–896.

[10] Zhang, H.; Shen, P. K. Recent development of polymer electrolyte membranes for fuel cells. *Chemical Reviews* **2012**, *112*, 2780–2832.

[11] van Aerle, N. A.; Tol, A. J. Molecular Orientation in Rubbed Polyimide Alignment Layers Used for Liquid-Crystal Displays. *Macromolecules* **1994**, *27*, 6520–6526.

[12] Sasaki, A.; Aoshima, H.; Nagano, S.; Seki, T. A versatile photochemical procedure to introduce a photoreactive molecular layer onto a polyimide film for liquid crystal alignment. *Polymer Journal 2012 44:6* **2012**, *44*, 639–645.

[13] Li, B.; He, T.; Li, Y.; Ding, M. Polyimide thin films as compensators for liquid crystal displays. *Polymers for Advanced Technologies* **1997**, *8*, 513–516.

[14] Denton, D. D.; Day, D. R.; Priore, D. F.; Senturia, S. D.; Anolick, E. S.; Scheider, D. Moisture diffusion in polyimide films in integrated circuits. *Journal of Electronic Materials* **1985**, *14*, 119–136.

[15] Czarczyńska, H.; Dziedzic, A.; Licznerski, B. W.; Łukaszewicz, M.; Seweryn, A. Fabrication and electrical properties of carbon/ polyesterimide thick resistive films. *Microelectronics Journal* **1993**, *24*, 689–696.

[16] Muruganand, S.; Narayandass, S. K.; Mangalaraj, D.; Vijayan, T. M. Dielectric and conduction properties of pure polyimide films. *Polymer International* **2001**, *50*, 1089–1094.

[17] Raju, G.; Katebian, A.; Jafri, S. Z. Breakdown voltages of polymers in the temperature range 23°-250°C. *IEEE Transactions on Dielectrics and Electrical Insulation* **2003**, *10*, 117–127.

[18] Simpson, J.; St.Clair, A. Fundamental insight on developing low dielectric constant polyimides. *Thin Solid Films* **1997**, *308-309*, 480–485.

[19] Hougham, G.; Tesoro, G.; Viehbeck, A.; Chapple-Sokot, J. D. Polarization Effects of Fluorine on the Relative Permittivity in Polyimides. *Macromolecules* **1994**, *27*, 5964–5971.

[20] Ma, R.; Baldwin, A. F.; Wang, C.; Offenbach, I.; Cakmak, M.; Ramprasad, R.; Sotzing, G. A. Rationally designed polyimides for high-energy density capacitor applications. *ACS Applied Materials and Interfaces* **2014**, *6*, 10445–10451.

[21] Liu, X. J.; Zheng, M. S.; Chen, G.; Dang, Z. M.; Zha, J. W. High-temperature polyimide dielectric materials for energy storage: theory, design, preparation and properties. *Energy & Environmental Science* **2022**, *15*, 56–81.

[22] Zheng, W.; Li, Z.; Chen, K.; Liu, S.; Chi, Z.; Xu, J.; Zhang, Y. Temperature-Resistant Intrinsic High Dielectric Constant Polyimides: More Flexibility of the Dipoles, Larger Permittivity of the Materials. *Molecules 2022, Vol. 27, Page 6337* **2022**, *27*, 6337.

[23] Tong, H.; Ahmad, A.; Fu, J.; Xu, H.; Fan, T.; Hou, Y.; Xu, J. Revealing the correlation between molecular structure and dielectric properties of carbonyl-containing polyimide dielectrics. *Journal of Applied Polymer Science* **2019**, *136*, 47883.

[24] Mercer, F. W.; Goodman, T. D. Effect of Structural Features and Humidity on the Dielectric Constant of Polyimides:. *High Performance Polymers.* **1991**, *3*, 297–310.

[25] Herr, D. E.; Nikolic, N. A.; Schultz, R. A. Chemistries for high reliability in electronics assemblies. *High Performance Polymers* **2001**, *13*, 79–100.

[26] Tesoro, G. C.; Rajendran, G. P.; Park, C.; Uhlmann, D. R. Imide Silanes: Adhesion promoters for polyimides. *Journal of Adhesion Science and Technology* **1987**, *1*, 39–51.

[27] Numata, S.; Oohara, S.; Fujisaki, K.; Imaizumi, J.; Kinjo, N. Thermal expansion behavior of various aromatic polyimides. *Journal of Applied Polymer Science* **1986**, *31*, 101–110.

[28] Numata, S.; Fujisaki, K.; Kinjo, N. Re-examination of the relationship between packing coefficient and thermal expansion coefficient for aromatic polyimides. *Polymer* **1987**, *28*, 2282–2288.

[29] Numata, S.; Kinjo, N.; Makino, D. Chemical structures and properties of low thermal expansion coefficient polyimides. *Polymer Engineering and Science* **1988**, *28*, 906–911.

[30] Hasegawa, M.; Matano, T.; Shindo, Y.; Sugimura, T. Spontaneous molecular orientation of polyimides induced by thermal imidization. 2. In-plane orientation. *Macromolecules* **1996**, *29*, 7897–7909.

[31] Buchwalter, L. P. Adhesion of polyimides to metal and ceramic surfaces: an overview. *Journal of Adhesion Science and Technology* **1989**, *4*, 697–721.

[32] Miwa, T.; Tawata, R.; Numata, S. Relationship between structure and adhesion properties of aromatic polyimides. *Polymer* **1993**, *34*, 621–624.

[33] Hergenrother, P. M. In *Polyimides*, 1st ed.; Wilson, D., Stenzenberger, H. D., Hergenrother, P. M., Eds.; Springer, Dordrecht, 1990; pp 158–186.

[34] Sroog, C. E. In *Polyimides*; Wilson, D., Stenzenberger, H. D., Hergenrother, P. M., Eds.; Pergamon, 1991; Vol. 16; pp 561–694.

[35] Bernier, G. A.; Kline, D. E. Dynamic mechanical behavior of a polyimide. *Journal of Applied Polymer Science* **1968**, *12*, 593–604.

[36] Nakamae, K.; Nishino, T.; Miki, N. Elastic modulus of the crystalline regions of thermoplastic polyimide. *High Performance Polymers* **1995**, *7*, 371–376.

[37] Joule, J. A.; Mills, K. *Heterocyclic Chemistry at a Glance: Second Edition*; John Wiley and Sons, 2012.

[38] Mehdipour-Ataei, S.; Tabatabaei-Yazdi, Z. *Encyclopedia of Polymer Science and Technology*; John Wiley & Sons, Ltd, 2015; pp 1–31.

[39] Bogert, M. T.; Renshaw, R. R. 4-Amino-o-Phtalic Acid And Some of its Derivatives. *Journal of the American Chemical Society* **1908**, *30*, 1135–1141.

[40] Elias, H.-G. In *Macromolecules*, 1st ed.; Elias, H.-G., Ed.; Wiley-VCH Verlag GmbH, 2005; Vol. 1; pp 431–509.

[41] Edwards, W. M. Polyimides of pyromellitic acid. 1955.

[42] Sroog, C. E. In *History of the Invention and Development of the Polyimides*, 1st ed.; Ghosh, M. K., Mittal, K. L., Eds.; CRC Press, 1996; pp 1–6.

[43] Edwards, W. M. Polyamide-acids, compositions thereof, and process for their preparation. 1965.

[44] Edwards, W. M. Aromatic polyimides and the process for preparing them. 1965.

[45] Breunig, M.; Dorner, M.; Senker, J. Ultramicroporous polyimides with hierarchical morphology for carbon dioxide separation. *Journal of Materials Chemistry A* **2021**, *9*, 12797–12806.

[46] Ioan, S.; Hulubei, C.; Popovici, D.; Musteata, V. E. Origin of dielectric response and conductivity of some alicyclic polyimides. *Polymer Engineering & Science* **2012**, *53*, 1430–1447.

[47] Baumgartner, B.; Bojdys, M. J.; Unterlass, M. M. Geomimetics for green polymer synthesis: Highly ordered polyimides via hydrothermal techniques. *Polymer Chemistry* **2014**, *5*, 3771–3776.

[48] Ishige, R.; Masuda, T.; Kozaki, Y.; Fujiwara, E.; Okada, T.; Ando, S. Precise Analysis of Thermal Volume Expansion of Crystal Lattice for Fully Aromatic Crystalline Polyimides by X-ray Diffraction Method: Relationship between Molecular Structure and Linear/Volumetric Thermal Expansion. *Macromolecules* **2017**, *50*, 2112–2123.

[49] Stenzenberger, H. Recent advances in thermosetting polyimides. *British Polymer Journal* **1988**, *20*, 383–396.

[50] Stenzenberger, H. Chemistry and properties of addition polyimides. *Polyimides* **1990**, 79–128.

[51] Stenzenberger, H. D. Addition polyimides. *Advances in Polymer Science* **1994**, *117*, 165–220.

[52] McKerrow, A. J.; Fox, M. A.; Leu, J.; Ho, P. S. Preparation and characterization of polyimide alternating copolymers incorporating N,N-bis-(4-anilino)-1,2,4,5-benzene bis(dicarboximide). *Journal of Polymer Science Part A: Polymer Chemistry* **1997**, *35*, 319–327.

[53] Volksen, W. Condensation polyimides: Synthesis, solution behavior, and imidization characteristics. *Advances in Polymer Science* **1994**, *117*, 111–164.

[54] Harris, F. W. In *Polyimides*; Wilson, D., Stenzenberger, H. D., Hergenrother, P. M., Eds.; Springer, Dordrecht, 1990; pp 1–37.

[55] Liaw, D. J.; Wang, K. L.; Huang, Y. C.; Lee, K. R.; Lai, J. Y.; Ha, C. S. Advanced polyimide materials: Syntheses, physical properties and applications. *Progress in Polymer Science* **2012**, *37*, 907–974.

[56] Bower, G. M.; Frost, L. W. Aromatic polyimides. *Journal of Polymer Science Part A: General Papers* **1963**, *1*, 3135–3150.

[57] Heberer, D. P.; Cheng, S. Z.; Barley, J. S.; Lien, S. H.; Bryant, R. G.; Harris, F. W. Crystallization and Morphology of Semicrystalline Polyimides. *Macromolecules* **1991**, *24*, 1890–1898.

[58] Chang, J. H.; Park, K. M. Thermal cyclization of the poly(amic acid): thermal, mechanical, and morphological properties. *European Polymer Journal* **2000**, *36*, 2185–2191.

[59] Chen, K.; Wang, T.; King, J.; Hung, A. Effect of imidization temperature on properties of polymide films. *Journal of Applied Polymer Science* **1993**, *48*, 291–297.

[60] Carothers, W. H. Polymers and polyfunctionality. *Transactions of the Faraday Society* **1936**, *32*, 39–49.

[61] Flory, P. J. *Principles of Polymer Chemistry*; Cornell Univ. Press: Ithaca, New York, 1953; Chapter VIII, pp 318–334.

[62] Unterlass, M. M.; Kopetzki, D.; Antonietti, M.; Weber, J. Mechanistic study of hydrothermal synthesis of aromatic polyimides. *Polymer Chemistry* **2011**, *2*, 1744–1753.

[63] Dao, B.; Hodgkin, J.; Morton, T. C. Important Factors Controlling Synthesis of Imides in Water:. *High Performance Polymers* **1999**, *11*, 205–218.

[64] Unterlass, M. Geomimetics and Extreme Biomimetics Inspired by Hydrothermal Systems—What Can We Learn from Nature for Materials Synthesis? *Biomimetics* **2017**, *2*, 8.

[65] Gron, L. U.; LaCroix, J. E.; Higgins, C. J.; Steelman, K. L.; Tinsley, A. S. Heck reactions in hydrothermal, sub-critical water: water density as an important reaction variable. *Tetrahedron Letters* **2001**, *42*, 8555–8557.

[66] Unterlass, M. M. Creating geomimetic polymers. 2015.

[67] Baumgartner, B.; Svirkova, A.; Bintinger, J.; Hametner, C.; Marchetti-Deschmann, M.; Unterlass, M. M. Green and highly efficient synthesis of perylene and naphthalene bisimides in nothing but water. *Chemical Communications* **2017**, *53*, 1229–1232.

[68] Matubayasi, N.; Wakai, C.; Nakahara, M. Structural study of supercritical water. I. Nuclear magnetic resonance spectroscopy. *The Journal of Chemical Physics* **1997**, *107*, 9133.

[69] Mizan, T. I.; Savage, P. E.; Ziff, R. M. Temperature Dependence of Hydrogen Bonding in Supercritical Water. *Journal of Physical Chemistry* **1996**, *100*, 403–408.

[70] Savage, P. E.; Rebacz, N. A. *Handbook of Green Chemistry*; John Wiley & Sons, Ltd, 2010; pp 331–361.

[71] Marshall, W. L.; Franck, E. U. Ion product of water substance, 0–1000 °C, 1–10,000 bars. New International Formulation and its background. *Journal of Physical and Chemical Reference Data* **1981**, *10*, 295.

[72] Sato, H.; Hirata, F. Theoretical Study for Autoionization of Liquid Water - Temperature Dependence of the Ionic Product (pKw). *Journal of Physical Chemistry A* **1998**, *102*, 2603–2608.

[73] Siskin, M.; Katritzky, A. R. Reactivity of organic compounds in superheated water: General background. *Chemical Reviews* **2001**, *101*, 825–835.

[74] Wagner, W.; Kretzschmar, H.-J. *International Steam Tables*, 2nd ed.; Springer Berlin Heidelberg, 2008; Vol. 1.

[75] Sengers, J. V.; Watson, J. T. R. Improved International Formulations for the Viscosity and Thermal Conductivity of Water Substance. *Journal of Physical and Chemical Reference Data* **1986**, *15*, 1291.

[76] ASME Research and Technology Committee on Water and Steam in Thermal Systems,; Subcommittee on Properties of Steam, *ASME Steam Tables, Compact Edition*; ASME, 2007.

[77] Uematsu, M.; Franck, E. U. Static Dielectric Constant of Water and Steam. *Journal of Physical and Chemical Reference Data* **1995**, *9*, 1291.

[78] Chandler, K.; Eason, B.; Liotta, C. L.; Eckert, C. A. Phase Equilibria for Binary Aqueous Systems from a Near-Critical Water Reaction Apparatus. *Industrial and Engineering Chemistry Research* **1998**, *37*, 3515–3518.

[79] Anderson, F. E.; Prausnitz, J. M. Mutual solubilities and vapor pressures for binary and ternary aqueous systems containing benzene, toluene, m-xylene, thiophene and pyridine in the region 100–200°C. *Fluid Phase Equilibria* **1986**, *32*, 63–76.

[80] Byrappa, K.; Yoshimura, M. Handbook of Hydrothermal Technology (Materials Science and Process Technology). **2012**, *1*.

[81] Morey, G. W.; Niggli, P. The Hydrothermal Formation of Silicates, A review. *Journal of the American Chemical Society* **1913**, *35*, 1086–1130.

[82] Rabenau, A. The Role of Hydrothermal Synthesis in Preparative Chemistry. *Angewandte Chemie International Edition in English* **1985**, *24*, 1026–1040.

[83] Lobachev, A. N. In *Crystallization Processes under Hydrothermal Conditions*; Lobachev, A. N., Ed.; Springer US, 1973.

[84] Roy, R. Accelerating the Kinetics of Low-Temperature Inorganic Syntheses. *Journal of Solid-State Chemistry* **1994**, *111*, 11–17.

[85] Yoshimura, M.; Suda, H. In *Hydroxyapatite and Related Materials*, 1st ed.; Brown, P. W., Constantz, B., Eds.; CRC Press, 1994; pp 45–72.

[86] Bunsen, R. Bemerkungen zu einigen Einwürfen gegen mehrere Ansichten über die chemisch-geologischen Erscheinungen in Island. *Justus Liebigs Annalen der Chemie* **1848**, *65*, 70–85.

[87] Senarmont, M. D. On the artificial formation of minerals in the humid way. *The London, Edinburgh, and Dublin Philosophical Magazine and Journal of Science* **1849**, *34*, 545–546.

[88] Schafhäutl, K. E. Die neuesten geologischen Hypothesen und ihr Verhältnis zur Naturwissenschaft überhaupt. *Gelehrte Anzeigen München* **1845**, *20*, 577.

[89] Morey, G. W. Hydrothermal Synthesis. *Journal of the American Ceramic Society* **1953**, *36*, 279–285.

[90] Walker, A. C. Hydrothermal Synthesis of Quartz Crystals. *Journal of the American Ceramic Society* **1953**, *36*, 250–256.

[91] Hodgkin, J. H.; Jackson, M. B.; Loder, J. W. Epoxy resins based on diaminobisimide compounds. 1991.

[92] Hawthorne, D. G.; Hodgkin, J. H.; Jackson, M. B.; Loder, J. W.; Morton, T. C. Preparation and characterization of some new diaminobisimides. *High Performance Polymers* **1994**, *6*, 287–301.

[93] Chiefari, J.; Dao, B.; Groth, A. M.; Hodgkin, J. H. Water as Solvent in Polyimide Synthesis: Thermoset and Thermoplastic Examples. *High Performance Polymers* **2003**, *15*, 269–279.

[94] Chiefari, J.; Dao, B.; Groth, A.; Hodgkin, J. In *Polyimides and Other High Temperature Polymers*; Mittal, K., Ed.; CRC Press, 2005; Vol. 3; pp 3–13.

[95] Chiefari, J.; Dao, B.; Groth, A. M.; Hodgkin, J. H. Water as solvent in polyimide synthesis II: Processable aromatic polyimides. *High Performance Polymers* **2006**, *18*, 31–44.

[96] Chiefari, J.; Dao, B.; Groth, A. M.; Hodgkin, J. H. Water as solvent in polyimide synthesis III: Towards the synthesis of polyamideimides. *High Performance Polymers* **2006**, *18*, 437–451.

[97] Brunel, R.; Marestin, C.; Martin, V.; Mercier, R. Water-borne Polyimides via Microwave-assisted Polymerization. *High Performance Polymers* **2009**, *22*, 82–94.

[98] Dao, B. N.; Groth, A. M.; Hodgkin, J. H. Microwave-Assisted Aqueous Polyimidization Using High-Throughput Techniques. *Macromolecular Rapid Communications* **2007**, *28*, 604–607.

[99] Unterlass, M. M.; Emmerling, F.; Antonietti, M.; Weber, J. From dense monomer salt crystals to CO2 selective microporous polyimides via solid-state polymerization. *Chemical Communications* **2014**, *50*, 430–432.

[100] Inoue, T.; Kumagai, Y.; Kakimoto, M. A.; Imai, T.; Watanabe, J. High-Pressure Synthesis and Properties of Aliphatic-Aromatic Polyimides via Nylon-Salt-Type Monomers Derived from Aliphatic Diamines with Pyromellitic Acid and Biphenyltetracarboxylic Acid. *Macromolecules* **1997**, *30*, 1921–1928.

[101] Itoya, K.; Kumagai, Y.; aki Kakimoto, M.; Imai, Y. High-Pressure Synthesis of Aliphatic Polyimides via Salt Monomers Composed of Aliphatic Diamines and Oxydiphthalic Acid. *Macromolecules* **1994**, *27*, 4101–4105.

[102] Goyal, M.; Inoue, T.; Kakimoto, M.; Imai, Y. High-pressure synthesis and properties of aliphatic–aromatic polyimides via nylon-salt-type monomers derived from aliphatic diamines and benzophenonetetracarboxylic acid - Goyal - 1998 - Journal of Polymer Science Part A: Polymer Chemistry - Wiley Online . *Journal of Polymer Science Part A: Polymer Chemistry* **1997**, *36*, 39–47.

[103] Imai, Y.; Fueki, T.; Inoue, T.; Kakimoto, M. Successful synthesis of a 1: 1 salt monomer derived from bis(4-aminophenyl) ether and pyromellitic acid for direct polycondensation to an aromatic polyimide - Imai - 1998 - Journal of Polymer Science Part A: Polymer Chemistry - Wiley Online Library. *Journal of Polymer Science Part A: Polymer Chemistry* **1997**, *36*, 1341–1344.

[104] Imai, Y. Rapid Synthesis of Polyimides from Nylon-Salt-Type Monomers. *Advances in Polymer Science* **1999**, *140*, 1–22.

[105] Baumgartner, B.; Puchberger, M.; Unterlass, M. M. Towards a general understanding of hydrothermal polymerization of polyimides. *Polymer Chemistry* **2015**, *6*, 5773–5781.

[106] Unterlass, M. M. Green Synthesis of Inorganic-Organic Hybrid Materials: State of the Art and Future Perspectives. *European Journal of Inorganic Chemistry* **2016**, *2016*, 1135–1156.

[107] Dao, B.; Groth, A. M.; Hodgkin, J. Differential reactivity of aromatic diamines during polyimide formation in water. *European Polymer Journal* **2009**, *45*, 1607–1616.

[108] Leimhofer, L.; Baumgartner, B.; Puchberger, M.; Prochaska, T.; Konegger, T.; Unterlass, M. M. Green one-pot synthesis and processing of polyimide-silica hybrid materials. *Journal of Materials Chemistry A* **2017**, *5*, 16326–16335.

[109] Taublaender, M. J.; Reiter, M.; Unterlass, M. M. Highly Crystalline, Nanostructured Polyimide Microparticles via Green and Tunable Solvothermal Polymerization. *Macromolecules* **2019**, *52*, 6318–6329.

[110] Taublaender, M. J.; Mezzavilla, S.; Thiele, S.; Glöcklhofer, F.; Unterlass, M. M. Hydrothermal Generation of Conjugated Polymers on the Example of Pyrrone Polymers and Polybenzimidazoles. *Angewandte Chemie International Edition* **2020**,

[111] Nefedov, P. P.; Lazareva, M. A.; Kurenbin, O. I.; Kudryavtsev, V. V.; Sklizkova, V. P.; Koton, M. M. Molecular weight chromatographic analysis of polyamic acids synthesized from p-phenylene diamine and 3,3,4,4-diphenyloxide tetracarboxylic dianhydride. *Polymer Science U.S.S.R.* **1981**, *23*, 1055–1064.

[112] Eskin, V. Y.; Baranovskaya, I. A.; Koton, M. M.; Kudryavtsev, V. V.; Sklizkova, V. P. Study of properties of poly-(4,4-hydroxydiphenylene) pyromellitic amido-acid and its esters in solutions. *Polymer Science U.S.S.R.* **1976**, *18*, 2699–2706.

[113] Sazanov, Y. N.; Florinsky, F. S.; Koton, M. M. Investigation of thermal and thermooxidative degradation of some polyimides containing oxyphenylene groups in the main chain. *European Polymer Journal* **1979**, *15*, 781–786.

[114] Bel'nikevich, N. G.; Denisov, V. M.; Korzhavin, L. N.; Frenkel, S. Y. Balance of chemical and physico-chemical transformations in solutions of polyamic acids on storage. *Polymer Science U.S.S.R.* **1981**, *23*, 1406–1413.

[115] Tong, Y.; Liu, T.; Veeramani, S.; Chung, T. S. Bulk viscosity and its unstable behavior upon storage in polyimide precursor solutions. *Industrial and Engineering Chemistry Research* **2002**, *41*, 4266–4272.

[116] Dine-Hart, R. A.; Wright, W. W. Preparation and fabrication of aromatic polyimides. *Journal of Applied Polymer Science* **1967**, *11*, 609–627.

[117] Frost, L. W.; Kesse, I. Spontaneous degradation of aromatic polypromellitamic acids. *Journal of Applied Polymer Science* **1964**, *8*, 1039–1051.

[118] Orwoll, R. A.; St. Clair, T. L.; Dobbs, K. D. Phase behavior of some polyamic acid plus ether systems. *Journal of Polymer Science: Polymer Physics Edition* **1981**, *19*, 1385–1393.

[119] Taublaender, M. J.; Reiter, M.; Unterlass, M. M. Exerting Additive-Assisted Morphological Control during Hydrothermal Polymerization. *Macromolecular Chemistry and Physics* **2018**, *219*, 1700397.

[120] Unterlass, M. M. Hot Water Generates Crystalline Organic Materials. *Angewandte Chemie International Edition* **2018**, *57*, 2292–2294.

[121] Baumgartner, B.; Bojdys, M. J.; Skrinjar, P.; Unterlass, M. M. Design Strategies in Hydrothermal Polymerization of Polyimides. *Macromolecular Chemistry and Physics* **2016**, *217*, 485–500.

[122] Taublaender, M. J.; Glöcklhofer, F.; Marchetti-Deschmann, M.; Unterlass, M. M. Green and Rapid Hydrothermal Crystallization and Synthesis of Fully Conjugated Aromatic Compounds. *Angewandte Chemie International Edition* **2018**, *57*, 12270–12274.

[123] Weiser, E. S.; Johnson, T. F.; Clair, T. L. S.; Echigo, Y.; Kaneshiro, H.; Grimsley, B. W. Polyimide Foams for Aerospace Vehicles. *High Performance Polymers* **2000**, *12*, 1–12.

[124] Hshieh, F.-Y.; Hirsch, D. B.; Beeson, H. D. Ignition and combustion of low-density polyimide foam. *Fire and Materials* **2003**, *27*, 119–130.

[125] Meador, M. A. B.; Nguyen, B. N.; Guo, H.; Vivod, S.; He, Z.; Malow, E.; Silva, R. Improvements to the synthesis of polyimide aerogels. *ACS Spring National Meeting* **2011**,

[126] Meador, M. A. B.; Malow, E. J.; Silva, R.; Wright, S.; Quade, D.; Vivod, S. L.; Guo, H.; Guo, J.; Cakmak, M. Mechanically strong, flexible polyimide aerogels cross-linked with aromatic triamine. *ACS Applied Materials and Interfaces* **2012**, *4*, 536–544.

[127] Meador, M. A. B.; Wright, S.; Sandberg, A.; Nguyen, B. N.; Van Keuls, F. W.; Mueller, C. H.; Rodríguez-Solís, R.; Miranda, F. A. Low dielectric polyimide aerogels as substrates for lightweight patch antennas. *ACS Applied Materials and Interfaces* **2012**, *4*, 6346–6353.

[128] Meador, M. A. B.; Alemán, C. R.; Hanson, K.; Ramirez, N.; Vivod, S. L.; Wilmoth, N.; McCorkle, L. Polyimide aerogels with amide cross-links: A low cost alternative for mechanically strong polymer aerogels. *ACS Applied Materials and Interfaces* **2015**, *7*, 1240–1249.

[129] Guo, H.; Meador, M. A. B.; McCorkle, L.; Quade, D. J.; Guo, J.; Hamilton, B.; Cakmak, M.; Sprowl, G. Polyimide aerogels cross-linked through amine functionalized polyoligomeric silsesquioxane. *ACS Applied Materials and Interfaces* **2011**, *3*, 546–552.

[130] Guo, H.; Meador, M. A. B.; McCorkle, L.; Quade, D. J.; Guo, J.; Hamilton, B.; Cakmak, M. Tailoring properties of cross-linked polyimide aerogels for better moisture resistance, flexibility, and strength. *ACS Applied Materials and Interfaces* **2012**, *4*, 5422–5429.

[131] Nguyen, B. N.; Scheiman, D. A.; Meador, M. A. B.; Guo, J.; Hamilton, B.; McCorkle, L. S. Effect of Urea Links in the Backbone of Polyimide Aerogels. *ACS Applied Polymer Materials* **2021**, *3*, 2027–2037.

[132] Weiser, E. S.; Baillif, F. F.; Grimsley, B. W.; Marchello, J. M. High Temperature Structural Foam - NASA Technical Reports Server (NTRS). *Proc. 43rd Int. SAMPE Symp.* **1997**,

[133] Farrissey, W. J.; Rose, J. S.; Carleton, P. S. Preparation of a polyimide foam. *Journal of Applied Polymer Science* **1970**, *14*, 1093–1101.

[134] Kampouris, E. M.; Papaspyrides, C. D. Solid state polyamidation of nylon salts: possible mechanism for the transition solid-melt. *Polymer* **1985**, *26*, 413–417.

[135] Papaspyrides, C. D. Solid-state polyamidation of nylon salts. *Polymer* **1988**, *29*, 114–117.

[136] Papaspyrides, C. D. Solid state polyamidation of aliphatic diamine-aliphatic diacid salts: a generalized mechanism for the effect of polycondensation water on reaction behaviour. *Polymer* **1990**, *31*, 490–495.

[137] Kriechbaum, K.; Cerrón-Infantes, D. A.; Stöger, B.; Unterlass, M. M. Shape-Anisotropic Polyimide Particles by Solid-State Polycondensation of Monomer Salt Single Crystals. *Macromolecules* **2015**, *48*, 8773–8780.

[138] Mathews, A. S.; Kim, I.; Ha, C. S. Fully aliphatic polyimides from adamantane-based diamines for enhanced thermal stability, solubility, transparency, and low dielectric constant. *Journal of Applied Polymer Science* **2006**, *102*, 3316–3326.

[139] Mathews, A. S.; Kim, I.; Ha, C. S. Synthesis, characterization, and properties of fully aliphatic polyimides and their derivatives for microelectronics and optoelectronics applications. *Macromolecular Research 2007 15:2* **2007**, *15*, 114–128.

[140] Matsumoto, T. Aliphatic Polyimides Derived from Polyalicyclic Monomers. *High Performance Polymers* **2001**, *13*.

[141] Bo, N.; Kobayashi, I. Polyester film and its manufacturing method. 2004.

[142] Ishikawa, M.; Fujitani, T. Method for producing melt viscosity reducing agent: composition and synthetic fiber. 2004.

[143] East, A. L. On the hydrolysis mechanisms of amides and peptides. *International Journal of Chemical Kinetics* **2018**, *50*, 705–709.

[144] Konopka, M.; Stefankiewicz, A. R. Expanding structural diversity in a library of disulfide macrocycles through in-situ imide hydrolysis. *Scientific Reports* **2022**, *12*, 1–8.

[145] Sacher, E. Dielectric properties of polyimide film. II. DC properties. *IEEE Transactions on Electrical Insulation* **1979**, *EI-14*, 85–93.

[146] Sacher, E.; Susko, J. R. Water permeation of polymer films. I. Polyimide. *Journal of Applied Polymer Science* **1979**, *23*, 2355–2364.

[147] Fujita, S.; Kamei, Y.; Tanaka, K. Effect of water absorption in polimide on electrical properties. *Proceedings of the 20001 IEEE 7th International Conference on Solid Dielectrics* **2001**, 183–186.

[148] Sacher, E.; Susko, J. R. Water permeation of polymer films. III. High-temperature polyimides. *Journal of Applied Polymer Science* **1981**, *26*, 679–686.

[149] Vermilyea, D. A. The physics of corrosion. *AIP Conference Proceedings* **1976**, *32*, 141.

[150] Melcher, J.; Daben, Y.; Arlt, G. Dielectric Effects of Moisture in Polyimide. *IEEE Transactions on Electrical Insulation* **1989**, *24*, 31–38.

[151] Denton, D. D.; Pranjoto, H. Gravimetric Measurements of Moisture Uptake in Polyimide Films Used in Integrated Circuit Packaging. *MRS Online Proceedings Library (OPL)* **1989**, *154*.

[152] Buchhold, R.; Nakladal, A.; Gerlach, G.; Sahre, K.; Eichhorn, K.-J.; Herold, M.; Gauglitz, G. Influence of Moisture-Uptake on Mechanical Properties of Polymers Used in Microelectronics. *MRS Online Proceedings Library (OPL)* **1998**, *511*, 359–364.

[153] Buchhold, R.; Nakladal, A.; Gerlach, G.; Sahre, K.; Müller, M.; Eichhorn, K.; Herold, M.; Gauglitz, G. A Study on the Microphysical Mechanisms of Adsorption in Polyimide Layers for Microelectronic Applications. *Journal of The Electrochemical Society* **1998**, *145*, 4012.

[154] Okamoto, K.; Tanaka, K.; Katsube, N.; Sueoka, O.; Ito, Y. Free Volumes in Polymers; Positron Annihilation vs. Other Methods. *Materials Science Forum* **1992**, *105-110*, 1675–1678.

[155] Dlubek, G.; Buchhold, R.; Hübner, C.; Nakladal, A. Water in Local Free Volumes of Polyimides: A Positron Lifetime Study. *Macromolecules* **1999**, *32*, 2348–2355.

[156] Hasell, T.; Little, M. A.; Chong, S. Y.; Schmidtmann, M.; Briggs, M. E.; Santolini, V.; Jelfs, K. E.; Cooper, A. I. Chirality as a tool for function in porous organic cages. *Nanoscale* **2017**, *9*, 6783–6790.

[157] Moylan, C. R.; Best, M. E.; Ree, M. Solubility of water in polyimides: Quartz crystal microbalance measurements. *Journal of Polymer Science Part B: Polymer Physics* **1991**, *29*, 87–92.

[158] Seo, J.; Cho, K. Y.; Han, H. Dependence of water sorption in polyimides on the internal linkage in the diamine component. *Polymer Degradation and Stability* **2001**, *74*, 133–137.

[159] Seo, J.; Han, H. Water diffusion studies in polyimide thin films. *Journal of Applied Polymer Science* **2001**, *82*, 731–737.

[160] Seo, J.; Cho, K.-Y.; Han, H. Dependence of water sorption in polyimides on the internal linkage in the diamine component. *Polymer Degradation and Stability* **2002**, *74*, 133–137.

[161] Seo, J.; Han, H. Water sorption behaviour of polyimide thin films with various internal linkages in the dianhydride component. *Polymer Degradation and Stability* **2002**, *77*, 477–482.

[162] Seo, J.; Jeon, J.; Gun Shul, Y.; Han, H. Water sorption and activation energy in polyimide thin films. *Journal of Polymer Science Part B: Polymer Physics* **2000**, *38*, 2714–2720.

[163] Chang, Y.-L.; Jou, J.-H. Temperature effect on solvent diffusion in rigid and semirigid polyimide films. *Journal of Polymer Science Part B: Polymer Physics* **1994**, *32*, 2143–2150.

[164] Pranjoto, H.; Denton, D. D. Gravimetric measurements of steady-state moisture uptake in spin-coated polyimide films. *Journal of Applied Polymer Science* **1991**, *42*, 75–83.

[165] Barrie, J. A.; Sagoo, P. S.; Johncock, P. The sorption and diffusion of water in bismaleimide resin. *Journal of Applied Polymer Science* **1987**, *33*, 2253–2258.

[166] Huang, J.; Cranford, R. J.; Matsuura, T.; Roy, C. Water vapor sorption and transport in dense polyimide membranes. *Journal of Applied Polymer Science* **2003**, *87*, 2306–2317.

[167] Zeng, C.; Li, J.; Chen, T.; Chen, J.; Chen, C. Dynamic sorption and transport of water vapor in dense polyimide membranes. *Journal of Applied Polymer Science* **2006**, *102*, 2189–2198.

[168] Xu, T.; Farris, R. J. Stresses associated with diffusion in polyimide and polyacrylics films. *Journal of Applied Polymer Science* **2005**, *99*, 2661–2670.

[169] Fick, A. Ueber Diffusion. *Annalen der Physik* **1855**, *170*, 59–86.

[170] Crank, J. *The Mathematics of Diffusion*, 2nd ed.; Oxford University Press, 1975.

[171] Frisch, H. L. Sorption and transport in glassy polymers–a review. *Polymer Engineering and Science* **1980**, *20*, 2–13.

[172] Comyn, J. In *Polymer Permeability*, 1st ed.; Comyn, J., Ed.; Springer Netherlands, 1985; pp 1–10.

[173] ISO 62:2008, Plastics — Determination of water absorption. 2008.

[174] ASTM D570 - 98(2018), Standard Test Method for Water Absorption of Plastics. 2018.

[175] Duncan, B. C.; Broughton, W. R. Absorption and diffusion of moisture In polymeric materials - NPL. 2007.

[176] Oliphant, T. E. Python for scientific computing. *Computing in Science and Engineering* **2007**, *9*, 10–20.

[177] Millman, K. J.; Aivazis, M. Python for scientists and engineers. *Computing in Science and Engineering* **2011**, *13*, 9–12.

[178] Harris, C. R. *et al.* Array programming with NumPy. *Nature* **2020**, *585*, 357–362.

[179] Johannson, F. mpmath: a Python library for arbitrary-precision floating-point arithmetic. 2010.

[180] Virtanen, P. *et al.* SciPy 1.0: fundamental algorithms for scientific computing in Python. *Nature Methods 2020 17:3* **2020**, *17*, 261–272.

[181] Xu, Y.; Chen, C.; Li, J. Sorption and Diffusion Characteristics of Water Vapor in Dense Polyimide Membranes. *Journal of Chemical and Engineering Data* **2007**, *52*, 2146–2152.

[182] Kim, S. I.; Shin, T. J.; Pyo, S. M.; Moon, J. M.; Ree, M. Structure and properties of rodlike poly(p-phenylene pyromellitimide)s containing short side groups. *Polymer* **1999**, *40*, 1603–1610.

[183] Pyo, S. M.; Kim, S. I.; Shin, Y. H.; Ree, M. Synthesis and characterization of fully rodlike poly(4,4'-biphenylene pyromellitimide)s with various short side groups. *Journal of Polymer Science Part A: Polymer Chemistry* **1999**, *37*, 937–957.

[184] Yang, Z.; Ma, P.; Li, F.; Guo, H.; Kang, C.; Gao, L. Ultrahigh thermal-stability polyimides with low CTE and required flexibility by formation of hydrogen bonds between poly(amic acid)s. *European Polymer Journal* **2021**, *148*, 110369.

[185] Boese, D.; Lee, H.; Yoon, D. Y.; Swalen, J. D.; Rabolt, J. F. Chain orientation and anisotropies in optical and dielectric properties in thin films of stiff polyimides. *Journal of Polymer Science Part B: Polymer Physics* **1992**, *30*, 1321–1327.

[186] Takizawa, K.; Fukudome, H.; Kozaki, Y.; Ando, S. Pressure-Induced Changes in Crystalline Structures of Polyimides Analyzed by Wide-Angle X-ray Diffraction at High Pressures. *Macromolecules* **2014**, *47*, 3951–3958.

[187] Ree, M.; Kim, K.; Woo, S. H.; Chang, H. Structure, chain orientation, and properties in thin films of aromatic polyimides with various chain rigidities. *Journal of Applied Physics* **1998**, *81*, 698.

[188] Terui, Y.; Ando, S. Coefficients of molecular packing and intrinsic birefringence of aromatic polyimides estimated using refractive indices and molecular polarizabilities. *Journal of Polymer Science Part B: Polymer Physics* **2004**, *42*, 2354–2366.

[189] Diaham, S.; Locatelli, M.-L.; Khazaka, R. BPDA-PDA Polyimide: Synthesis, Characterizations, Aging and Semiconductor Device Passivation. *High Performance Polymers - Polyimides Based - From Chemistry to Applications* **2012**,

[190] Hsiao, S. H.; Chen, Y. J. Structure-property study of polyimides derived from PMDA and BPDA dianhydrides with structurally different diamines. *European Polymer Journal* **2002**, *38*, 815–828.

[191] Okamoto, K.-I.; Tanihara, N.; Watanabe, H.; Tanaka, K.; Kita, H.; Nakamura, A.; Kusuki, Y.; Nakagawa, K. Sorption and diffusion of water vapor in polyimide films. *Journal of Polymer Science Part B: Polymer Physics* **1992**, *30*, 1223–1231.

[192] Banerjee, S. Introduction to Semifluorinated High-Performance Polymers. *Handbook of Specialty Fluorinated Polymers: Preparation, Properties, and Applications* **2015**, 1–9.

[193] Mikami, K.; Itoh, Y.; Yamanaka, M. Fluorinated Carbonyl and Olefinic Compounds: Basic Character and Asymmetric Catalytic Reactions†. *Chemical Reviews* **2003**, *104*, 1–16.

[194] Dalvi, V. H.; Rossky, P. J. Molecular origins of fluorocarbon hydrophobicity. *Proceedings of the National Academy of Sciences of the United States of America* **2010**, *107*, 13603.

[195] Ando, S.; Matsuura, T.; Sasaki, S. Per fluorinated Polyimide Synthesis. *Macromolecules* **1992**, *25*, 5858–5860.

[196] Dine-Hart, R. A.; Wright, W. W. Effect of structural variations on the thermo-oxidative stability of aromatic polyimides. *Die Makromolekulare Chemie* **1972**, *153*, 237–254.

[197] Ando, S.; Matsuura, T.; Sasaki, S. Synthesis and Properties of Perfluorinated Polyimides. *Fluoropolymers 2* **2002**, 277–303.

[198] Hougham, G.; Tesoro, G.; Shaw, J. Synthesis and Properties of Highly Fluorinated Polyimides. *Macromolecules* **1994**, *27*, 3642–3649.

[199] Grein, F. Twist Angles and Rotational Energy Barriers of Biphenyl and Substituted Biphenyls. *Journal of Physical Chemistry A* **2002**, *106*, 3823–3827.

[200] Holmes, S. A.; Thomas, T. D. Electron Distribution in Trifluoromethylbenzenes. Electron Donation by the Trifluoromethyl Group. *Journal of the American Chemical Society* **1975**, *97*, 2337–2341.

[201] Wu, A. X.; Drayton, J. A.; Rodriguez, K. M.; Qian, Q.; Lin, S.; Smith, Z. P. Influence of Aliphatic and Aromatic Fluorine Groups on Gas Permeability and Morphology of Fluorinated Polyimide Films. *Macromolecules* **2020**, *53*, 5085–5095.

[202] Brandt, W. W.; Anysas, G. A. Diffusion of gases in fluorocarbon polymers. *Journal of Applied Polymer Science* **1963**, *7*, 1919–1931.

[203] Mensitieri, G.; Scherillo, G.; Manna, P. L.; Musto, P. Sorption Thermodynamics of CO2, H2O, and CH3OH in a Glassy Polyetherimide: A Molecular Perspective. *Membranes 2019* **2019**, *9*, 23.

[204] Tanaka, K.; Kita, H.; Okano, M.; Okamoto, K.-I. Permeability and permselectivity of gases in fluorinated and non-fluorinated polyimides. *Polymer* **1992**, *33*, 585–592.

[205] Matsumoto, K.; Xu, P. Gas permeation of aromatic polyimides. II. Influence of chemical structure. *Journal of Membrane Science* **1993**, *81*, 23–30.

[206] Privalko, V. P.; Lipatov, Y. S. Glass transition and chain flexibility of linear polymers. *Journal of Macromolecular Science, Part B: Physics* **1974**, *9*, 551–564.

[207] Peiffer, D. G. Degrees of freedom of polymeric molecules and their effect on physical properties. *Journal of Macromolecular Science, Part B: Physics* **1977**, *15*, 595–611.

[208] Hanwell, M. D.; Curtis, D. E.; Lonie, D. C.; Vandermeersch, T.; Zurek, E.; Hutchison, G. R. Avogadro: an advanced semantic chemical editor, visualization, and analysis platform. *Journal of Cheminformatics* **2012**, *4*, 1–17.

[209] Seo, J.; Han, H.; Lee, A.; Han, J. Effect of Isomeric Oxydiphenylene Diamine on the Water Sorption Behavior of High Temperature Polyimide Thin Films. *Polymer Journal 1999 31:4* **1999**, *31*, 324–331.

[210] Madzarevic, Z. P.; Schut, H.; Čížek, J.; Dingemans, T. J. Free Volume in Poly(ether imide) Membranes Measured by Positron Annihilation Lifetime Spectroscopy and Doppler Broadening of Annihilation Radiation. *Macromolecules* **2018**, *51*, 9925–9932.

[211] Qiu, G.; Ma, W.; Jiao, Y.; Wu, L. Low-dielectric-constant aromatic homopolyimide and copolyimide derived from pyromellitic dianhydride, 4,4-oxydianiline, 2,2-bis[4-(4-aminephenoxy)phenyl]propane, 1,4-bis(4-aminophenoxy)benzene, or 1,3-bis(4-aminophenoxy)benzene. *Journal of Applied Polymer Science* **2019**, *136*, 47405.

[212] Satou, H.; Suzuki, H.; Makino, D. In *Polyimides*, 1st ed.; Wilson, D., Stenzenberger, H. D., Hergenrother, P. M., Eds.; Springer, Dordrecht, 1990; pp 227–251.

[213] Wilson, D. In *Polyimides*, 1st ed.; Wilson, D., Stenzenberger, H. D., Hergenrother, P. M., Eds.; Springer, Dordrecht, 1990; pp 187–226.

[214] Sazanov, Y. N.; Shibaev, L. A. High temperature degradation of compounds modelling polyimide fragments. *Thermochimica Acta* **1976**, *15*, 43–54.

[215] Sazanov, Y. N.; Shibaev, L. A.; Antonova, T. A. Comparative thermal analysis (CTA) of thermally-stable polymers and model compounds. Polyimides and model compounds. *Journal of Thermal Analysis and Calorimetry* **1980**, *18*, 65–75.

[216] Sazanov, Y. N. Thermoanalytical investigation of high-temperature transformations of polyimides. *Journal of Thermal Analysis and Calorimetry* **1988**, *34*, 1117–1139.

[217] Laius, L. A.; Dergacheva, Y. N.; Bessonov, M. I.; Koton, M. M. The nature of the higher thermal stability of rigid polyimides. *Polymer Science U.S.S.R.* **1984**, *26*, 1094–1102.

[218] Sazanov, Y. N. Kinetics of the thermal degradation of polyimides. *Journal of thermal analysis 1982 23:1* **1982**, *23*, 65–71.

[219] Stump, B. L.; Snyder, W. J. Thermal Degradation of Polyimides by Thermogravimetric Analysis. *High Performance Polymers* **1989**, *1*, 247–262.

[220] ASTM E2550-17, Standard Test Method for Thermal Stability by Thermogravimetry. 2017.

[221] Cella, J. A. Degradation and stability of polyimides. *Polymer Degradation and Stability* **1992**, *36*, 99–110.

[222] Koton, M. M.; Sazanov, Y. N. Thermogravimetric study of the effect of the chemical structure of polyimides on their thermal stability. *Journal of thermal analysis 1975 7:1* **1975**, *7*, 165–171.

[223] Tamai, S.; Kuroki, T.; Shibuya, A.; Yamaguchi, A. Synthesis and characterization of thermally stable semicrystalline polyimide based on 3,4-oxydianiline and 3,3,4,4-biphenyltetracarboxylic dianhydride. *Polymer* **2001**, *42*, 2373–2378.

[224] Doyle, C. D. Estimating Thermal Stability of Experimental Polymers by Empirical Thermogravimetric Analysis. *Analytical Chemistry* **1961**, *33*, 77–79.

[225] Prime, R. B.; Bair, H. E.; Vyazovkin, S.; Gallagher, P. K.; Riga, A. In *Thermal Analysis of Polymers: Fundamentals and Applications*; Menczel, J. D., Prime, R. B., Eds.; John Wiley & Sons, Ltd, 2009; pp 241–317.

[226] Li, L.; Guan, C.; Zhang, A.; Chen, D.; Qing, Z. Thermal stabilities and the thermal degradation kinetics of polyimides. *Polymer Degradation and Stability* **2004**, *84*, 369–373.

[227] Saba, N.; Jawaid, M. A review on thermomechanical properties of polymers and fibers reinforced polymer composites. *Journal of Industrial and Engineering Chemistry* **2018**, *67*, 1–11.

[228] Ramgobin, A.; Fontaine, G.; Bourbigot, S. Thermal Degradation and Fire Behavior of High Performance Polymers. *Polymer Reviews* **2019**, *59*, 55–123.

[229] DIN EN ISO 11358-1:2020-12, Plastics - Thermogravimetry (TG) of polymers - Part 1: General principles. 2020.

[230] Sircar, A. K. Analysis of Elastomer Vulcanizate Composition by TG-DTG Techniques. *Rubber Chemistry and Technology* **1992**, *65*, 503–526.

[231] Koton, M. M.; Sazanov, Y. N. Thermal degradation of polypyromellitimides. *Polymer Science U.S.S.R.* **1973**, *15*, 1857–1863.

[232] Brunner, P. H.; Roberts, P. V. The significance of heating rate on char yield and char properties in the pyrolysis of cellulose. *Carbon* **1980**, *18*, 217–224.

[233] Homaeigohar, S.; Kabir, R.; Elbahri, M. Size-Tailored Physicochemical Properties of Monodisperse Polystyrene Nanoparticles and the Nanocomposites Made Thereof. *Scientific Reports 2020 10:1* **2020**, *10*, 1–11.

[234] Jiang, L.; Yang, X. R.; Gao, X.; Xu, Q.; Das, O.; Sun, J. H.; Kuzman, M. K. Pyrolytic Kinetics of Polystyrene Particle in Nitrogen Atmosphere: Particle Size Effects and Application of Distributed Activation Energy Method. *Polymers* **2020**, *12*.

[235] Fathollahi, M.; Pourmortazavi, S. M.; Hosseini, S. G. Particle Size Effects on Thermal Decomposition of Energetic Material. *Journal of Energetic Materials* **2008**, *26*, 52–69.

[236] Sovizi, M. R.; Hajimirsadeghi, S. S.; Naderizadeh, B. Effect of particle size on thermal decomposition of nitrocellulose. *Journal of Hazardous Materials* **2009**, *168*, 1134–1139.

[237] Dinetz, S. F.; Bird, E. J.; Wagner, R. L.; Fountain, A. W. A comparative study of the gaseous products generated by thermal and ultra-violet laser pyrolyses of the polyimide PMDA-ODA. *Journal of Analytical and Applied Pyrolysis* **2002**, *63*, 241–249.

[238] Klemchuk, P. P.; Horng, P. L. Perspectives on the stabilization of hydrocarbon polymers against thermo-oxidative degradation. *Polymer Degradation and Stability* **1984**, *7*, 131–151.

[239] Mickelson, R. W.; Einhorn, I. N. The kinetics of polymer decomposition through thermogravimetric analysis. *Thermochimica Acta* **1970**, *1*, 147–158.

[240] Belyakov, V. K.; Kosobutskii, V. A. The electron structure and thermal stability of aromatic polyamides and polyhetero-arylenes. *Polymer Science U.S.S.R.* **1976**, *18*, 2798–2808.

[241] Arnold, C. Stability of high-temperature polymers. *Journal of Polymer Science: Macromolecular Reviews* **1979**, *14*, 265–378.

[242] Żurakowska-Országh, J.; Orzeszko, A.; Kobiela, S. ESR study of thermal destruction of polypyromellitimides. *European Polymer Journal* **1977**,

[243] Michaelis, L.; Schubert, M. P.; Granick, S. The Free Radicals of the Type of Wurster's Salts. *Journal of the American Chemical Society* **1939**, *61*, 1981–1992.

[244] Higasi, K. Molecular Configuration of Diphenyl Ether as Revealed by Dielectric Relaxation Times and Molar Kerr Constants. *Bulletin of the Chemical Society of Japan* **1962**, *35*, 692–696.

[245] Li, Q.; Fang, X.; Wang, Z.; Gao, L.; Ding, M. Polyimides from isomeric oxydiphthalic anhydrides. *Journal of Polymer Science Part A: Polymer Chemistry* **2003**, *41*, 3249–3260.

[246] Ni, H.; Zhang, X.; Liu, J.; Yang, S. Intrinsically heat-sealable polyimide films derived from 2,3,3,4-oxydiphthalic anhydride and aromatic diamines with various ether linkages. *High Performance Polymers* **2016**, *29*, 362–371.

[247] Sun, Z.; Dong, L.; Zhuang, Y.; Cao, L.; Ding, M.; Feng, Z. Beta relaxation in polyimides. *Polymer* **1992**, *33*, 4728–4731.

[248] Mundhenke, R. F.; Schwartz, W. T. Chemistry and Properties of 4,4'-Oxydiphthalic Anhydride Based Polyimides:. *High Performance Polymers* **1990**, *2*, 57–66.

[249] Ballauff, M. Stiff-Chain Polymers - Structure, Phase Behavior, and Properties. *Angewandte Chemie International Edition in English* **1989**, *28*, 253–267.

[250] Yi, L.; Huang, W.; Yan, D. Polyimides with side groups: Synthesis and effects of side groups on their properties. *Journal of Polymer Science Part A: Polymer Chemistry* **2016**, *55*, 533–559.

[251] Tsuda, Y. In *Polyimides and Other High Temperature Polymers: Synthesis, Characterization and Applications, Volume 5*, 1st ed.; Mittal, K. L., Ed.; CRC Press, 2009; Vol. 5; pp 27–52.

[252] Hasegawa, M.; Shindo, Y.; Sugimura, T.; Ohshima, S.; Horie, K.; Kochi, M.; Yokota, R.; Mita, I. Photophysical processes in aromatic polyimides. Studies with model compounds. *Journal of Polymer Science Part B: Polymer Physics* **1993**, *31*, 1617–1625.

[253] Hasegawa, M.; Horie, K. Photophysics, photochemistry, and optical properties of polyimides. *Progress in Polymer Science* **2001**, *26*, 259–335.

[254] Ando, S.; Terui, Y.; Aiki, Y.; Ishizuka, T. Synthesis and Properties of Fully Aromatic Nonfluorinated Polyimides Exhibiting High Transparency and Low Thermal Expansion. *Journal of Photopolymer Science and Technology* **2005**, *18*, 333–336.

[255] Yang, S. Y.; Ge, Z. Y.; Yin, D. X.; Liu, J. G.; Li, Y. F.; Fan, L. Synthesis and characterization of novel fluorinated polyimides derived from 4,4-[2,2,2-trifluoro-1-(3-trifluoromethylphenyl)ethylidene]diphthalic anhydride and aromatic diamines. *Journal of Polymer Science Part A: Polymer Chemistry* **2004**, *42*, 4143–4152.

[256] Sato, Y.; Yoshida, M.; Ando, S. Optical Properties of Rod-like Fluorinated Polyimides and Model Compounds Derived from Diamines having High Electron-donating Properties. *Journal of Photopolymer Science and Technology* **2006**, *19*, 297–304.

[257] Fedotova, O. Y.; Nesterova, Y. I.; Vinokurova, T. I.; Trezvov, A. V. Investigation of chemical changes occurring during the heat treatment of aromatic polyamides and polyimides. *Polymer Science U.S.S.R.* **1974**,

[258] Okabe, T.; Morikawa, A. Synthesis of polyimides from 3,3-dihydroxybenzidine and conversion to polybenzoxazoles. *High Performance Polymers* **2008**, *20*, 53–66.

[259] Bell, V. L.; Stump, B. L.; Gager, H. Polyimide structure–property relationships. II. Polymers from isomeric diamines. *Journal of Polymer Science: Polymer Chemistry Edition* **1976**, *14*, 2275–2291.

[260] Marinović-Cincović, M.; Babić, D.; Džunuzović, E.; Popov-Pergal, K.; Rančić, M. Thermal, oxidative and radiation stability of polyimides. Part IV: Polyimides based on N-[4-benzoyl-2-(2,5-dioxo-2,5-dihydro-pyrrol-1-yl)-phenyl]-acetamide and different diamines. *Polymer Degradation and Stability* **2007**, *92*, 1730–1736.

[261] Bell, V. L. Polyimide structure–property relationships. I. Polymers from fluorene-derived diamines. *Journal of Polymer Science: Polymer Chemistry Edition* **1976**, *14*, 225–235.

[262] Vinogradova, S. V.; Vygodskii, Y. S.; Vorob'ev, V. D.; Churochkina, N. A.; Chudina, L. I.; Spirina, T. N.; Korshak, V. V. Chemical cyclization of poly(Amido-acids) in solution. *Polymer Science U.S.S.R.* **1974**, *16*, 584–589.

[263] Takekoshi, T. In *Polyimides Fundamentals and Applications*; Ghosh, M. K., Mittal, K. L., Eds.; CRC Press, 1996; pp 7–48.

[264] Hasegawa, M. Development of Solution-Processable, Optically Transparent Polyimides with Ultra-Low Linear Coefficients of Thermal Expansion. *Polymers 2017, Vol. 9, Page 520* **2017**, *9*, 520.

[265] Fink, J. K. *High Performance Polymers: Second Edition*, 2nd ed.; Elsevier, 2014; pp 1–420.

[266] Tamai, S.; Yamaguchi, A.; Ohta, M. Melt processible polyimides and their chemical structures. *Polymer* **1996**, *37*, 3683–3692.

[267] Menges, F. Spectragryph - optical spectroscopy software. 2020; `https://www.effemm2.de/spectragryph/`.

[268] Yeo, H.; Goh, M.; Ku, B. C.; You, N. H. Synthesis and characterization of highly-fluorinated colorless polyimides derived from 4,4-((perfluoro-[1,1-biphenyl]-4,4-diyl)bis(oxy))bis(2,6-dimethylaniline) and aromatic dianhydrides. *Polymer* **2015**, *76*, 280–286.

[269] Chen, C. H.; Lin, C. H.; Wang, M. W.; Juang, T. Y. Low Dielectric Polyetherimides Derived from Bis[4-(4-(4-aminophenoxy)-2-tert-butylphenoxy)phenyl] Sulfone and 4,4-Bis[4-(4-aminophenoxy)-2-tert-butylphenoxy]perfluorobiphenyl. *ACS Omega* **2017**, *2*, 4800–4807.

[270] Ikeda, T.; Aprahamian, I.; Stoddart, J. F. Blue-colored donor-acceptor [2]rotaxane. *Organic Letters* **2007**, *9*, 1481–1484.

[271] Kim, S. D.; Byun, T.; Lee, B.; Kim, S. Y.; Chung, I. S. Rigid-Rod Polyamides from 3,3-bis-(trifluoromethyl)-4,4-diamino-1,1-biphenyl. *Macromolecular Chemistry and Physics* **2015**, *216*, 1341–1347.

[272] Schmidt, H.; Schultz, G. II. Ueber Diphenylbenzole. *Justus Liebigs Annalen der Chemie* **1880**, *203*, 118–137.

[273] Wang, J.; Freeman, H. S.; Claxton, L. D. Synthesis and mutagenic properties of 4,4-diamino-p-terphenyl and 4,4-diamino-p-quaterphenyl. *Coloration Technology* **2007**, *123*, 34–38.

A. Structures of Employed PI Systems

A.1 PI Systems in DVS and TGA measurements

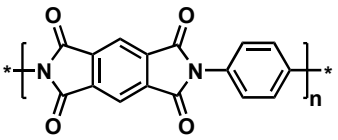

PMDA-pPDA

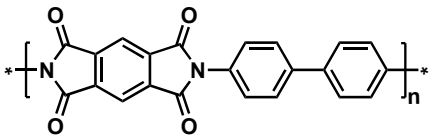

PMDA-Bz

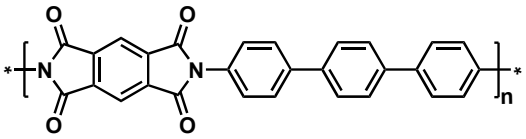

PMDA-DATP

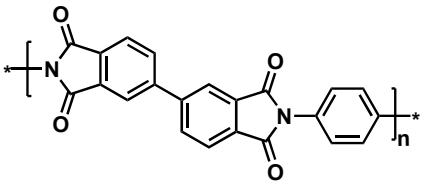

sBPDA-pPDA

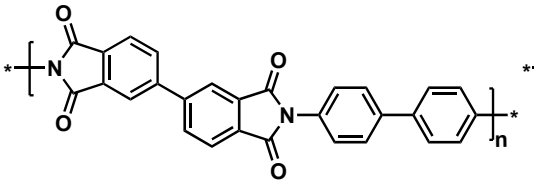

sBPDA-Bz

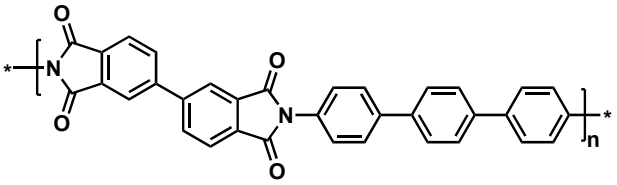

sBPDA-DATP

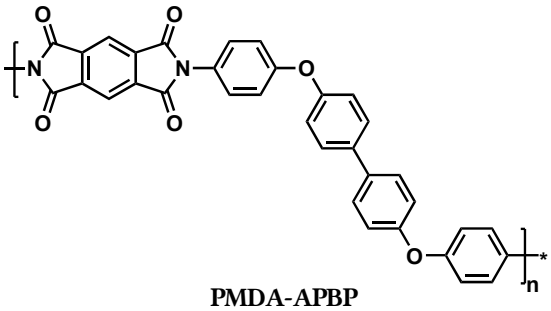

PMDA-APBP

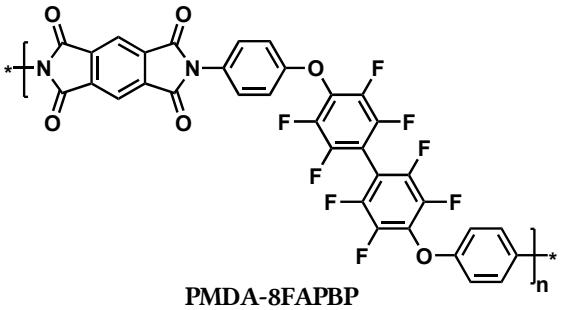

PMDA-8FAPBP

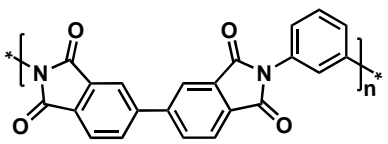

sBPDA-mPDA

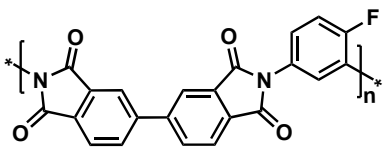

sBPDA-1FmPDA

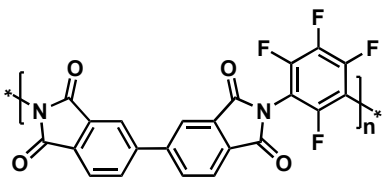

sBPDA-4FmPDA

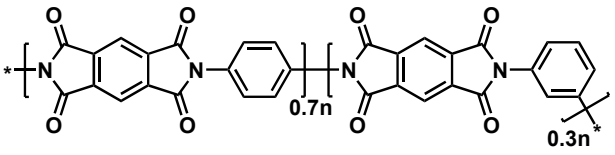

PMDA-[0.3mPDA+0.7pPDA]

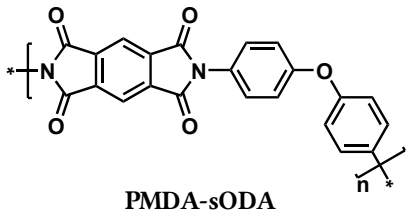

PMDA-sODA

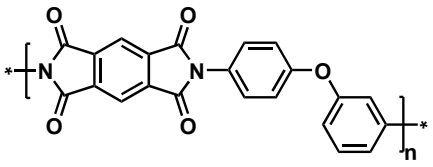

PMDA-aODA

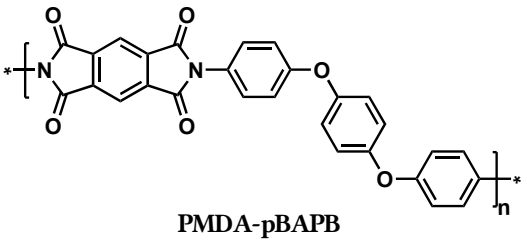

PMDA-pBAPB

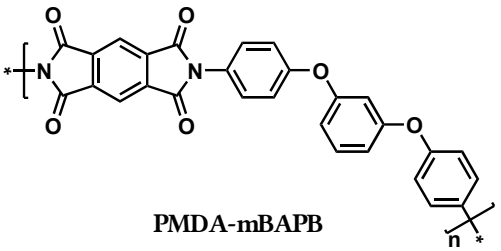

PMDA-mBAPB

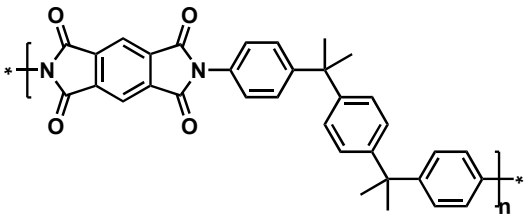

PMDA-pBISA

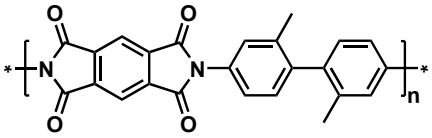

PMDA-mDMBz

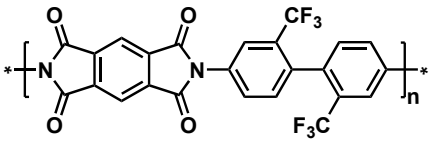

PMDA-mTFBz

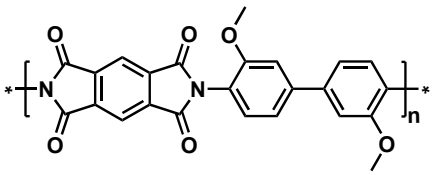

PMDA-oDIAN

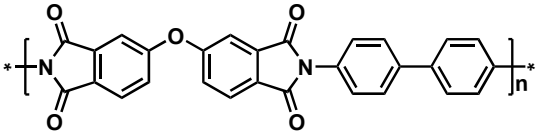

sODPA-Bz

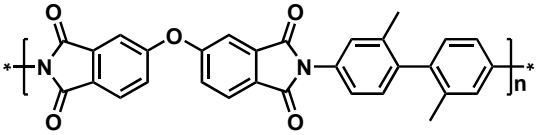

sODPA-mDMBz

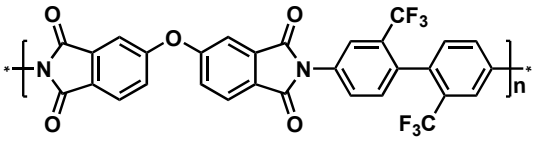

sODPA-mTFBz

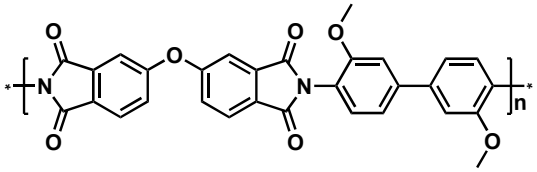

sODPA-oDIAN

A.2 Additional PI Systems in TGA measurements

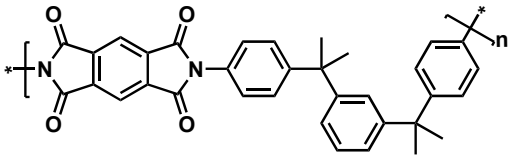

PMDA-mBISA

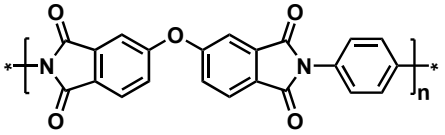

sODPA-pPDA

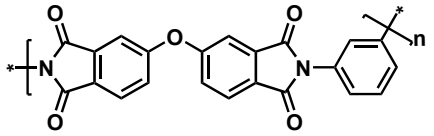

sODPA-mPDA

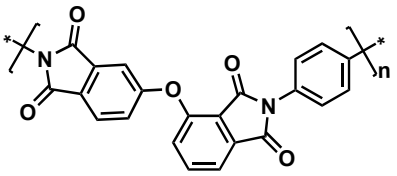

aODPA-pPDA

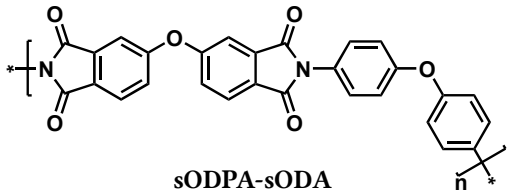

sODPA-sODA

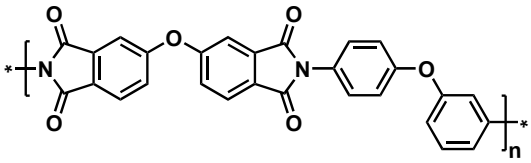

sODPA-aODA

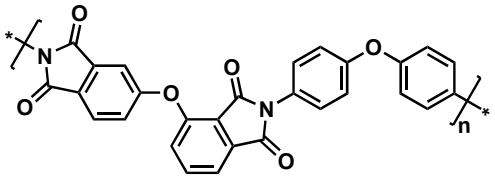

aODPA-sODA

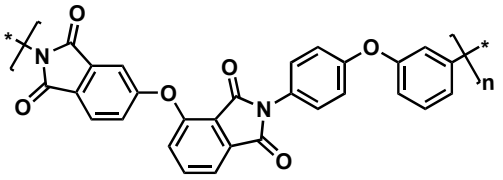

aODPA-aODA

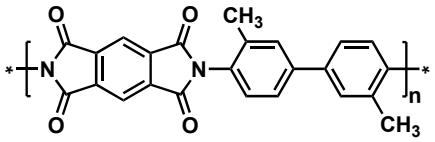

PMDA-oDMBz

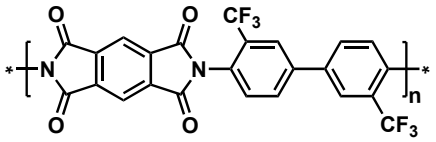

PMDA-oTFBz

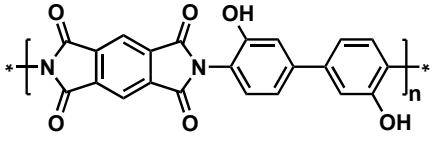

PMDA-oDHBz

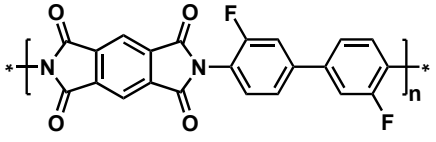

PMDA-oDFBz

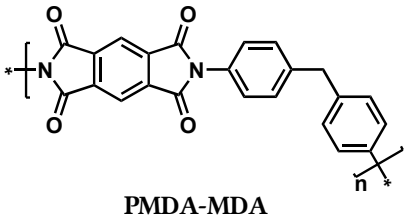

PMDA-MDA

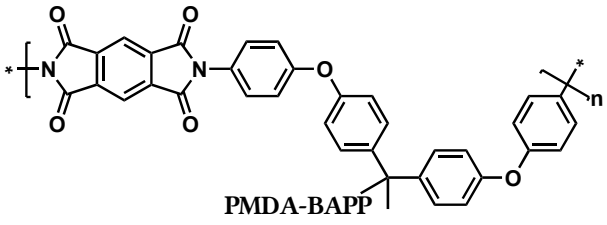

PMDA-BAPP

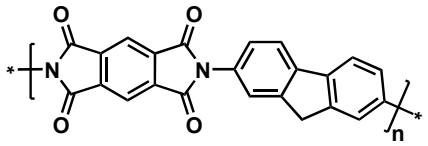

PMDA-DAF

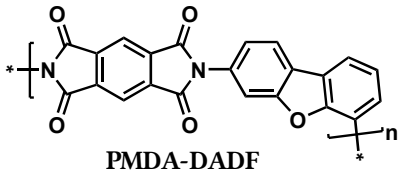

PMDA-DADF

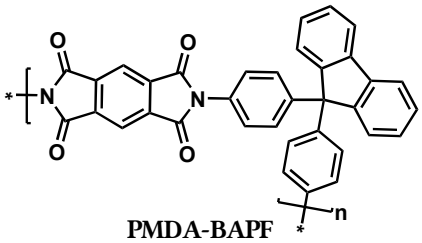

PMDA-BAPF

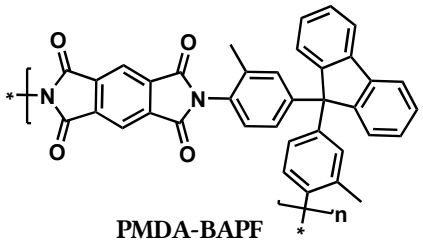

PMDA-BAPF

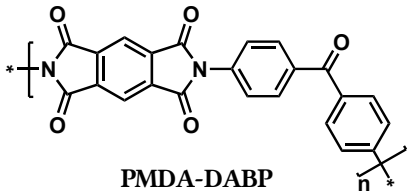

PMDA-DABP

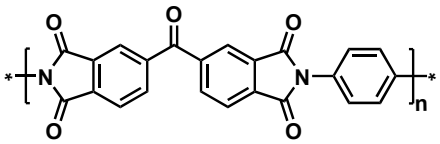

BTDA-pPDA

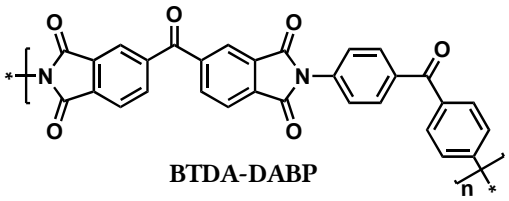

BTDA-DABP

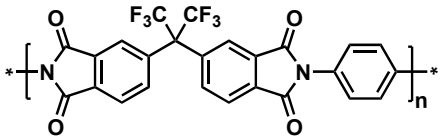

6FDA-pPDA

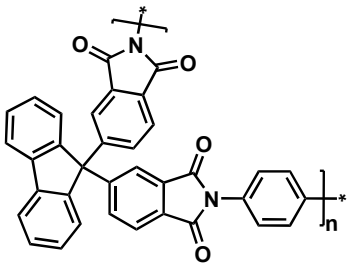

BPAF-pPDA

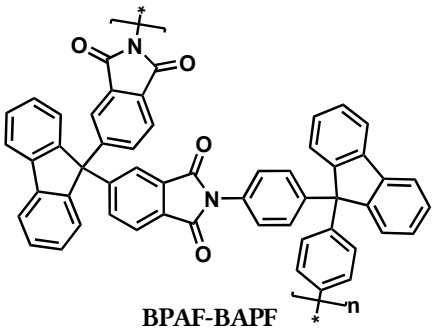

BPAF-BAPF

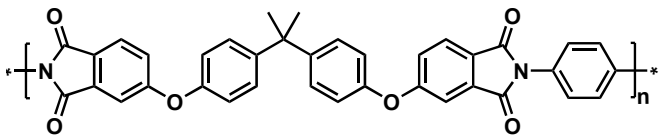

BPADA-pPDA

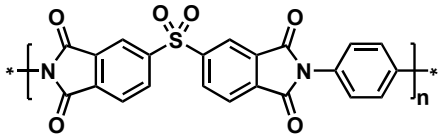

DSDA-pPDA

B. Experimental Details

B.1 Measurement Methods

Powder X-ray diffraction (PXRD) measurements were conducted on a *PANalytical* X'Pert Pro multipurpose diffractometer operating in Bragg-Brentano geometry and with a Cu anode at 40 kV and 40 mA, and using an X-Celerator multichannel detector. Powder samples were mounted as loose powders on (100) Si wafers utilized as sample holders, while film samples were attached to these wafers utilizing a thin layer of Vaseline or prepared and cured directly on these wafers. The diffraction patterns were recorded mostly between 5°and 60°(2θ Cu-$K\alpha_1$), but also between 1°and 30°(2θ Cu-$K\alpha_1$), with 80.01 s/step (later 160.02 s/step) and a step size of 0.01 Å, (later 0.02 Å), while sample holders where rotated during the measurements with 4 s/turn. As instrument control software *PANalytical* X'Pert-PRO version 2.2B (20140619) and version 2.2F (20161117) and for collecting measurement data *PANalytical* Data Collector 5.3 - 6.0a were used. Single crystal X-ray diffraction (SCXRD) analysis was carried out by Berthold Stöger on a *Bruker* KAPPA APEX II diffractometer.

Attenuated total reflectance Fourier transform infrared (ATR-FTIR) analysis was conducted on a *Bruker* Tensor 27 in ATR mode, equipped with a *PIKE* MIRacle single-reflection ATR unit, using *Bruker* OPUS software (version 4.0) for data collection and Spectragryph optical spectroscopy software (version 1.2.15) for data analysis.[267] Resolution was set to 2 - 4 cm^{-1}, and spectra were recorded from 4000 - 600 cm^{-1}. ^{1}H and ^{19}F solution nuclear magnetic resonance (NMR) spectra were recorded on a *Bruker* AVANCE 250 and a *Bruker* AVANCE 400 equipped with 5 mm inverse-broad probe heads and z-gradient units.

Optical microscopy was done on a *LEICA* M 125 microscope, images were taken using the software LAS v3.7. Scanning electron microscopy (SEM) was performed by Marianne Lahnsteiner and Miriam M. Unterlass using a *Quanta* 200F FEI microscope. For that, samples were typically measured at 5 kV or 10 kV, with a working distance of 9 - 10 mm and spot size 2.0 or 2.5. Prior to analysis, samples were loaded on carbon-coated stubs and coated by sputtering with Au/Pd 60/40 alloy layer of 17 nm thickness using a *Quarum* Q105T S sample preparation system.

B.2 Synthesis of Monomers

B.2.1 Synthesis of 8FBABP (4,4′-bis(4-aminophenoxy)octafluorobiphenyl)

Preparation of 4,4′-bis(4-nitrophenoxy)octafluorobiphenyl

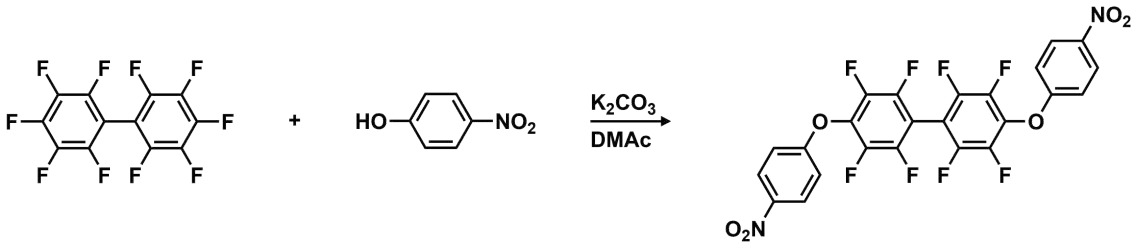

Figure B.1

Entry	Amount	Molar Mass	Equivalents
Decafluorobiphenyl	9.01 g	334.12 g mol^{-1}	1.00 eq.
4-Nitrophenol	8.25 g	139.11 g mol^{-1}	2.20 eq.
K_2CO_3	8.31 g	138.21 g mol^{-1}	2.23 eq.
N,*N*-Dimethylacetamid, anhydrous	80 ml	-	-

Step 1: A 250-ml three-neck flask equipped with a magnetic stirrer, an argon inlet, a thermometer and a reflux condenser was charged with dry *N*,*N*-dimethylacetamid, 4-nitrophenol and K_2CO_3 while flushing with argon. While stirring and maintaining a slight argon stream, decafluorobiphenyl was carefully added and residues were washed from the beaker walls with small amounts of dry *N*,*N*-dimethylacetamid. A slight but clear formation of gas bubbles emerging from the solution could be observed. The reaction mixture was heated to approximately 68 °C and left to stir for 23 h while the temperature of the solution slowly rose to 73 °C.

Step 2: The solution was left to cool down to room temperature and poured into 160 ml of deionized water in order to precipitate the product. The resulting dispersion was centrifuged at high rotational speeds for several minutes and decanted, after which the precipitate was redispersed, centrifuged and decanted two more times. It should be noted that two centrifuge beakers shattered during that procedure, which led to significant losses in product.

Step 3: The moist crude product (approx. 15 g) was dissolved in approximately 100 ml

refluxing acetone and the solution was left to cool slowly down to room temperature, while still being immersed in the warm oil bath. After leaving the product to crystallize overnight, colorless and transparent single crystals were obtained yielding 78 % of theory.

^{1}H NMR (250 MHz, DMSO-d6:) δ 5.01 (s, 4H), 7.55 (sex, 4H), 8.32 (sex, 4H)

^{19}F NMR (250 MHz, DMSO-d6:) δ -137.62 - -137.80 (m, 4F), −153.22 (sex, 4F)

This reaction was done following synthetic procedures found in literature.[268,269]

Preparation of 4,4′-bis(4-aminophenoxy)octafluorobiphenyl

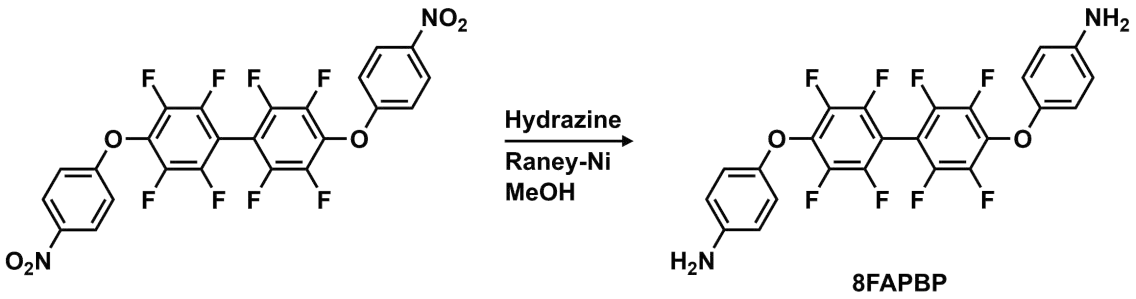

Figure B.2

Entry	Amount	Molar Mass	Equivalents
4,4'-Bis(4-nitrophenoxy)octafluorobiphenyl	5.36 g	572.32 g mol^{-1}	1 eq.
Hydrazine monohydrate	25 ml	50.06 g mol^{-1}	64 eq.
Raney nickel, aqueous slurry	2.53 g	-	-
Methanol	100 ml	-	-

Step 1: A 250-ml three-neck flask equipped with a magnetic stirrer, an argon inlet, a reflux condenser and pressure equalizing dropping funnel was charged with methanol and the dinitro compound. The mixture was argon-bubbled for several minutes while cooling it to 0 °C in an ice bath. The aqueous slurry containing Raney-Ni was washed into the mixture with the help of a few milliliters of methanol while keeping the argon stream bubbling through the mixture. While keeping the mixture cooled in the ice bath, hydrazine monohydrate was slowly added via the dropping funnel at approximately one drop per second. A lively formation of gas bubbles emerging from the mixture could be observed. The reaction mixture was stirred for approximately 24 hours while allowing it to slowly warm up to room temperature.

Step 2: Afterwards, the catalyst was separated from the solution by filtering the reaction mixture over a few-centimeter thick pad of Celite. The resulting clear solution was partially evaporated in a rotary evaporator, while greatest caution was exercised to ensure the methanol and hydrazine vapors were condensed into the evaporator's receiving flask being filled with water and cooled in an ice bath. A reddish precipitate emerged from the residual hydrazine-water azeotrope while evaporating. This mixture was cooled to -20 °C overnight which caused more product to precipitate. Afterwards, the product was filtered over a Por.3 glass filter and washed with deionized water several times before drying it with air suction within the glass filter. The product obtained consisted of yellowish, crystalline flakes yielding 73 % of theory.

^{1}H NMR (400 MHz, DMSO-d6): δ 6.91 (sex, 4H), 6.56 (sex, 4H)

^{19}F NMR (400 MHz, DMSO-d6): δ -139.05 - -139.12 (m, 4F), −154.62 (sex, 4F)

B.2.2 Synthesis of oDFBz (3,3′-difluoromethylbenzidine)

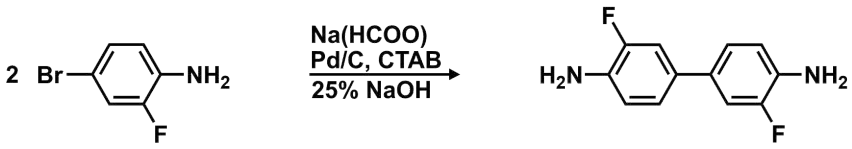

Figure B.3

Entry	Amount	Molar Mass	Equivalents
4-Bromo-2-fluoroaniline	4.75 g	190.01 g mol^{-1}	1 eq.
Sodium formate	3.5 g	68.01 g mol^{-1}	2 eq.
Cetrimonium bromide (CTAB)	1.0 g	-	-
Pd/C	0.50 g	-	-
NaOH, 25 wt% solution	15 ml	-	-

Note: This compound was synthesized by Markus Fitzka in the framework of a curricular internship and following synthetic procedures found in literature.[270]

Step 1: 4-Bromo-2-fluoroaniline, 1.7 g sodium formate, CTAB and Pd/C were added to the NaOH solution and heated to reflux. After three hours another 1.8 g sodium formate were added and the reaction was refluxed for another 24 h.

Step 2: After the reaction was complete, black and grey solids were visible, which were filtered over a Büchner funnel and thoroughly washed with ethyl acetate. The product

contained within the aqueous filtrate was then extracted with ethyl acetate and washed with water twice. The organic layer was dried with $MgSO_4$, filtered and the solvent was evaporated. The resulting black liquid was stored overnight at room temperature, leading to a black precipitate. The black solid was then purified by column chromatography. For this, 70 g of silica gel were used as stationary phase and pure dichloromethane was used as eluent. Three fractions were collected of which the first one contained the desired product, which yielded 7.3 % of theory.

^{1}H NMR (250 MHz, DMSO-d6): δ 5.10 (s, 4H), 6.75 (t, 2H), 7.16 (dd, 4H)

B.2.3 Synthesis of oTFBz (3,3′-bis(trifluoromethyl)benzidine)

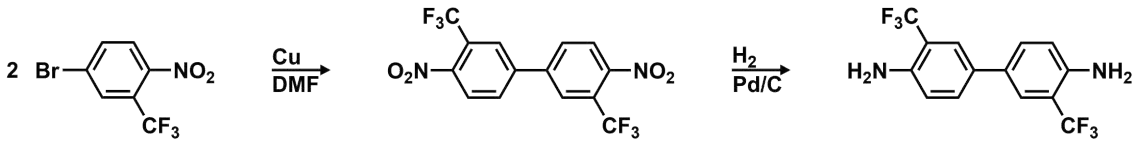

Figure B.4

Entry	Amount	Molar Mass	Equivalents
5-Bromo-2-nitrobenzotrifluoride	5.00 g	270.00 g mol^{-1}	1 eq.
Copper granules	4.8 g	-	-
CuI	traces	-	-
N,*N*-Dimethylformamide	10 ml	-	-
2N HCl	-	-	-
Tetrahydrofuran	-	-	-

Note: This compound was synthesized by Markus Fitzka in the framework of a curricular internship and following synthetic procedures found in literature.[271].

Step 1: The copper granules were milled with an agate mortar in order to increase its reactive surface area. Then it was added to a reaction solution containing 5-bromo-2-nitrobenzotrifluoride and a catalytic amount of CuI in DMF in a two-necked round bottom flask, which was equipped with a magnetic stirrer and a reflux condenser. The reaction mixture was heated to reflux for 72 h.

Step 2: After letting it cool down to room temperature, the solution was filtrated. The filtrate was then poured into 200 mL of 2N HCl, leading to a yellow solution containing fine orange particles. After adding another 200 mL of 2N HCl and subsequent stirring,

the solution was filtered again. The solvent was evaporated in a rotary evaporator and the residual water was evaporated in a drying oven at 80 °C overnight, during which the solid turned green overnight.

Step 3: The crude product was recrystallized in chloroform and precipitated at -20 °C overnight. The obtained yellow solid was then filtered off using a Büchner funnel, yielding 20.4 % the dinitro compound.

^{1}H NMR (250 MHz, DMSO-d6): δ 8.31 (d, 2H), 8.43 (m, 4H)

Step 4: Prior to reduction, the dinitro compound was purified by sublimation at 180 °C and a pressure of 2.5 µbar. The obtained purified dinitro compound was then reduced with H_2 over Pd/C in a hydrogen autoclave, for which it was given into a glass vial equipped with a magnetic stirrer and charged with methanol and catalytic amounts of Pd/C. After giving the mixture into the autoclave, it was charged with 50 bar of H_2 three times while stirring and then left under this reducing atmosphere for 20 h while the pressure slowly decreased. Then a minor amount of tetrahydrofuran was added and the mixture was filtered over a pad of Celite. After washing the Celite pad with tetrahydrofuran several times, the solvent was evaporated off and the desired product was obtained as violet powder in a quantitative yield.

^{1}H NMR (250 MHz, DMSO-d6): δ 5.62 (s, 4H), 6.90 (d, 2H), 7.55 - 7.47 (m, 4H)

B.2.4 Synthesis of DATP (4,4′′-diamino-*p*-terphenyl)

Preparation of 4,4′′-dinitro-*p*-terphenyl

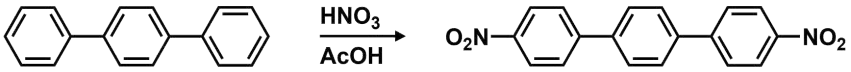

Figure B.5

Entry	Amount	Molar Mass	Equivalents
p-Terphenyl	20.59 g	230.31 g mol^{-1}	1 eq.
Red fuming nitric acid	30 ml	-	-
Glacial acetic acid	300 ml	-	-

Step 1: A 250-ml three-neck flask equipped with a rather big magnetic stirrer, a reflux condenser and pressure equalizing dropping funnel was charged with terphenyl and

50 ml of glacial acetic acid. The mixture was cooled to approximately 0 °C in an ice bath and the fuming nitric acid was added dropwise over the course of 30 min while stirring vigorously. The stirring was continued for 20 min while allowing the solution to slightly warm up to room temperature. Afterwards, the mixture was warmed to approximately 70 °C with a heat gun and stirred for another 30 min, after which another 100 ml of acetic acid were added while allowing the mixture to stir for another 30 min.

Step 2: The precipitate contained in the reaction mixture were filtered over a Por.3 glass filter and washed three times with 50 ml acetic acid each and subsequently washed three times with approximately 25 ml of acetone, yielding 33.4 % the yellowish dinitro compound.

^{1}H NMR (250 MHz, DMSO-d6): δ 7.08 (s, 4H), 8.06 (d, 4H), 8.34 (d, 4H)

This reaction was done following synthetic procedures found in literature.[272,273]

Preparation of 4,4′′-Diamino-*p*-terphenyl

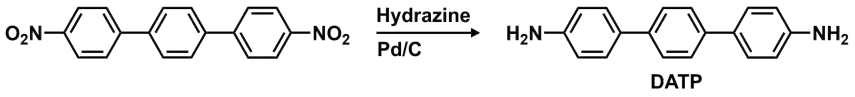

Figure B.6

Entry	Amount	Molar Mass	Equivalents
4,4′′-Dinitro-*p*-terphenyl	5.28 g	320.30 g mol^{-1}	1 eq.
Hydrazine monohydrate	40 g	-	60 eq.
Pd/C	0.53 g	-	-
2-Methoxyethanol	250 ml	-	-

Step 1: A 500-ml three-neck flask equipped with a magnetic stirrer, an argon inlet, a reflux condenser and pressure equalizing dropping funnel was charged with 2-methoxyethanol, the catalyst and the dinitro compound. The mixture was argon-bubbled for several minutes before hydrazine monohydrate was slowly added via the dropping funnel at approximately one drop per second, which yielded a yellowish green suspension.

Step 2: The reaction mixture was slowly heated up to 80 °C, which led to the dissolution of the starting product, while keeping a mild but constant stream of argon. After two hours of stirring, the reaction mixture was heated to reflux and kept for one more hour. Afterwards, the hot reaction mixture was filtered the over a few-centimeter thick

pad of Celite, in order to separate the catalyst and the filter pad was washed two times with 15 ml of methoxyethanol. The resulting clear solution was partially evaporated in a rotary evaporator, while greatest caution was exercised to ensure the hydrazine vapors were condensed into the evaporator's receiving flask being filled with water and cooled in an ice bath. An white precipitate emerged from the residual solvent while evaporating. This mixture was cooled to -20 °C overnight which caused more product to precipitate. Afterwards, the product was filtered over a Por.3 glass filter and washed with deionized water and cold acetone several times before drying it with air suction within the glass filter. The product obtained consisted of off-white crystalline flakes yielding 93 % of theory.

^{1}H NMR (250 MHz, DMSO-d6): δ 5.22 (s, 4H), 6.69 - 6.63 (m, 4H), 7.42 - 7.36 (m, 4H), 7.55 (s, 4H)

C. PXRD Diffractogram Collection

C.1 PMDA-pPDA

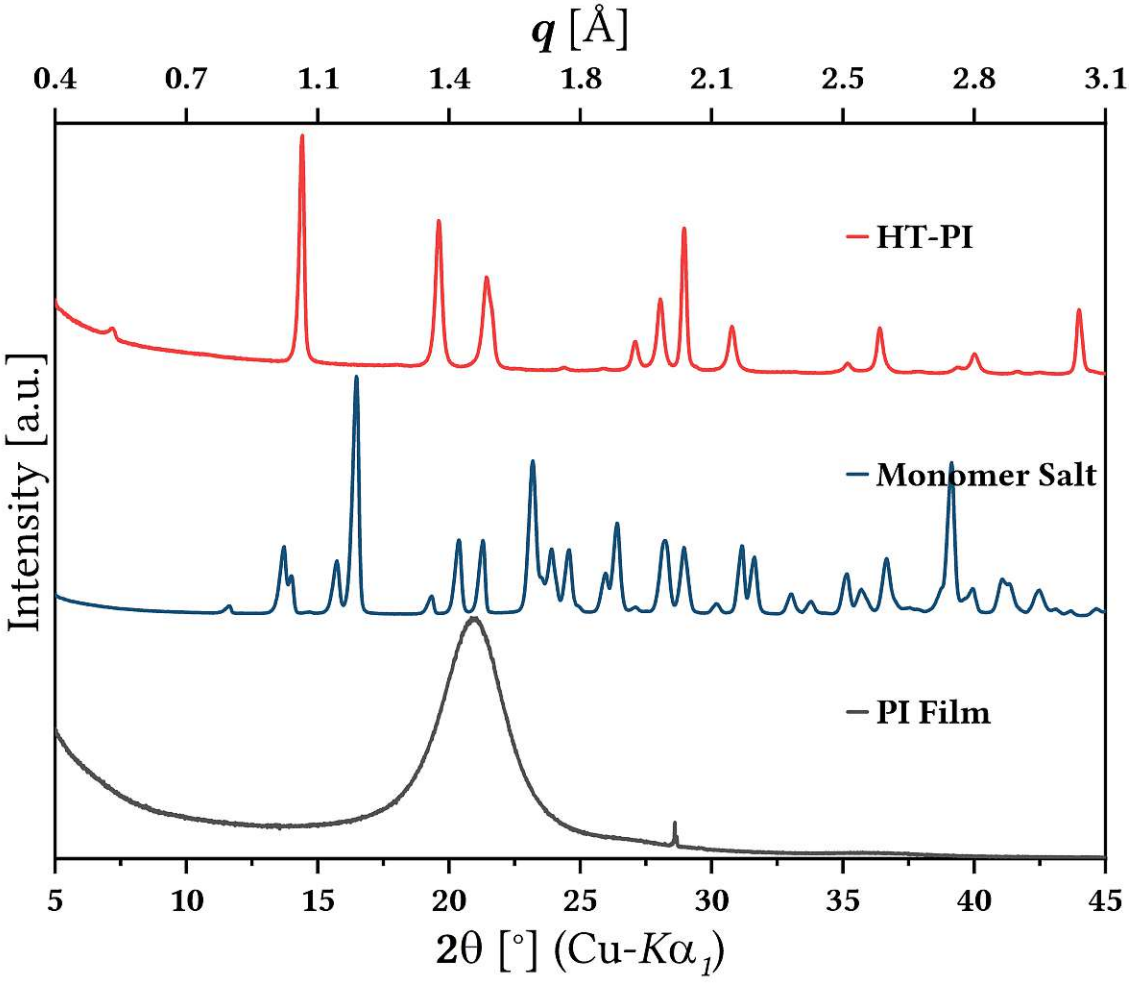

Figure C.1: PXRD patterns of a hydrothermally synthesized PMDA-pPDA PI, its monomer-salt precursor, and of a PI film of the same system.

C.2 PMDA-mPDA

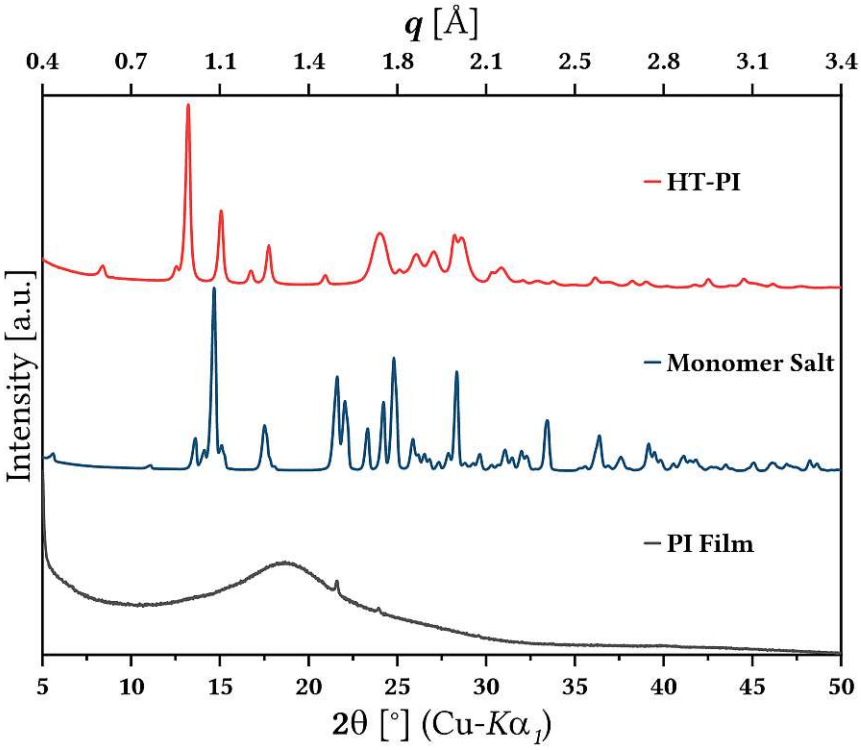

Figure C.2: PXRD patterns of a hydrothermally synthesized PMDA-mPDA PI, its monomer-salt precursor, and of a PI film of the same system.

C.3 PMDA-Bz

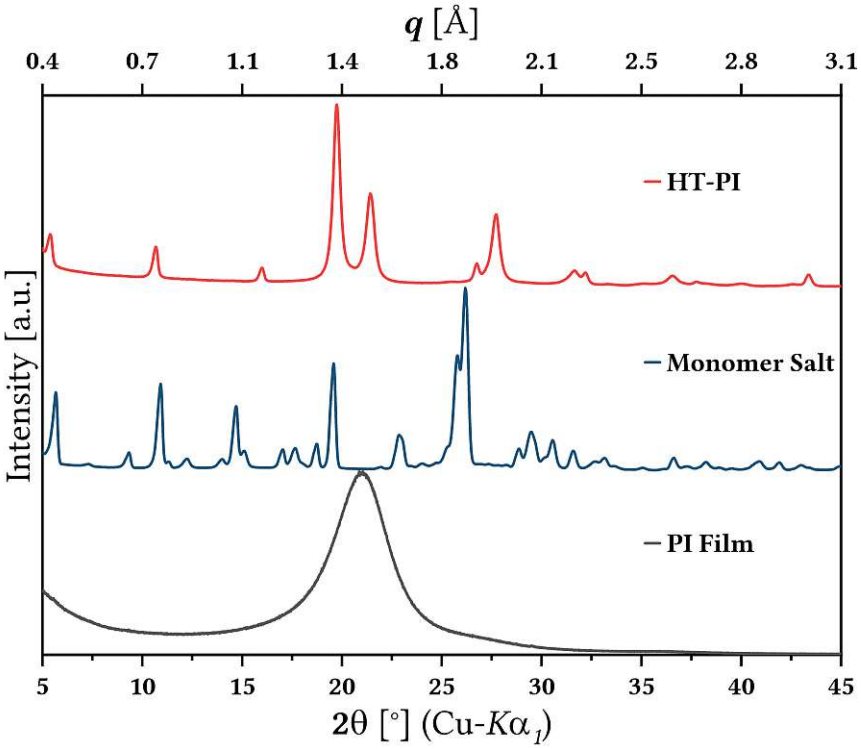

Figure C.3: PXRD patterns of a hydrothermally synthesized PMDA-Bz PI, its monomer-salt precursor, and of a PI film of the same system.

C.4 PMDA-DATP

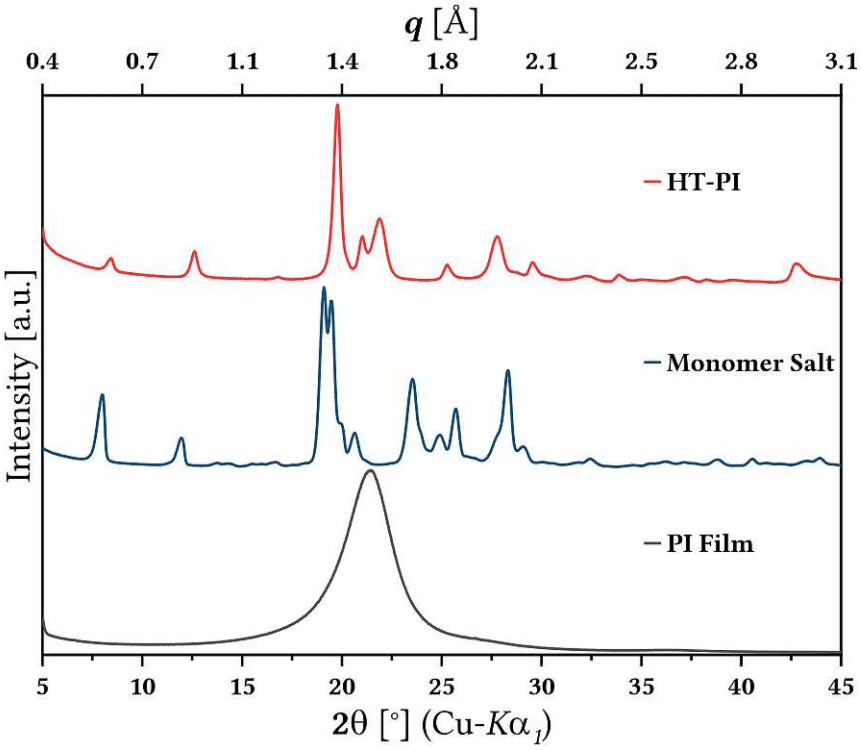

Figure C.4: PXRD patterns of a hydrothermally synthesized PMDA-DATP PI, its monomer-salt precursor, and of a PI film of the same system.

C.5 sBPDA-pPDA

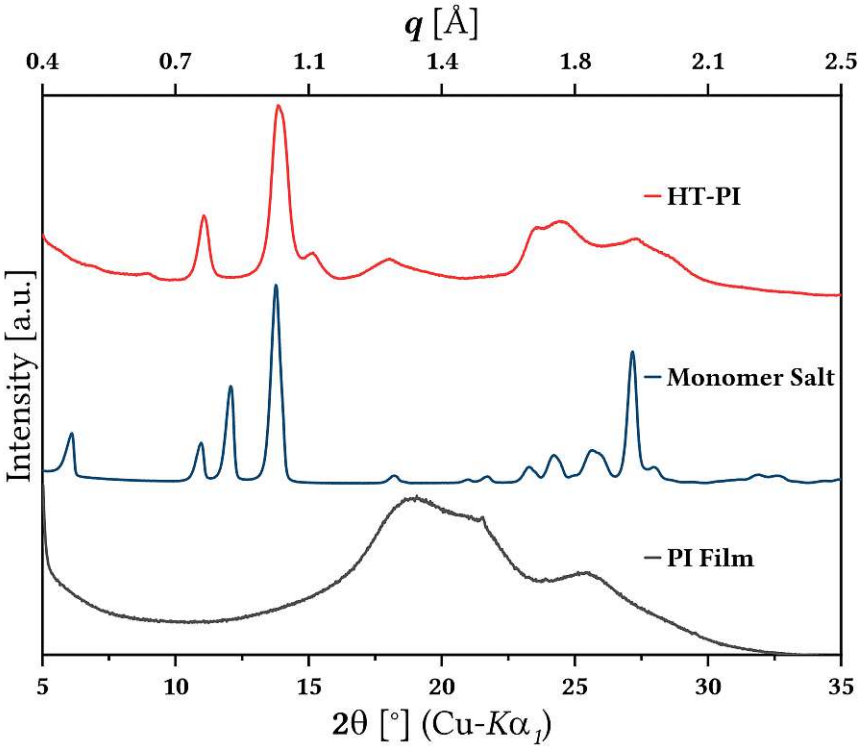

Figure C.5: PXRD patterns of a hydrothermally synthesized sBPDA-pPDA PI, its monomer-salt precursor, and of a PI film of the same system.

C.6 sBPDA-mPDA

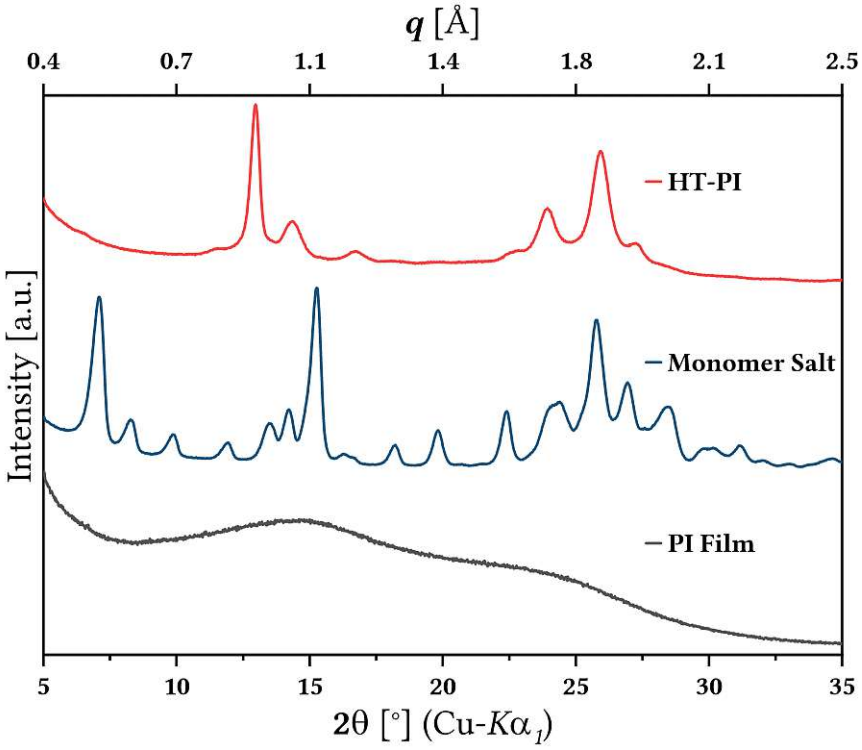

Figure C.6: PXRD patterns of a hydrothermally synthesized sBPDA-mPDA PI, its monomer-salt precursor, and of a PI film of the same system.

C.7 sBPDA-1FmPDA

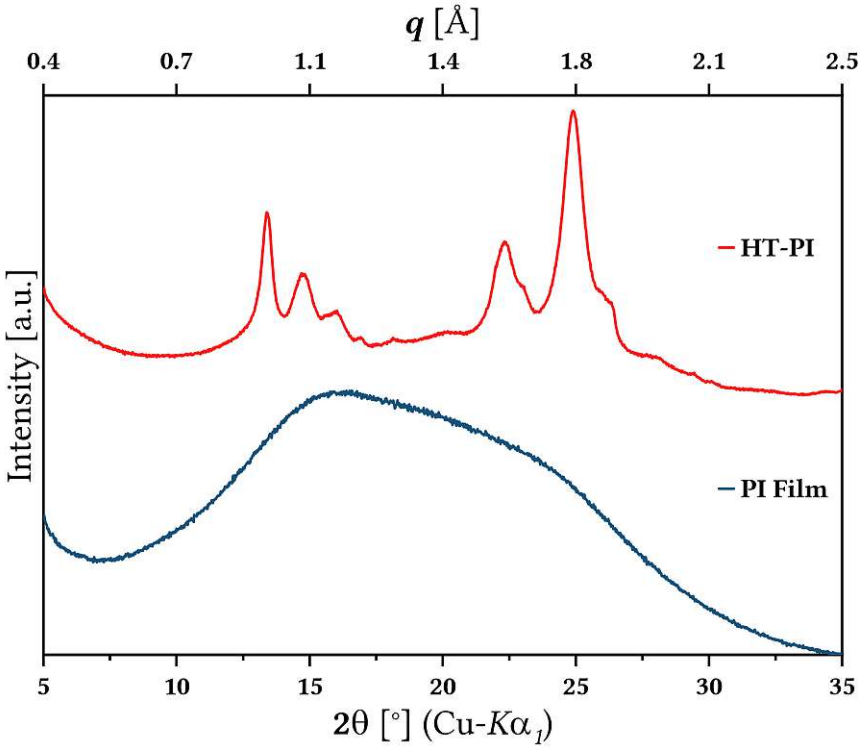

Figure C.7: PXRD patterns of a hydrothermally synthesized PI and of a PI film of the sBPDA-1FmPDA system.

C.8 sBPDA-4FmPDA

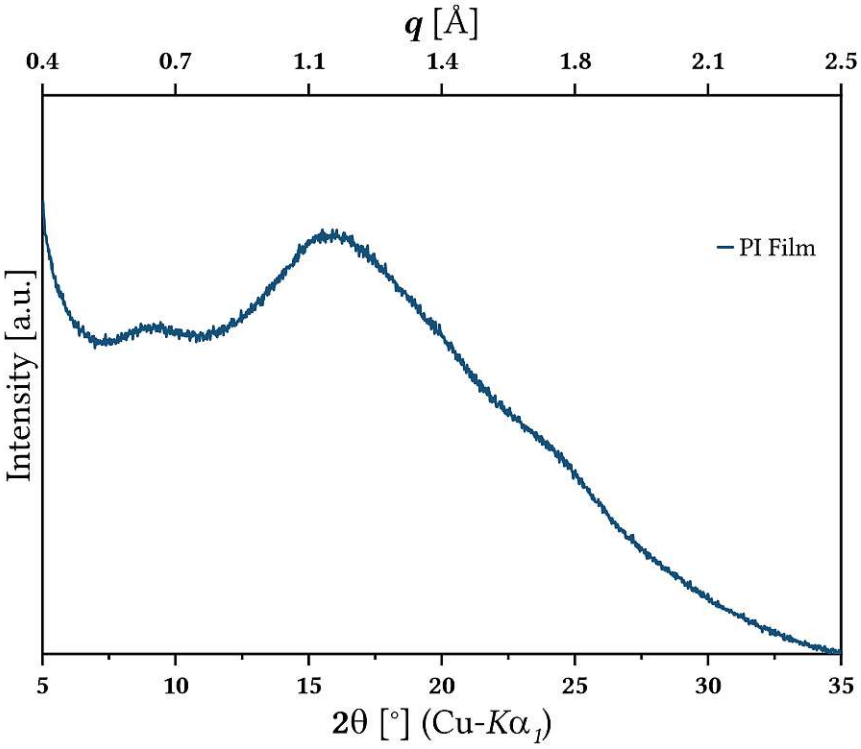

Figure C.8: PXRD pattern of a PI film of the sBPDA-4FPDA system.

C.9 sBPDA-Bz

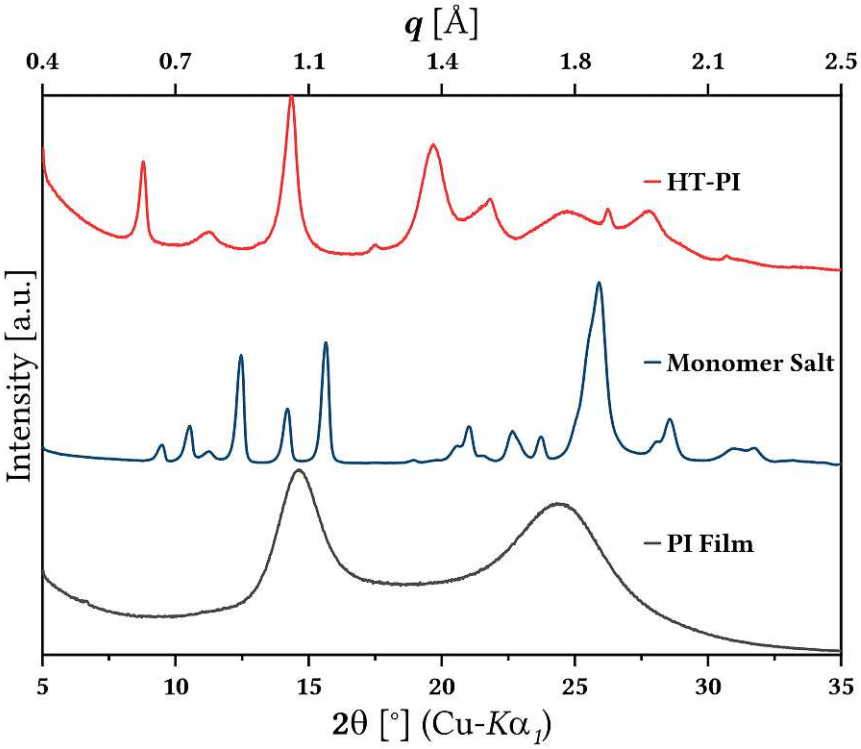

Figure C.9: PXRD patterns of a hydrothermally synthesized sBPDA-Bz PI, its monomer-salt precursor, and of a PI film of the same system.

C.10 sBPDA-DATP

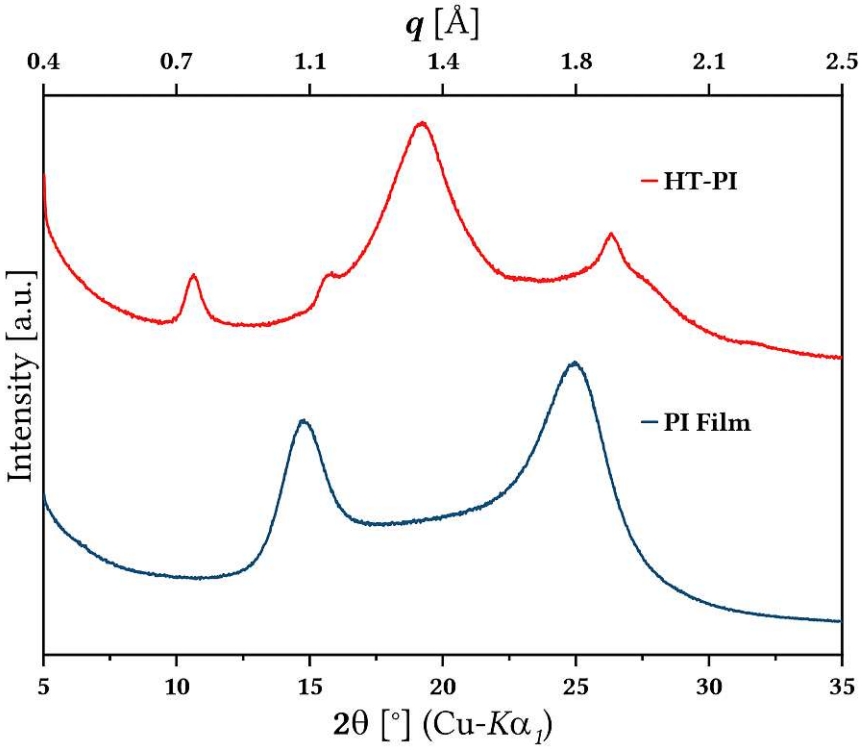

Figure C.10: PXRD patterns of a hydrothermally synthesized sBPDA-DATP PI, its monomer-salt precursor, and of a PI film of the same system.

C.11 PMDA-oDMBz

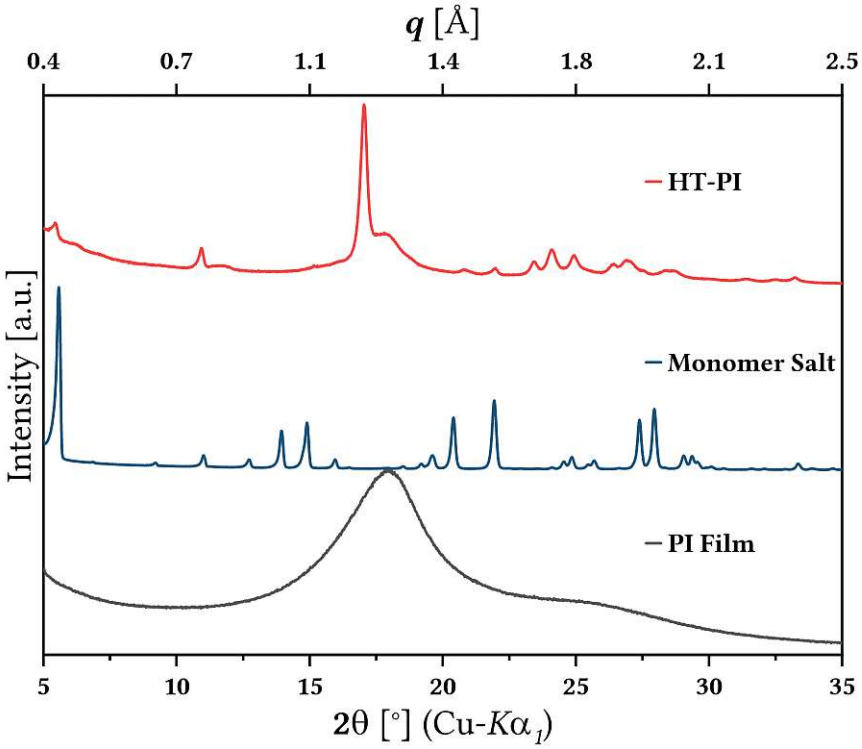

Figure C.11: PXRD patterns of a hydrothermally synthesized PMDA-oDMBz PI, its monomer-salt precursor, and of a PI film of the same system.

C.12 PMDA-mDMBz

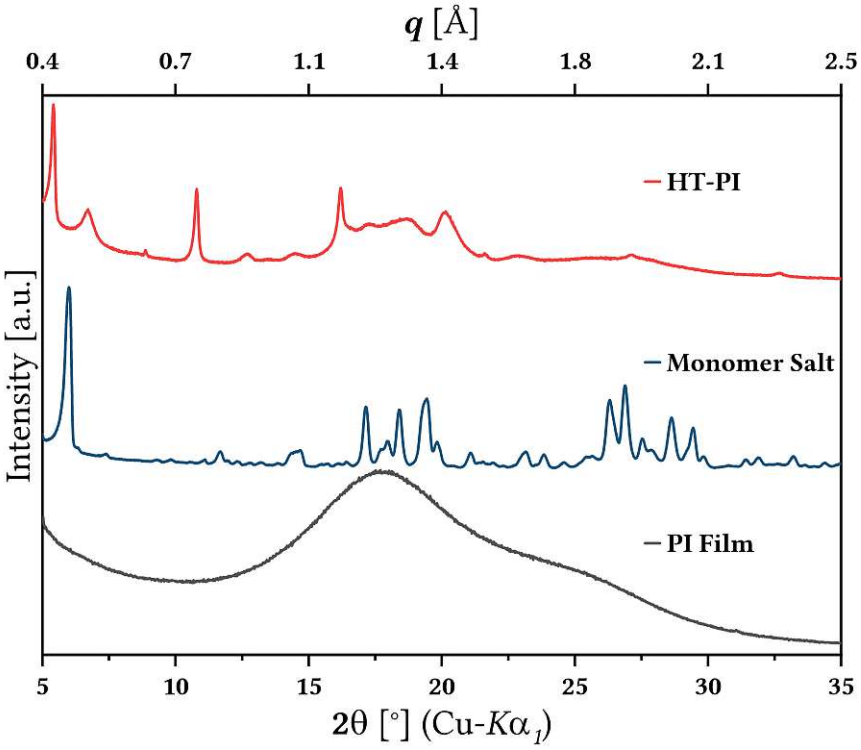

Figure C.12: PXRD patterns of a hydrothermally synthesized PMDA-mDMBz PI, its monomer-salt precursor, and of a PI film of the same system.

C.13 PMDA-oTMBz

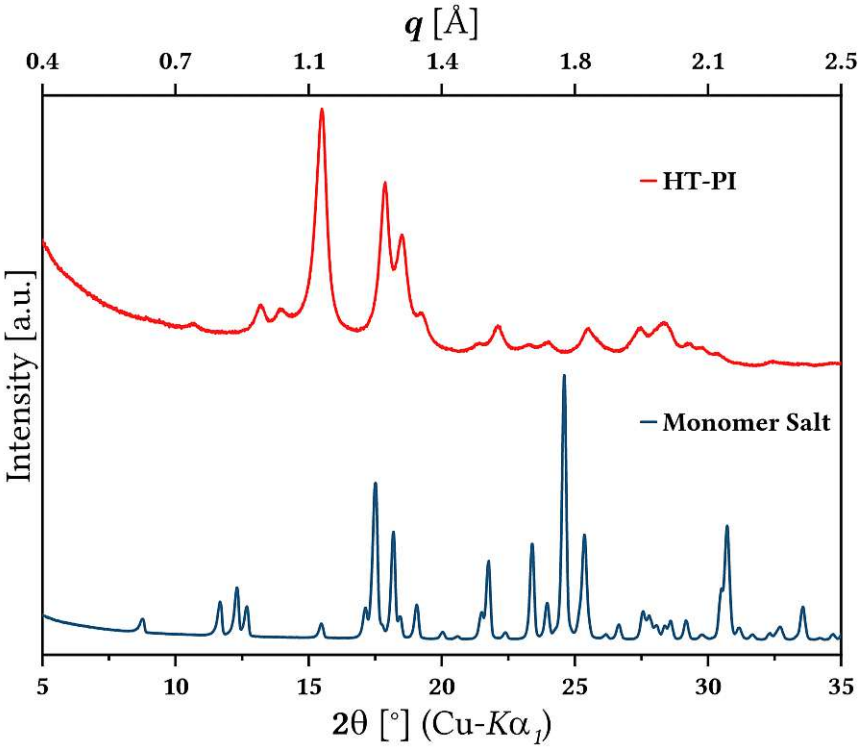

Figure C.13: PXRD patterns of a hydrothermally synthesized PMDA-oTMBz PI and its monomer-salt precursor.

C.14 PMDA-oDIAN

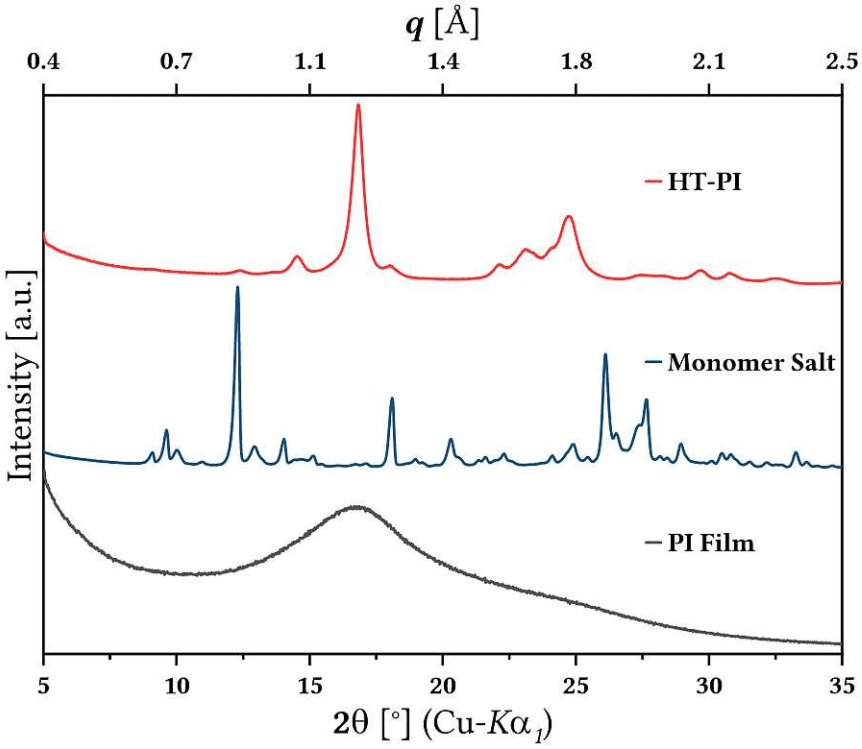

Figure C.14: PXRD patterns of a hydrothermally synthesized PMDA-oDIAN PI, its monomer-salt precursor, and of a PI film of the same system.

C.15 PMDA-oTFBz

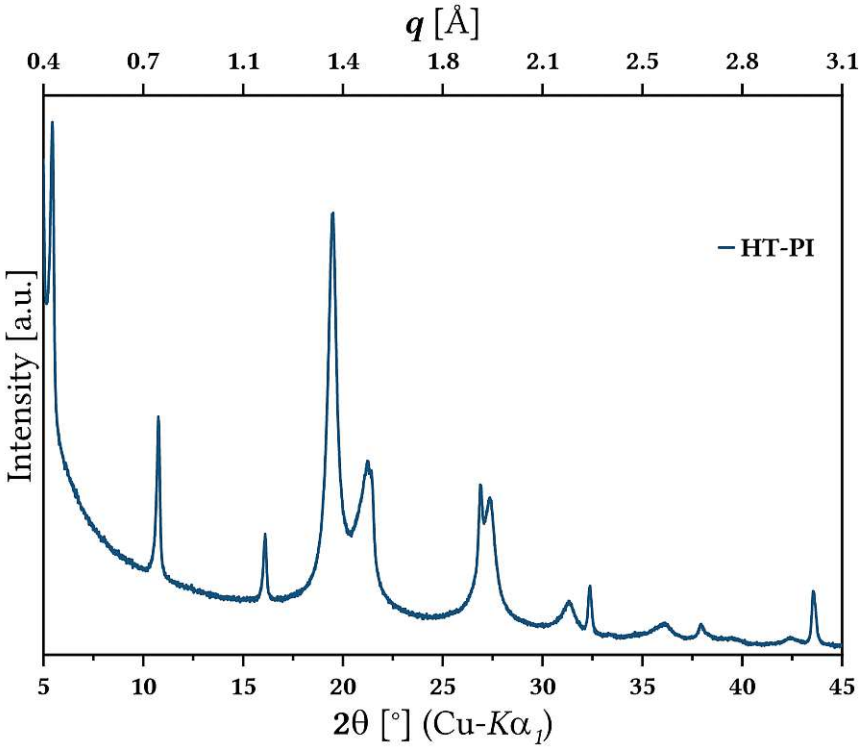

Figure C.15: PXRD pattern of a hydrothermally synthesized PMDA-oTFBz PI.

C.16 PMDA-mTFBz

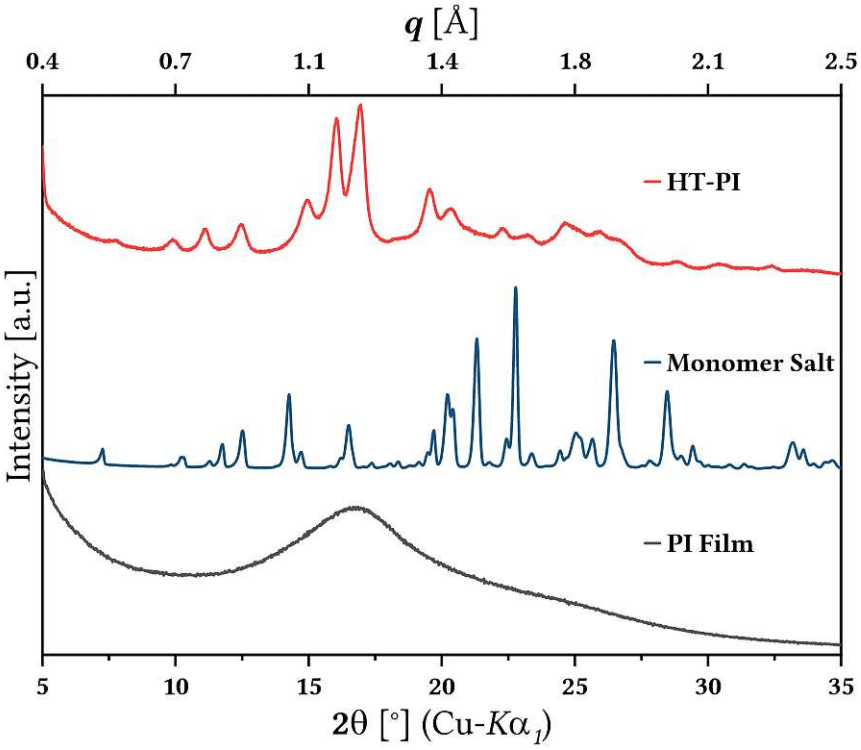

Figure C.16: PXRD patterns of a hydrothermally synthesized PMDA-mTFBz PI, its monomer-salt precursor, and of a PI film of the same system.

C.17 PMDA-oDFBz

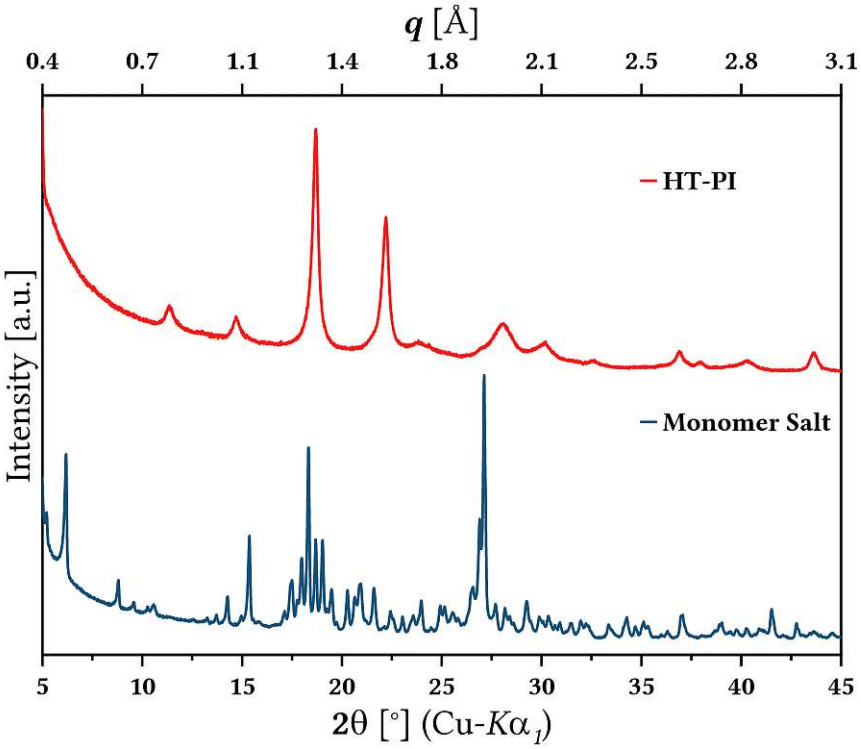

Figure C.17: PXRD pattern of a hydrothermally synthesized PMDA-oTFBz PI and its monomer-salt precursor.

C.18 PMDA-oDHBz

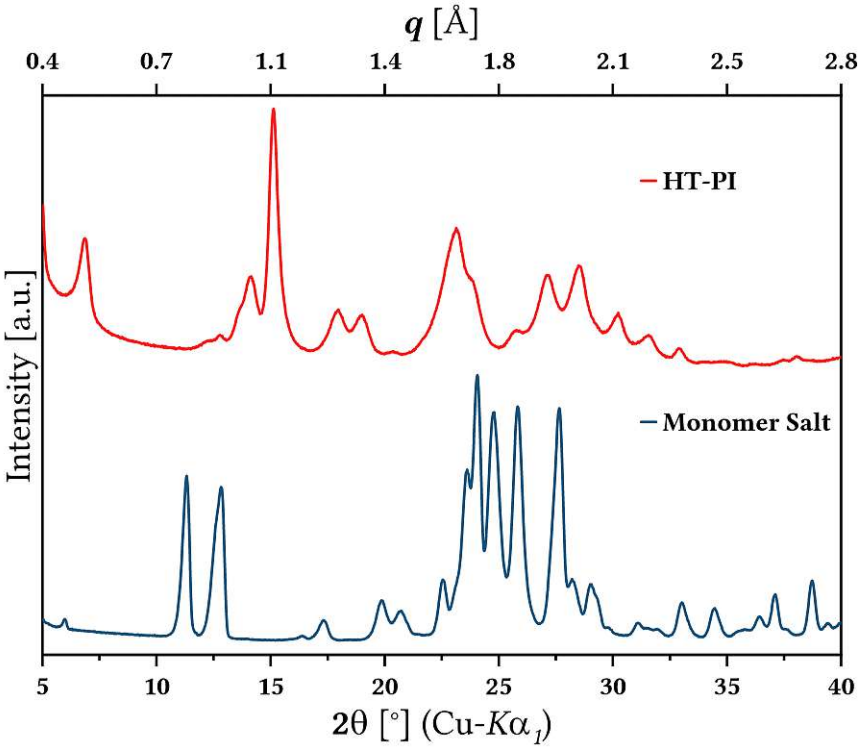

Figure C.18: PXRD patterns of a hydrothermally synthesized PMDA-oDHBz PI and its monomer-salt precursor.

C.19 PMDA-sODA

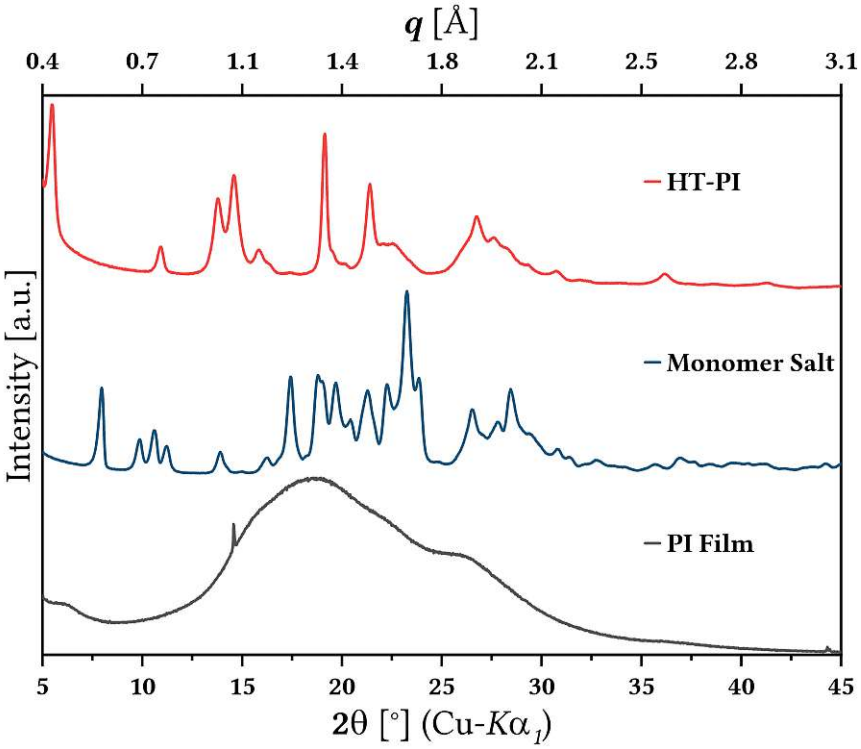

Figure C.19: PXRD patterns of a hydrothermally synthesized PMDA-sODA PI, its monomer-salt precursor, and of a PI film of the same system.

C.20 PMDA-aODA

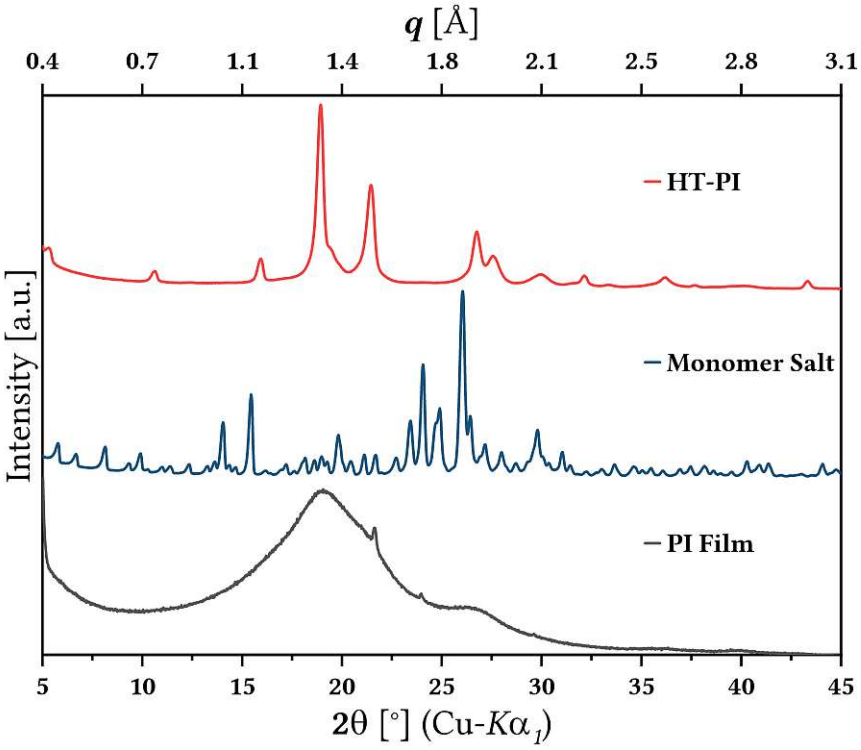

Figure C.20: PXRD patterns of a hydrothermally synthesized PMDA-aODA PI, its monomer-salt precursor, and of a PI film of the same system.

C.21 PMDA-pBAPB

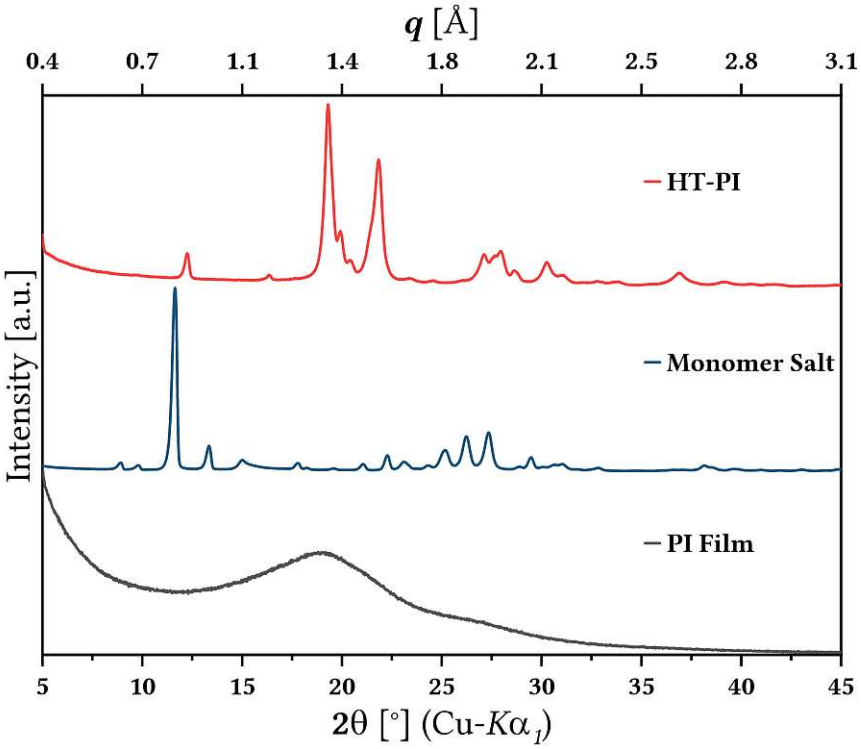

Figure C.21: PXRD patterns of a hydrothermally synthesized PMDA-pBAPB PI, its monomer-salt precursor, and of a PI film of the same system.

C.22 PMDA-mBAPB

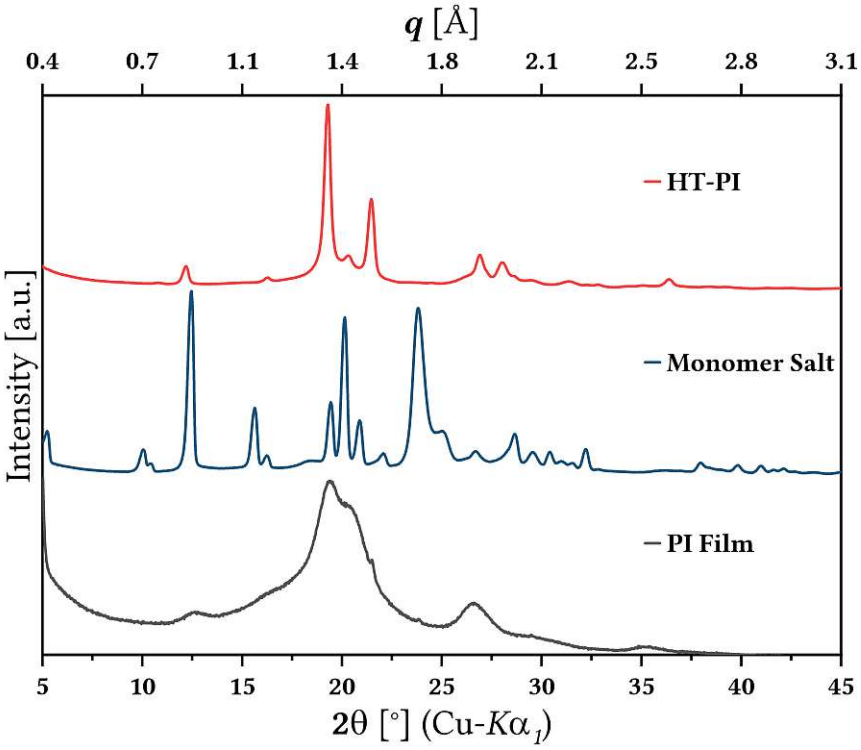

Figure C.22: PXRD patterns of a hydrothermally synthesized PMDA-mBAPB PI, its monomer-salt precursor, and of a PI film of the same system.

C.23 PMDA-pBISA

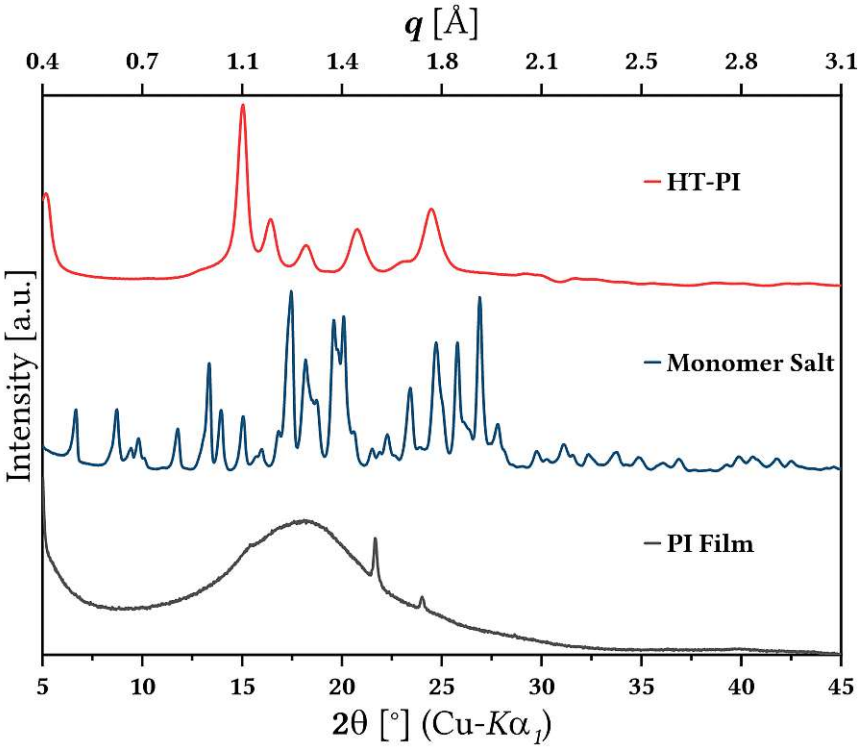

Figure C.23: PXRD patterns of a hydrothermally synthesized PMDA-pBISA PI, its monomer-salt precursor, and of a PI film of the same system.

C.24 PMDA-mBISA

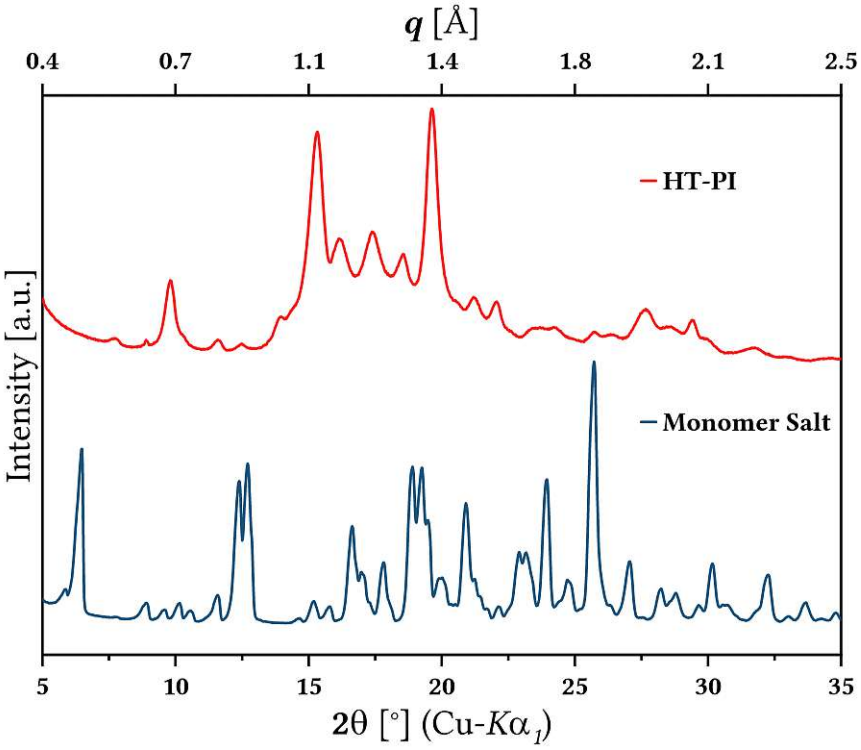

Figure C.24: PXRD patterns of a hydrothermally synthesized PMDA-mBISA PI and its monomer-salt precursor.

C.25 PMDA-APBP

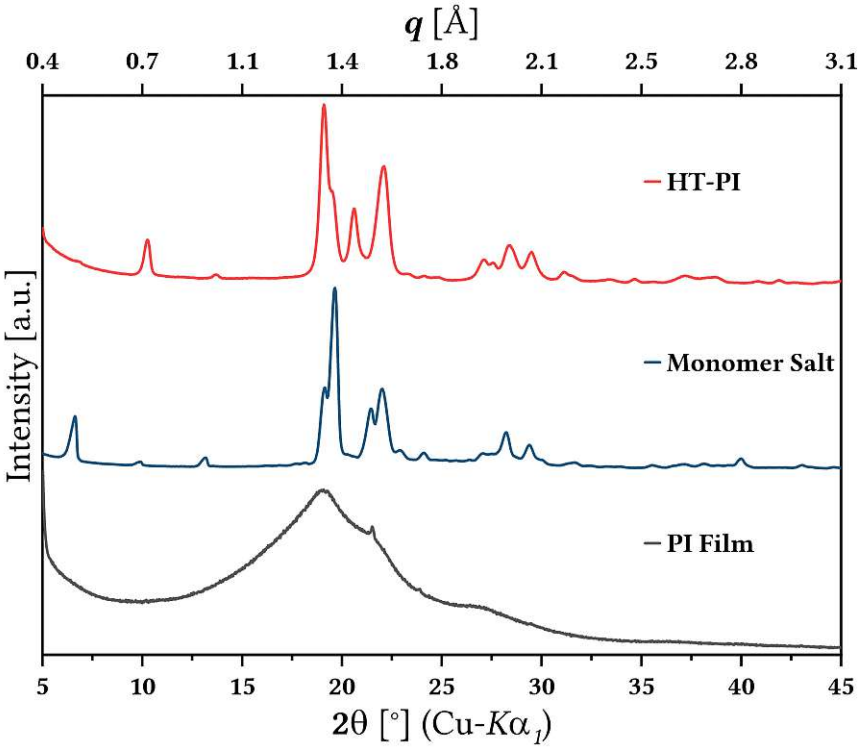

Figure C.25: PXRD patterns of a hydrothermally synthesized PMDA-APBP PI, its monomer-salt precursor, and of a PI film of the same system.

C.26 PMDA-8FAPBP

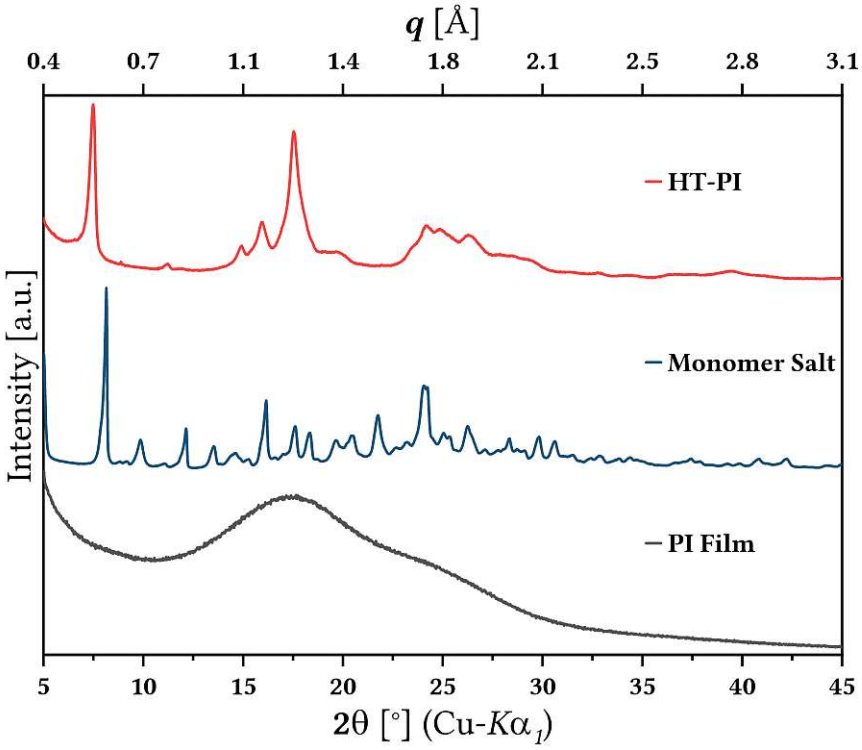

Figure C.26: PXRD patterns of a hydrothermally synthesized PMDA-8FAPBP PI, its monomer-salt precursor, and of a PI film of the same system.

C.27 PMDA-BAPP

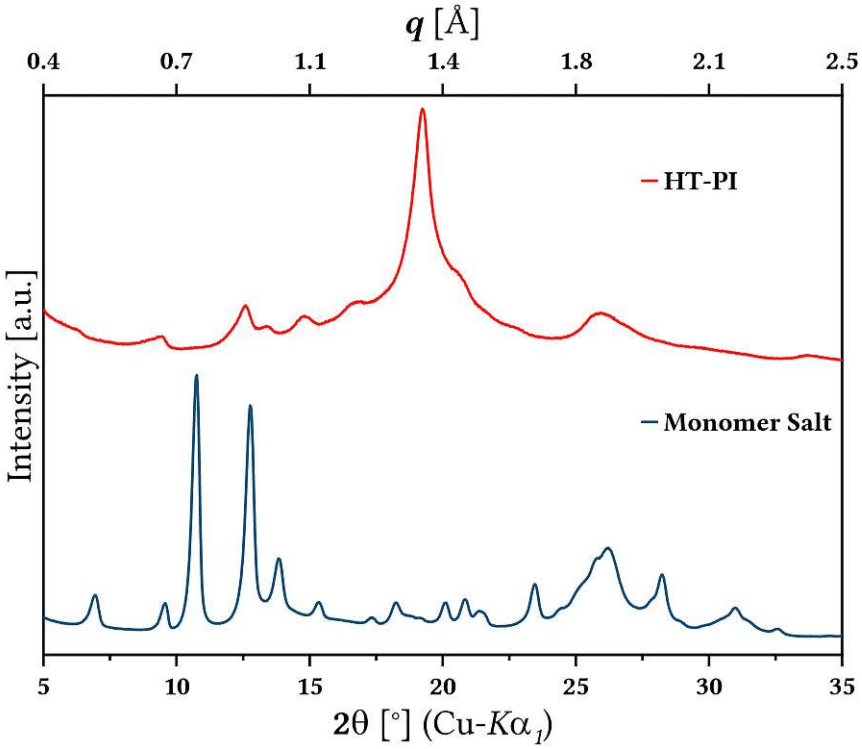

Figure C.27: PXRD patterns of a hydrothermally synthesized PMDA-BAPP PI and its monomer-salt precursor.

C.28 PMDA-6FBAPP

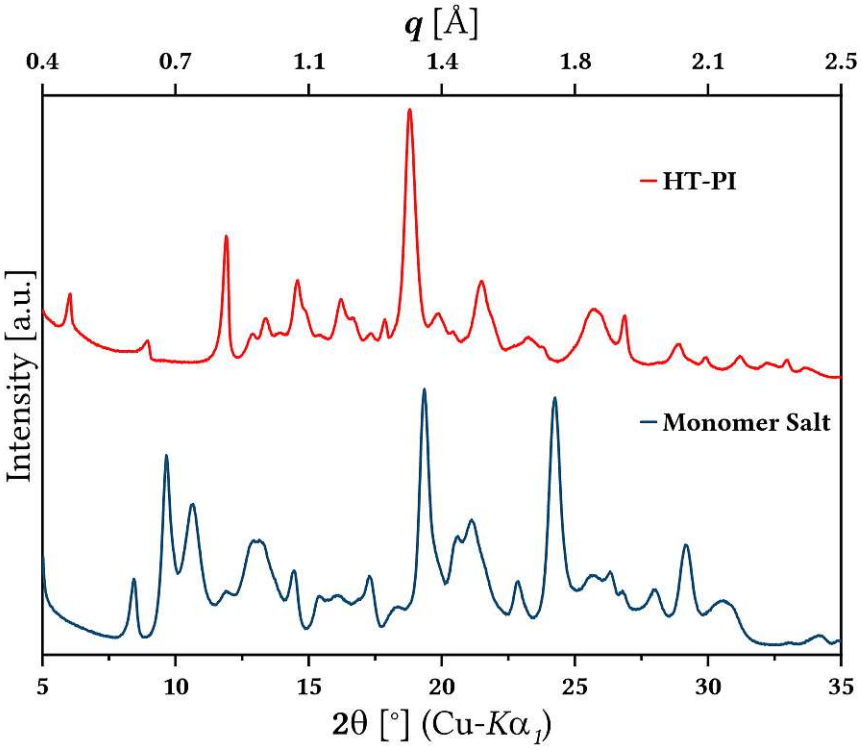

Figure C.28: PXRD patterns of a hydrothermally synthesized PMDA-6FBAPP PI and its monomer-salt precursor.

C.29 PMDA-MDA

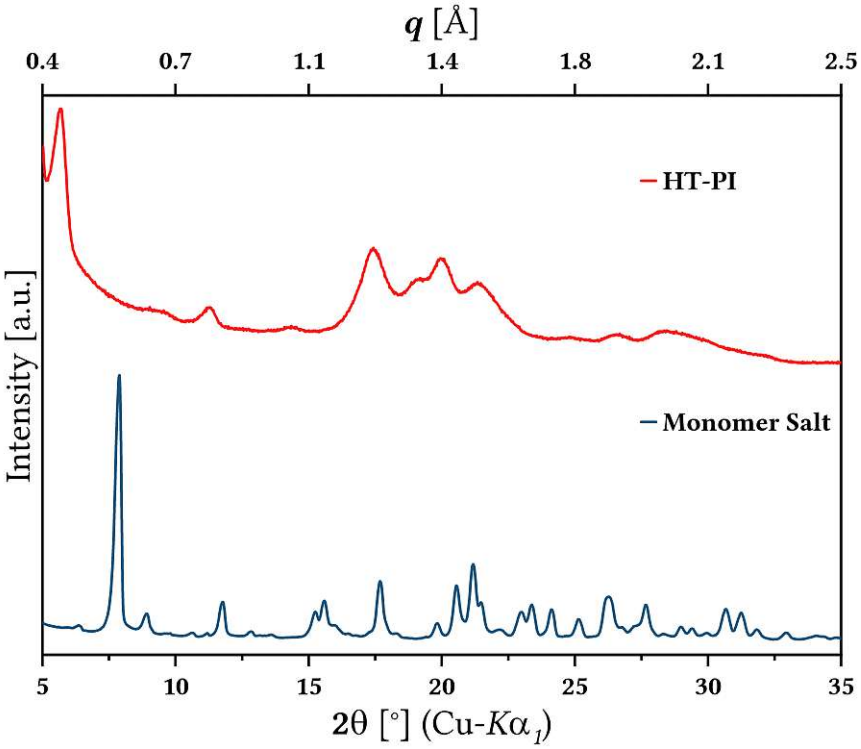

Figure C.29: PXRD patterns of a hydrothermally synthesized PMDA-MDA PI and its monomer-salt precursor.

C.30 PMDA-DAF

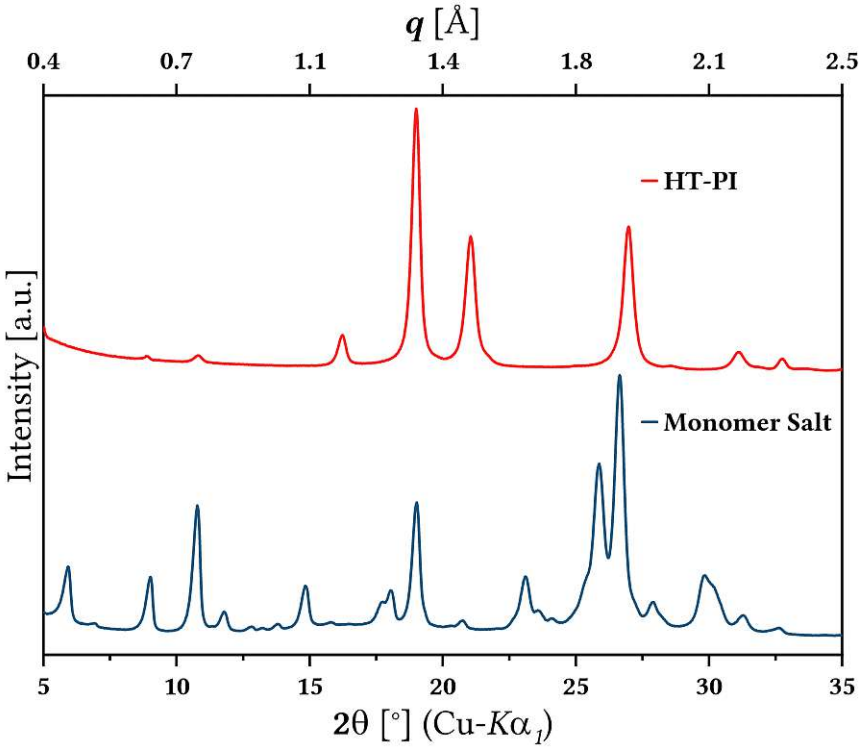

Figure C.30: PXRD patterns of a hydrothermally synthesized PMDA-DAF PI and its monomer-salt precursor.

C.31 PMDA-DADF

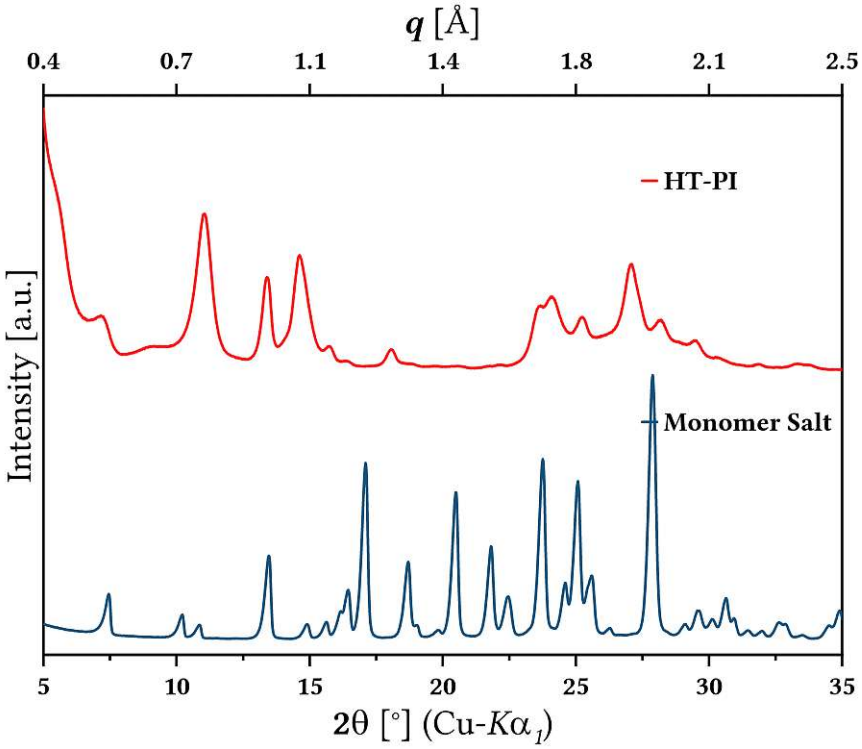

Figure C.31: PXRD patterns of a hydrothermally synthesized PMDA-DADF PI and its monomer-salt precursor.

C.32 PMDA-BAPF

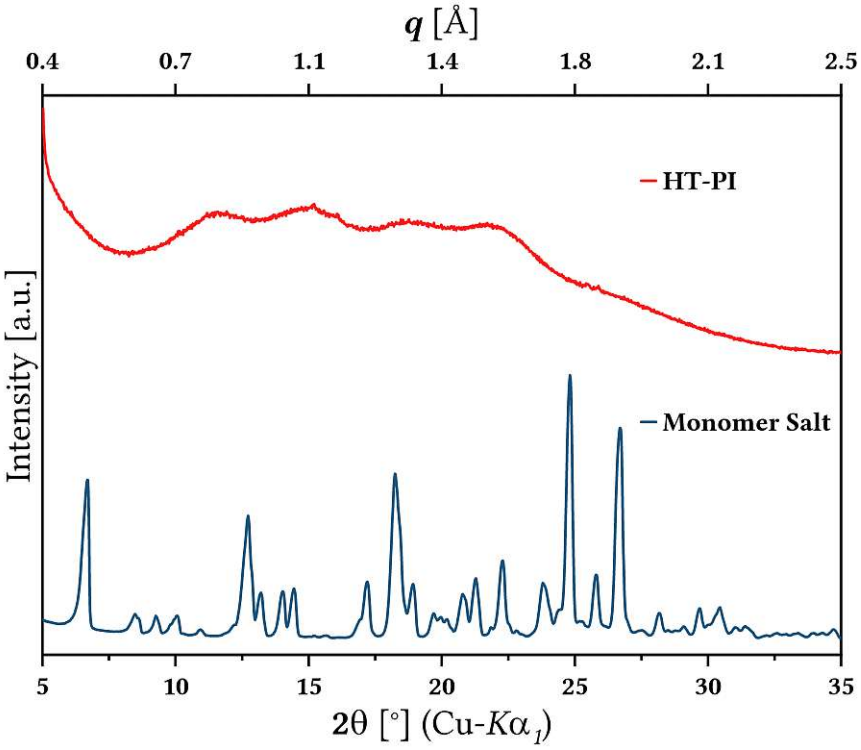

Figure C.32: PXRD patterns of a hydrothermally synthesized PMDA-BAPF PI and its monomer-salt precursor.

C.33 PMDA-MeBAPF

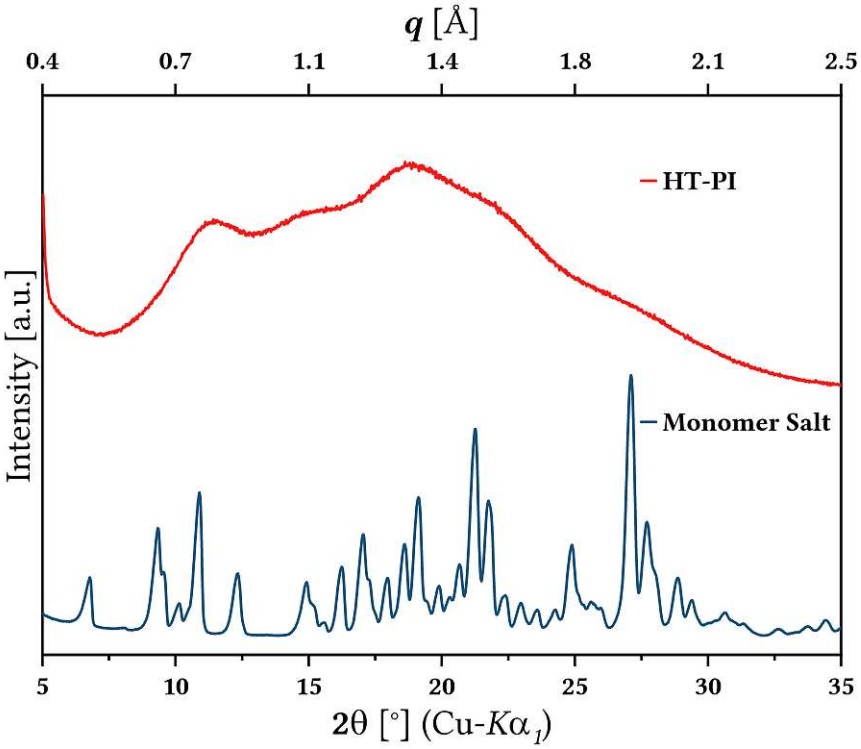

Figure C.33: PXRD patterns of a hydrothermally synthesized PMDA-MeBAPF PI and its monomer-salt precursor.

C.34 sODPA-pPDA

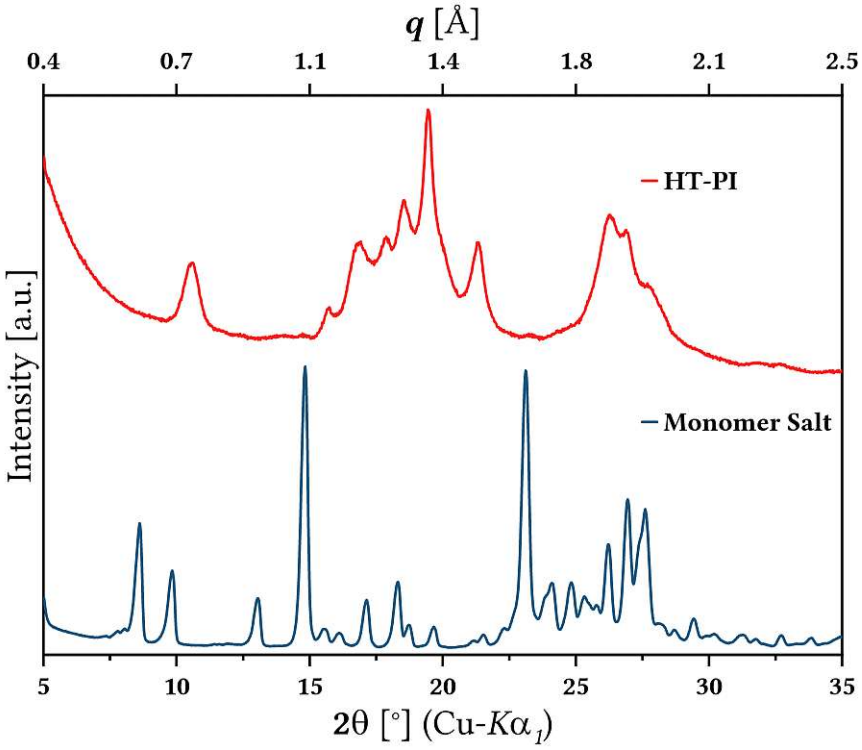

Figure C.34: PXRD patterns of a hydrothermally synthesized sODPA-pPDA PI and its monomer-salt precursor.

C.35 sODPA-mPDA

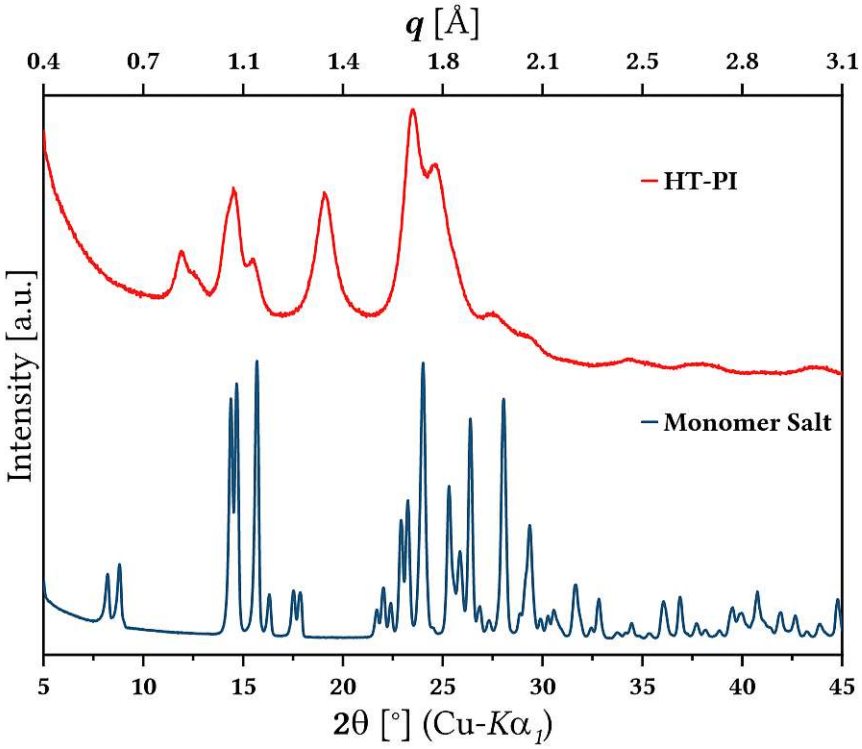

Figure C.35: PXRD patterns of a hydrothermally synthesized sODPA-mPDA PI and its monomer-salt precursor.

C.36 sODPA-Bz

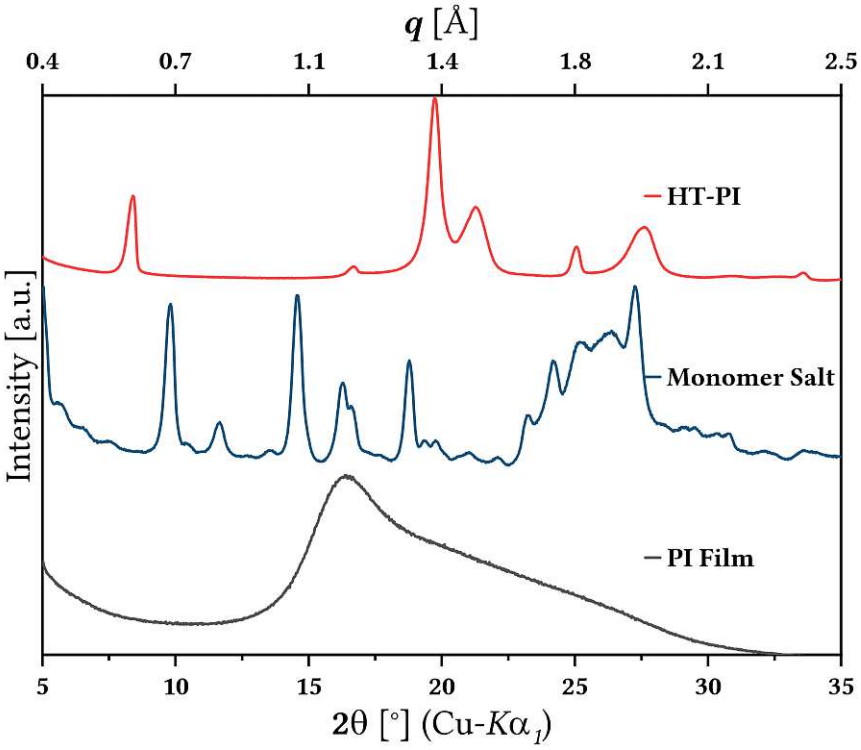

Figure C.36: PXRD patterns of a hydrothermally synthesized sODPA-Bz PI, its monomer-salt precursor, and of a PI film of the same system.

C.37 sODPA-oDIAN

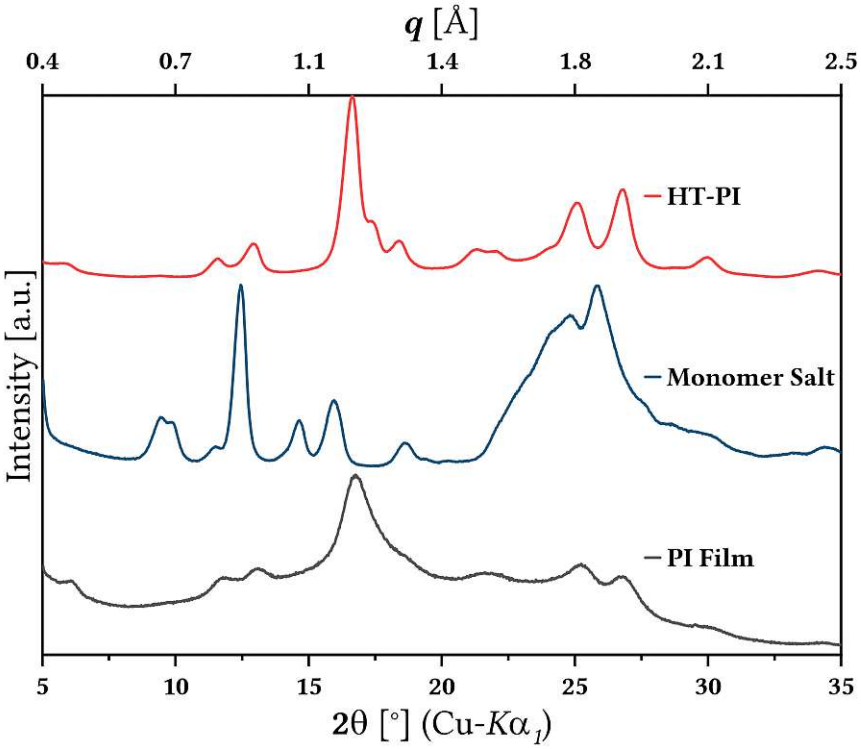

Figure C.37: PXRD patterns of a hydrothermally synthesized sODPA-oDIAN PI, its monomer-salt precursor, and of a PI film of the same system.

C.38 sODPA-mDMBz

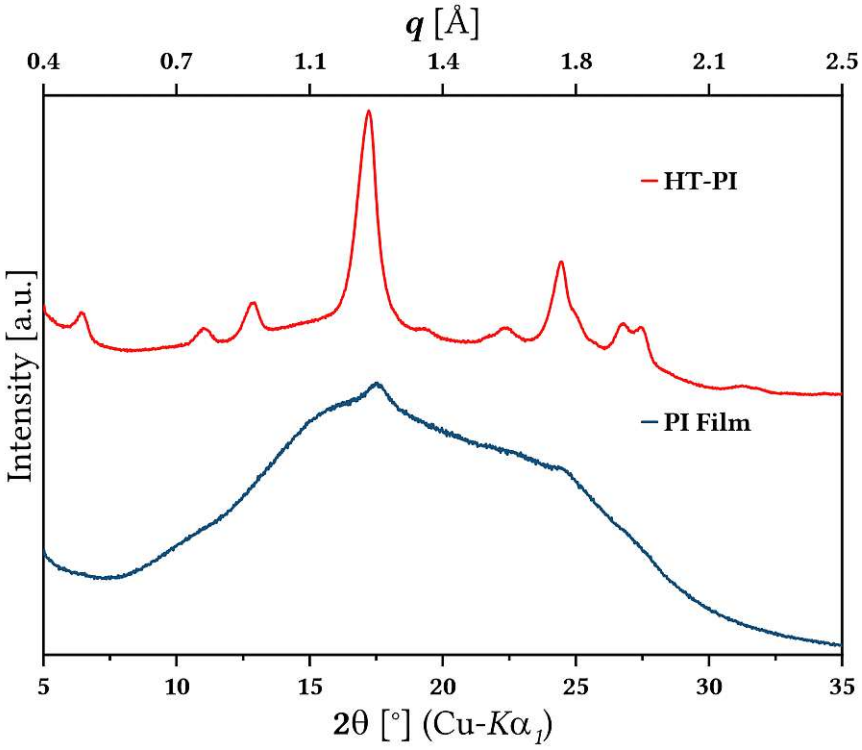

Figure C.38: PXRD patterns of a hydrothermally synthesized sODPA-mDMBz PI and of a PI film of the same system.

C.39 sODPA-oDMBz

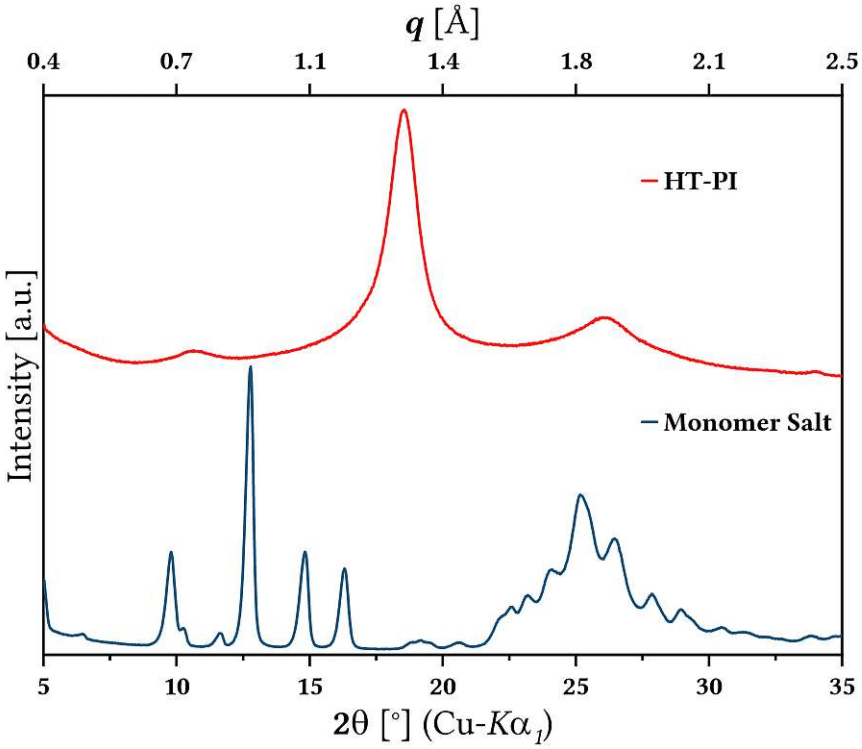

Figure C.39: PXRD patterns of a hydrothermally synthesized sODPA-oDMBz PI and its monomer-salt precursor.

C.40 sODPA-mTFBz

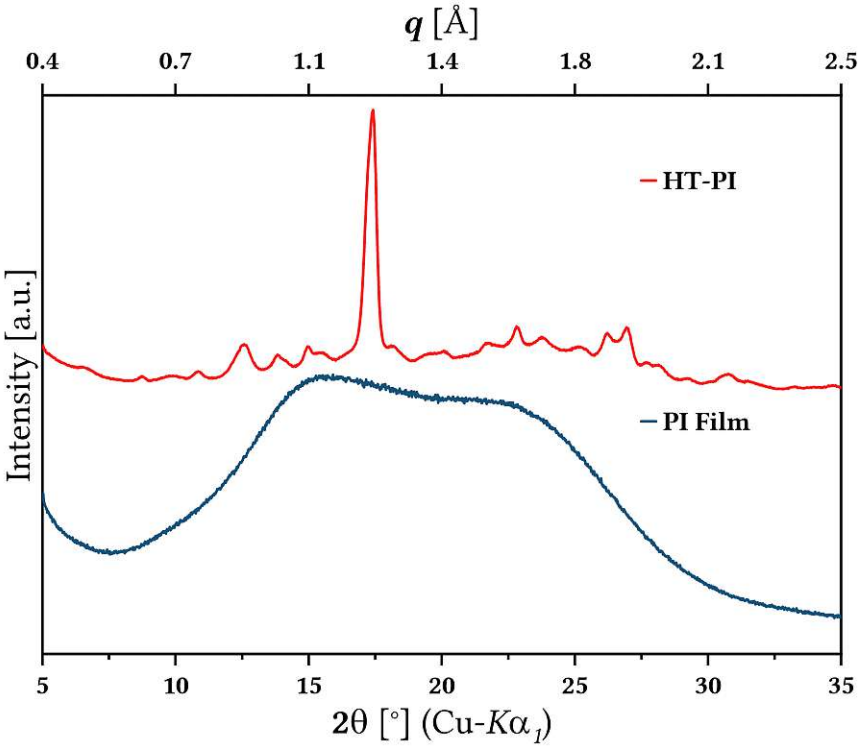

Figure C.40: PXRD patterns of a hydrothermally synthesized sODPA-mTFBz PI and of a PI film of the same system.

C.41 ODPA-ODA

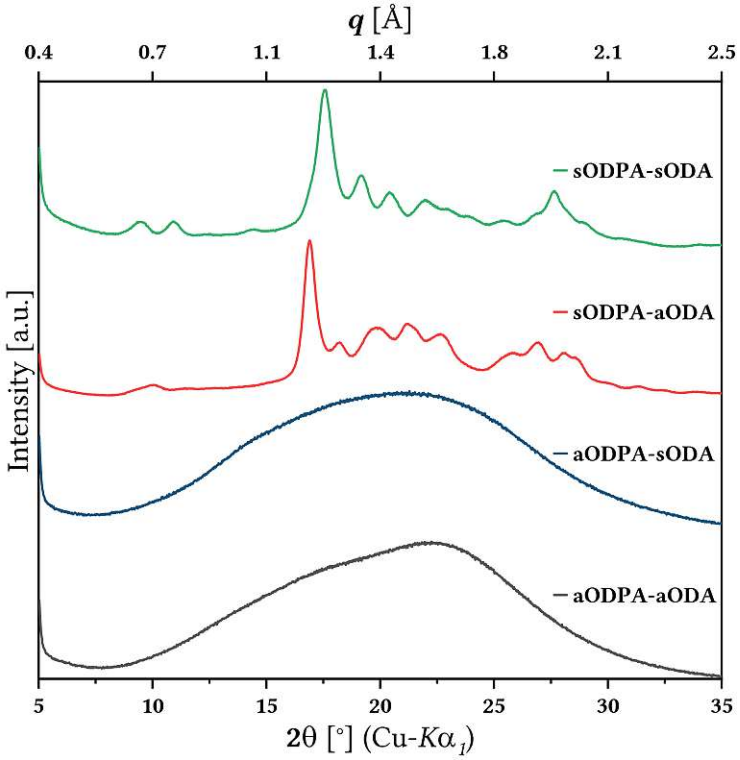

Figure C.41: PXRD patterns of hydrothermally synthesized sODPA-sODA, sODPA-aODA, aODPA-sODA, and aODPA-aODA systems.

C.42 aODPA-pPDA

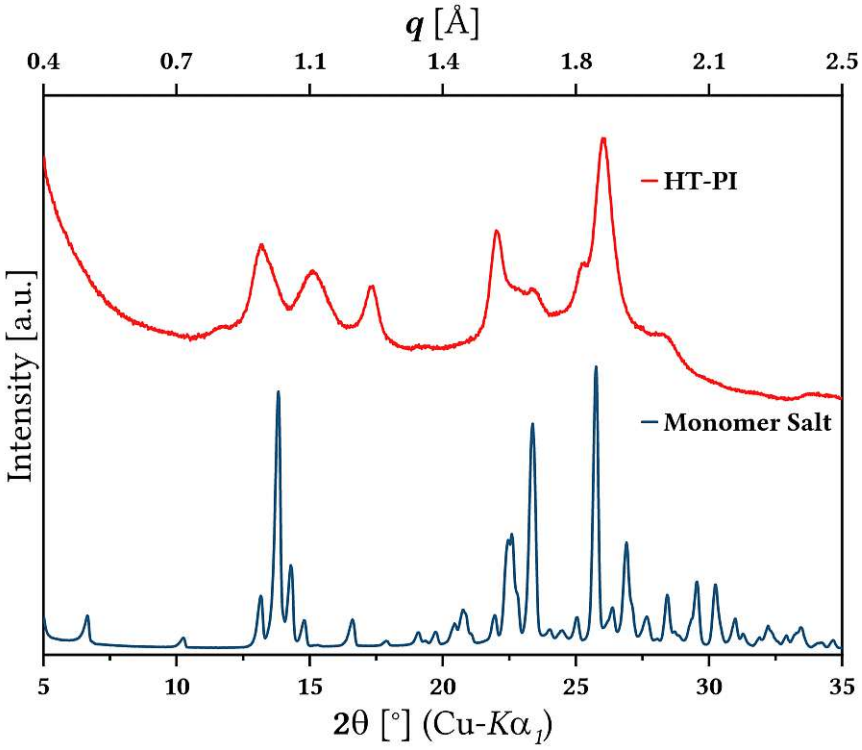

Figure C.42: PXRD patterns of a hydrothermally synthesized aODPA-pPDA PI and its monomer-salt precursor.

C.43 aBDPA-pPDA

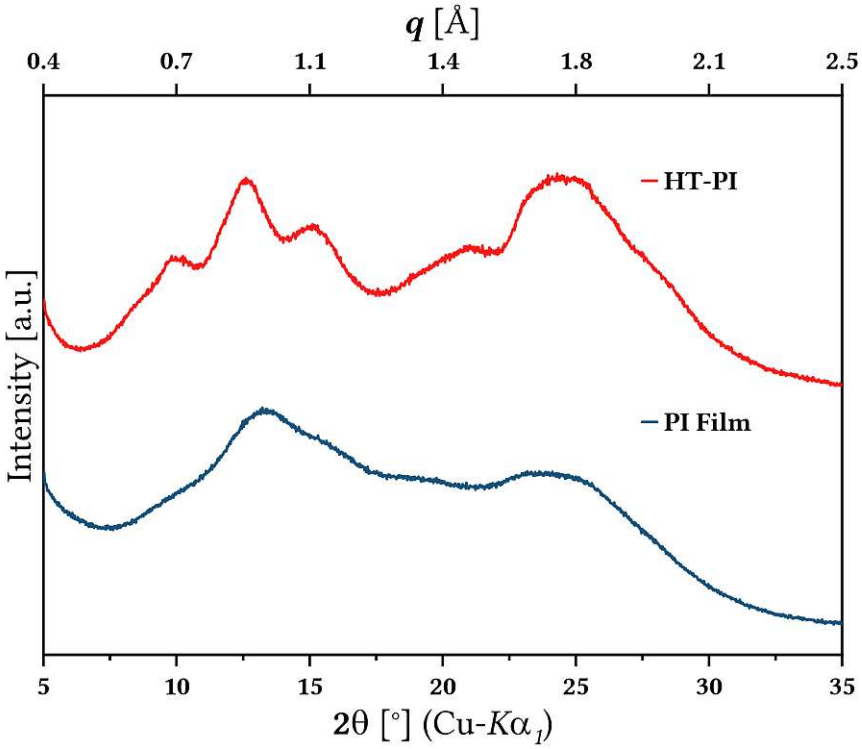

Figure C.43: PXRD patterns of a hydrothermally synthesized aBDPA-pPDA PI and of a PI film of the same system.

C.44 BTDA-pPDA

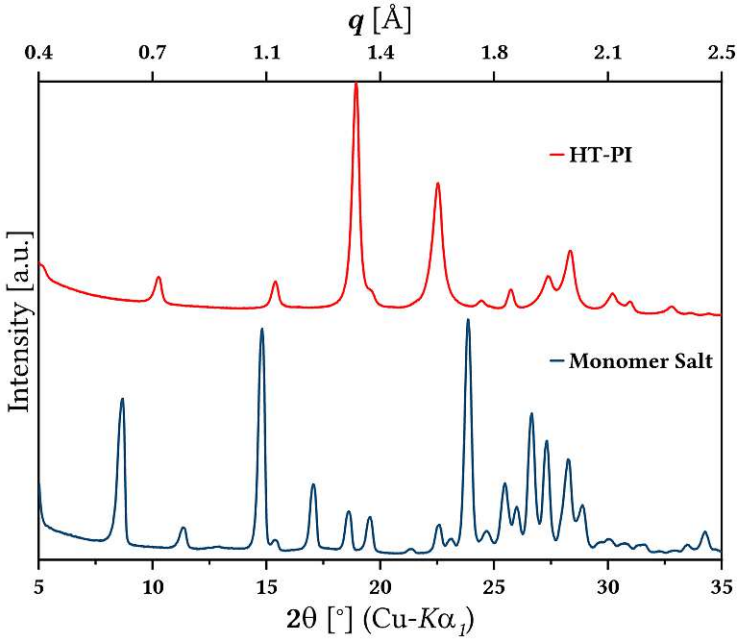

Figure C.44: PXRD patterns of a hydrothermally synthesized BTDA-pPDA PI and its monomer-salt precursor.

C.45 Various PI Systems

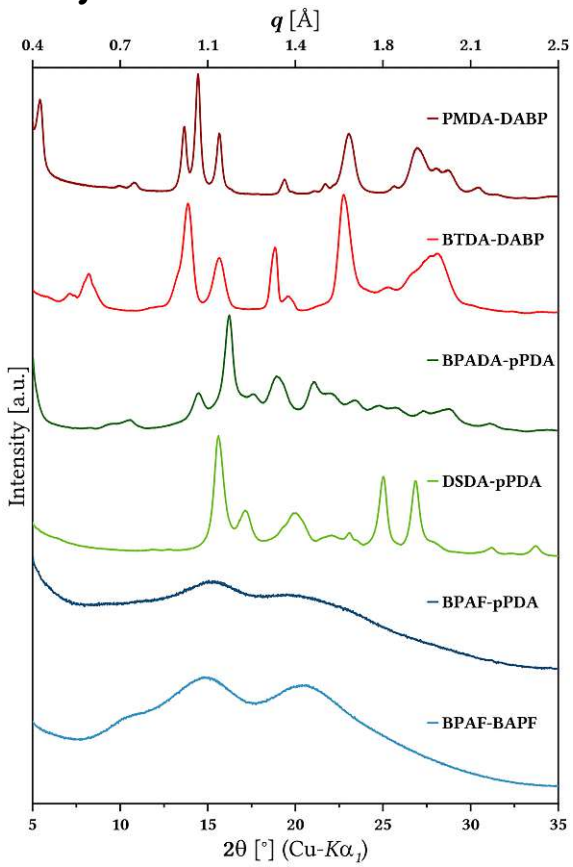

Figure C.45: PXRD patterns of hydrothermally synthesized PMDA-DABP, BTDA-DABP, BPADA-pPDA, DSDA-pPDA, BPAF-pPDA and BPAF-BAPF systems.

D. Supplementary Data: DVS

D.1 Influence of Specimen Dimensions

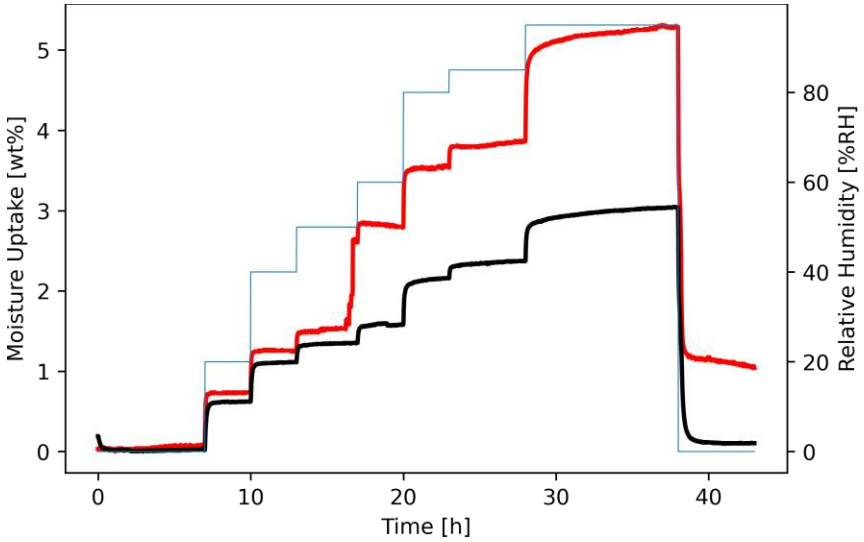

Figure D.1: Measurements of two different spin-coated PMDA-Bz samples using the first measurement method. The black line depicts the mass change of an approx. 1.85 cm^2-sized specimen having a thickness of less than 10 µm, the red line depicts the mass change of an approx. 0.96 cm^2-sized specimen having a thickness of more than 20 µm, and the blue line depicts the targeted RH of this program.

D.2 Data Series Obtained from DVS measurements

D.2.1 PMDA-pPDA

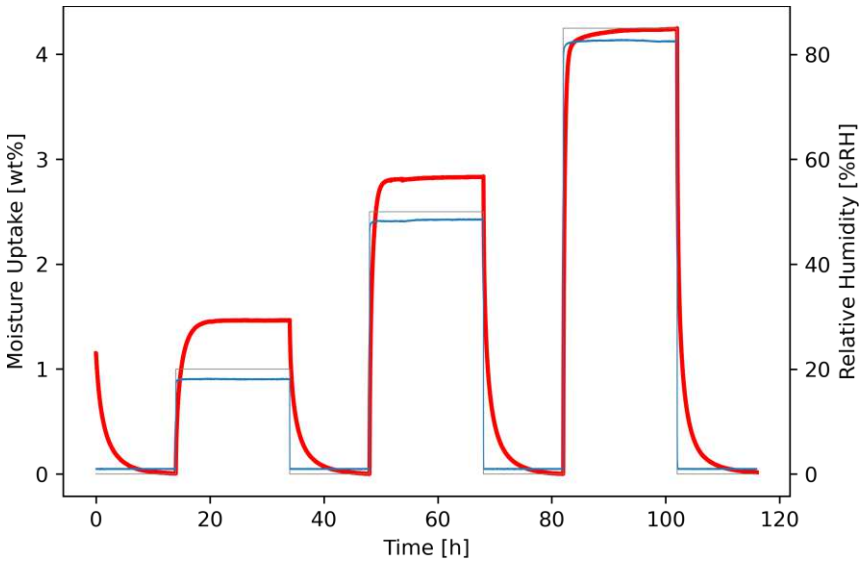

Figure D.2: Full refined measurement profile (116 h total length, two specimens) of PMDA-pPDA used for determining both moisture uptake and diffusion coefficients. The red line depicts the relative sample mass, the gray line depicts the targeted RH and the blue line depicts the actual RH.

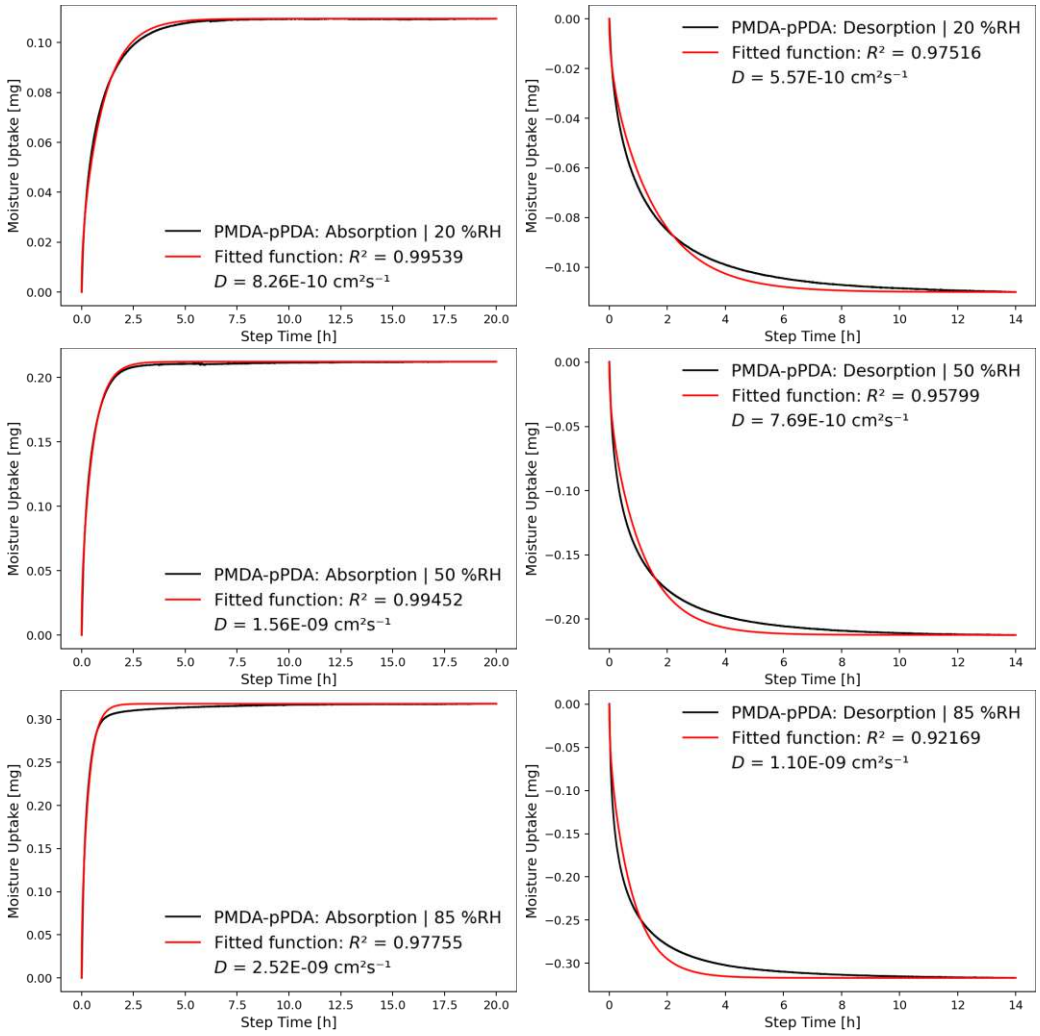

Figure D.3: Each sorption step of the refined PMDA-pPDA measurement, separated for calculating the diffusion coefficients by fitting Crank's mass diffusion formula to the data series.

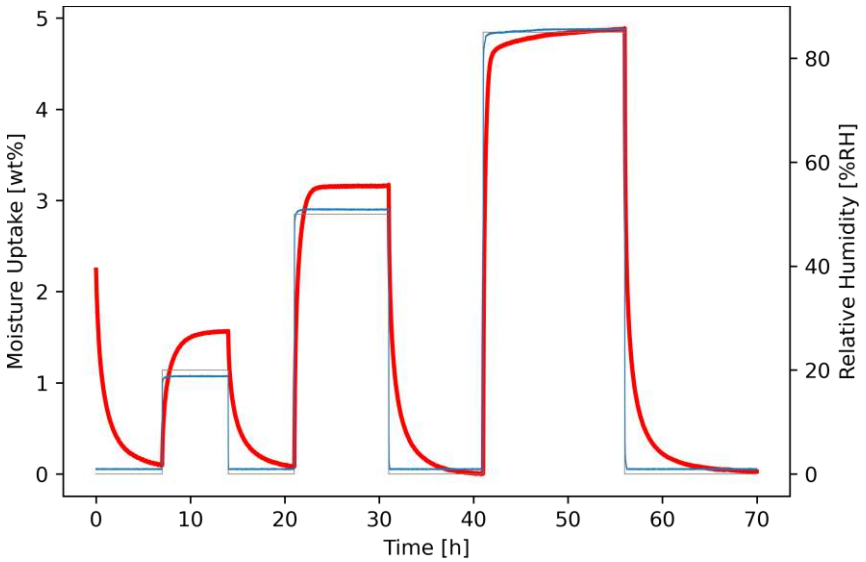

Figure D.4: Initial measurement profile (70 h total length) of PMDA-pPDA, excluded from obtaining results for moisture uptake or diffusion coefficients due to insufficient step duration. The red line depicts the relative sample mass, the gray line depicts the targeted RH and the blue line depicts the actual RH.

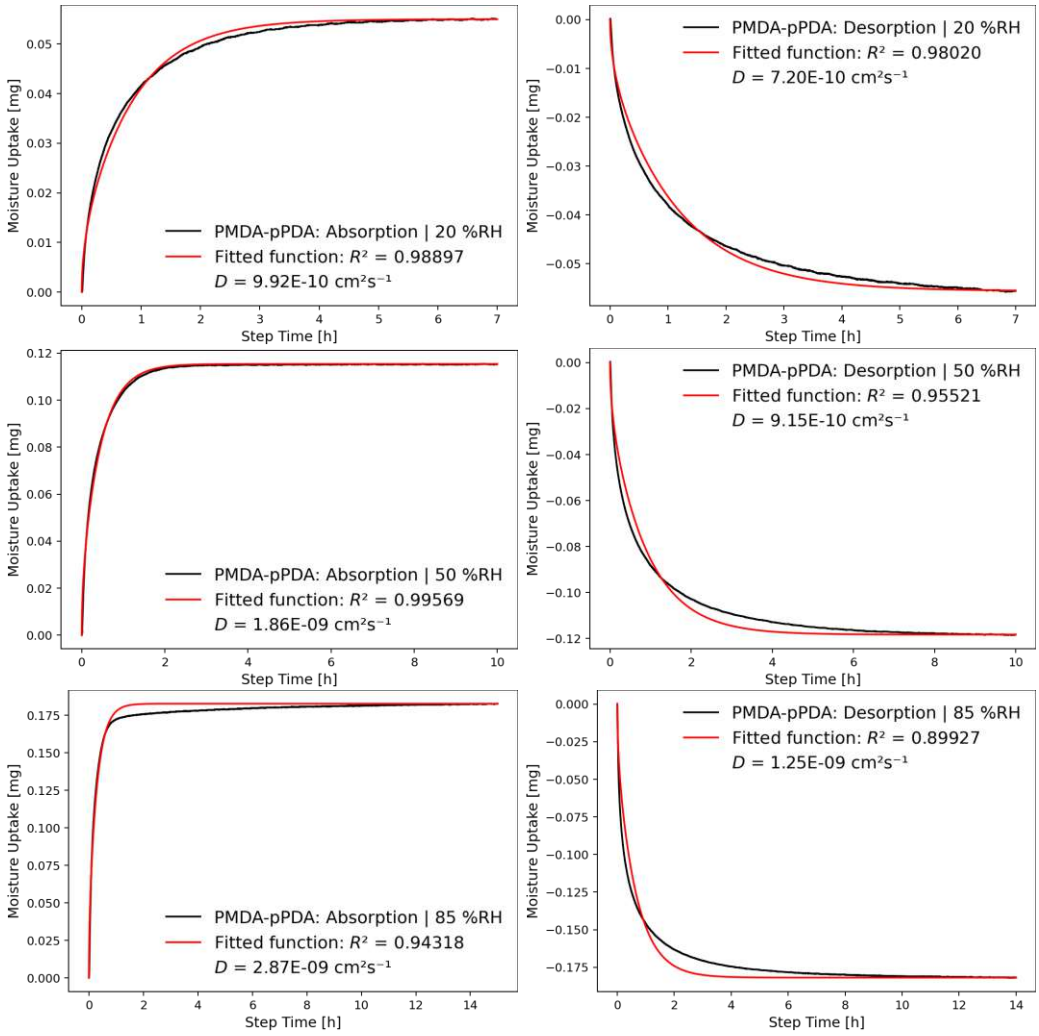

Figure D.5: Each sorption step of the discarded PMDA-pPDA measurement, separated for calculating the (discarded) diffusion coefficients by fitting Crank's mass diffusion formula to the data series.

D.2.2 PMDA-Bz

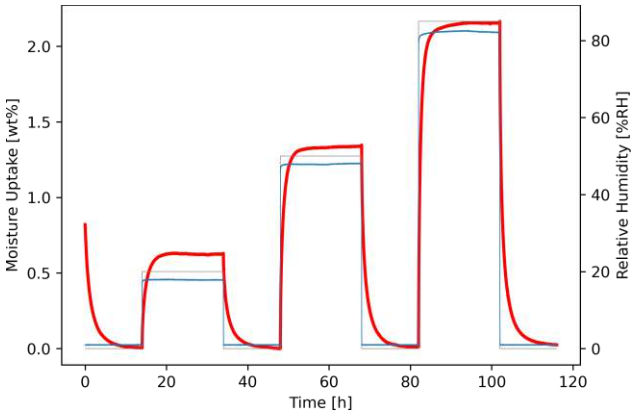

Figure D.6: Full refined measurement profile (116 h total length, two specimens) of PMDA-Bz used for determining both moisture uptake and diffusion coefficients. The red line depicts the relative sample mass, the gray line depicts the targeted RH and the blue line depicts the actual RH.

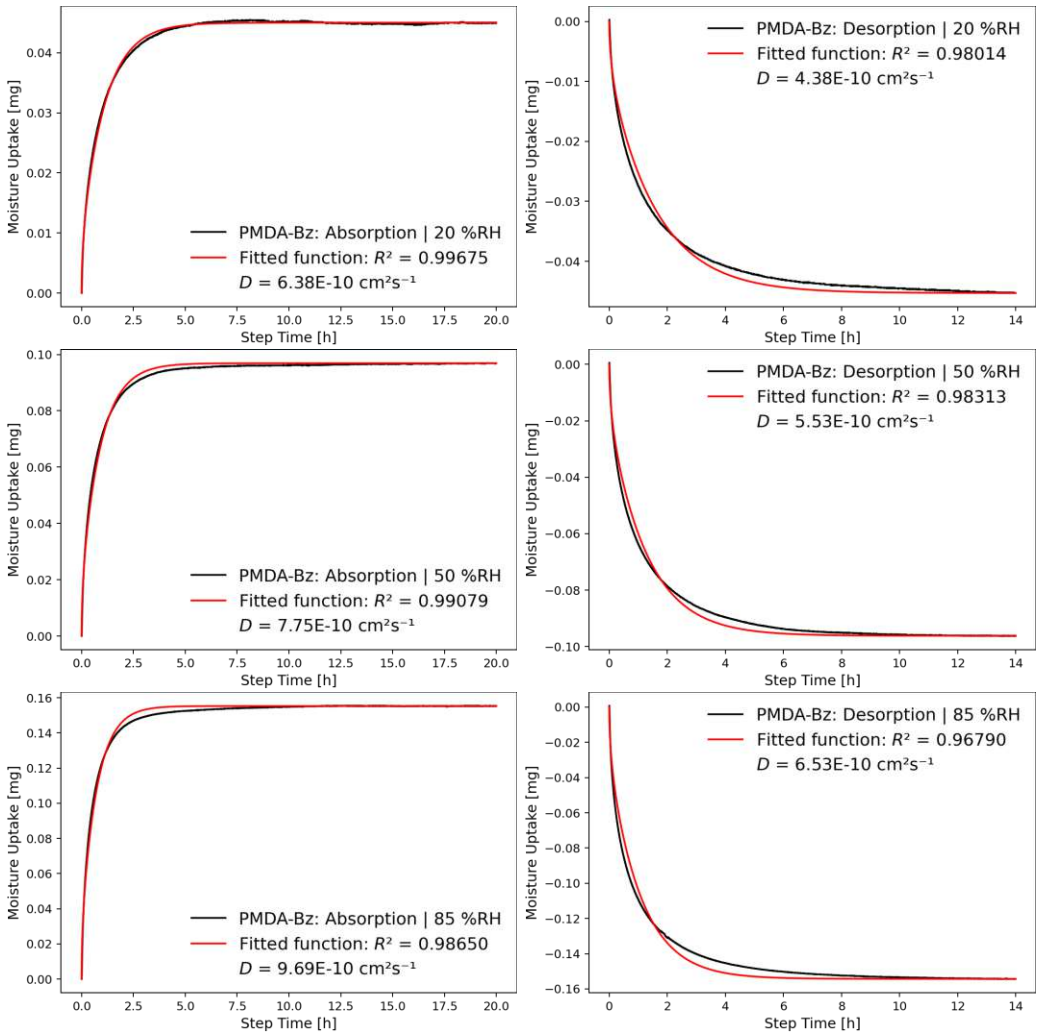

Figure D.7: Each sorption step of the refined PMDA-Bz measurement, separated for calculating the diffusion coefficients by fitting Crank's mass diffusion formula to the data series.

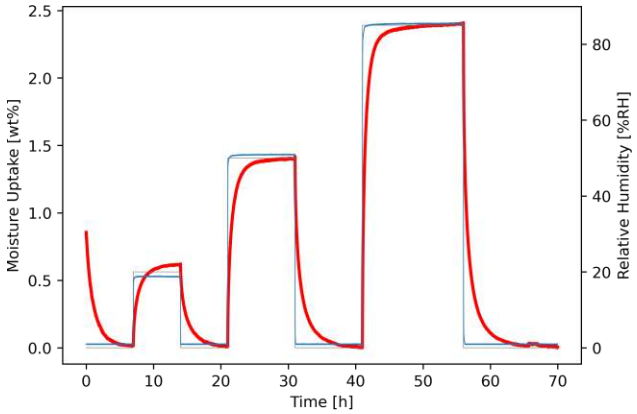

Figure D.8: Initial measurement profile (70 h total length) of PMDA-Bz, excluded from obtaining results for moisture uptake or diffusion coefficients due to insufficient step duration. The red line depicts the relative sample mass, the gray line depicts the targeted RH and the blue line depicts the actual RH.

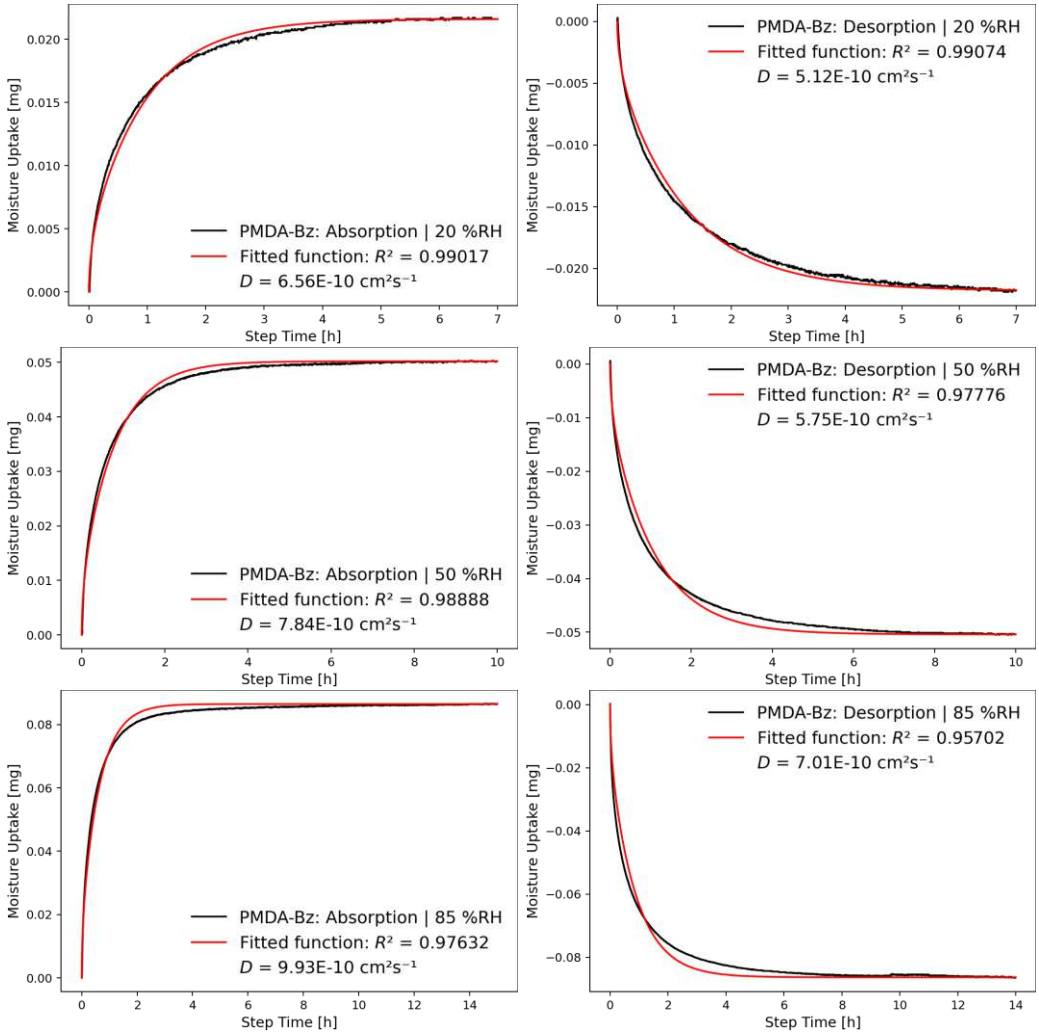

Figure D.9: Each sorption step of the discarded PMDA-Bz measurement, separated for calculating the (discarded) diffusion coefficients by fitting Crank's mass diffusion formula to the data series.

D.2.3 PMDA-DATP

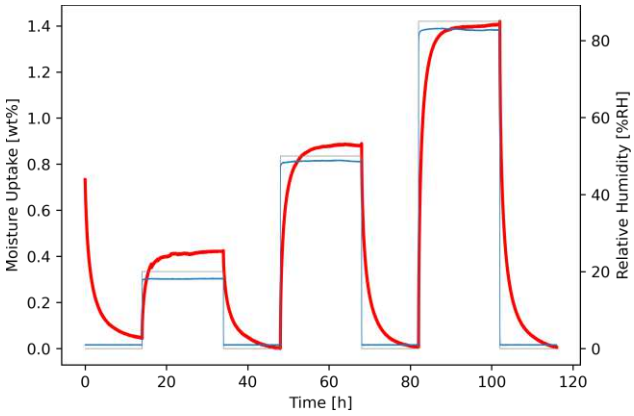

Figure D.10: Full refined measurement profile (116 h total length, two specimens) of PMDA-DATP used for determining both moisture uptake and diffusion coefficients. The red line depicts the relative sample mass, the gray line depicts the targeted RH and the blue line depicts the actual RH.

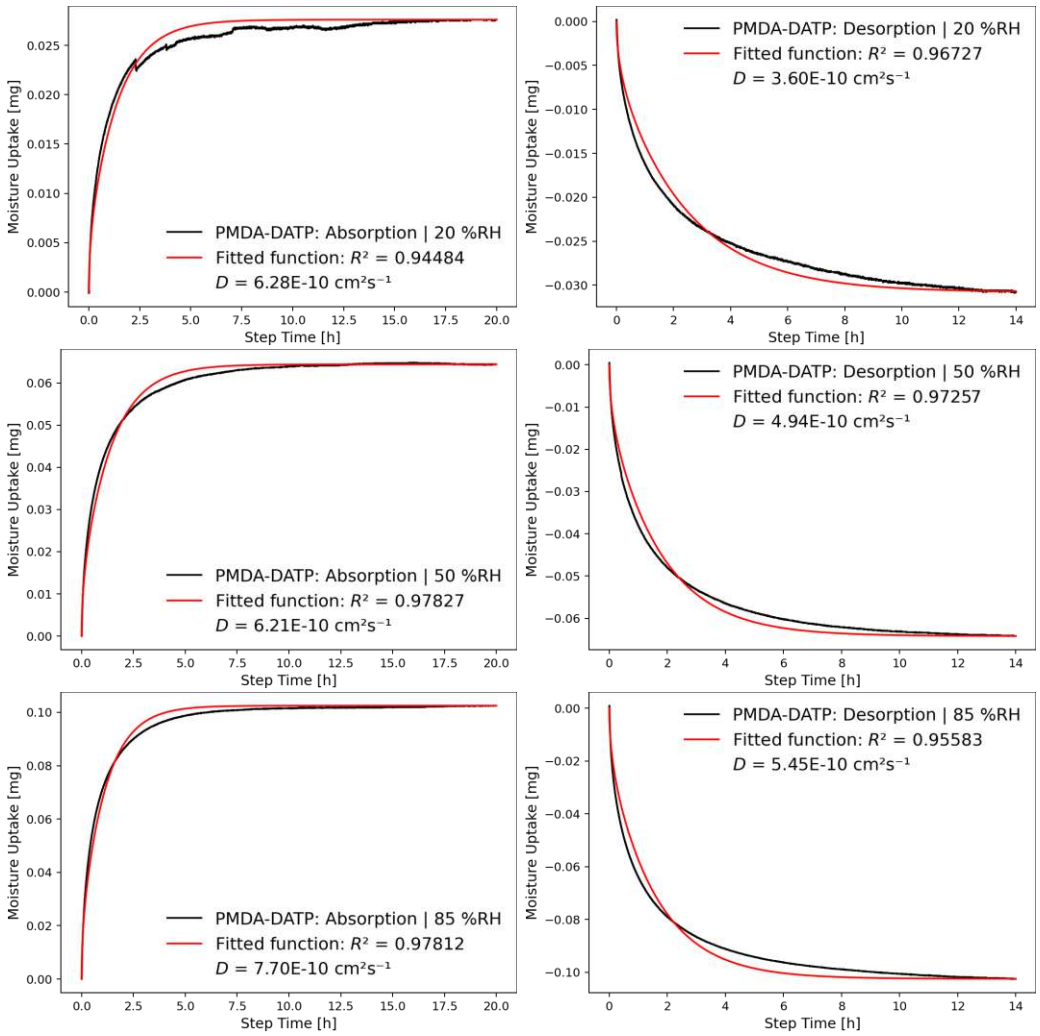

Figure D.11: Each sorption step of the refined PMDA-DATP measurement, separated for calculating the diffusion coefficients by fitting Crank's mass diffusion formula to the data series.

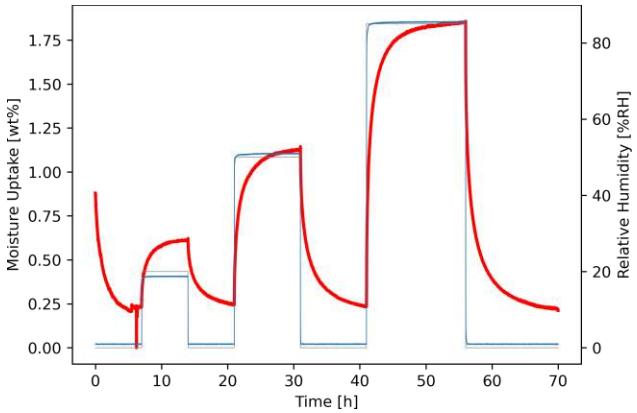

Figure D.12: Initial measurement profile (70 h total length) of PMDA-DATP, excluded from obtaining results for moisture uptake or diffusion coefficients due to insufficient step duration. The red line depicts the relative sample mass, the gray line depicts the targeted RH and the blue line depicts the actual RH.

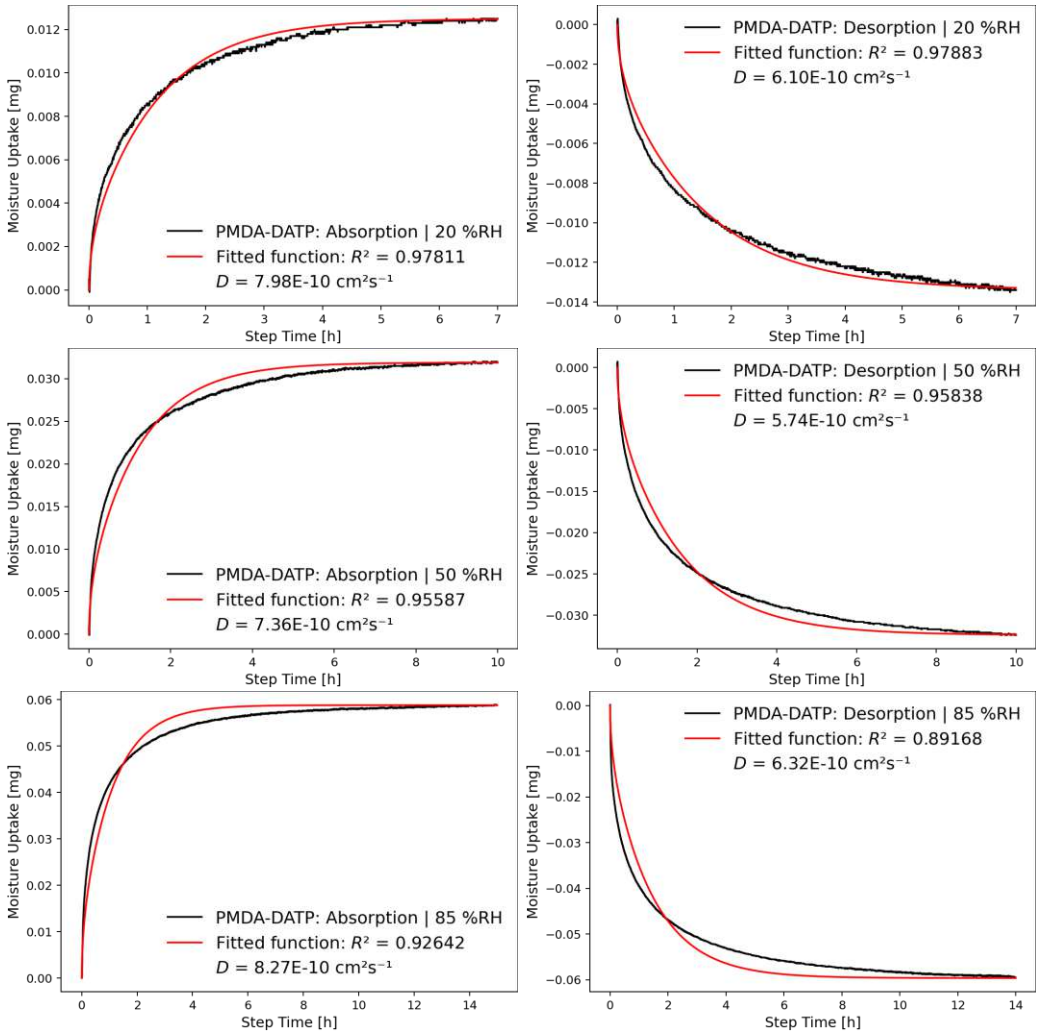

Figure D.13: Each sorption step of the discarded PMDA-DATP measurement, separated for calculating the (discarded) diffusion coefficients by fitting Crank's mass diffusion formula to the data series.

D.2.4 sBPDA-pPDA

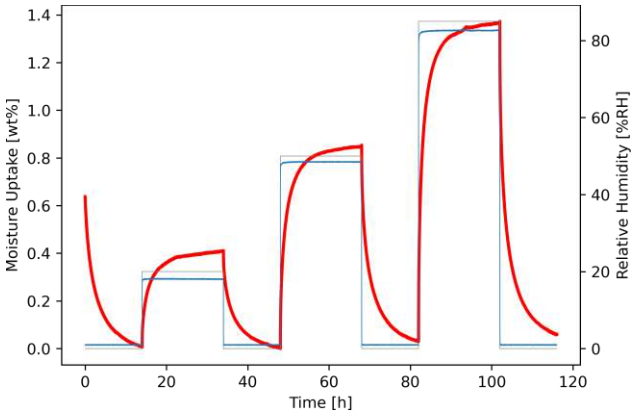

Figure D.14: Full refined measurement profile (116 h total length, two specimens) of sBPDA-pPDA used for determining both moisture uptake and diffusion coefficients. The red line depicts the relative sample mass, the gray line depicts the targeted RH and the blue line depicts the actual RH.

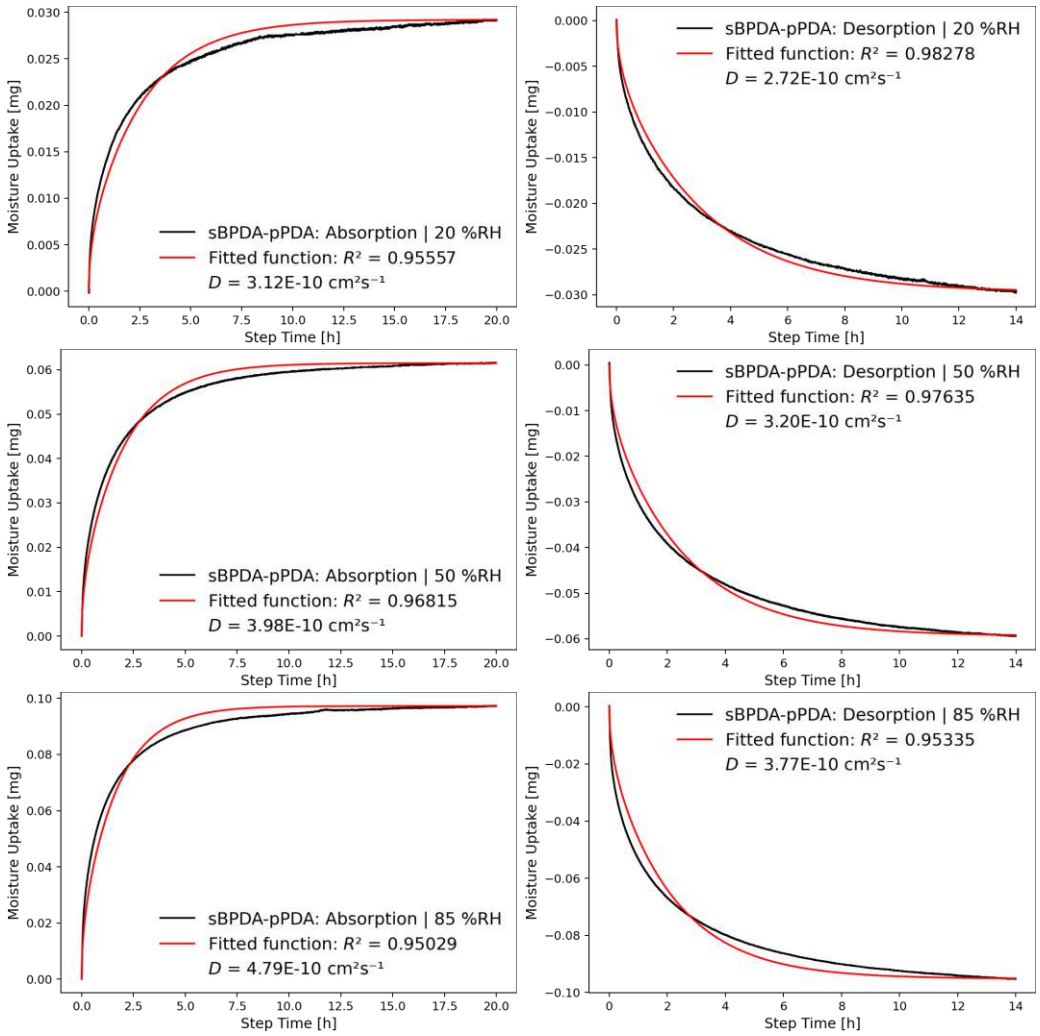

Figure D.15: Each sorption step of the refined sBPDA-pPDA measurement, separated for calculating the diffusion coefficients by fitting Crank's mass diffusion formula to the data series.

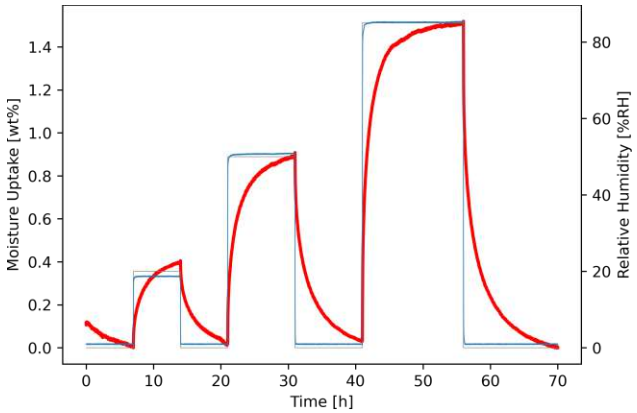

Figure D.16: Initial measurement profile (70 h total length) of sBPDA-pPDA, excluded from obtaining results for moisture uptake or diffusion coefficients due to insufficient step duration. The red line depicts the relative sample mass, the gray line depicts the targeted RH and the blue line depicts the actual RH.

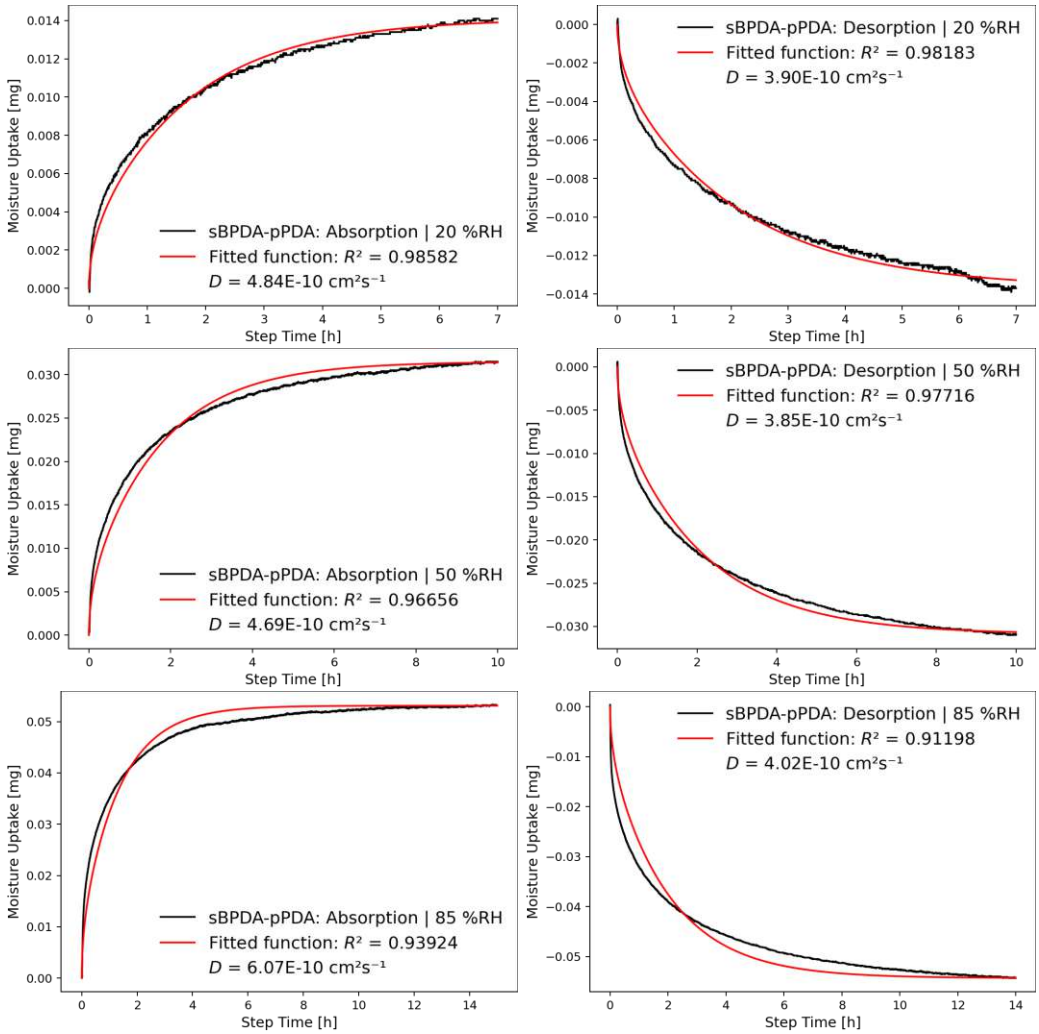

Figure D.17: Each sorption step of the discarded sBPDA-pPDA measurement, separated for calculating the (discarded) diffusion coefficients by fitting Crank's mass diffusion formula to the data series.

D.2.5 sBPDA-Bz

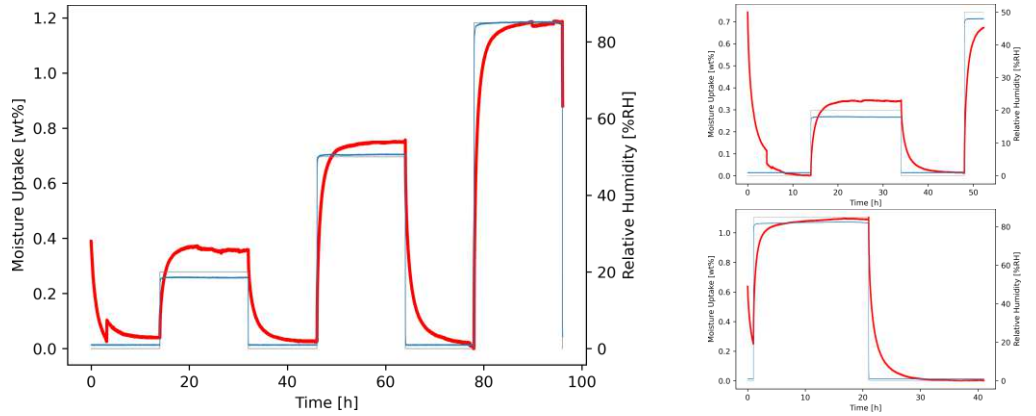

Figure D.18: Full refined measurement profile (116 h total length, two specimens) of sBPDA-Bz used for determining both moisture uptake and diffusion coefficients, including separately repeated measurements for the 20 %RH ab- and desorption steps and the 85 %RH desorption step. The red lines depict the relative sample mass, the gray lines depict the targeted RH and the blue lines depict the actual RH.

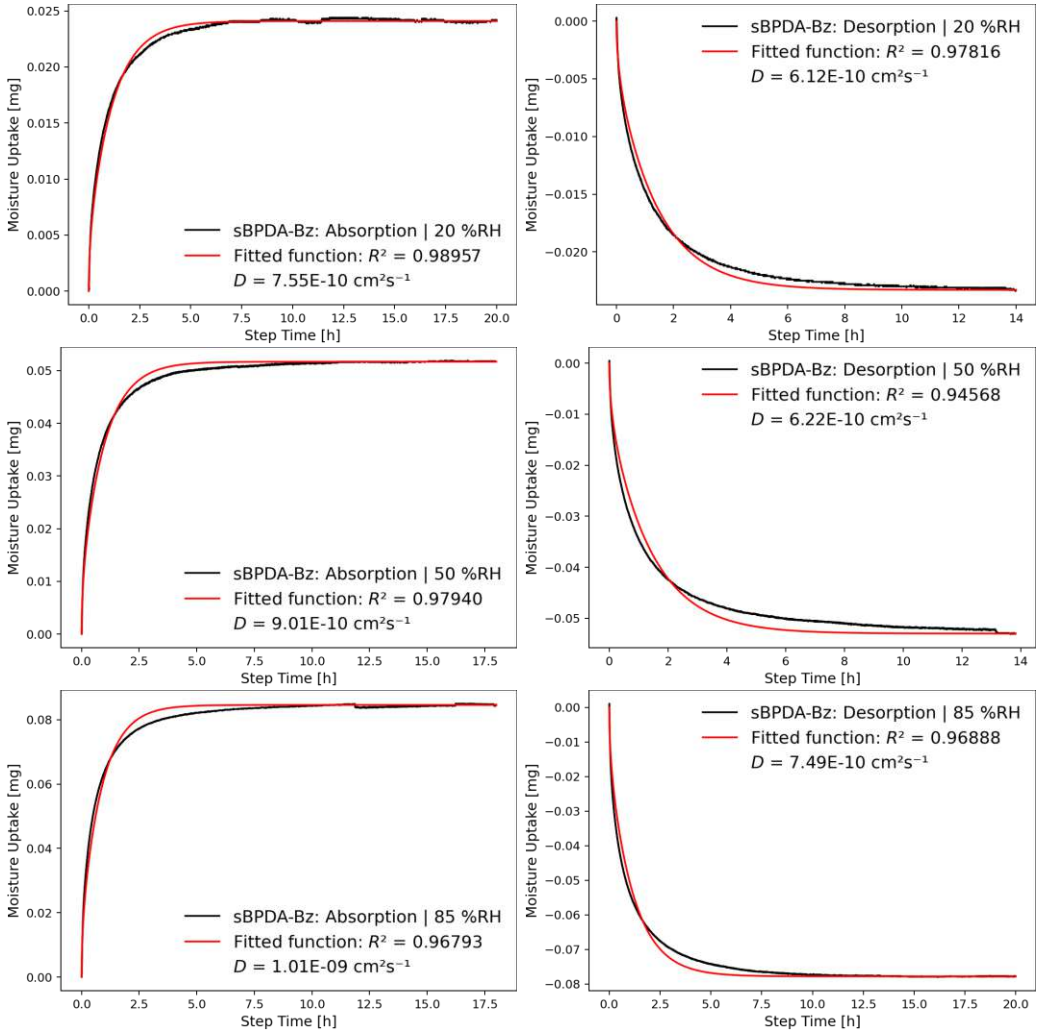

Figure D.19: Each sorption step of the refined sBPDA-Bz measurement, separated for calculating the diffusion coefficients by fitting Crank's mass diffusion formula to the data series.

D.2.6 sBPDA-DATP

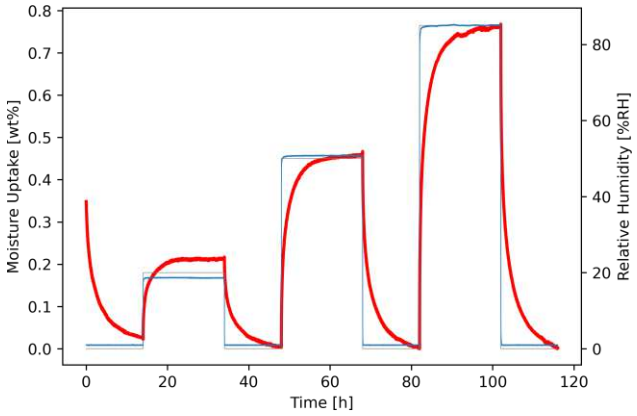

Figure D.20: Full refined measurement profile (116 h total length, two specimens) of sBPDA-DATP used for determining both moisture uptake and diffusion coefficients. The red line depicts the relative sample mass, the gray line depicts the targeted RH and the blue line depicts the actual RH.

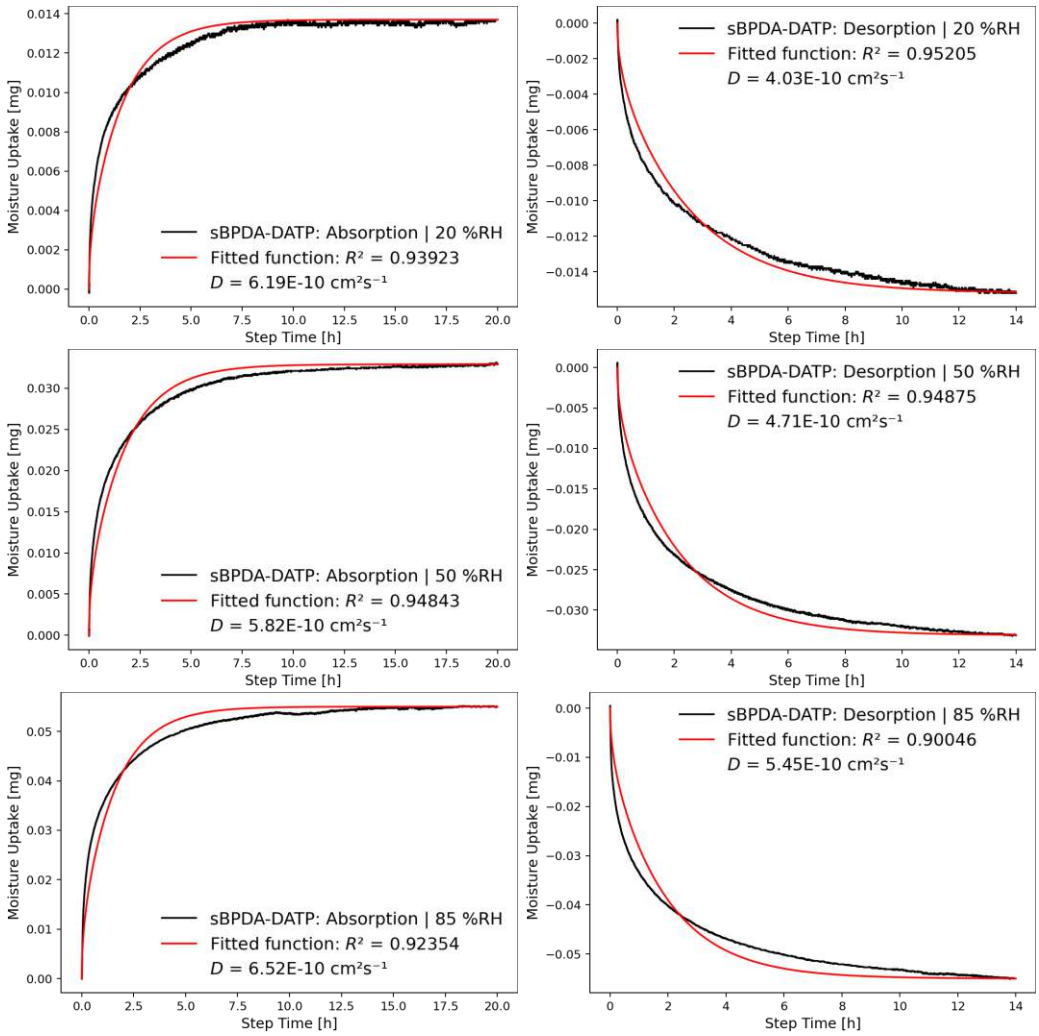

Figure D.21: Each sorption step of the refined sBPDA-DATP measurement, separated for calculating the diffusion coefficients by fitting Crank's mass diffusion formula to the data series.

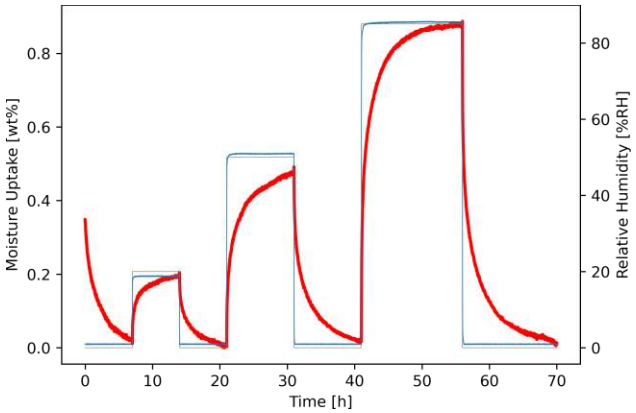

Figure D.22: Initial measurement profile (70 h total length) of sBPDA-DATP, excluded from obtaining results for moisture uptake or diffusion coefficients due to insufficient step duration. The red line depicts the relative sample mass, the gray line depicts the targeted RH and the blue line depicts the actual RH.

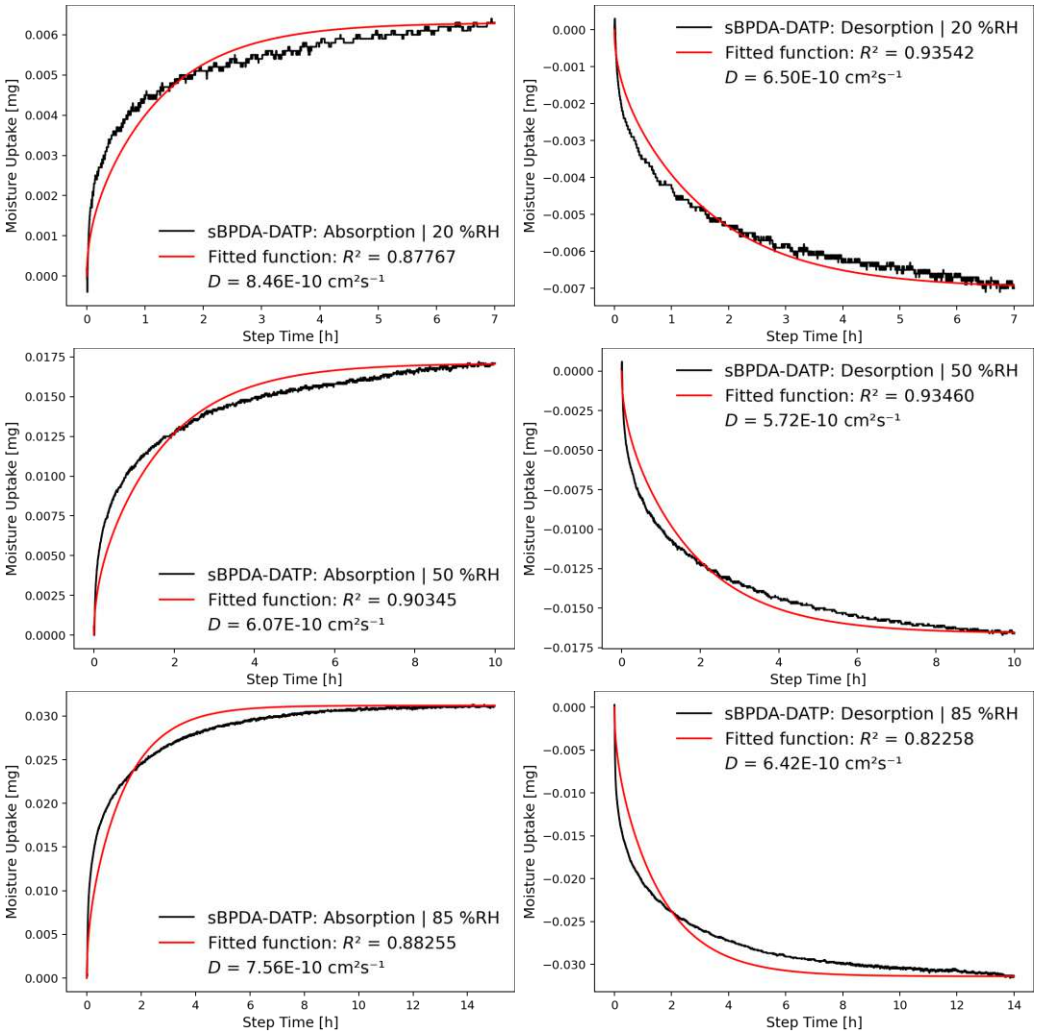

Figure D.23: Each sorption step of the discarded sBPDA-DATP measurement, separated for calculating the (discarded) diffusion coefficients by fitting Crank's mass diffusion formula to the data series.

D.2.7 PMDA-APBP

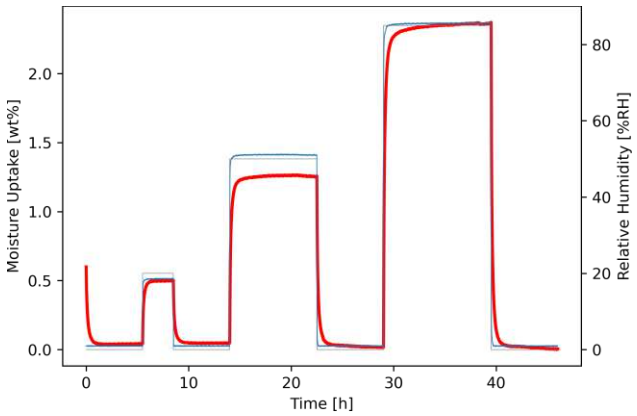

Figure D.24: Full refined measurement profile (46 h total length) of PMDA-APBP used for determining both moisture uptake and diffusion coefficients. The red line depicts the relative sample mass, the gray line depicts the targeted RH and the blue line depicts the actual RH.

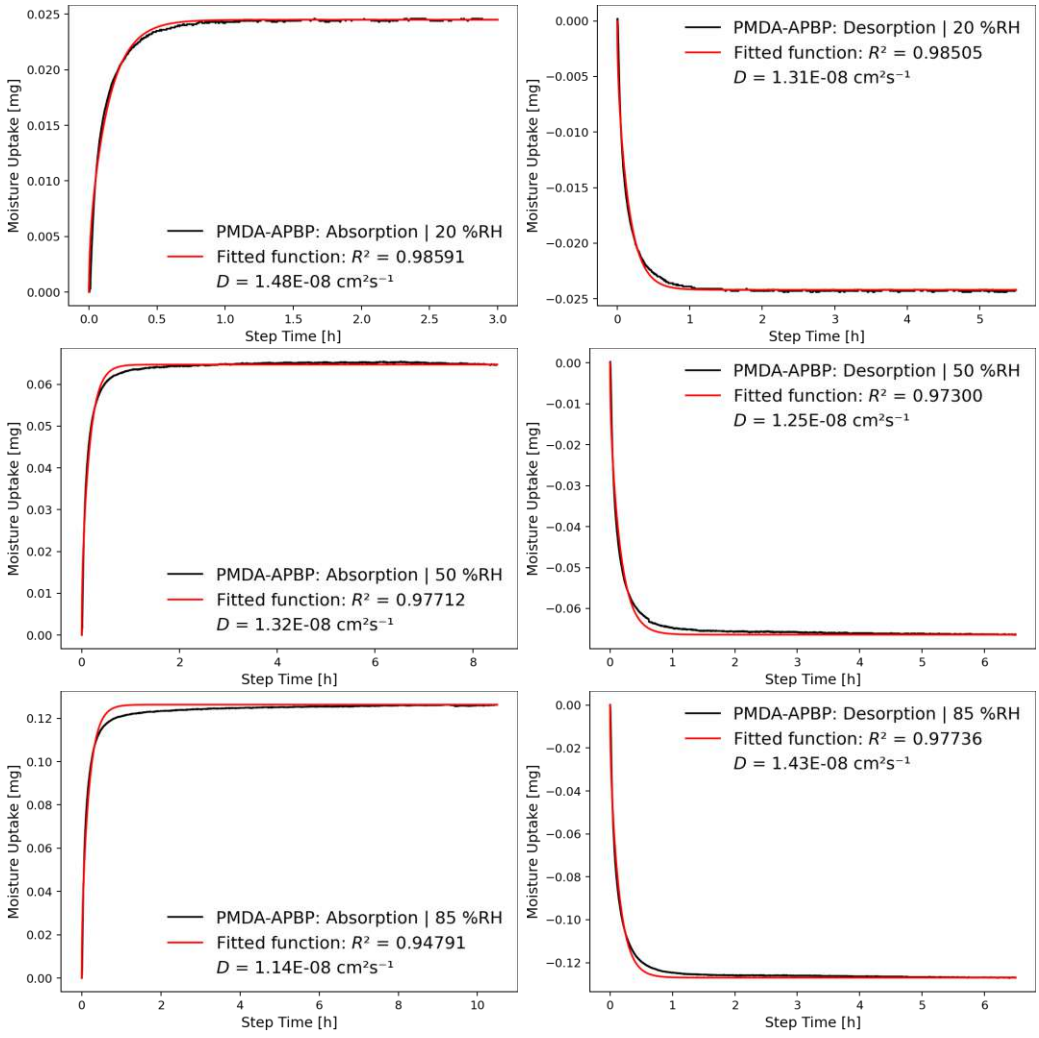

Figure D.25: Each sorption step of the refined PMDA-APBP measurement, separated for calculating the diffusion coefficients by fitting Crank's mass diffusion formula to the data series.

D.2.8 PMDA-8FAPBP

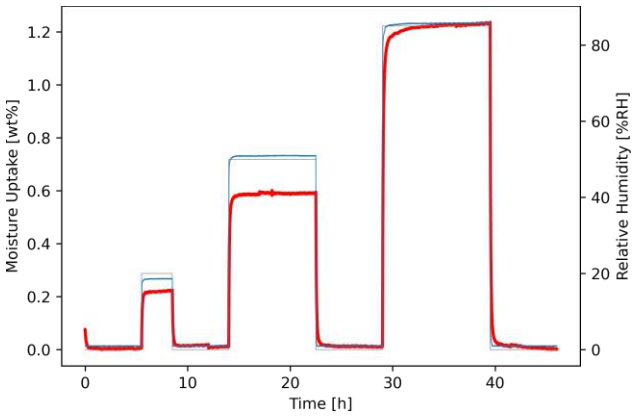

Figure D.26: Full refined measurement profile (46 h total length) of PMDA-8FAPBP used for determining both moisture uptake and diffusion coefficients. The red line depicts the relative sample mass, the gray line depicts the targeted RH and the blue line depicts the actual RH.

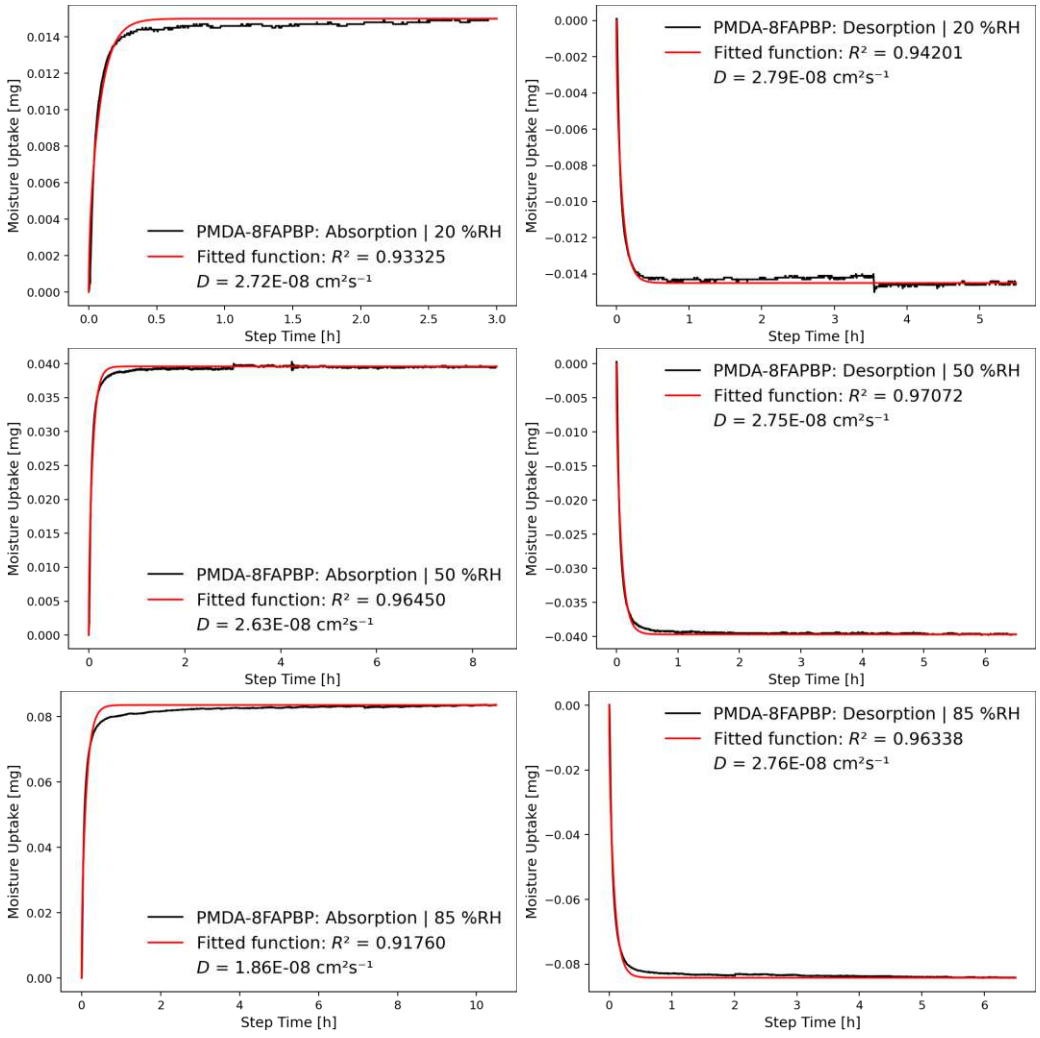

Figure D.27: Each sorption step of the refined PMDA-8FAPBP measurement, separated for calculating the diffusion coefficients by fitting Crank's mass diffusion formula to the data series.

D.2.9 sBPDA-mPDA

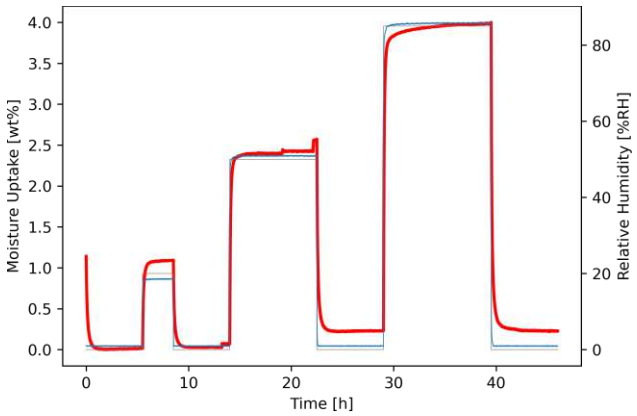

Figure D.28: Full refined measurement profile (46 h total length) of sBPDA-mPDA used for determining both moisture uptake and diffusion coefficients. The red line depicts the relative sample mass, the gray line depicts the targeted RH and the blue line depicts the actual RH.

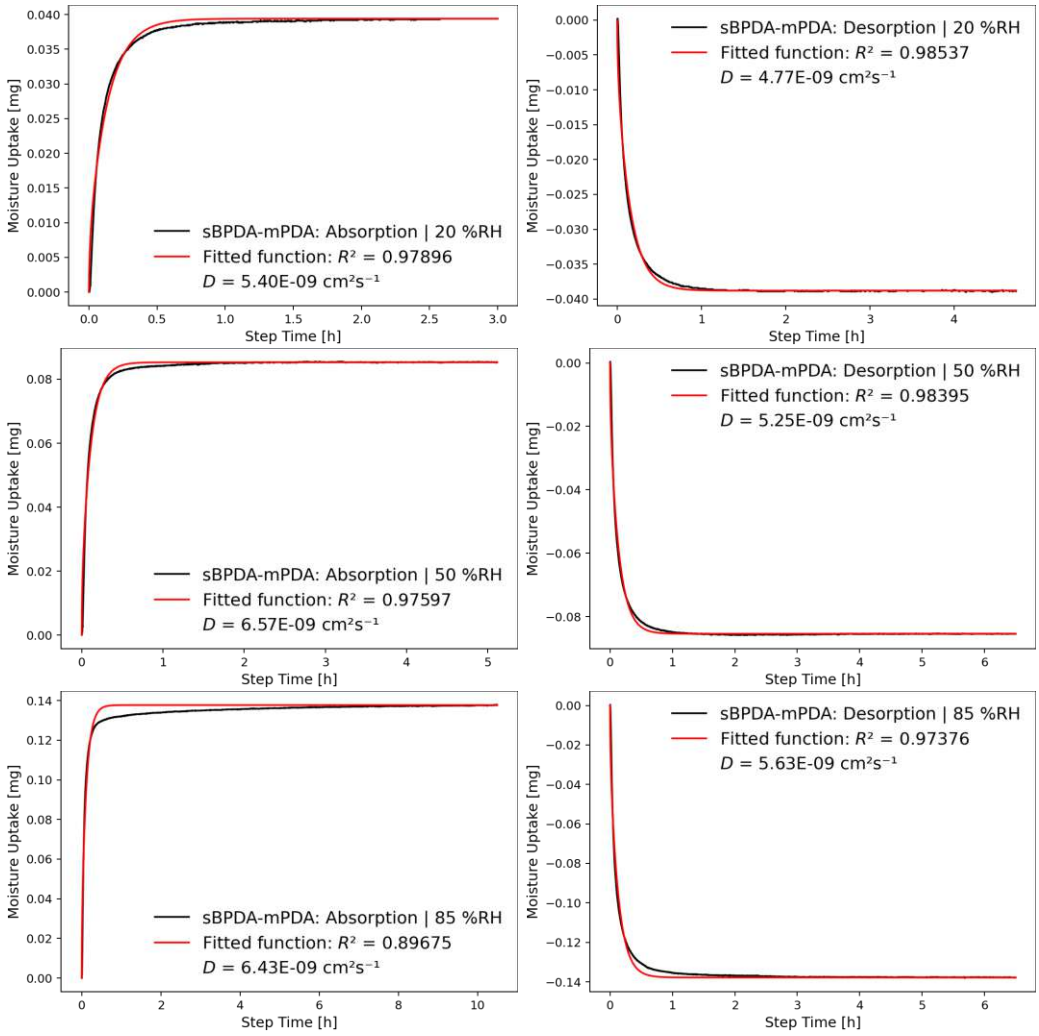

Figure D.29: Each sorption step of the refined sBPDA-mPDA measurement, separated for calculating the diffusion coefficients by fitting Crank's mass diffusion formula to the data series.

D.2.10 sBPDA-1FmPDA

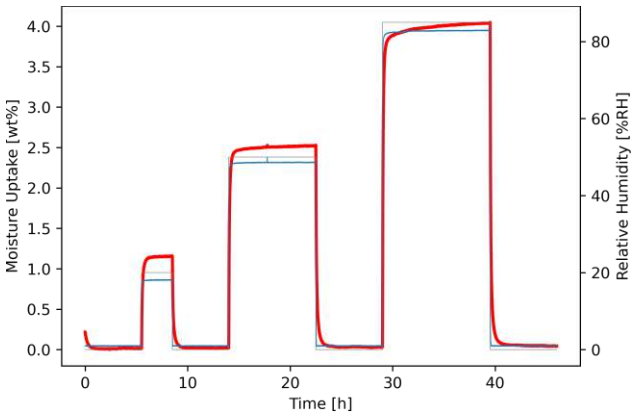

Figure D.30: Full refined measurement profile (46 h total length) of sBPDA-1FmPDA used for determining both moisture uptake and diffusion coefficients. The red line depicts the relative sample mass, the gray line depicts the targeted RH and the blue line depicts the actual RH.

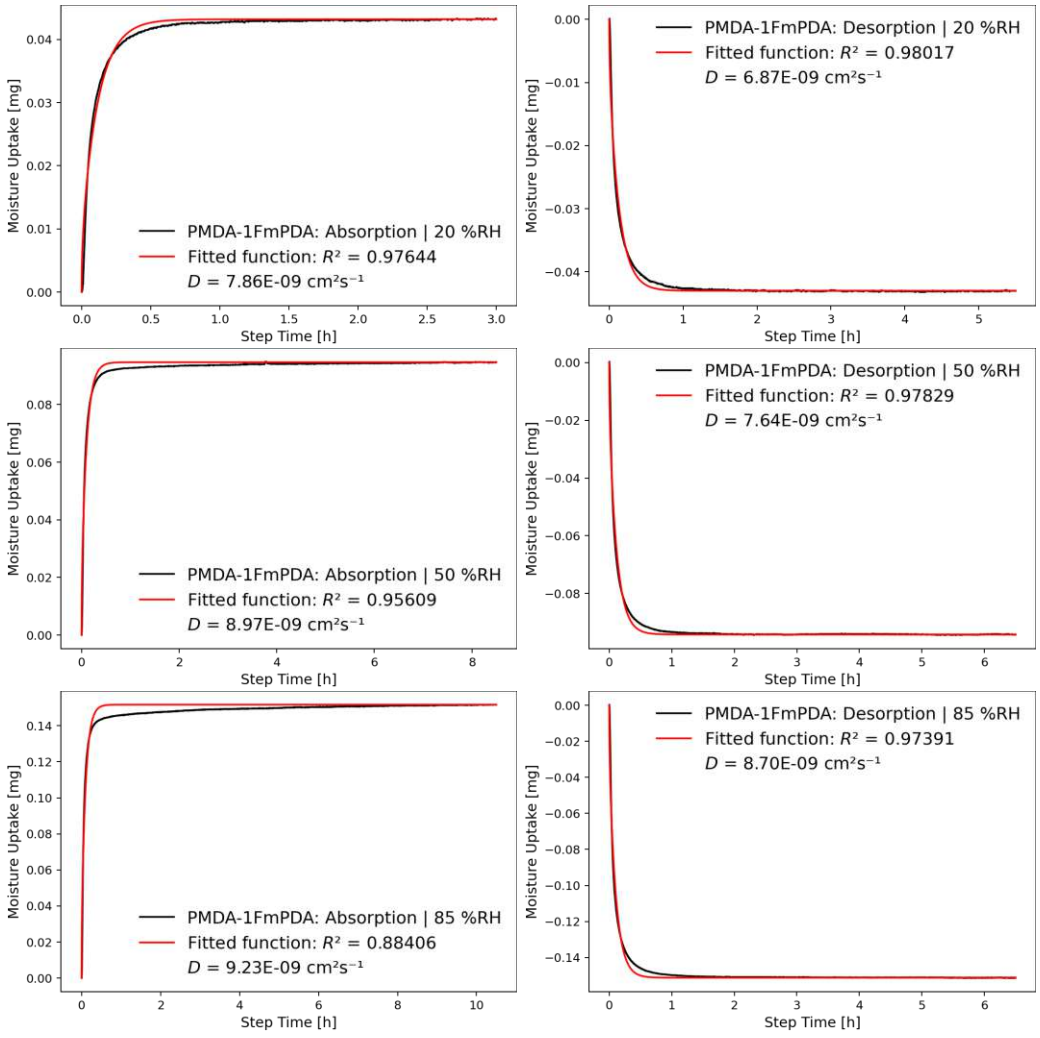

Figure D.31: Each sorption step of the refined sBPDA-1FmPDA measurement, separated for calculating the diffusion coefficients by fitting Crank's mass diffusion formula to the data series.

D.2.11 sBPDA-4FmPDA

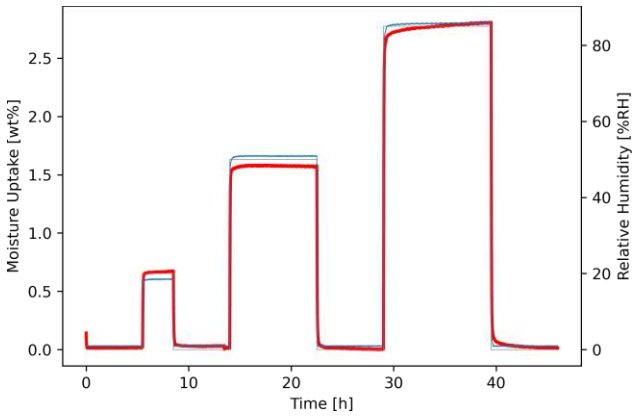

Figure D.32: Full refined measurement profile (46 h total length) of sBPDA-4FmPDA used for determining both moisture uptake and diffusion coefficients. The red line depicts the relative sample mass, the gray line depicts the targeted RH and the blue line depicts the actual RH.

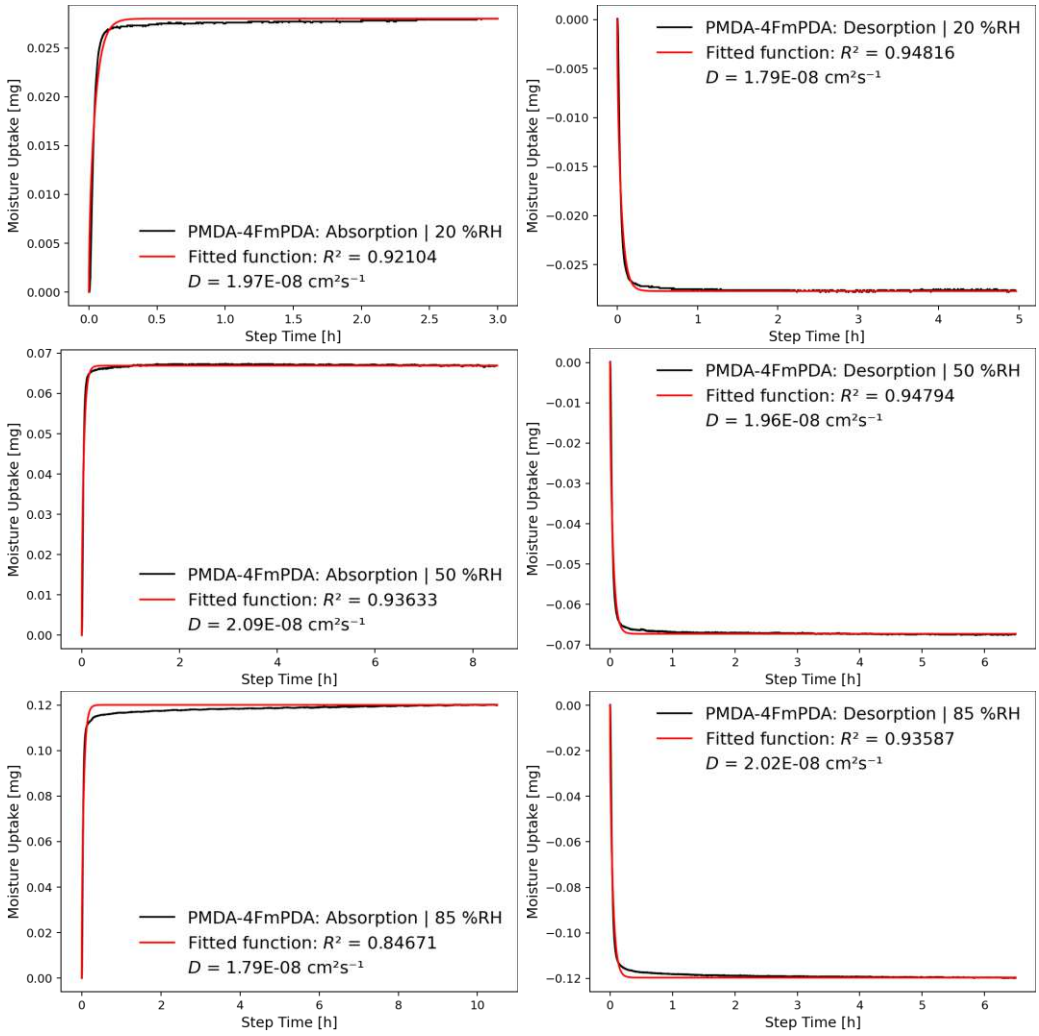

Figure D.33: Each sorption step of the refined sBPDA-4FmPDA measurement, separated for calculating the diffusion coefficients by fitting Crank's mass diffusion formula to the data series.

D.2.12 PMDA-[0.3·mPDA+0.7·pPDA]

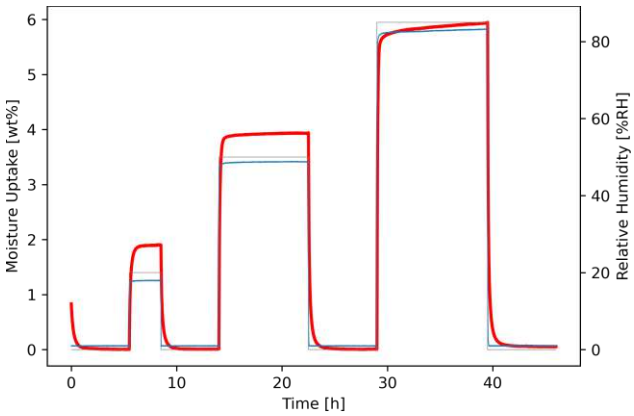

Figure D.34: Full refined measurement profile (46 h total length) of PMDA-[0.3·mPDA+0.7·pPDA] used for determining both moisture uptake and diffusion coefficients. The red line depicts the relative sample mass, the gray line depicts the targeted RH and the blue line depicts the actual RH.

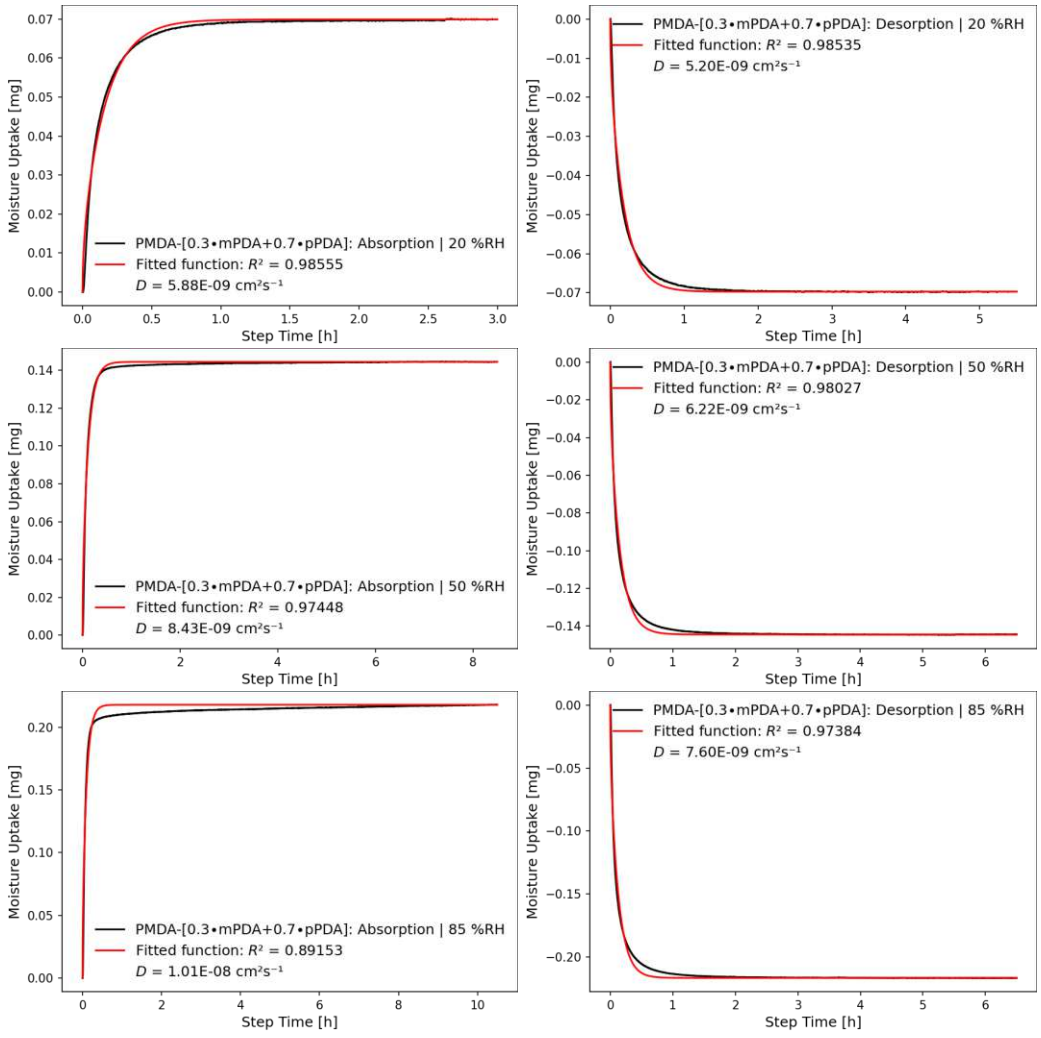

Figure D.35: Each sorption step of the refined PMDA-[0.3·mPDA+0.7·pPDA] measurement, separated for calculating the diffusion coefficients by fitting Crank's mass diffusion formula to the data series.

D.2.13 PMDA-sODA

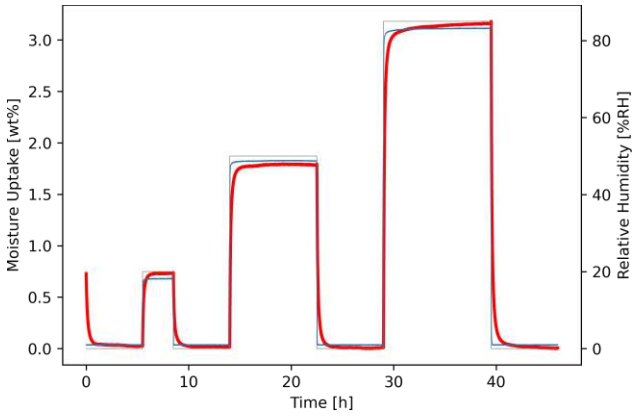

Figure D.36: Full refined measurement profile (46 h total length) of PMDA-sODA used for determining both moisture uptake and diffusion coefficients. The red line depicts the relative sample mass, the gray line depicts the targeted RH and the blue line depicts the actual RH.

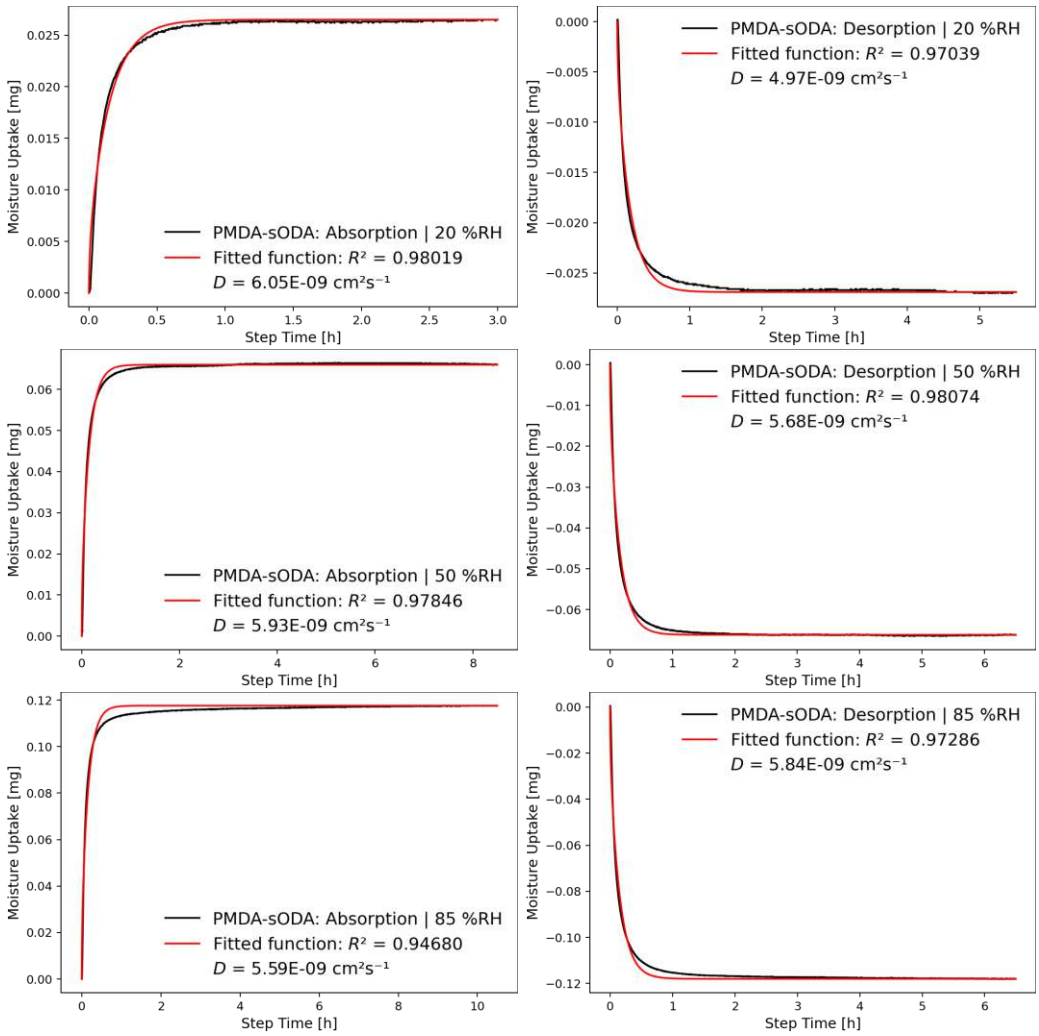

Figure D.37: Each sorption step of the refined PMDA-sODA measurement, separated for calculating the diffusion coefficients by fitting Crank's mass diffusion formula to the data series.

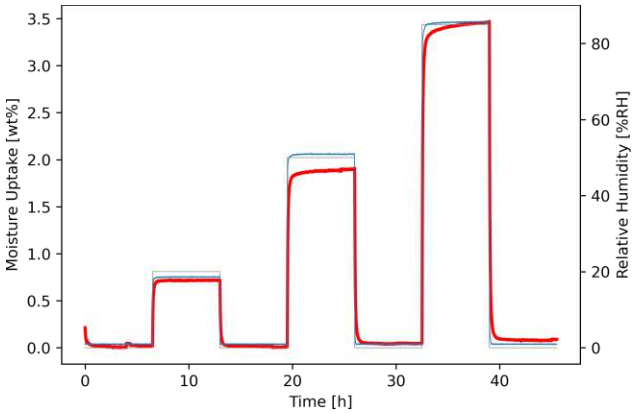

Figure D.38: Initial measurement profile (45.5 h total length) of PMDA-sODA, excluded from obtaining results for moisture uptake or diffusion coefficients due to insufficient step duration. The red line depicts the relative sample mass, the gray line depicts the targeted RH and the blue line depicts the actual RH.

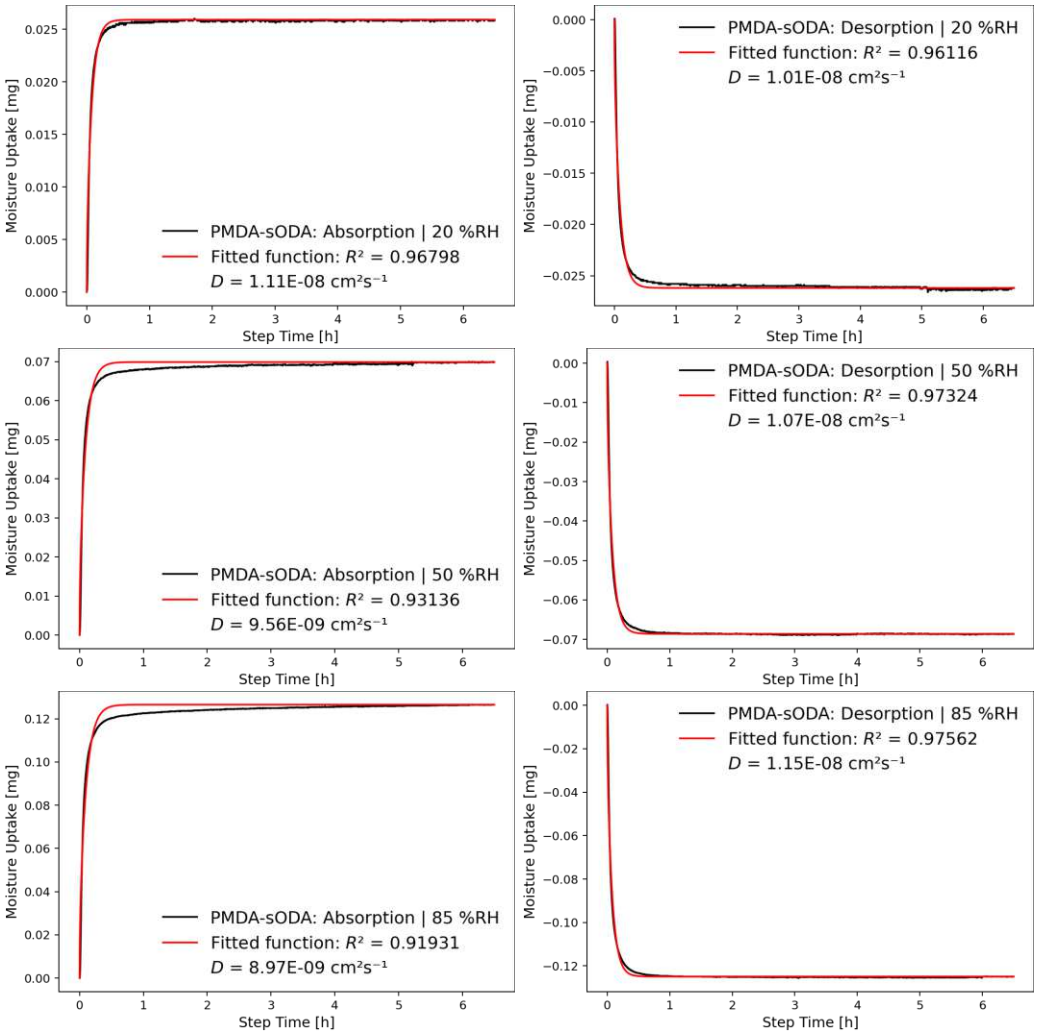

Figure D.39: Each sorption step of the discarded PMDA-sODA measurement, separated for calculating the (discarded) diffusion coefficients by fitting Crank's mass diffusion formula to the data series.

D.2.14 PMDA-aODA

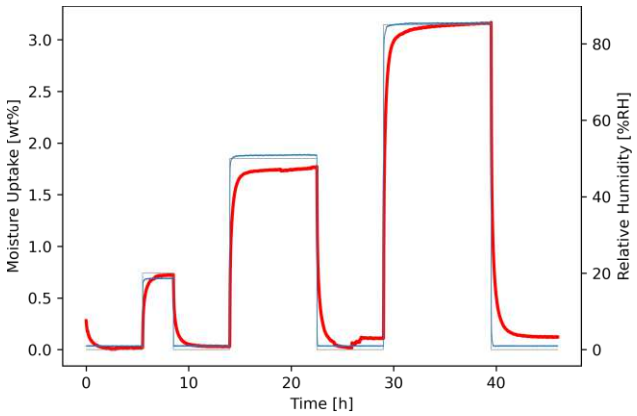

Figure D.40: Full refined measurement profile (46 h total length) of PMDA-aODA used for determining both moisture uptake and diffusion coefficients. The red line depicts the relative sample mass, the gray line depicts the targeted RH and the blue line depicts the actual RH.

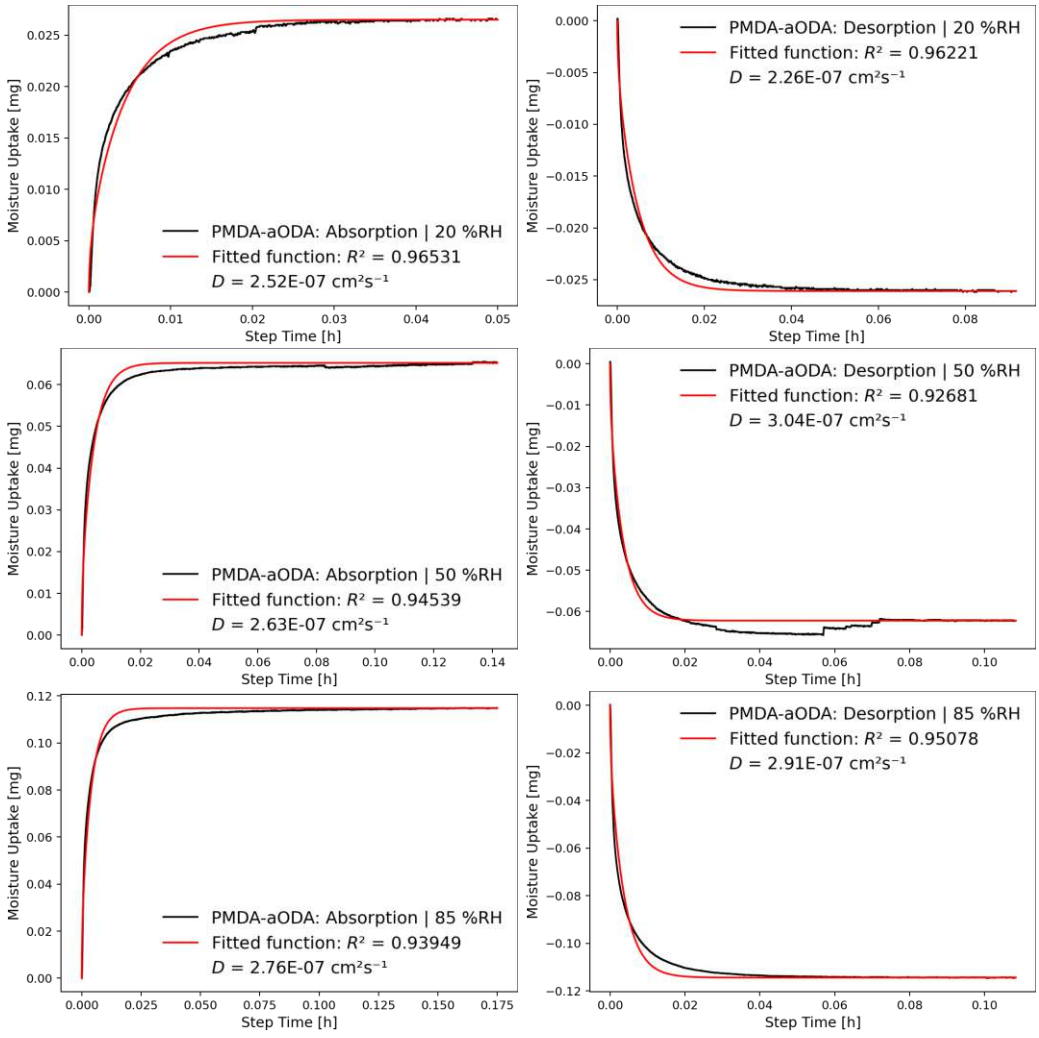

Figure D.41: Each sorption step of the refined PMDA-aODA measurement, separated for calculating the diffusion coefficients by fitting Crank's mass diffusion formula to the data series.

D.2.15 PMDA-pBAPB

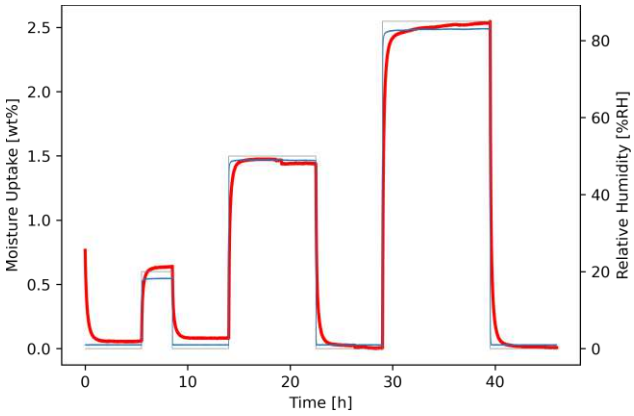

Figure D.42: Full refined measurement profile (46 h total length) of PMDA-pBAPB used for determining both moisture uptake and diffusion coefficients. The red line depicts the relative sample mass, the gray line depicts the targeted RH and the blue line depicts the actual RH.

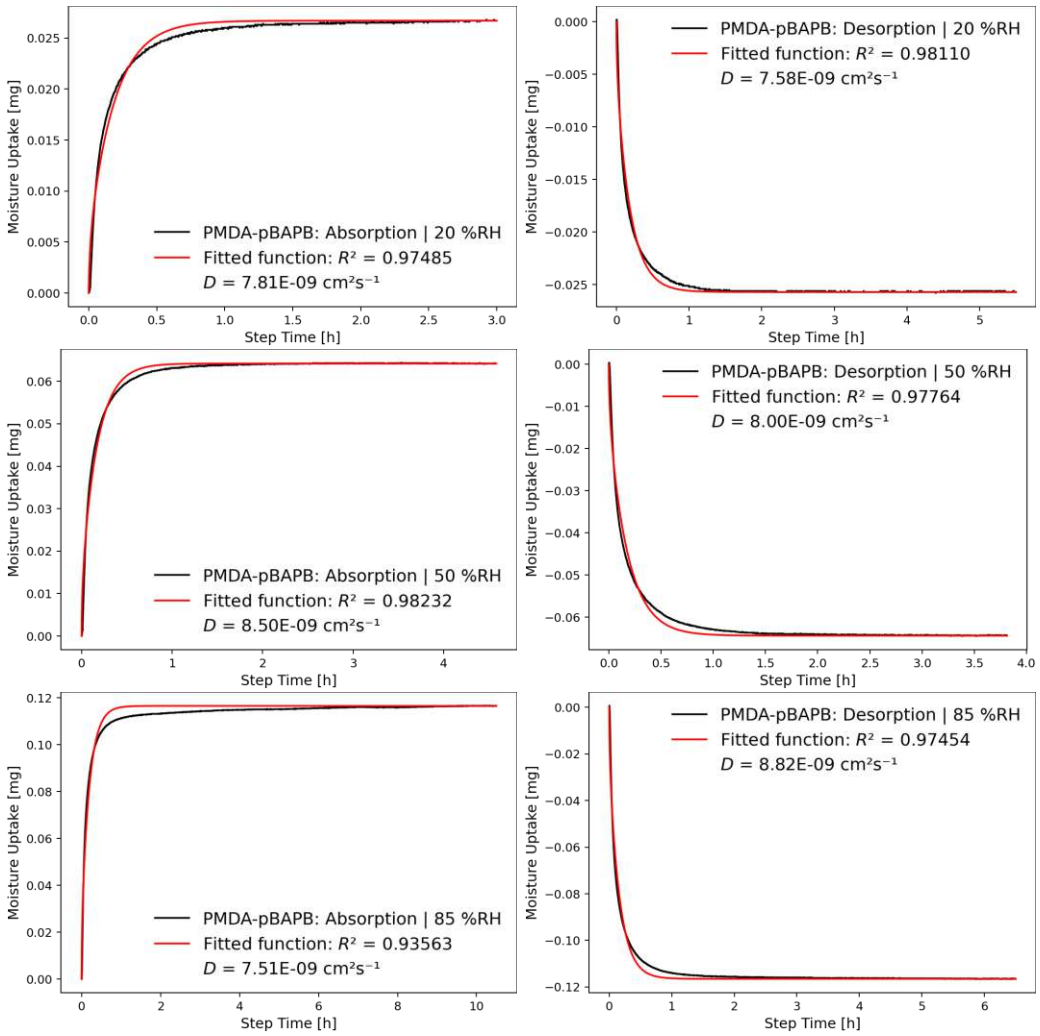

Figure D.43: Each sorption step of the refined PMDA-pBAPB measurement, separated for calculating the diffusion coefficients by fitting Crank's mass diffusion formula to the data series.

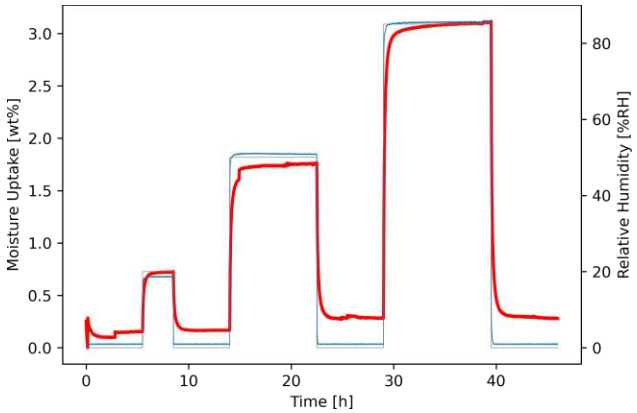

Figure D.44: Initial measurement profile (46 h total length) of PMDA-pBAPB, excluded from obtaining results for moisture uptake or diffusion coefficients due to a measurement error occuring in a key position during the 50 %RH absorption step . The red line depicts the relative sample mass, the gray line depicts the targeted RH and the blue line depicts the actual RH.

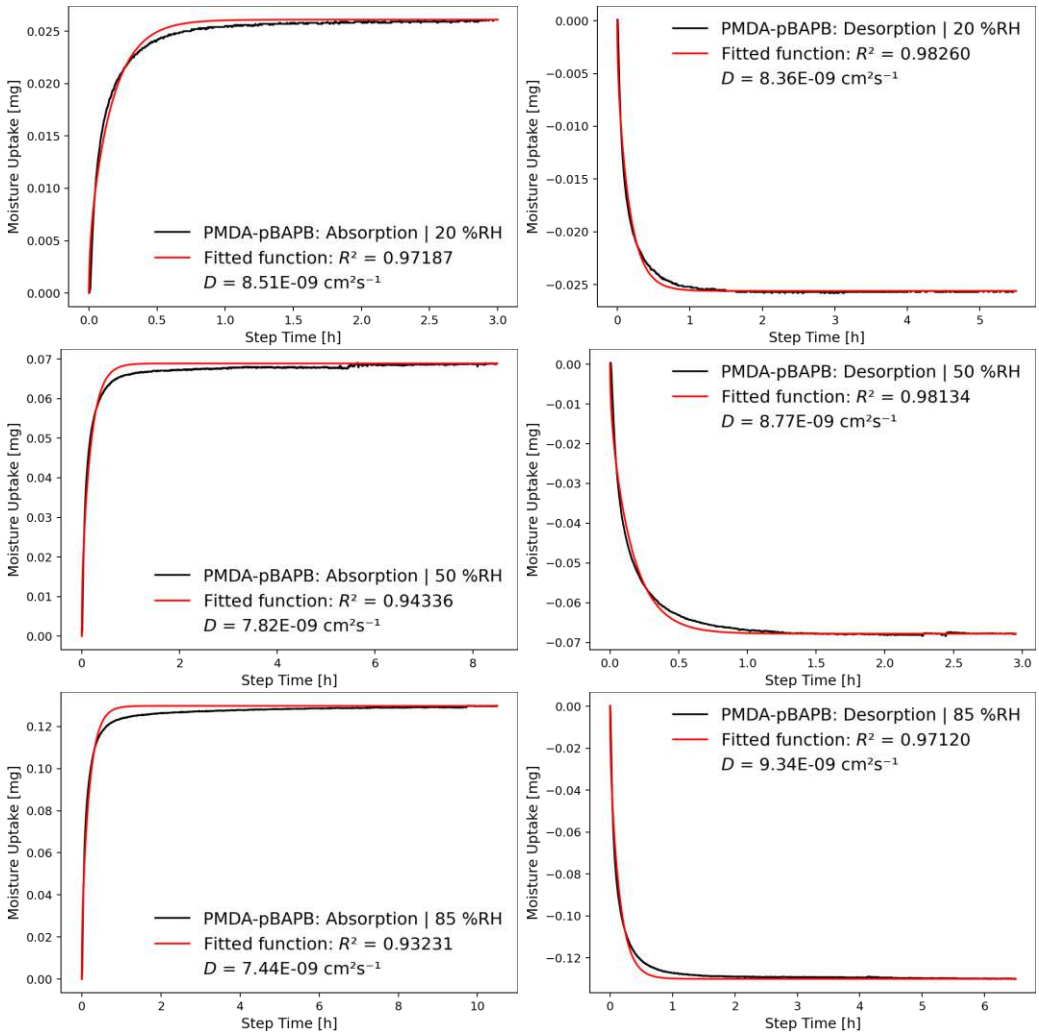

Figure D.45: Each sorption step of the discarded PMDA-pBAPB measurement, separated for calculating the (discarded) diffusion coefficients by fitting Crank's mass diffusion formula to the data series.

D.2.16 PMDA-mBAPB

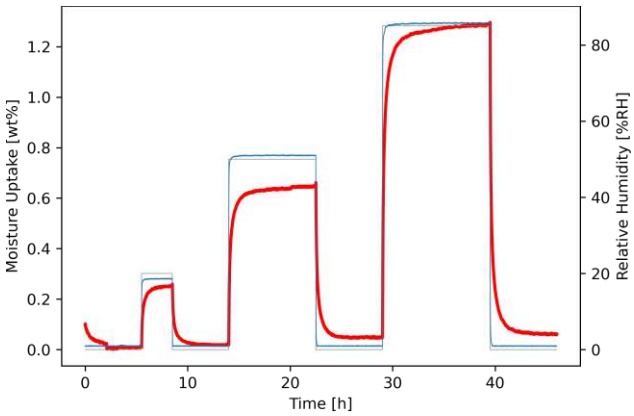

Figure D.46: Full refined measurement profile (46 h total length) of PMDA-mBAPB used for determining both moisture uptake and diffusion coefficients. The red line depicts the relative sample mass, the gray line depicts the targeted RH and the blue line depicts the actual RH.

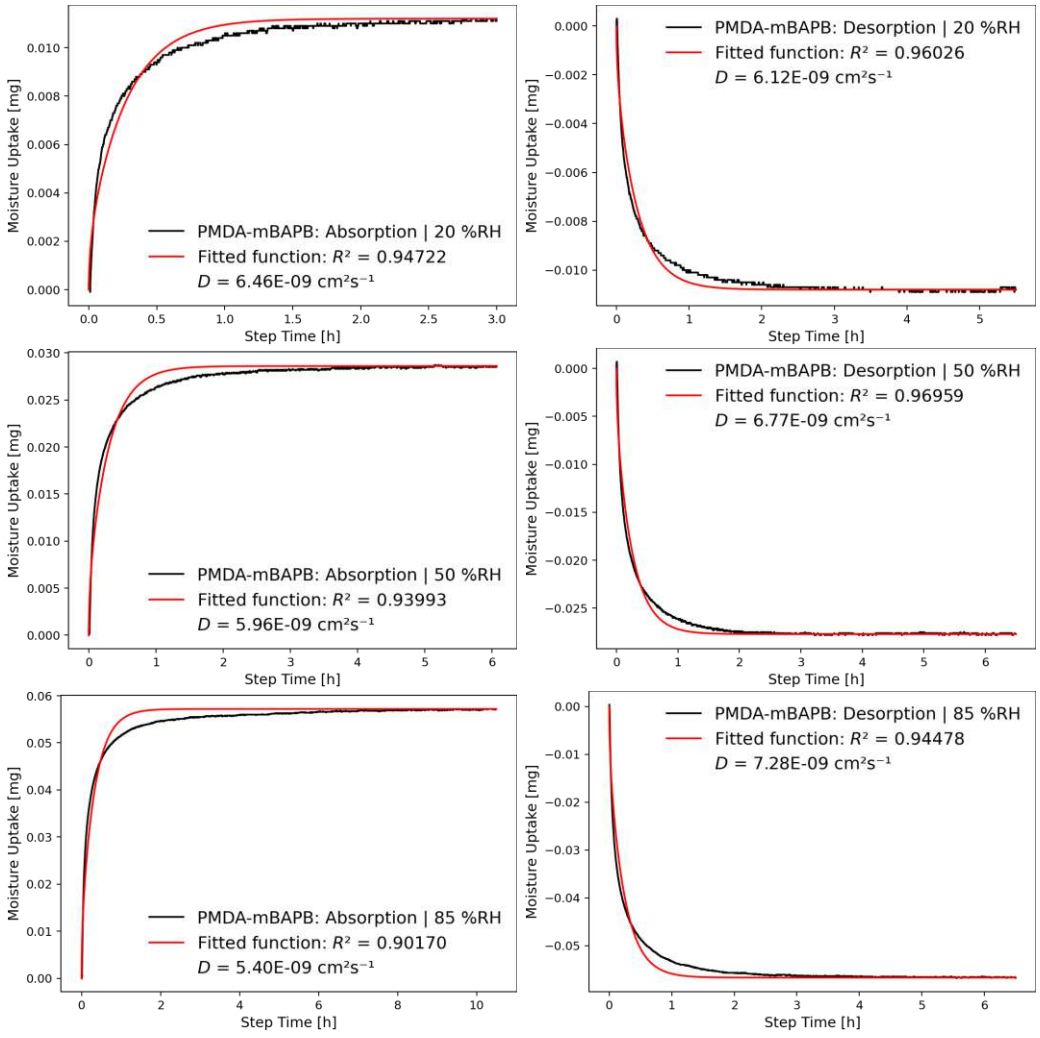

Figure D.47: Each sorption step of the refined PMDA-mBAPB measurement, separated for calculating the diffusion coefficients by fitting Crank's mass diffusion formula to the data series.

D.2.17 PMDA-pBISA

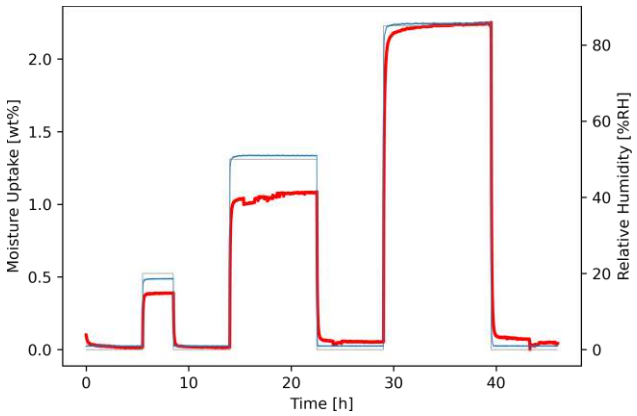

Figure D.48: Full refined measurement profile (46 h total length) of PMDA-pBISA used for determining both moisture uptake and diffusion coefficients. The red line depicts the relative sample mass, the gray line depicts the targeted RH and the blue line depicts the actual RH.

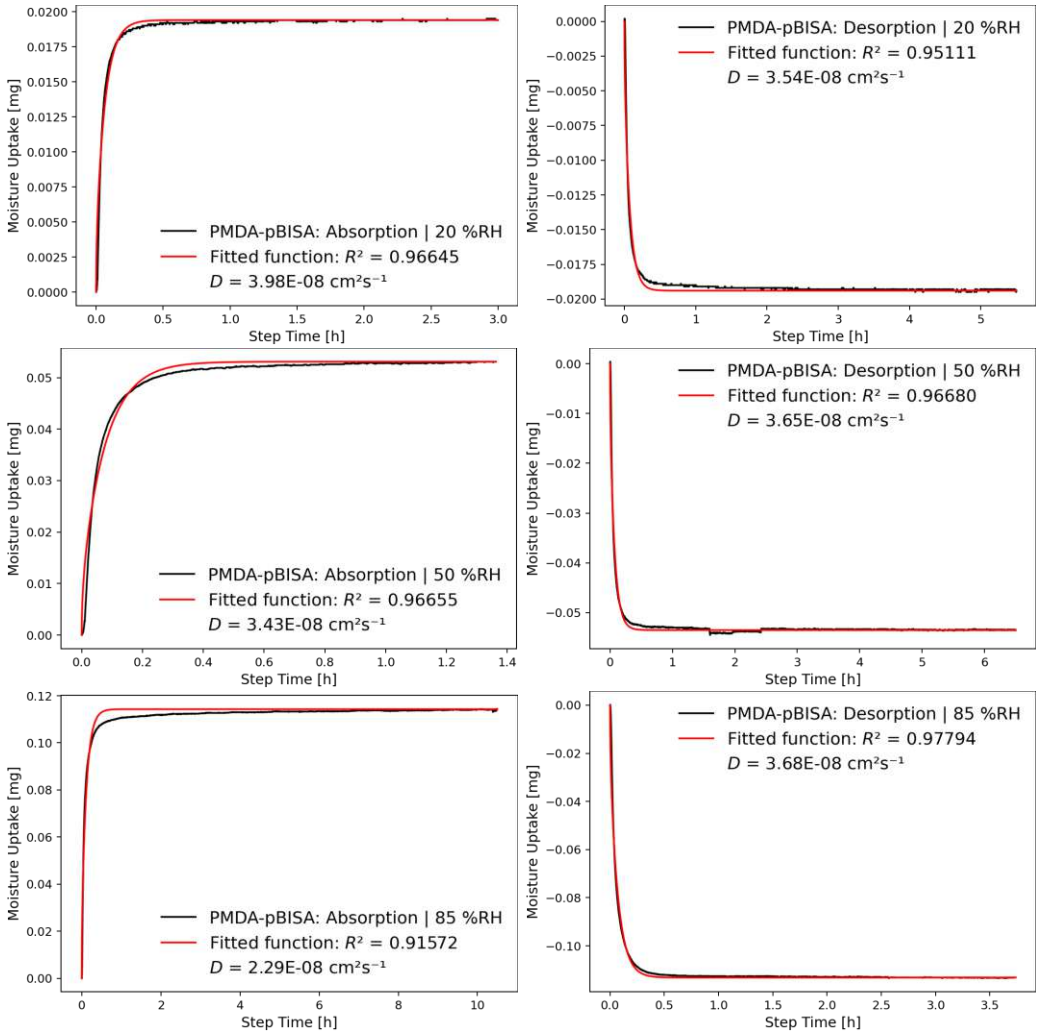

Figure D.49: Each sorption step of the refined PMDA-pBISA measurement, separated for calculating the diffusion coefficients by fitting Crank's mass diffusion formula to the data series.

D.2.18 PMDA-mDMBz

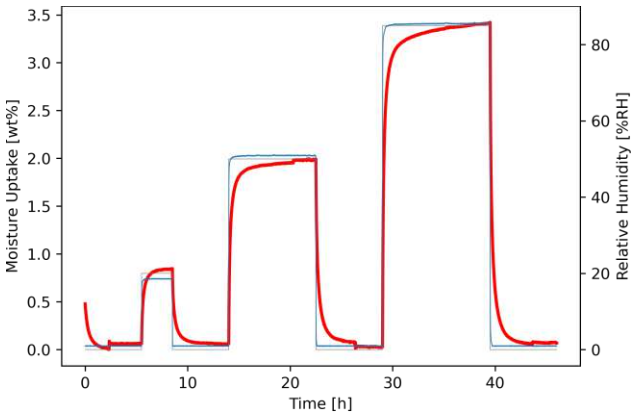

Figure D.50: Full refined measurement profile (46 h total length) of PMDA-mDMBz used for determining both moisture uptake and diffusion coefficients. The red line depicts the relative sample mass, the gray line depicts the targeted RH and the blue line depicts the actual RH.

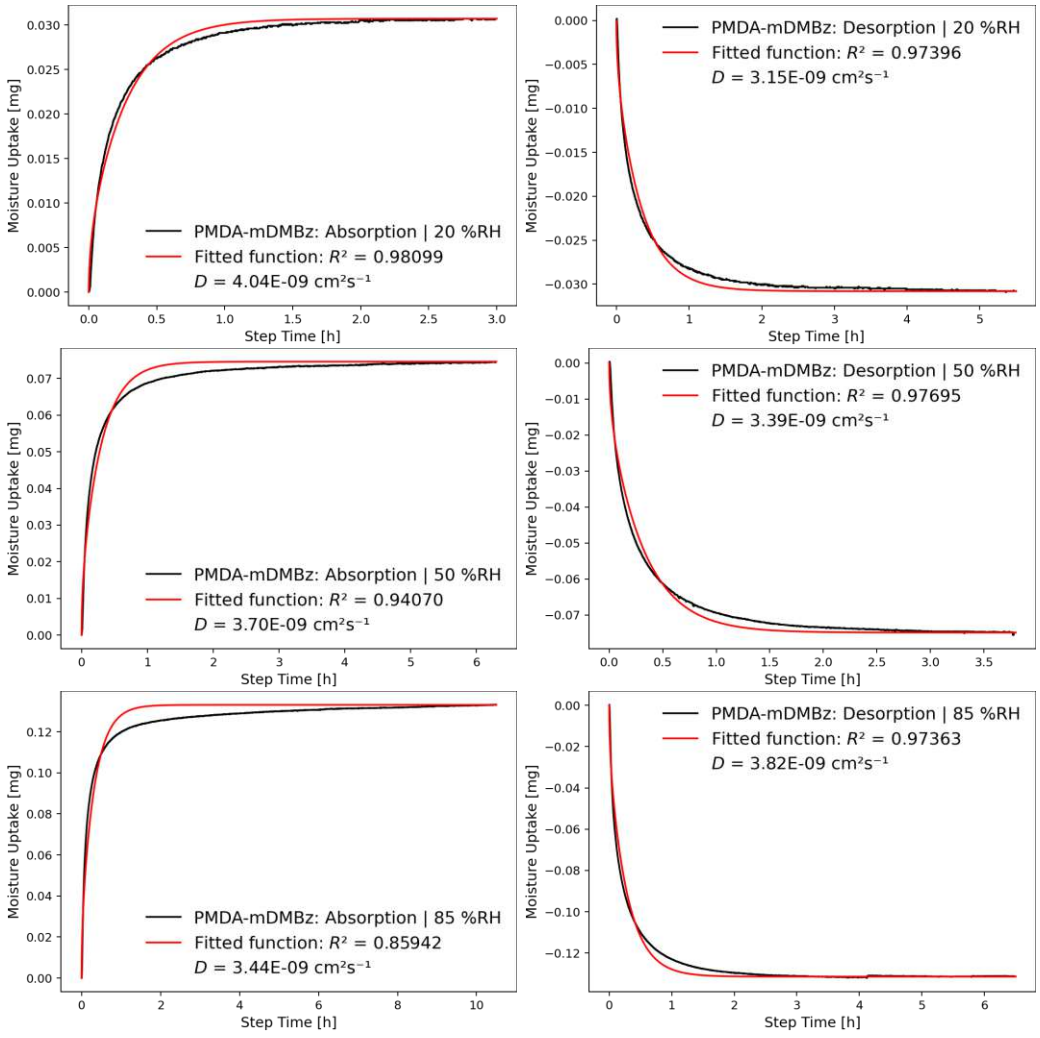

Figure D.51: Each sorption step of the refined PMDA-mDMBz measurement, separated for calculating the diffusion coefficients by fitting Crank's mass diffusion formula to the data series.

D.2.19 PMDA-mTFBz

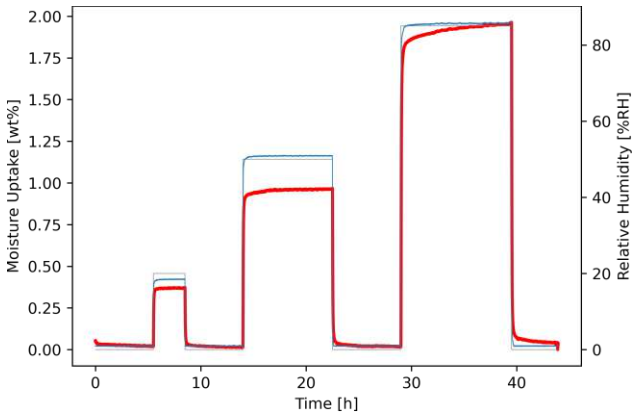

Figure D.52: Full refined measurement profile (46 h total length) of PMDA-mTFBz used for determining both moisture uptake and diffusion coefficients. The red line depicts the relative sample mass, the gray line depicts the targeted RH and the blue line depicts the actual RH.

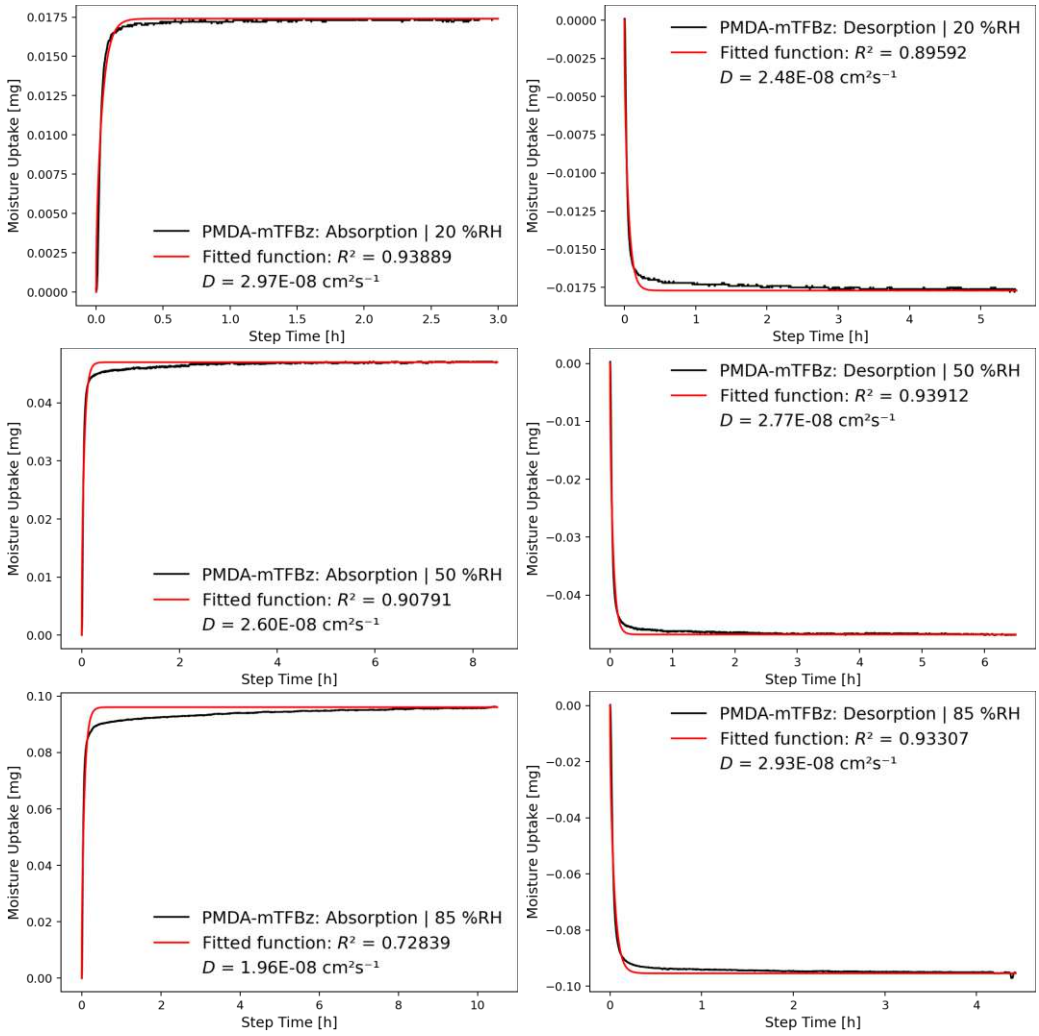

Figure D.53: Each sorption step of the refined PMDA-mTFBz measurement, separated for calculating the diffusion coefficients by fitting Crank's mass diffusion formula to the data series.

D.2.20 PMDA-oDIAN

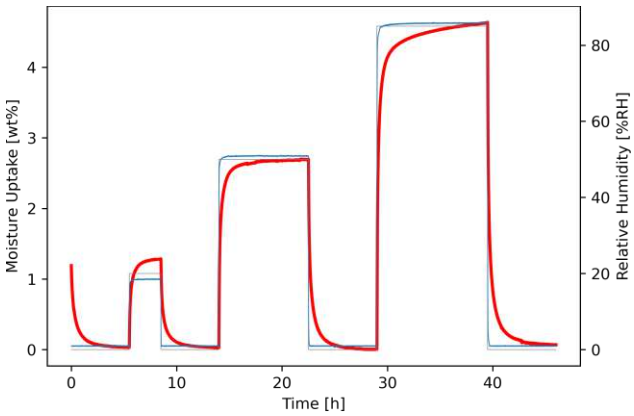

Figure D.54: Full refined measurement profile (46 h total length) of PMDA-oDIAN used for determining both moisture uptake and diffusion coefficients. The red line depicts the relative sample mass, the gray line depicts the targeted RH and the blue line depicts the actual RH.

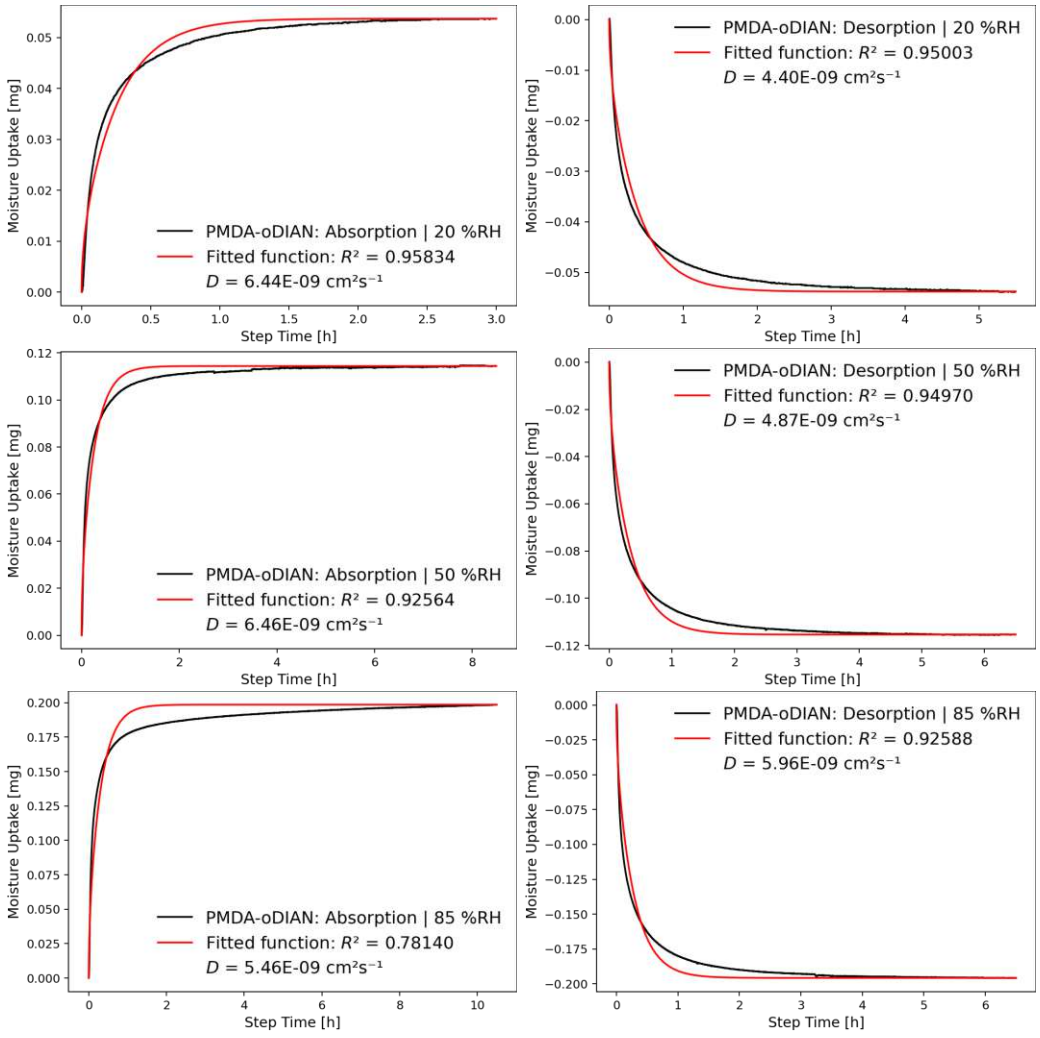

Figure D.55: Each sorption step of the refined PMDA-oDIAN measurement, separated for calculating the diffusion coefficients by fitting Crank's mass diffusion formula to the data series.

D.2.21 sODPA-Bz

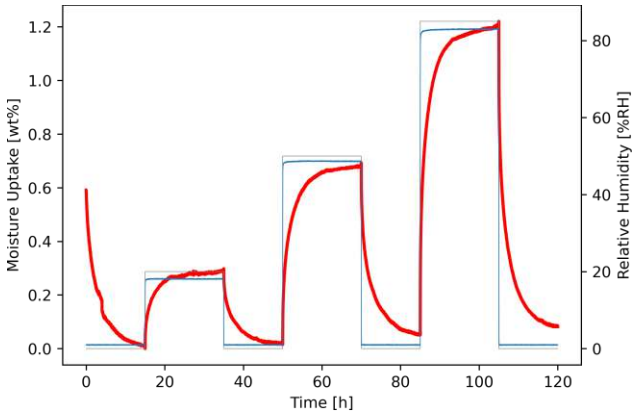

Figure D.56: Full refined measurement profile (120 h total length) of sODPA-Bz used for determining both moisture uptake and diffusion coefficients. The red line depicts the relative sample mass, the gray line depicts the targeted RH and the blue line depicts the actual RH.

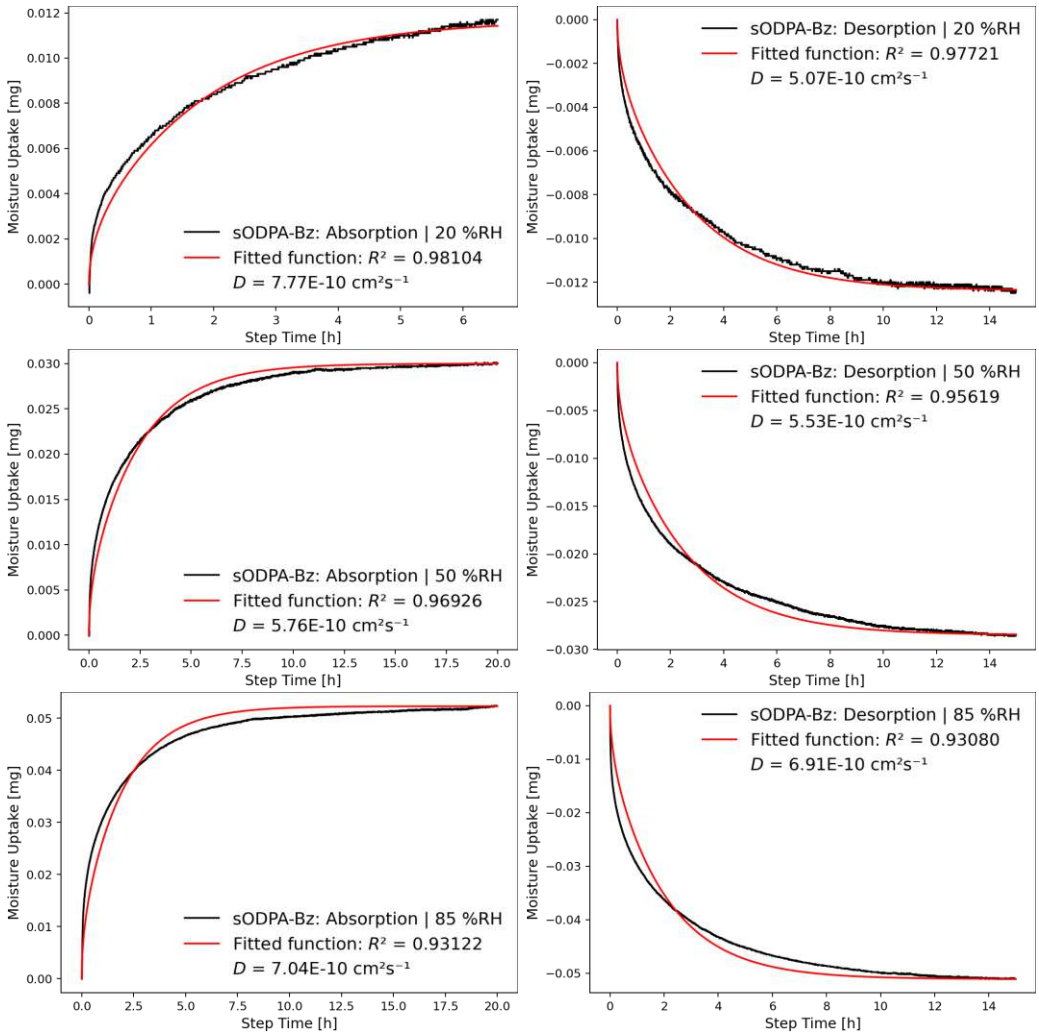

Figure D.57: Each sorption step of the refined sODPA-Bz measurement, separated for calculating the diffusion coefficients by fitting Crank's mass diffusion formula to the data series.

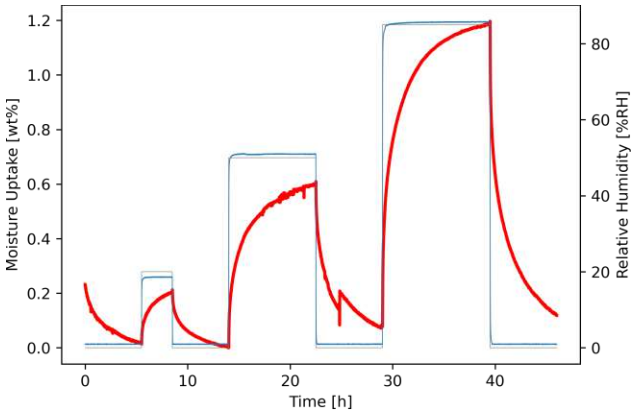

Figure D.58: Initial measurement profile (46 h total length) of sODPA-Bz, excluded from obtaining results for moisture uptake or diffusion coefficients due to insufficient step duration. The red line depicts the relative sample mass, the gray line depicts the targeted RH and the blue line depicts the actual RH.

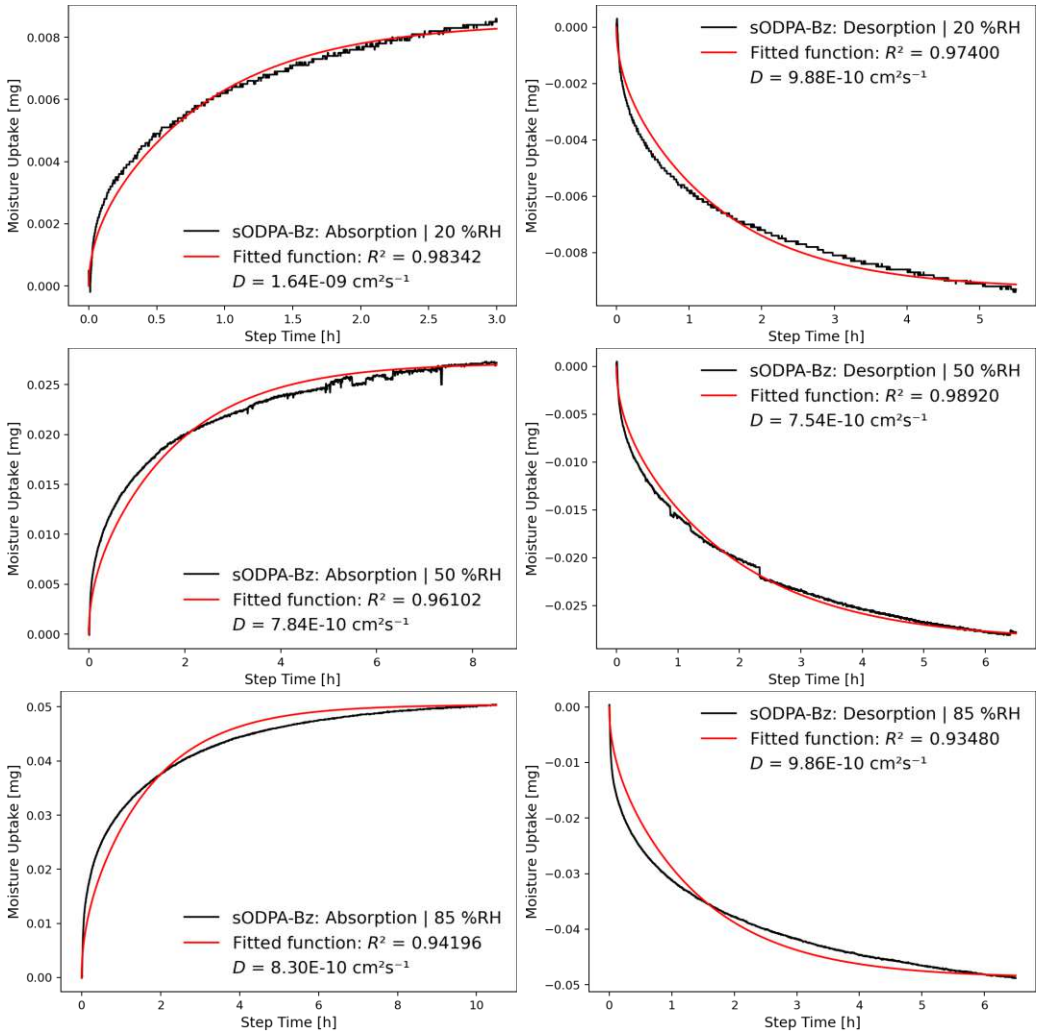

Figure D.59: Each sorption step of the discarded sODPA-Bz measurement, separated for calculating the (discarded) diffusion coefficients by fitting Crank's mass diffusion formula to the data series.

D.2.22 sODPA-mDMBz

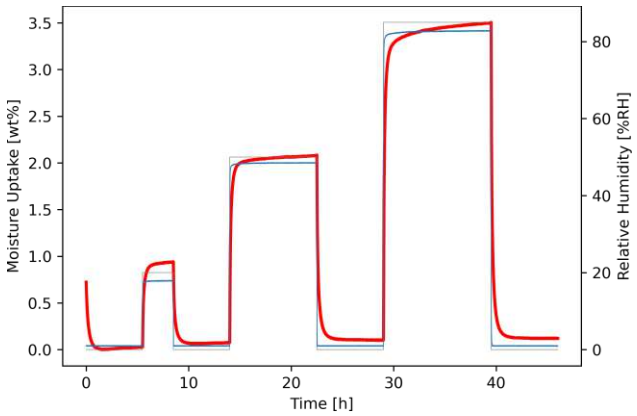

Figure D.60: Full refined measurement profile (46 h total length) of sODPA-mDMBz used for determining both moisture uptake and diffusion coefficients. The red line depicts the relative sample mass, the gray line depicts the targeted RH and the blue line depicts the actual RH.

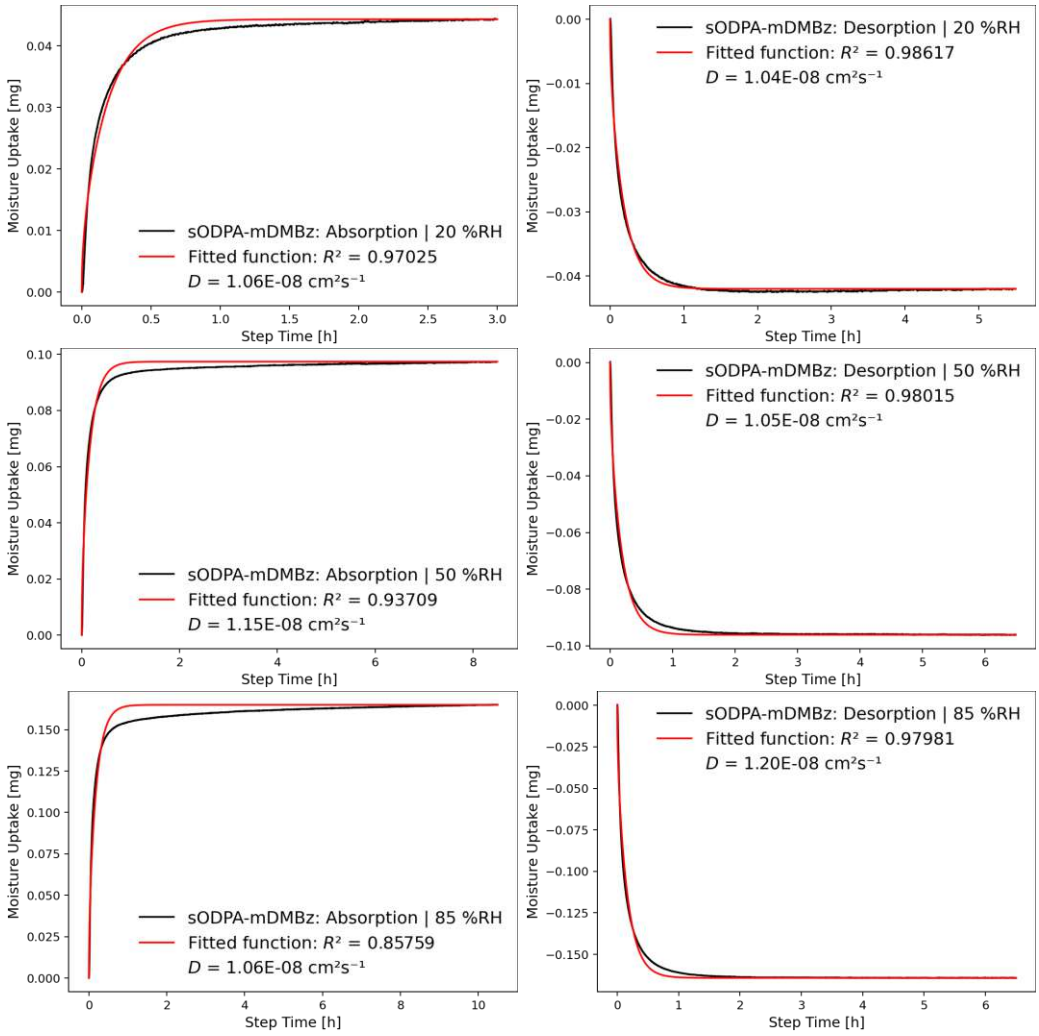

Figure D.61: Each sorption step of the refined PMDA-mDMBz measurement, separated for calculating the diffusion coefficients by fitting Crank's mass diffusion formula to the data series.

D.2.23 sODPA-mTFBz

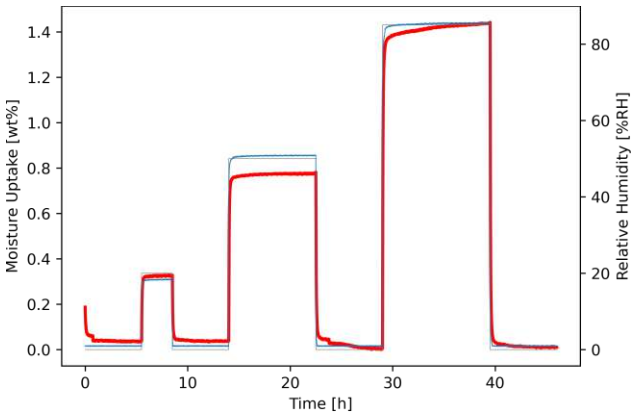

Figure D.62: Full refined measurement profile (46 h total length) of PMDA-mTFBz used for determining both moisture uptake and diffusion coefficients. The red line depicts the relative sample mass, the gray line depicts the targeted RH and the blue line depicts the actual RH.

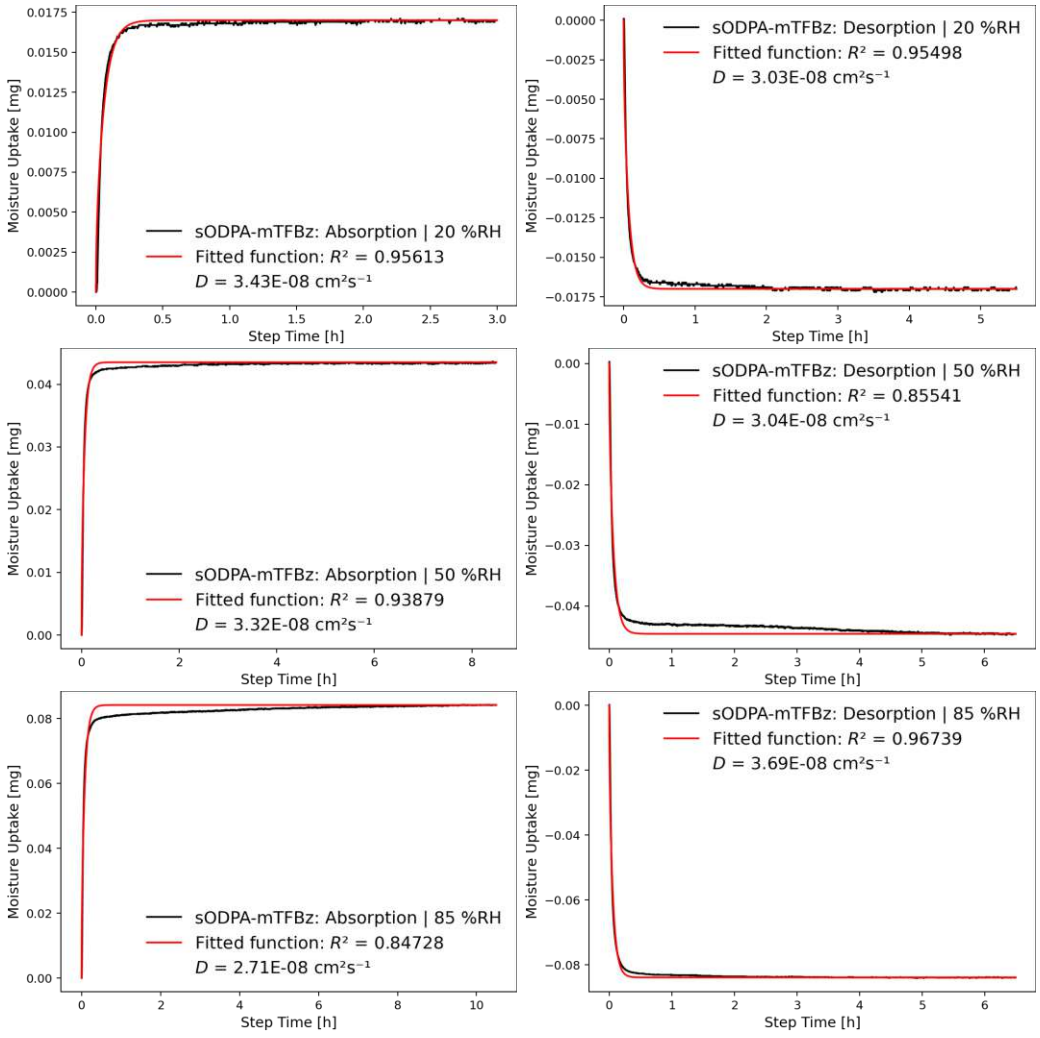

Figure D.63: Each sorption step of the refined PMDA-mTFBz measurement, separated for calculating the diffusion coefficients by fitting Crank's mass diffusion formula to the data series.

D.2.24 sODPA-oDIAN

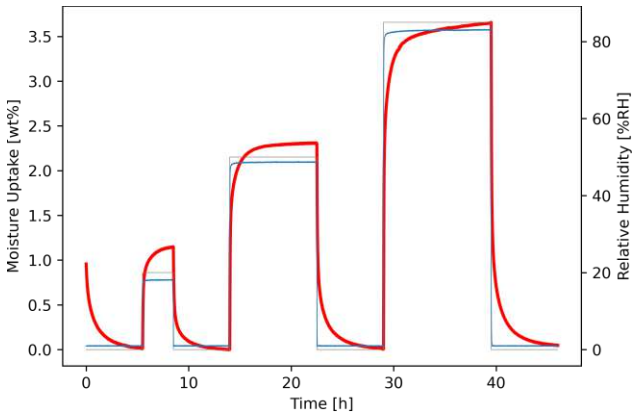

Figure D.64: Full refined measurement profile (46 h total length) of sODPA-oDIAN used for determining both moisture uptake and diffusion coefficients. The red line depicts the relative sample mass, the gray line depicts the targeted RH and the blue line depicts the actual RH.

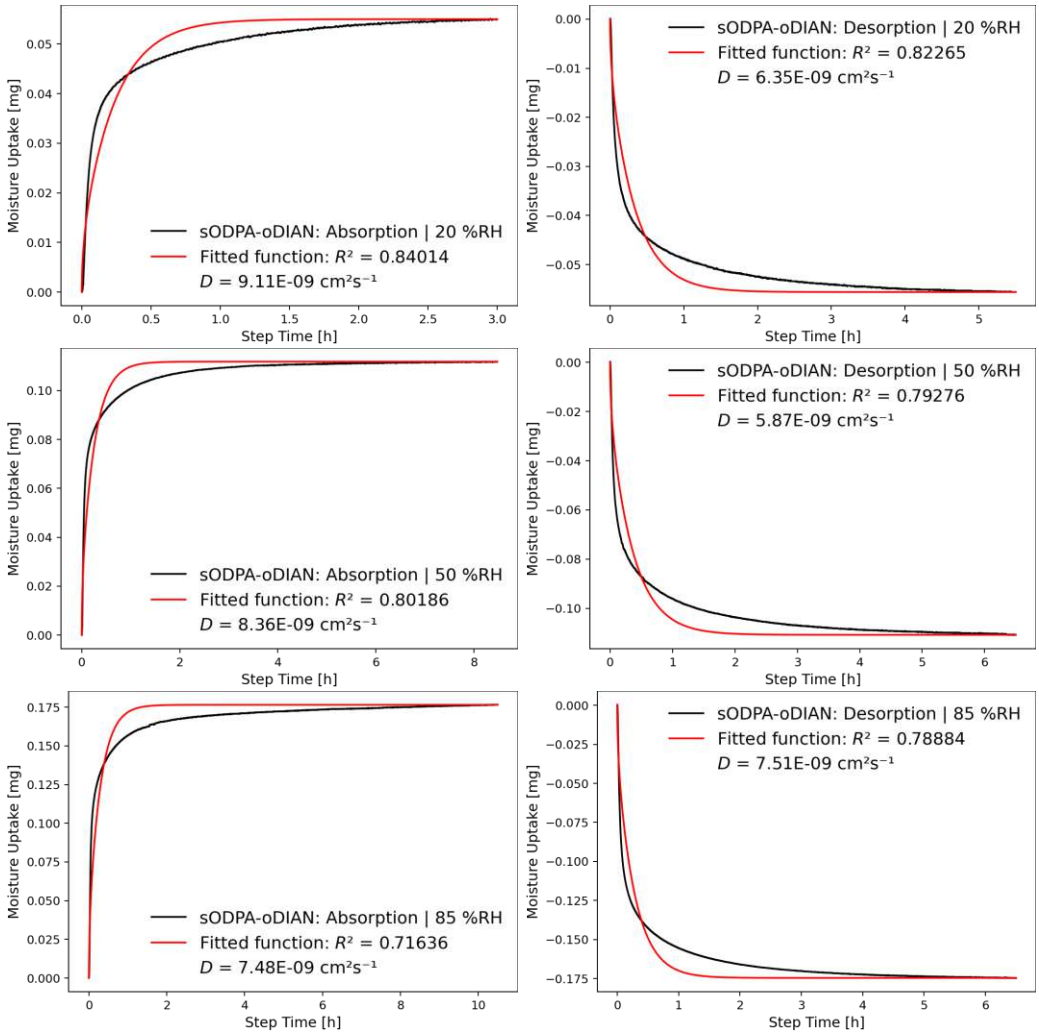

Figure D.65: Each sorption step of the refined sODPA-oDIAN measurement, separated for calculating the diffusion coefficients by fitting Crank's mass diffusion formula to the data series.

Publications

2) M. Fortea-Verdejo, E. Bumbaris, C. Burgstaller, A. Bismarck and K.-Y. Lee, *International Materials Reviews* **2017**, vol. 01/2017, 1-24. "Plant fibre-reinforced polymers: where do we stand in terms of tensile properties?"
1) M. Fortea-Verdejo, E. Bumbaris, K.-Y. Lee, and A. Bismarck, *Materials Science Forum* **2015**, vol. 825-826, 1063-1067. "Bacterial Cellulose Reinforced Flax Fiber Composites: Effect of Nanocellulose Loading on Composite Properties"

Conference Contributions

9) POSTER: "Tuning High-Performance Polyimides for Microelectronics", E. K. Bumbaris and M. M. Unterlass, Infineon Campeon Innovation Week 2019, Oct 24th, Munich, Germany.
8) POSTER: "Tuning High-Performance Polyimides for Microelectronics", E. K. Bumbaris and M. M. Unterlass, Infineon Regensburg Innovation Week 2019, June, Regensburg, Germany.
7) POSTER: "Tuning High-Performance Polyimides for Microelectronics", E. K. Bumbaris and M. M. Unterlass, Infineon University Day 2018, Nov 11th, Villach, Austria.
6) POSTER: "Tuning High-Performance Polyimides for Microelectronics", E. K. Bumbaris and M. M. Unterlass, Infineon Campeon Innovation Week 2018, Oct 24th, Munich, Germany.
5) POSTER: "Tuning High-Performance Polyimides for Microelectronics", E. K. Bumbaris and M. M. Unterlass, Infineon Regensburg Innovation Week 2018, Jun 19th-21st, Regensburg, Germany.
4) TALK: "Environmentally Friendly Generation of High-Performance Polyimide Foams Using Monomer Salts", E. K. Bumbaris and M. M. Unterlass, Vienna Young Scientists Symposium 2018, Jun 7th-8th, Vienna, Austria
3) POSTER: "Synthesis of Ammonium Carboxylate Monomer Salts and their Solid-State Polymerization to Polyimides", E. K. Bumbaris and M. M. Unterlass, 17th Austrian Chemistry Days 2017, Sept 25th-28th, Salzburg, Austria.
2) TALK: "Studying a Non-Classical Monomer Salt as Polyimide Precursor", E. K. Bumbaris and M. M. Unterlass, FuNMat 2017, Sept 20th-22nd, Plzeň, CZ.
1) POSTER: "Novel Monomer Salts and Their Solid-State Polymerization to Polyimides", E. K. Bumbaris and M. M. Unterlass, Danube Vltava Sava Polymer Meeting (DVSPM) 2017, September 5th-8th, Vienna, Austria.

Awards

1) "Best Poster Award" at the Austrian Chemistry Days 2017, Salzburg, Austria